UNIVERSITY OF CALIFORNIA, SAN DIEGO

Design Considerations for 400 GHz InP/InGaAs Heterojunction Bipolar Transistors

A dissertation submitted in partial satisfaction of the

requirements for the degree of Doctor of Philosophy

in

Electrical Engineering (Applied Physics)

by

James Chingwei Li

Committee in charge:

Peter M. Asbeck, Chair
Prabhakar Bandaru
Massimiliano Di Ventra
Silvanus S. Lau
Yuan Taur

2006

The dissertation of James Chingwei Li is

approved, and it is acceptable in quality and

form for publication on microfilm:

_____

_____

_____

_____

_____

Chair

University of California, San Diego

2006

This dissertation is dedicated to my wife,

who has started a new life in the United States for me

and eagerly awaited its completion.

TABLE OF CONTENTS

LIST OF FIGURES

LIST OF TABLES

ACKNOWLEDGEMENTS

To Professor Peter M. Asbeck, I thank you for four years of mentorship and guidance. You have tolerated a stubborn young engineer, and in your own way, you have tempered my impatience and challenged my abilities.

I gratefully acknowledge Professors Prabhakar Bandaru, Massimiliano DiVentra, S.S. Lau, and Yuan Taur for serving on my committee. You have forced me to consider new points of view and avenues of thought throughout the writing of this dissertation.

I would like to thank Marko Sokolich, Tahir Hussain, and Donald A. Hitko for acting as off-campus advisors and reviewing reams of manuscript. I must also thank Mary Chen, Charles Fields, Rajesh Rajavel, Yakov Royter, Steven Thomas III, and the many members of the Microelectronics staff. The many pages of experiment and simulation that follow have benefited greatly from discussions with you and would not have been possible without the wafers you worked so hard to fabricate. To the two directors of MEL, William Stachina and David Chow, thank you for your financial support and keeping the relationship between UCSD and HRL alive.

To Peter J. Zampardi, thank you for turning me to the "dark side". I do not exaggerate when I say that your advice has changed the course of my life. Your family has provided me a home away from home during the trips to Los Angeles. You have truly been both friend and colleague.

Finally, I want to thank my parents who have given me the skills, spirit, and discipline that have guided me through life. This dissertation is the fruit of your life's

work. The early morning commutes to Los Angeles would not have been possible without the long phone calls to my sister. You kept me on the road physically and spiritually. To my wife, thank you for your patience and strength during these last two years. You have restored balance in my life and I am looking forward to spending the rest of our lives together.

Chapter 2, in full, has been submitted for publication in Solid State Electronics, 2006. The contributions from the co-authors Tahir Hussain, Donald A. Hitko, Yakov Royter, Charles H. Fields, Ivan Milosavljevic, Stephen Thomas III, Rajesh D. Rajavel, and Marko Sokolich of HRL Laboratories, L.L.C., and Peter M. Asbeck of UCSD are appreciated. The author of this dissertation was the primary investigator and primary author of this publication. This work was sponsored by the Defense Advanced Research Projects Agency (DARPA) through AFRL Contract F33615-02-1286 (TFAST). The authors would like to thank Mark Banbrook, Cristian Cismaru, and Peter J. Zampardi of Skyworks Solutions, Inc. for their assistance with low temperature S-parameter measurements.

Chapter 3, in full, is a reprint as it appears in the Proceedings of the 2003 International Symposium on Compound Semiconductors. The contributions from the coauthors Tahir Hussain, Donald A. Hitko, Charles H. Fields, and Marko Sokolich of HRL Laboratories, L.L.C., and Peter M. Asbeck of UCSD are appreciated. The author of this dissertation was the primary investigator and primary author of this publication. This work was sponsored by the Defense Advanced Research Projects Agency (DARPA) through AFRL Contract F33615-02-1286 (TFAST). The authors would like to thank John Zolper of DARPA, and John King and Mark Pacer of AFRL for their support. In

addition, the donation of simulation software and technical support from ISE Inc. is greatly appreciated.

Chapter 4, in full, is a reprint as it appears in the Technical Digest of the 2005 Compound Semiconductors IC Symposium. The contributions from the co-authors Tahir Hussain, Donald A. Hitko, and Marko Sokolich of HRL Laboratories, L.L.C., and Peter M. Asbeck of UCSD are appreciated. The author of this dissertation was the primary investigator and primary author of this publication. This work was sponsored by the Defense Advanced Research Projects Agency (DARPA) through AFRL Contract F33615-02-1286 (TFAST). We thank Dr. John Zolper and Dr. Stephen Pappert of DARPA, and Mr. Mark Pacer and Dr. Charles Cerny of AFRL for their support. We also thank the many contributors to the TFAST effort at HRL, and especially members of HRL's High Speed Circuits Laboratory for wafer fabrication.

Chapter 5, in full, has been submitted for publication to the IEEE Transactions on Electron Devices. The contributions from the co-authors Donald A. Hitko and Marko Sokolich of HRL Laboratories, L.L.C., and Peter M. Asbeck of UCSD are appreciated. The author of this dissertation was the primary investigator and primary author of this publication.

Chapter 7, in full, is a reprint as it appears in the IEEE Electron Device Letters, vol. 26, no, 3, pp. 136-138, March 2005. The contributions from the co-authors Mary Chen, Donald A. Hitko, Charles H. Fields, Binqiang Shi, Rajesh Rajavel, and Marko Sokolich of HRL Laboratories, L.L.C., and Peter M. Asbeck of UCSD are appreciated. The author of this dissertation was the primary investigator and primary author of this publication.

This work was sponsored by the Defense Advanced Research Projects Agency (DARPA) through AFRL Contract F33615-02-1286 (TFAST).

Chapter 8, in full, has been submitted for publication to the IEEE Transactions on Electron Devices. The contributions from the co-authors Yakov Royter, Tahir Hussain, Mary Y. Chen, Charles H. Fields, Rajesh D. Rajavel, Steven S. Bui, Binqiang Shi, Donald A. Hitko, David H. Chow, and Marko Sokolich of HRL Laboratories, L.L.C., and Peter M. Asbeck of UCSD are appreciated. The author of this dissertation was the primary investigator and primary author of this publication. This work was sponsored by the Defense Advanced Research Projects Agency (DARPA) through AFRL Contract F33615-02-1286 (TFAST).

Appendix C, in full, is a reprint as it appears in Solid State Electronics, vol. 50, 2006. The contributions from the co-authors Tahir Hussain and Marko Sokolich of HRL Laboratories, L.L.C., and Peter M. Asbeck of UCSD are appreciated. The author of this dissertation was the primary investigator and primary author of this publication. This work was sponsored by the Defense Advanced Research Projects Agency (DARPA) through AFRL Contract F33615-02-1286 (TFAST). We also thank the many contributors to the TFAST effort at HRL, and especially members of HRL's High Speed Circuits Laboratory for wafer fabrication.

VITA

June 1997	B.S. Electrical Science and Engineering, Massachusetts Institute of Technology
1998 – 1999	Teaching Assistant, Department of Electrical Engineering and Computer Science, Massachusetts Institute of Technology
January 1999	M.Eng. Electrical Engineering and Computer Science, Massachusetts Institute of Technology
1997 – 2000	Engineer, BiCMOS Modeling and Characterization Department, IBM Microelectronics
2000 – 2002	Member of the Technical Staff, Advanced III-V Devices Group, Rockwell Scientific Company
2002 – 2006	Research Assistant, University of California, San Diego
June 2006	Ph.D. Electrical Engineering University of California, San Diego

PUBLICATIONS AND PRESENTATIONS

J.C. Li, Y. Royter, T. Hussain, M.Y. Chen, C.H. Fields, R.D. Rajavel, S.S. Bui, B. Shi, D.A. Hitko, D.H. Chow, P.M. Asbeck, and M. Sokolich, "Investigation into the Scalability of Selectively Implanted Buried Sub-Collector (SIBS) for Sub-Micron InP DHBTs", *IEEE Transactions on Electron Devices*, In Review.

J.C. Li, T. Hussain, D.A. Hitko, Y. Royter, C.H. Fields, I. Milosavljevic, S. Thomas III, R.D. Rajavel, P.M. Asbeck, and M. Sokolich, "Reduced Temperature *S*-Parameter Measurements of 400+ GHz Sub-Micron InP DHBTs", *Solid State Electronics*, In Review.

J.C. Li, D.A. Hitko, M. Sokolich, and P. M. Asbeck, "Experimental Method to Thermally De-embed Pads from R_{TH} Measurements", *IEEE Transactions on Electron Devices*, In Review.

J.C. Li, M.Y. Chen, Z. Lao, R. D. Rajavel, S. Thomas III, S.S. Bui, B. Shi, K.V. Guinn, J.R. Duvall, D.A. Hitko, D.H. Chow, and M. Sokolich, "200 GHz InP DHBT Technology using Selectively Implanted Buried Sub-Collector (SIBS) for Broadband Amplifiers", *IEEE Electron Device Letters*, In Review.

J.C. Li, M. Sokolich, T. Hussain, and P.M. Asbeck, "Physical Modeling of Degenerately Doped Compound Semiconductors for High Performance HBT Design", *Solid State Electronics*, Accepted for publication.

R.D. Rajavel, M.Y. Chen, Y. Royter, J.C. Li, S.S. Bui, D.H. Chow, M. Sokolich, T. Hussain, and D.A. Hitko, "Re-growth of Transistors on Implanted InP", *2006 Indium Phosphide and Related Materials Conference Proceedings*, 2006.

P.J. Zampardi, M. Sun, L. Rushing, K. Nellis, K. Choi, J.C. Li and R. Welser, "Demonstration of a Low Vref PA Based on InGaAsN Technology", *2006 IEEE Topical Workshop on Power Amplifiers for Wireless Communications*, 2006.

J.C. Li, T. Hussain, D.A. Hitko, P.M. Asbeck, and M. Sokolich, "Characterization and Modeling of Thermal Effects in Sub-Micron InP DHBTs", *2005 IEEE Compound Semiconductor Integrated Circuit Symposium Technical Digest*, pp. 65-68, Oct. 2005.

D.A. Hitko, T. Hussain, J.C. Li, C.H. Fields, and K. Elliott, "Circuit Design Considerations for 100 GHz Clock Rates", *2005 IEEE Compound Semiconductor Integrated Circuit Symposium Technical Digest*, pp. 252-255, Oct. 2005.

J.C. Li, M. Chen, D.A. Hitko, C.H. Fields, B. Shi, R. Rajavel, P.M. Asbeck, and M. Sokolich, "A submicrometer 252 GHz f_T and 283 GHz f_{MAX} InP DHBT with reduced C_{BC} using selectively implanted buried subcollector (SIBS)", *IEEE Electron Device Letters*, vol. 26, no. 3, pp. 136-138, March 2005.

T. Hussain, Y. Royer, D. Hitko, M. Montes, M. Madhav, I. Milosavljevic, R. Rajavel, S. Thomas, M. Antcliffe, A. Arthur, Y. Boegeman, M. Sokolich, J. Li, and P. Asbeck, "First Demonstration of Sub-0.25 μm Width Emitter InP DHBTs with >400 GHz f_t and >400 GHz f_{max}", *2004 IEEE International Electron Devices Meeting*, pp. 553-556, Dec. 2004.

M. Sokolich, M.Y. Chen, R.D. Rajavel, D.H. Chow, Y. Royter, S. Thomas III, C.H. Fields, B. Shi, S.S. Bui, J.C. Li, D.A. Hitko, K.R. Elliott, "InP HBT integrated circuit technology with selectively implanted subcollector and regrown device layers", *IEEE Journal of Solid State Circuits*, vol. 39, no. 10, pp. 1615-1621, Oct. 2004.

C. Cismaru, J.C. Li, and P.J. Zampardi, "Technique for Measuring Base-Emitter Misalignment Using Split Base Structure", *2004 Bipolar/BiCMOS Circuits and Technology Meeting Proceedings*, pp. 32-35, Sept. 2004.

M. Feng, R.K. Price, R. Chan, T. Chung, R.D. Dupuis, D.M. Keogh, J.C. Li, A.M. Conway, D. Qiao, S. Raychaudhuri, and P.M. Asbeck, "Current Status of GaN Heterojunction Bipolar Transistors", *2004 IEEE Bipolar Circuits and Technology Meeting Proceedings*, pp. 26-31, Sept. 2004.

J.C. Li, D.M. Keogh, S. Raychaudhuri. A. Conway, D. Qiao, and P.M. Asbeck, "Analysis of High DC Current Gain Structures for GaN/InGaN/GaN HBTs", *IEEE Lester Eastman Conference on High Performance Devices Proceedings*, pp. 201-206, Aug. 2004.

D.M. Keogh, J.C. Li, A.M. Conway, D. Qiao, S. Raychaudhuri, R.D. Dupuis, M. Feng, and P.M. Asbeck, "Analysis of GaN HBT Structures for High Power, High Efficiency Microwave Amplifiers", *IEEE Lester Eastman Conference on High Performance Devices Proceedings*, pp. 207-212, Aug. 2004.

A. Conway, J.C. Li, and P.M. Asbeck, "Effects of Gate Recess Depth on Pulsed I-V Chracteristics of AlGaN/GaN HFETs", *2003 International Semiconductor Device Research Symposium Digest*, pp. 439-440, Dec. 2003.

M. Sokolich, M.Y. Chen, D.H. Chow, Y. Royter, S. Thomas III, C.H. Fields, D.A. Hitko, B. Shi, M. Montes, S.S. Bui, Y.K. Boegemann, A. Arthur, J. Duvall, R. Martinez, T. Hussain, R.D. Rajavel, J.C. Li, K. Elliott, and J.D. Thompson, "InP HBT Intergrated Circuit Technology with Selectively Implanted Subcollector and Regrown Device Layers", *2003 IEEE Gallium Arsenide Integrated Circuit Symposium Technical Digest*, pp. 219-222, Nov. 2003.

J.C. Li, P.M. Asbeck, T. Hussain, D. A. Hitko, C. H. Fields, and M. Sokolich, "Effects of Device Design on the Thermal Properties of InP HBTs", *2003 International Symposium on Compound Semiconductors Technical Digest*, pp. 205-206, Aug. 2003.

J.C. Li, P.J. Zampardi, and V. Pho, "Predictive Modeling of InGaP/GaAs HBT Noise Parameters from DC and S-Parameter Data", *2003 Gallium Arsenide Manufacturing Technology Conference Digest*, 8.4, May 2003.

B. Brar, J.C. Li, R.L. Pierson, and J.A. Higgins, "InP HBTs - Present Status and Future Trends", *2002 IEEE Bipolar Circuits and Technology Meeting Proceedings*, pp. 155-161, Sept. 2002.

R.E. Welser, P.M. DeLuca, C.R. Lutz, B.E. Landini, M. Chaplin, K.S. Stevens, T.L. Wolfsdorf-Brenner, R.J. Welty, P.M. Asbeck, A. Ikhlassi, J.C. Li, and R.L. Pierson, "Pathway for HBT turn-on voltage reduction on a GaAs platform", *2001 Gallium Arsenide Manufacturing Technology Conference Digest*, 2.4, 2001.

ABSTRACT OF THE DISSERTATION

Design Considerations for 400 GHz InP/InGaAs Heterojunction Bipolar Transistors

by

James Chingwei Li

Doctor of Philosophy in Electrical Engineering (Applied Physics)

University of California, San Diego, 2006

Professor Peter M. Asbeck, Chair

The relatively wide bandgap, high low-field mobility, and high peak velocity of many compound semiconductors are inherent material advantages treasured by device engineers. For these reasons, InP and InGaAs compounds have emerged as the dominant semiconductor material system for Heterojunction Bipolar Transistors (HBTs) whose f_T and f_{MAX} exceeds 400GHz. High performance has been achieved through a combination of bandgap engineering and geometry scaling to delay the onset of Kirk effect and to reduce parasitic elements, respectively. This dissertation investigates the performance limitations of existing InP/InGaAs HBTs fabricated using a traditional mesa process and presents two methods to enhance performance.

Increases in the collector current density without sufficiently aggressive emitter area and voltage scaling have resulted in a rapid increase in the thermal resistance (R_{TH}) and junction temperature (T_j) of state-of-the-art InP/InGaAs HBTs. Measurements in this dissertation show a f_T increase of 8-10% with a 75˚C decrease in T_{amb}. Estimations of T_j using measured R_{TH} values show >75˚C rise over T_{amb} due to self-heating at peak f_T, indicating that 10% or more improvement in f_T is possible if self-heating were minimized or eliminated. A 3-D thermal model has been developed to explore the thermal optimization of HBT design and predict R_{TH} in an IC environment. A new experimental method to thermally de-embed the effects of the test environment has also been developed.

Velocity overshoot and quasi-ballistic transport, phenomena that occur readily in III-V materials, are expected to play a dominant role in device performance. Experimental data indicate that the electron velocity exceeds the steady-state velocity by a factor of two or more. A 2-D electro-thermal model was developed to explore the nature of carrier transport through these devices. Several critical modifications to the device simulator and proper calibration of material parameters are discussed.

Finally, an adaptation of the Selective Implanted Collector, used in silicon bipolar transistors, is presented for InP/InGaAs HBTs. The new HBT structure, designated Selectively Implanted Buried Sub-collector (SIBS), is used to simultaneously reduce the collector transit time and base-collector capacitance. The electrical properties and scalability of SIBS is studied through a series of DC, CV, and RF measurements.

1. INTRODUCTION

1.0 Motivation

Research and development of InP-based HBTs have been active areas for several decades, but the pace of this development has increased recently due to the rapid growth of the internet and other communications systems. The ability of InP-based HBTs to achieve both superior speed and voltage handling capability (up to output swings of 11.0 V at 45 Gbps data rates [1-1]), provides unique opportunities for device and circuit designers. Few semiconductor materials have the ability to be used for high-performance digital, mixed-signal, and analog ICs with little change in the device design. Since the existing markets for InP-based HBTs emphasize superior performance over cost and integration, there is a persistent need to comprehend and model the electro-thermal properties of each generation of InP-based HBTs. The newest generations of devices with f_T and f_{MAX} values on the order of 400 GHz have aggressively scaled device geometries deep into the sub-micron regime, but the emitter area scaling has not kept pace with the increase in operating current density. The resulting rise in power density represents a potential barrier to the utilization of existing devices in ICs and the further improvement of device performance. This dissertation explores performance limits both through experiment and simulation and presents a set of guidelines for the design of 400 GHz InP-based HBTs.

1.1 Compound Semiconductor Materials

Many in the semiconductor industry consider InP and InGaAs compounds as exotic materials, but these two semiconductors offer several key advantages over the most widely used semiconductor, silicon. Table 1-1 compares several material properties of InP; $In_{0.53}Ga_{0.47}As$, which is lattice matched to InP; and silicon. It is clear that both InP and $In_{0.53}Ga_{0.47}As$ provide a significant advantage in electron effective mass, peak velocity, and low-field mobility. With low-field electron mobility that ranges from 4X to 8.75X greater than silicon, parasitic resistances throughout an electron device can be significantly reduced. This advantage also extends to the high-field regime where the electron peak velocity is 2.0X to 2.5X greater than silicon. For an electron traversing a drift region (collector of a bipolar transistor or the drain-side channel of a FET), the overall transit time can be 50% or less than the comparable silicon device. In compound semiconductor devices, both high performance Hetero-junction Bipolar Transistors (HBTs) and Field Effect Transistors (FETs), these material advantages have been leveraged to produce the fastest transistors in the world.

Table 1-1: Summary of key material parameters for InP, $In_{0.53}Ga_{0.47}As$, and Si at T = 300 K. All values are taken from [1-2].

Material Property at T = 300K	Units	InP	$In_{0.53}Ga_{0.47}As$	Si
Bandgap	eV	1.35	0.75	1.12
Thermal Conductivity	W/cm·K	0.68	0.05	1.5
Electron effective mass	m_o	0.078	0.041	0.98/0.19
Electron peak velocity	$x10^7$cm/s	2.5	3	1
Electron mobility ($N_D = 1x10^{17}$ cm^{-3})	$cm^2/V{\cdot}s$	3200	7000	800

Despite the overwhelming advantages of compound semiconductors in electron transport, silicon does hold two critical advantages in addition to a high quality oxide and oxide interfaces over most compound semiconductors, thermal conductivity and Density

Of States (DOS). In general, the higher thermal conductivity of silicon allows greater power and higher transistor densities to be achieved. Conversely, the high thermal conductivity reduces self-heating and any of its negative consequences on performance and robustness. The higher electron effective mass corresponds to a higher conduction band DOS, which allows a higher donor concentration to be used before the onset of high doping effects e.g. degeneracy and band filling. These two deficiencies have plagued compound semiconductor devices and may impede future advancements in performance.

For the device engineer, it is not the individual properties of any one semiconductor that are important, but the variety of material properties from which to choose. The narrow bandgap and high low-field mobility of $In_{0.53}Ga_{0.47}As$ is frequently paired with the wider bandgap and higher thermal conductivity InP to provide the best compromise of electrical properties. In addition to InGaAs, InAlAs and GaAsSb compounds can also be grown lattice matched or strained on InP. These materials have differing carrier transport properties as well as bandgap and electron affinities. Figure 1-1 illustrates the numerous material choices and hetero-interfaces that are available to device engineers working in the InP material system. The silicon industry has adopted the use of Silicon-Germanium alloys, which has introduced a narrower bandgap material to device engineers, but the deviation from silicon is relative small. The freedom to choose a material based on the desired electrical properties, and the ability to integrate it with others into the layer structure of an electron device forms the cornerstone of bandgap engineering. This is the one true advantage of compound semiconductors over silicon.

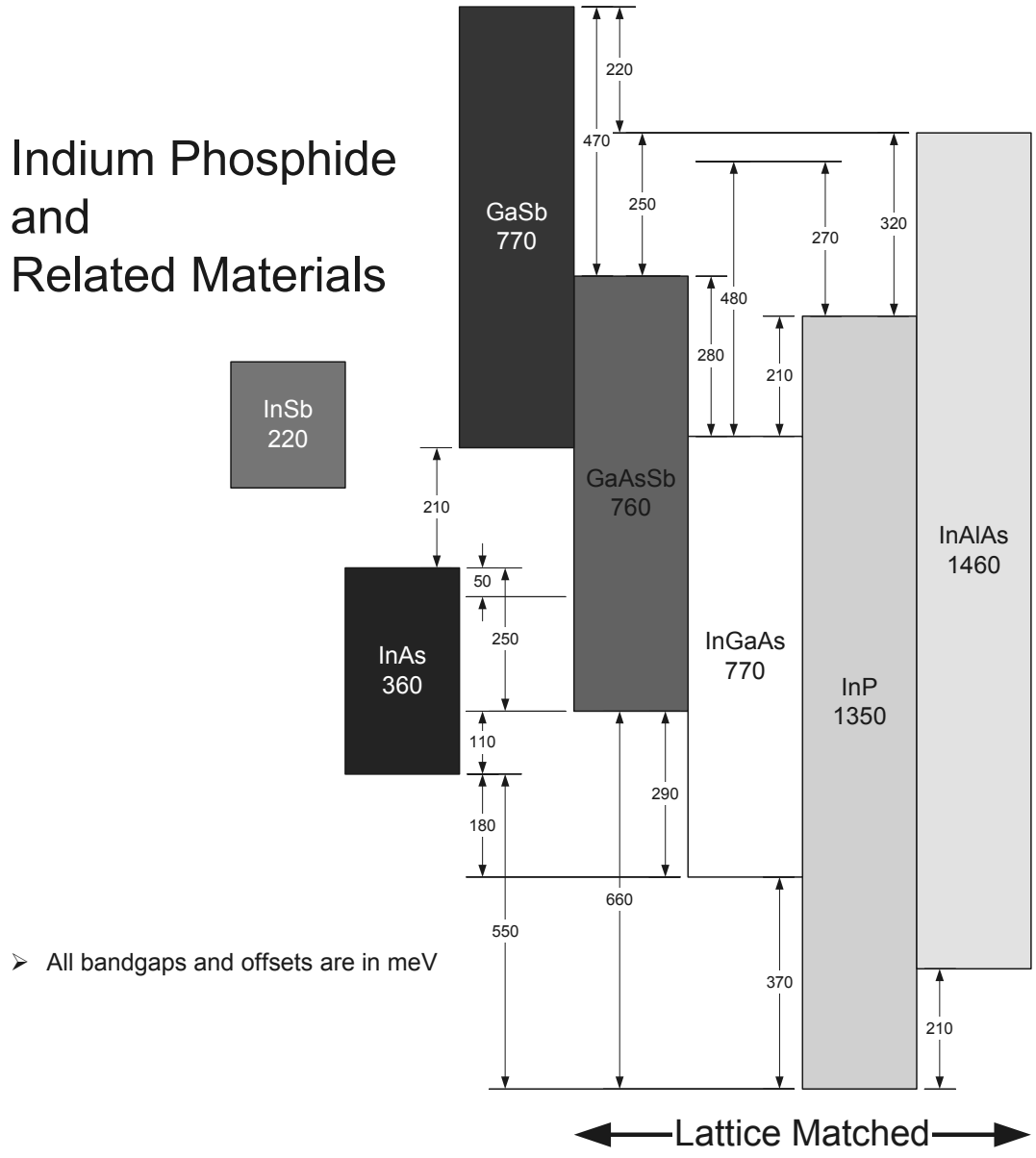

Figure 1-1: Bandgap and band line-ups of InP and its related materials.

1.2 HBT Structure

The fabrication of InP-based HBTs is relatively simple compared to any of the commercially available SiGe HBT process technologies. Molecular Beam Epitaxy

(MBE) or Metal-Organic Chemical Vapor Deposition (MOCVD) is used to grow the device layers on a semi-insulating InP substrate. For the fabrication of 400 GHz InP-based HBTs, MBE is the preferred means of growth due to its precision at depositing layers thinner than 5 nm. All device layers are typically grown prior to any wafer processing, and the subsequent processing steps only remove the unwanted material.

The ability to perform bandgap engineering allows the emphasis to be placed on material growth and not wafer processing. Figure 1-2 shows the basic structure and the common layers of a conventional triple-mesa compound semiconductor HBT. The emitter, base-collector, and sub-collector layers form the three mesas, and metal contacts are deposited on each. This structure is common to nearly all compound semiconductor HBTs, and it is the selection of materials for each of these layers that determines the HBT type and electrical characteristics. Common to all compound semiconductor HBTs is the presence of a hetero-junction between a narrower bandgap base and a wider bandgap emitter. However, HBTs are further sub-divided into two categories based on the material selection in the collector. A Single Heterojunction Bipolar Transistor (SHBT) has one hetero-interface at the base-emitter junction and the Double Heterojunction Bipolar Transistor (DHBT) has an additional hetero-interface at the base-collector junction. Table 1-2 lists the typical materials used for InP-based SHBTs and DHBTs. The proper material selection for each layer for optimum electrical characteristics can be found in [1-3].

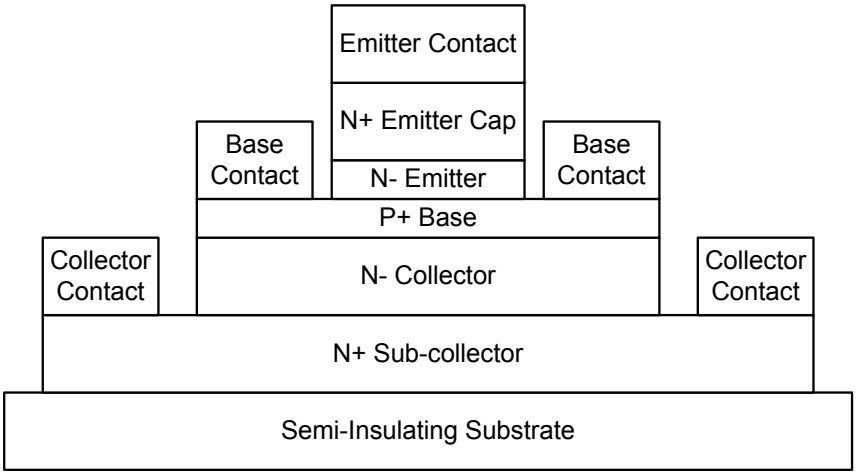

Figure 1-2: Schematic cross-section of a canonical triple-mesa HBT structure.

Table 1-2: Typical materials selection for the layers of a InP-based HBT.

Layer	Type	SHBT	DHBT
Emitter Cap	N+	InGaAs	InGaAs
Emitter	N-	InAlAs or InP	InAlAs or InP
Base	P+	InGaAs	InGaAs
Collector	N-	InGaAs	InP
Sub-collector	N+	InGaAs or InP	InGaAs or InP
Substrate	S.I.	InP	InP

1.3 HBT Performance

Many different factors must be considered in the design of a high performance HBT, but for the purposes of this discussion, the performance of an HBT will be narrowly judged by two small-signal figures of merit, f_T and f_{MAX}. f_T is defined as the frequency at which unity current gain is achieved, and f_{MAX} is defined similarly as the frequency at which unity power gain is achieved. Although materials selection plays an important role, the doping concentrations and geometry for each layer are equally important in determining HBT performance. The selection of these physical properties can be divided into three categories of scaling: vertical, horizontal, and power. Each category has a single relation that dominates the design process, but the interaction of

these different relations is not straight forward. It is the task of the device designer to balance the concerns of one category against the remaining two.

1.3.1 Vertical Scaling

The effect of vertical scaling on the high speed performance of the ideal Bipolar Junction Transistor (BJT) is governed by the following relation [1-3],

$$f_T = \frac{1}{2\pi\tau_{ec}} = \frac{kT}{nqI_C}\left(C_{BE} + C_{BC}\right) + (R_E + R_C)C_{BC} + \tau_B + \tau_C \qquad (1\text{-}1)$$

where R_E and R_C are the emitter and collector resistances, respectively; C_{BE} and C_{BC} are the base-emitter and base-collector capacitances, respectively; and I_C is the collector current. The reduction of the base and collector thicknesses reduces the time required to transit these regions, τ_B and τ_C. However, thinning the base increases the lateral sheet resistance of this layer and the total base resistance, R_B. The thinning of the collector is balanced by an increase in the base-collector capacitance, C_{BC}. From Equation (1-1), the need to optimize R_E, R_C, C_{BE}, and I_C in order to realize an increase in f_T due to reduced τ_B and τ_C is evident.

1.3.2 Horizontal Scaling

The effect of horizontal scaling on high speed performance is governed by the following deceptively simple relation [1-3],

$$f_{MAX} = \sqrt{\frac{f_T}{8\pi R_B C_{BC}}} \qquad (1\text{-}2)$$

where f_T is defined by Equation (1-1). The trade-offs involved in collector design for high f_{MAX} are not self-evident. C_{BC} appears directly in Equation (1-2), but the collector

thickness and indirectly C_{BC} affect f_T as well. Any increases in R_B and C_{BC} from vertical scaling can be offset by the reduction of the base contact to emitter mesa spacing and the total base-collector junction area as seen in Figure 1-2. However, both of these actions demand improvements in wafer processing, and horizontal geometry reductions cannot be so aggressive that process variation dominates device performance.

1.3.3 Power Scaling

If the BJT collector current, I_C, is increased, the first term on the right hand side of Equation (1-1) decreases, and the theoretical maximum value of f_T is determined by the remaining three terms. In reality, f_T begins to decrease well before this theoretical maximum is reached, and the roll-off of f_T is a result of the Kirk effect [1-4]. Qualitatively, the Kirk effect describes the condition where the free-electrons entering the collector are so numerous that they begin to screen the collector space charge. Once this occurs, the applied collector voltage is shielded from the base-collector junction; the electric field in the collector changes rapidly; and carrier transport is disrupted resulting in the breakdown of Equation (1-1) and the roll-off of f_T. The critical current density where the f_T roll-off occurs is defined by the following relation [1-5],

$$J_{Kirk} = \nu_{sat}\left\{qN_C + \frac{2\varepsilon_C\left(V_{CB} + V_{bi}\right)}{t_c^2}\right\} \tag{1-3}$$

where v_{sat} is the carrier saturation velocity; ε_C is the collector dielectric constant; V_{CB} is the applied collector-base voltage; and V_{bi} is the base-collector built-in potential. By increasing the collector doping, N_C, and decreasing the collector thickness, t_C, J_{Kirk} can be increased, and the device can be allowed to more closely approach the maximum

theoretical f_T described by Equation (1-1). However, the rules that govern vertical and horizontal scaling do not allow t_C to be blindly reduced. In addition, increasing N_C will usually result in an increase in C_{BC} unless t_C is small enough to allow the collector to remain fully-depleted. It is the task of the device designer to increase J_{Kirk} so that the BJT can reach the maximum theoretical f_T described by Equation (1-1) without reducing the maximum theoretical f_T. Equation (1-3) is a general relation derived for long, uniformly doped collectors. The study of Kirk effect in modern devices requires a more generalized form of Equation (1-3) and is thoroughly discussed in [1-5].

1.4 Outline of the Dissertation

The work presented in this dissertation includes simulations and experiments designed to uncover the performance limitations and establish guidelines for the design of 400 GHz InP/InGaAs HBTs. The rapid evolution of these devices in the last four years has significantly altered the balance between various device parameters. It is this shift in balance that has forced previously insignificant factors into the limelight. Each chapter of this dissertation provides extensive background on its own subject matter as well as its relation to the overall dissertation. In most instances, each chapter also corresponds to a distinct journal publication.

Chapter 2 introduces the current state-of-the-art InP/InGaAs HBTs and their electrical behavior. Using well established methods of parameter extraction, key device parameters are quantified and compared for various emitter geometries. The measurements and analysis are then performed over a series of ambient temperatures (T_{amb}) in order to determine the components of the forward delay time that are

responsible for the observed f_T variation. These measurements also establish the degree of f_T improvement that can be expected if self-heating is minimized or eliminated through optimal thermal management.

Armed with this information, Chapter 3 presents the initial design study of the thermal optimization of InP-based HBTs. The impact of various materials, device geometries, and device layout variations on R_{TH} are explored. These simulation results were used as a guideline for the devices presented in Chapter 2 and subsequent fabrication runs. When compared to the previous generation of 1.0 μm wide emitter InP-based HBTs, the preliminary model showed reasonable agreement with experimental data, but several deficiencies were identified. Chapter 4 presents an improved 3-D thermal model and a comparison to the devices presented in Chapter 2. The addition of several features to better represent the fabricated HBT structure and collector heat source improved the correlation to experimental data significantly. Experimental methods to determine R_{TH} are limited to low dissipated powers, but the simulation is unencumbered by this limit. Additional results are presented showing the utility of the model by predicting the power dependence of R_{TH}; the effect of process variations on R_{TH}; thermally de-embedding the pads; and estimating the effective R_{TH} in an IC environment. To reinforce the simulation results presented in Chapters 3 and 4 as well as to illustrate the importance of test structure design on R_{TH} measurements, Chapter 5 presents an experimental method to de-embed the effects of probe pads.

With a good understanding of the thermal properties of InP-based HBTs, Chapter 6 explores the electro-thermal behavior of these devices. Appendix C follows with the modifications necessary for the proper modeling of degenerately doped InP and InGaAs

thin films, which are needed to fabricate HBTs capable of 400 GHz performance. An introduction to hydrodynamic simulations and device modeling is presented in Appendix D. Using the methodology presented in these appendices, Chapter 6 discusses the calibration of high-field transport models used to simulate velocity overshoot and ballistic transport. The high electron velocities and capacitance cancellation observed in Chapter 2 can be predicted, allowing the impact of many subtle aspects of device design to be explored through simulation.

The final contribution to this dissertation is the discussion of a new adaptation of the Selective Implanted Collector (SIC) from silicon bipolar transistors to InP HBTs, known as a Selectively Implanted Buried Sub-collector (SIBS). This device structure allows the simultaneous reduction of C_{BC} and τ_C. The implementation of SIBS requires the use of ion implantation and sub-micron fabrication techniques, which is introduced in Chapter 7. Chapter 8 presents a detailed investigation of the electrical properties and scalability of SIBS and its impact on device performance.

Chapter 9 summarizes the key findings in each of the preceding chapters, and emphasizes the design considerations established by this dissertation. This work shows that both thermal and electro-thermal behavior must be considered in the quest for ultimate performance. At the same time, new, as yet unanswered questions are raised, and suggestions for future research and design opportunities are discussed.

1.5 References

[1-1] J.C. Li, M.Y. Chen, Z. Lao, R.D. Rajavel, S. Thomas III, S.S. Bui, B. Shi, K.V. Guinn, J.R. Duvall, D.A. Hitko, D.H. Chow, and M. Sokolich, "200 GHz InP DHBT Technology using Selectively Implanted Buried Sub-Collector (SIBS) for Broadband Amplifers", *IEEE Electron Device Letters*, In Review.

[1-2] B. Brar, J.C. Li, R.L. Pierson, and J.A. Higgins, "InP HBTs - Present Status and Future Trends", *2002 IEEE Bipolar Circuits and Technology Meeting Proceedings*, pp. 155-161, Sept. 2002.

[1-3] W. Liu, *Handbook of III-V Heterojunction Bipolar Transistors*, New York, USA: John Wiley & Sons, 1998.

[1-4] C.T. Kirk, "A Theory of Transistor Cuttoff Frequency (f_T) Falloff at High Current Densities", *IRE Transactions on Electron Devices*, vol. ED-9, pp. 164-174, 1962.

[1-5] P.J. Zampardi, "A Study of New Base Pushout Effect in Modern Bipolar Transistors", *UCLA Ph.D. Thesis*, 1997.

2. REDUCED TEMPERATURE *S*-PARAMETER MEASUREMENTS OF 400+ GHZ SUB-MICRON INP DHBTS

2.0 Abstract

The high operating power density and aggressively scaled geometries associated with 400+ GHz InP-Based DHBTs present a new challenge in device design and thermal management. In order to assess the effects of self-heating on the RF performance, *S*-parameters of six InP DHBTs with varying emitter dimensions were measured over a 75 ˚C ambient temperature range. An 8-10% increase in peak f_T is observed as the temperature is reduced. Data analysis indicates that reductions in the base and collector transit times and the base-emitter charging times are responsible for the peak f_T improvement. The calculated electron velocities exceed $6x10^7$ cm/s, indicating velocity overshoot plays a critical role in the reduction of the transit times. When emitter scaling are considered, the total transit time variation is directly correlated to the rise in junction temperature. Using previously measured thermal resistance values, a 77 ˚C to 116 ˚C minimum junction temperature rise is estimated from self-heating. Therefore, the 8-10% increase in peak f_T is a reasonable estimate of the performance to be recovered by minimizing self-heating. Improved intra-device thermal management through device design is an important supplement to geometry scaling as a means to enhance device performance.

2.1 Introduction

The f_T of InP-based Single Hetero-junction HBTs (SHBTs) has been reported to exceed 500 GHz [2-1],[2-2] and more recently, InP-based Double Hetero-junction HBTs (DHBTs) have crossed the 400 GHz barrier [2-3],[2-4]. In order for HBTs to achieve this level of RF performance, the device dimensions must be aggressively scaled to reduce parasitic resistances and capacitances [2-5], and the onset of Kirk effect must be delayed to allow the device to operate at higher current densities [2-6]. Although dimensional scaling increases the device thermal resistance (R_{TH}), the total device power generally decreases due to the reduced emitter area (A_E). However, RF performance continues to drive the collector current density (J_C) higher, and at present, J_C exceeds 5 mA/μm^2 and approaches 10 mA/μm^2. In addition, the bandgaps of lattice matched materials in the InP system have not allowed V_{BE} or V_{CE} to be reduced significantly below 1.0 V. As a result, the total power density currently exceeds 7.5 mW/μm^2 and will soon reach 15 mW/μm^2. Unfortunately, dimensional scaling has not yet been adequately aggressive to reduce or even maintain constant power dissipation.

Although SHBTs have achieved the highest f_T values, the poor thermal conductivity and narrow bandgap of InGaAs have prevented SHBTs from gaining wider acceptance in ultra-high performance and high power applications. InP has nearly twice the bandgap of InGaAs and over ten times the thermal conductivity [2-7]. These properties make InP the logical choice over InGaAs for the collector [2-8],[2-9]. In order to build upon these material advantages, 3D thermal simulations have been used to study the impact of DHBT device design on R_{TH} [2-10]. Although these simulations have driven

improvements in DHBT design, thermal effects continue to play a significant role in 400+ GHz devices, and the cooperative heating, resulting from densely packing devices in a circuit, only magnifies the thermal management problem. To the authors' knowledge, this work presents the first quantitative data, on >400 GHz sub-micron emitter InP DHBTs, showing the degree of performance degradation due to self-heating and other thermal effects. S-parameter measurements of DHBTs with emitter widths of 250 nm and 400 nm and emitter lengths of 2, 4, 6, and 8 μm show as much as a 10% increase in the unity current gain cutoff frequency (f_T) as the ambient temperature (T_{amb}) decreased by 75 ˚C. Using this data, critical device parameters are extracted to diagnose the device quantity responsible for the observed performance improvement. Previously presented measured and simulated R_{TH} values [2-11] are then used to estimate the junction temperature rise (ΔT_j) and the RF performance in the case when all self-heating is minimized or even eliminated.

2.2 Device Structure and Fabrication

Molecular Beam Epitaxy is used to grow all device layers on a <100> semi-insulating InP substrate prior to device processing. The composite n+ sub-collector is comprised of 300 nm InP and 25 nm $In_{0.53}Ga_{0.47}As$ layers to minimize both collector sheet and contact resistance. A 120 nm InP collector and base-collector grade is lightly doped n-type to ensure that the collector is fully depleted at zero base-collector voltage. The p+ base is a 35 nm InGaAs layer and is compositionally graded to improve both base transit time and DC current gain. An abrupt n/n+ 90 nm InP emitter, and a composite n+

75 nm $In_{0.53}Ga_{0.47}As$ and pseudo-morphic InAs emitter cap complete the device layer structure.

Fabrication of these sub-micron DHBTs utilized a combination of Electron Beam Lithography (EBL) and optical lithography. The emitter metal was patterned using EBL and lift-off, and the emitter mesa was etched using a combination of dry and wet techniques to provide the necessary anisotropy and selectivity necessary to produce 250 nm wide emitter fingers. The base metal was also defined by EBL in order to minimize the total base-collector capacitance (C_{BC}). The remaining front-end processing steps were typical for a triple mesa HBT process, and the devices were passivated using a low-K dielectric. Two levels of interconnect, where each metal level is 0.8 μm thick and the inter-level spacing is 1.0 μm, were utilized for electrical contacts to the device.

2.3 Measurements at Reduced T_{amb}

In order to investigate the performance loss due to self-heating, high performance DHBTs were characterized at T_{amb} from –50 ºC to +25 ºC in 25 ºC increments. Over this limited temperature range, the reduction in T_{amb} should correspond to a comparable decrease in T_j. DC and RF measurements were performed on DHBTs with six different emitter areas, 0.25x4 μm^2, 0.25x6 μm^2, 0.25x8 μm^2, 0.40x2 μm^2, 0.40x4 μm^2, and 0.40x6 μm^2, in order to verify proper transistor operation. Using GGB Industries Inc. Ground-Signal-Ground (GSG) RF probes and HP11612B force-sense bias networks to prevent oscillation, both forward Gummel and common emitter IV curves were taken with a HP4142B mainframe. Figure 2-1 and Figure 2-2 show the representative DC characteristics of A_E = 0.40x4 μm^2 and A_E = 0.25x4 μm^2 DHBTs, respectively. Devices

with an emitter width (W_E) of 250 nm exhibit a peak DC current gain (β) equal to or greater than 70 at T_{amb} = +25 ˚C while devices with a W_E = 400 nm exhibit a peak β exceeding 100.

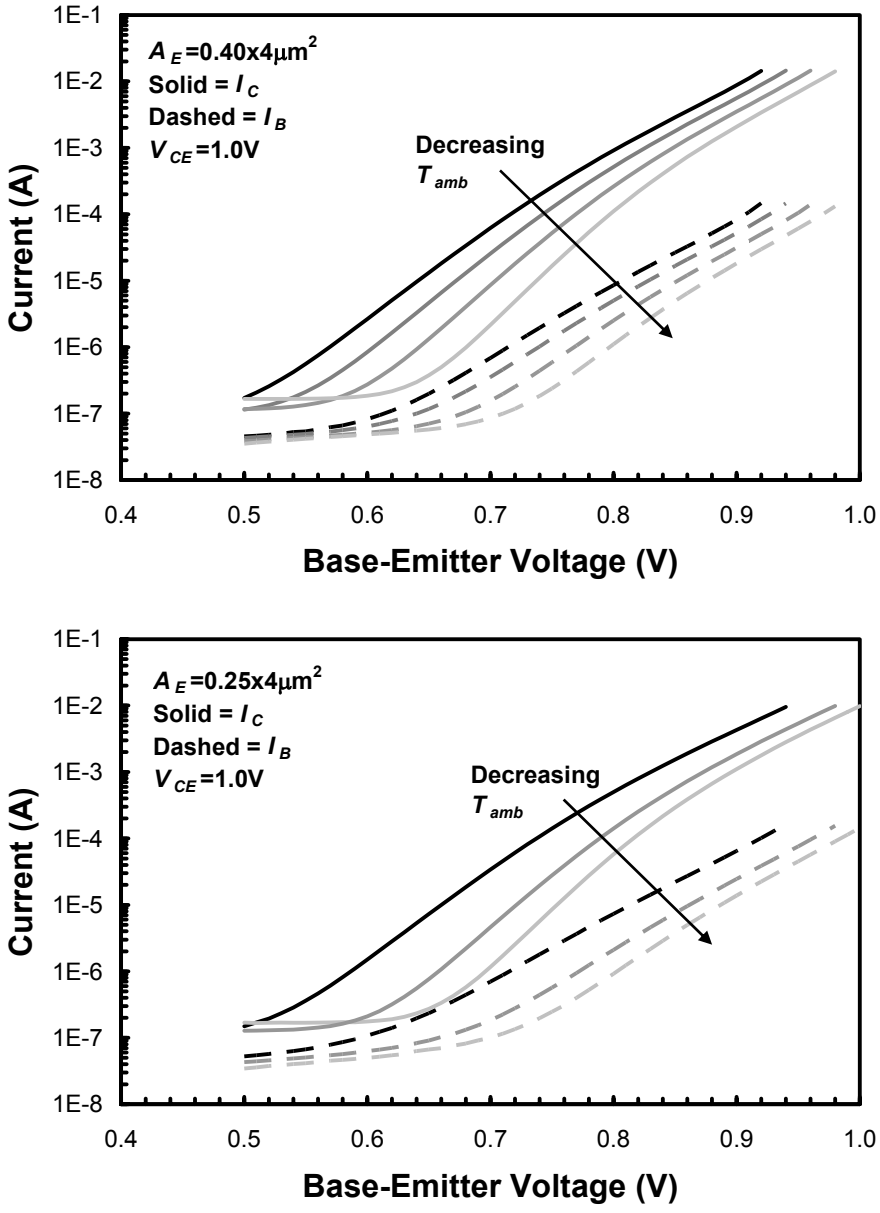

Figure 2-1: Forward Gummel curves of an A_E = 0.40x4 μm^2 DHBT (top) at T_{amb} = +25 ˚C, 0 ˚C, -25 ˚C, -50 ˚C and an A_E = 0.25x4 μm^2 DHBT (bottom) at T_{amb} = +25 ˚C, -25 ˚C, -50 ˚C.

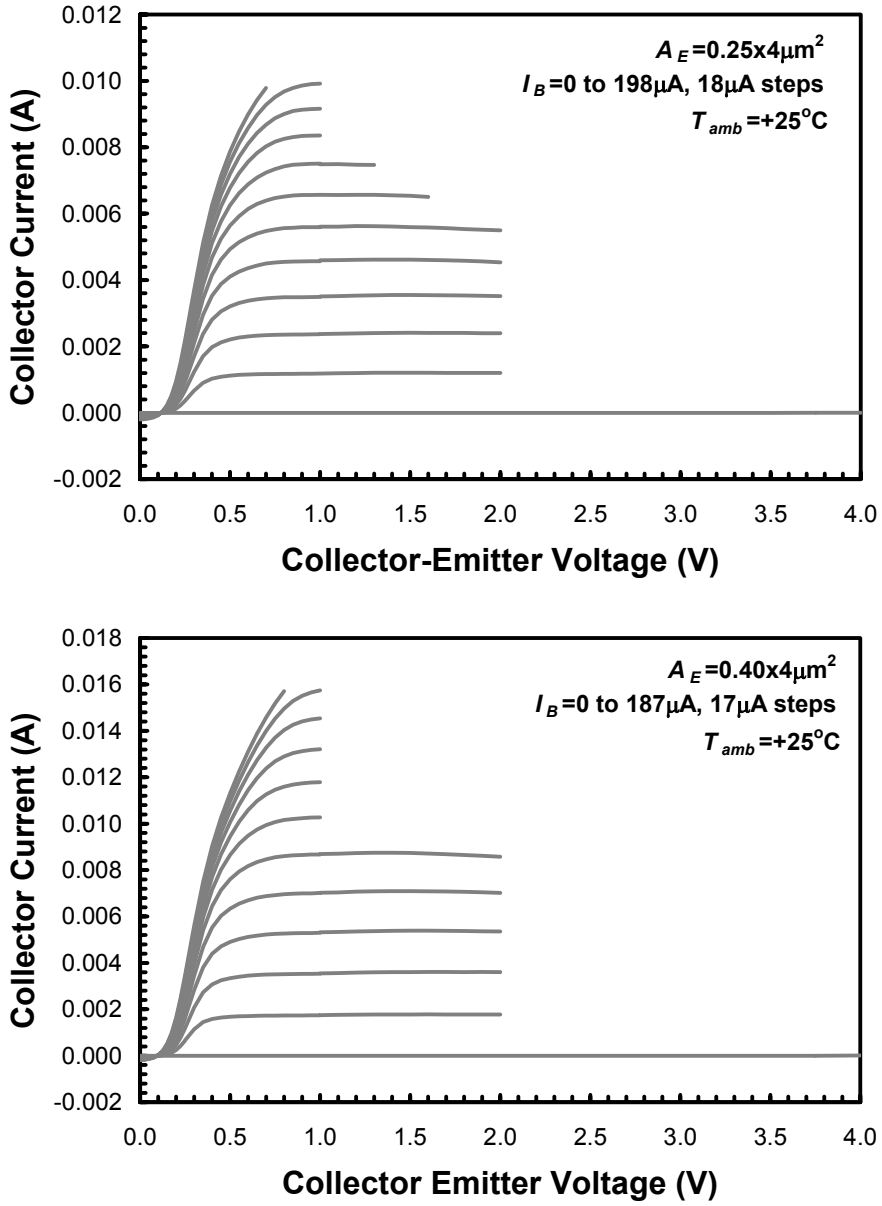

Figure 2-2: Common emitter I-V curves for an A_E = 0.40x4 μm² DHBT (top) and A_E = 0.25x4 μm² (bottom) at T_{amb} = +25 ˚C.

S-parameter measurements were performed with a HP8510C network analyzer over a frequency range from 0.4 GHz to 40.4 GHz. After using a Short-Open-Load-Thru off-wafer calibration, on-wafer open and short circuit pad structures were measured to de-embed the associated pad parasitics from the device measurements [2-12]. The unity

current gain cutoff frequency (f_T) and the unity power gain cutoff frequency (f_{MAX}) are determined from –20 dB/dec extrapolations of $|h_{21}|$ and U, respectively. The top portion of Figure 2-3 shows the small signal current gain, $|h_{21}|$, and the unilateral power gain, U, versus frequency of an A_E = 0.40x4.0 μm^2 DHBT biased near peak f_T at T_{amb} = 25 ºC and V_{CE} = 1.4 V. The bottom portion of Figure 2-3 shows the significant increase in f_T versus I_C for the same A_E = 0.40x4 μm^2 DHBT biased at a V_{CE} = 1.4 V. Due to the measurement time required to complete a full frequency sweep, the f_T values from the bottom portion of Figure 2-3 and other f_T versus I_C curves are determined from a single frequency point at 40 GHz. Over this 75 ˚C temperature range from T_{amb} = +25 ˚C to T_{amb} = -50 ˚C, peak f_T increases from 438 GHz to 480 GHz, but the I_C at which peak f_T occurs is unchanged. Similar data illustrating the same trend for an A_E = 0.25x4 μm^2 DHBT have been previously published [2-11].

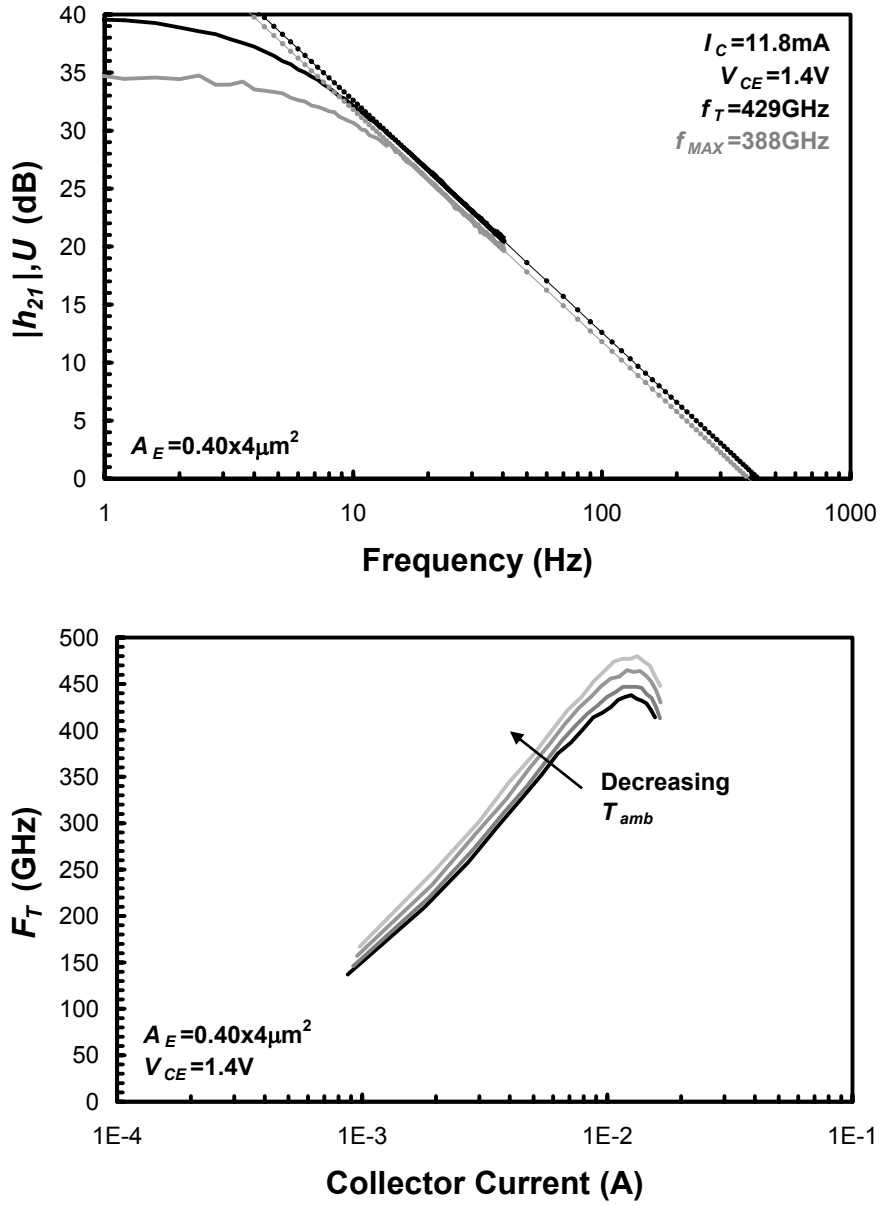

Figure 2-3: Small current gain, $|h_{21}|$, and unilateral power gain, U, versus frequency (top) and current gain cutoff frequency, f_T, versus collector current, I_C, (bottom) for an A_E = 0.40x4 μm^2 device.

2.4 Parameter Determination

Due to the large quantity of data, discussions concerning parameter determination will be focused on the A_E = 0.25x4 μm^2 and A_E = 0.40x4 μm^2 devices. The remaining

four devices are used to illustrate trends in the emitter length (L_E) and W_E scaling. Using the following equation from [2-13],

$$\frac{1}{2\pi f_T} = \tau_{ec} = \frac{\eta kT}{qI_C}(C_{BE} + C_{BC}) + \tau_B + \tau_C + (R_E + R_C)C_{BC} \tag{2-1}$$

device data are analyzed here to determine the component of the forward transit time, τ_{ec}, responsible for the increase in peak f_T with decreasing T_{amb}. By plotting $\tau_{ec} = 1/2\pi f_T$ versus $1/I_C$ and extrapolating τ_{ec} to the $1/I_C = 0$ condition, the contribution of the base-emitter charging term, $\tau_{be} = (\eta kT/qI_C)*(C_{BE}+C_{BC})$, can be eliminated from τ_{ec}. The *y*-intercept from this extrapolation yields the extrapolated forward transit time (τ_{f0}), which is composed of the base transit time (τ_B); collector transit time (τ_C); and the base-collector charging time ($\tau_{bc} = (R_E+R_C)C_{BC}$). With the determination of the emitter resistance (R_E); collector resistance (R_C); and the base-collector capacitance (C_{BC}), the collector charging time can be separated from the transit times. The separation of τ_{ec} into three components, base-emitter charging time, base-collector charging time, and the transit times will identify the device parameter responsible for the T_{amb} dependence. It is important to note that this analysis assumes τ_B, τ_C, and τ_{BC} to be independent of I_C in order to partition the various delay times. Otherwise, the interpretation of τ_{BE} and its dependence over T_{amb} is less than straight-forward.

2.4.1 Base Resistance (R_B)

From Pelke [2-14] and Spiegel [2-15], R_B can be determined directly from *S*-parameter measurements by plotting the $\mathrm{Re}\{Z_{11}\text{-}Z_{12}\}$ over frequency and bias. For the devices under investigation, some variation in $\mathrm{Re}\{Z_{11}\text{-}Z_{12}\}$ is observed over the 0.4 GHz

to 40.4 GHz *S*-parameter measurement range, as shown in Figure 2-4. R_B is determined from a least squares fit to the data between 1 GHz and 10 GHz. Although some variation in R_B is anticipated over the I_C and V_{CE} range, a nominal value near peak f_T is sufficient to understand the trends in f_{MAX} and R_E over T_{amb}. Table 2-1 summarizes the R_B values extracted from *Z*-parameters at V_{CE} = 1.2 V and various T_{amb}. All but the shortest devices, the A_E = 0.25x4 μm^2 and A_E = 0.40x2 μm^2, show less than a 1.0 Ω variation in R_B over the complete range of T_{amb}. Such a small variation in resistance is within the repeatability error of the measurement; therefore, R_B is treated as a constant over temperature. For the two shortest and therefore smallest A_E devices, the R_B variation is more likely to be a reflection of the measurement difficulty associated with high input impedance, low power devices than any true trend with respect to temperature. It may be noted that the R_B variation for the A_E = 0.25x4 μm^2 device is only 1.3 Ω, but the much higher input impedance A_E = 0.40x2 μm^2 device shows a 3.0 Ω variation. Given the relatively temperature independent manner of R_B, the change in f_{MAX} can only be attributed to f_T and/or C_{BC}.

Table 2-1: R_B values extracted from Re{Z_{11}-Z_{12}} at V_{CE} = 1.2 V and various T_{amb}.

W_E (nm)	L_E (μm)	T_{amb} (°C)	f_T (GHz)	f_{MAX} (GHz)	R_B (Ω)
250	4.0	+25	413	396	14.9
		0	423	410	15.0
		-25	436	411	15.4
		-50	446	427	16.2
	6.0	+25	419	374	11.8
		0	433	388	12.1
		-25	446	397	12.3
		-50	460	404	12.4
	8.0	+25	419	357	10.5
		0	437	367	10.6
		-25	443	375	10.6
		-50	458	383	10.6
400	2.0	+25	425	327	41.7
		0	438	320	41.3
		-25	450	325	40.1
		-50	460	339	39.1
	4.0	+25	432	368	17.4
		0	447	377	17.1
		-25	458	381	17.2
		-50	467	391	17.6
	6.0	+25	431	356	13.3
		0	444	368	13.5
		-25	456	372	13.5
		-50	463	373	13.4

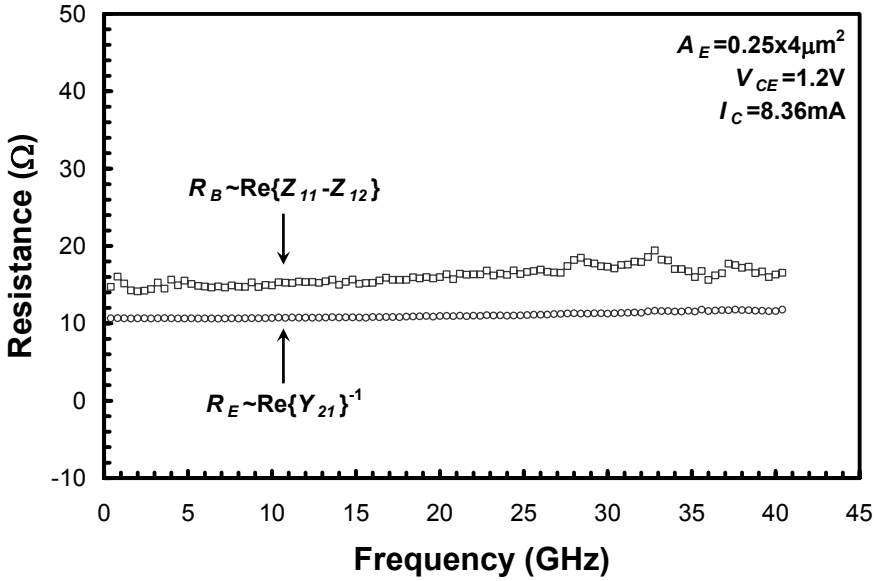

Figure 2-4: Frequency dependence of the extracted R_E and R_B of an A_E = 0.25x4 μm^2 biased near peak f_T (V_{CE} = 1.2 V, I_C = 8.33 mA).

2.4.2 Emitter Resistance (R_E)

R_E is determined from the inverse trans-conductance, $1/g_m$, method, using the following expression where finite R_B and β_f are considered.

$$\frac{1}{g_m} = \frac{\eta kT}{qI_C} + \frac{R_B}{\beta_f} + \left(\frac{\beta_f + 1}{\beta_f}\right) R_E \tag{2-2}$$

The method applied to *S*-parameter data requires the inverse of the small signal g_m, $\mathrm{Re}\{Y_{21}(\omega_o)\}^{-1}$, to be plotted against $1/I_C$. The lowest V_{CE} value of 1.0 V was selected in order to minimize self-heating and its impact on the R_E extraction procedure. Since $\mathrm{Re}\{Y_{21}(\omega_o)\}^{-1}$ is constant over frequency as shown by Figure 2-4, ω_o = 40 GHz is used to determine R_E. By extrapolating the resulting curves to the $1/I_C = 0$ condition, the *y*-intercept yields R_E. The *y*-intercept generated from the *Y*-parameter data requires the removal of the R_B/β_f term and the $(\beta_f + 1)/\beta_f$ factor before R_E can be determined. Most high-performance HBTs have sufficiently high β_F and low R_B that these correction terms are small. Table 2-2 lists the extracted R_E values for the devices under investigation. A slight decrease in R_E is observed with decreasing T_{amb} from Table 2-2, but the change in R_E is at a maximum of 7%.

Table 2-2: Summary of extracted R_E values at V_{CE} = 1.0 V over T_{amb}.

		R_E (Ω)			
W_E (nm)	L_E (μm)	+25˚C	0˚C	-25˚C	-50˚C
250	4	6.6	6.3	6.3	6.2
	6	4.7	4.5	4.5	4.4
	8	3.7	3.6	3.5	3.5
400	2	11.6	11.3	11.2	11.2
	4	5.8	5.7	5.7	5.7
	6	4.2	4.1	4.1	4.2

2.4.3 Collector Resistance (R_C)

The determination of R_C poses the greatest challenge of all the device parameters found in Equation (2-1), because of the limited number of methods for the direct extraction of this parameter. The inverse trans-conductance method, presented previously for R_E determination, cannot be applied to the reverse Gummel with equal success, because R_B is significantly higher than R_C and β_r is less than unity. At the same time, a reverse Gummel forces the base-collector junction into forward bias and base-collector depletion reduces in thickness. The reduction in the depletion region thickness reveals the low doped collector, which will contribute significantly to the total R_C measured. Other DC methods, such as Flyback, are susceptible to the same phenomena and likely to over-estimate R_C during normal device operation. Pelke [2-14] presents a similar method to extract R_C from Re$\{Z_{22}$-$Z_{21}\}$ at high frequencies, but the presence of extrinsic C_{BC} complicates the extraction procedure [2-15]. For the devices in this investigation, the measured data is scattered over the *S*-parameter frequency range and lacks an asymptotic value required for R_C determination.

In order to obtain some measure of R_C directly from measured data, large area TLM structures and the drawn device dimensions can be used to estimate R_C. The following expression is used to estimate the unit collector resistance, R_C',

$$R_C^{'} = R_C L_{C,CON} = \frac{R_{C,CON}}{nW_{C,CON}} + \frac{1}{3}R_{C,SH}\left(\frac{W_{C,CON}}{n}\right) + R_{C,SH}\left(\frac{W_{sep}}{n}\right) + \frac{1}{3}R_{C,SH}\left(\frac{W_{mesa}}{2n}\right) \quad (2\text{-}3)$$

where $R_{C,CON}$ and $R_{C,SH}$ are the measured quantities corresponding to the sub-collector specific contact resistance and the sheet resistance, respectively. The collector contact length, width, and multiplicity are represented by $L_{C,CON}$, $W_{C,CON}$, and n, respectively.

W_{sep} is the distance between the collector contact and base-collector mesa and W_{mesa} is the base-collector mesa width. Equation (2-3) assumes that the transfer length is equal to or greater than $W_{C,CON}$; neglects the distributed resistance of the collector metal; and neglects the non-scalable portion of R_C associated with access to high levels of metallization. Therefore, all variables in Equation (2-3) are identical between the W_E = 250 nm and W_E = 400 nm devices, except for a 150 nm difference in W_{mesa}. Based on a $R_{C,SH}$ = 12 Ω/□ and a $R_{C,CON}$ = 20 Ω·μm^2, the calculated R_C' is approximately 16 Ω·μm for both W_E = 250 nm and W_E = 400 nm devices. Since the sub-collector doping and materials are nearly identical to the emitter cap, minimal variation of R_C with T_{amb} is anticipated.

2.4.4 Base-Collector Capacitance (C_{BC})

With the value of R_E and R_C determined, the last parameter required to determine τ_{bc} is C_{BC}. By plotting Imag$\{-Y_{12}(\omega)\}/2\pi f$, the frequency and bias dependence of C_{BC} can be observed from RF measurements. Figure 2-5 shows the relatively constant behavior of C_{BC} over the measured frequency range for an A_E = 0.25x4 μm^2 at T_{amb} = +25 ˚C and the various V_{CE}. Both V_{BE} and V_{CE} are forced to zero for the curve labeled "Zero-Bias". For the remainder of the curves in Figure 2-5, V_{CE} is forced to the value indicated, but the device is biased near peak f_T by forcing I_B. For the same A_E and T_{amb}, Figure 2-6 shows the dependence of C_{BC} with I_C for various V_{CE}. At a fixed V_{CE} and low I_C, V_{CB} is large and positive, and all the C_{BC} curves converge to the fully depleted dielectric capacitance. Despite the lower V_{CB} at higher I_C, Figure 2-6 also shows C_{BC} decreasing for all V_{CE} and it continues to decrease until the onset of Kirk effect, after which an increase in C_{BC} is

observed. The reduction in C_{BC} is attributed to the screening of the collector space charge by free electrons entering the collector from the base. The remaining five devices under investigation show similar behavior with variations in V_{CE} and I_C.

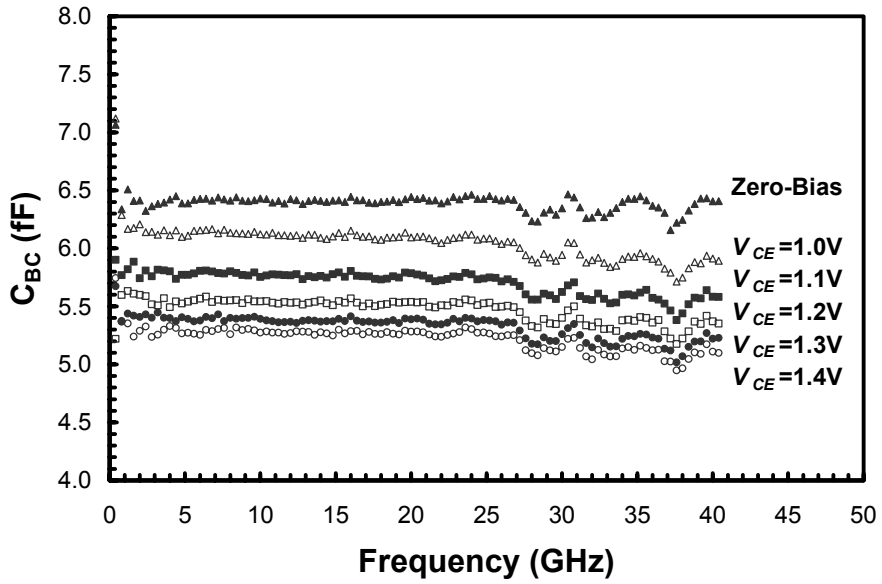

Figure 2-5: Frequency dependence of C_{BC} for an A_E = 0.25x4 μm^2 device at T_{amb} = +25 ˚C for various bias conditions. For the curve labeled "Zero-Bias", both V_{BE} and V_{CE} are zero. For the remaining curves, V_{CE} is held constant at the value shown, and the device is biased near peak f_T by forcing I_B.

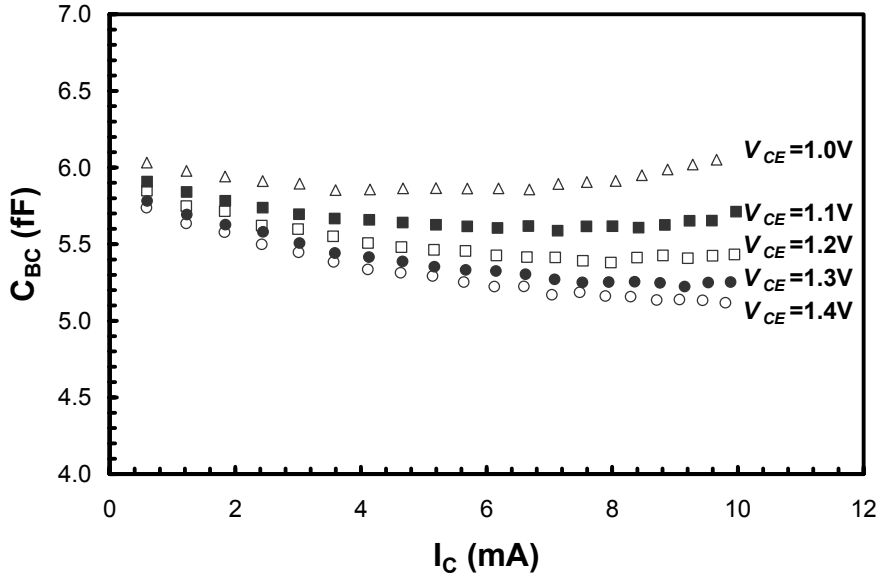

Figure 2-6: I_C dependence of C_{BC} for an A_E = 0.25x4 μm^2 device at T_{amb} = +25 ˚C and various V_{CE}.

Table 2-3 summarizes the extracted C_{BC} values for all six HBTs under investigation over all measured V_{CE} and T_{amb} values. The zero-bias C_{BC}, shown as V_{CE} = 0.0 V in Table 2-3, for all devices show some reduction with decreasing T_{amb}, but the variation is less than 1.0 fF. The C_{BC} variation with T_{amb} drops to 0.2 fF or less once the device is biased at a higher V_{CE} and an I_C near peak f_T. Under normal operating conditions, C_{BC} can be considered a constant over the T_{amb} range and is not the source of the f_T increase with reduced T_{amb}.

Table 2-3: Dependence of C_{BC}, extracted from a complete frequency sweep at a single forced I_B, with V_{CE} and T_{amb} for all six HBTs investigated.

A_E = 0.25x4 μm²				
V_{CE}(V)	**25˚C**	**0˚C**	**-25˚C**	**-50˚C**
0.0	6.4	6.3	6.2	6.1
1.0	6.2	6.2	6.1	6.0
1.1	5.8	5.8	5.7	5.7
1.2	5.6	5.5	5.5	5.5
1.3	5.4	5.4	5.3	5.3
1.4	5.3	5.2	5.2	5.2

A_E = 0.40x2 μm²				
V_{CE} (V)	**25˚C**	**0˚C**	**-25˚C**	**-50˚C**
0.0	4.5	4.5	4.4	4.3
1.0	4.4	4.3	4.2	4.2
1.1	4.1	4.1	4.0	4.0
1.2	3.9	3.9	3.9	3.9
1.3	3.8	3.8	3.8	3.7
1.4	3.7	3.7	3.7	3.7

A_E = 0.25x6 μm²				
V_{CE}(V)	**25˚C**	**0˚C**	**-25˚C**	**-50˚C**
0.0	8.9	8.7	8.6	8.4
1.0	8.5	8.4	8.4	8.3
1.1	8.0	7.9	7.9	7.9
1.2	7.6	7.6	7.6	7.5
1.3	7.4	7.3	7.3	7.3
1.4	7.2	7.1	7.1	7.1

A_E = 0.40x4 μm²				
V_{CE}(V)	**25˚C**	**0˚C**	**-25˚C**	**-50˚C**
0.0	7.5	7.4	7.3	7.2
1.0	7.2	7.1	7.2	7.1
1.1	6.7	6.7	6.7	6.6
1.2	6.4	6.4	6.4	6.3
1.3	6.2	6.2	6.2	6.1
1.4	6.1	6.0	6.0	6.0

A_E = 0.25x8 μm²				
V_{CE}(V)	**25˚C**	**0˚C**	**-25˚C**	**-50˚C**
0.0	11.3	11.1	10.9	10.7
1.0	10.7	10.7	10.7	10.6
1.1	10.0	10.0	10.0	10.0
1.2	9.6	9.5	9.6	9.5
1.3	9.3	9.2	9.3	9.2
1.4	9.1	9.0	9.0	9.0

A_E = 0.40x6 μm²				
V_{CE}(V)	**25˚C**	**0˚C**	**-25˚C**	**-50˚C**
0.0	10.4	10.2	10.0	9.8
1.0	9.9	9.7	9.6	9.7
1.1	9.2	9.1	9.1	9.1
1.2	8.8	8.7	8.7	8.7
1.3	8.5	8.4	8.4	8.4
1.4	8.3	8.2	8.2	8.2

2.4.5 Base-Emitter Capacitance (C_{BE})

To understand the temperature dependence of τ_{be}, the temperature dependence of both C_{BE} and C_{BC} must be determined. C_{BE} is extracted from the $\text{Imag}\{Y_{11}(\omega)+Y_{12}(\omega)\}/\omega$ and similar to C_{BC}, it is found to be independent of frequency. Table 2-4 shows the extracted C_{BE} values for all six devices under investigation over all measured V_{CE} and T_{amb}. For each table entry, the DHBT is biased at a fixed I_B while a complete frequency sweep is performed. Little variation and no trend in C_{BE} are observed with increasing V_{CE} due to the minimal change in I_C with increasing V_{CE}. An equally small variation and lack of trend is observed with decreasing T_{amb}. The observed variations in C_{BE} at various T_{amb} are caused by the small variations in I_C resulting from the fixed I_B used to drive each device. If I_B were tuned to yield the same I_C for each V_{CE} and T_{amb}, the variations in C_{BE} would likely be eliminated.

Table 2-4: Dependence of C_{BE}, extracted from a complete frequency sweep at a single forced I_B, with V_{CE} and T_{amb} for all six HBTs investigated.

A_E = 0.25x4 μm²				
V_{CE}(V)	25˚C	0˚C	-25˚C	-50˚C
0.0	4.3	4.2	4.3	4.3
1.0	28.1	29.4	29.1	29.9
1.1	27.7	28.9	28.7	28.9
1.2	27.2	28.1	28.1	28.2
1.3	27.6	28.1	27.9	27.9
1.4	27.5	28.2	28.0	28.4

A_E = 0.40x2 μm²				
V_{CE}(V)	25˚C	0˚C	-25˚C	-50˚C
0.0	3.5	3.2	3.1	3.1
1.0	22.5	22.4	21.4	21.0
1.1	21.9	21.7	21.0	20.7
1.2	21.5	21.4	20.7	20.3
1.3	21.7	21.1	20.6	20.6
1.4	21.8	20.9	20.3	20.7

A_E = 0.25x6 μm²				
V_{CE}(V)	25˚C	0˚C	-25˚C	-50˚C
0.0	5.8	5.7	6.0	5.7
1.0	42.5	42.0	42.4	42.8
1.1	41.6	41.1	41.8	41.5
1.2	41.1	40.8	41.1	41.1
1.3	41.1	40.9	41.2	41.1
1.4	41.0	41.0	40.9	41.1

A_E = 0.40x4 μm²				
V_{CE}(V)	25˚C	0˚C	-25˚C	-50˚C
0.0	5.5	5.1	5.1	5.4
1.0	40.9	40.0	41.2	40.9
1.1	40.6	39.0	40.6	39.8
1.2	39.8	38.8	39.8	39.6
1.3	39.7	38.9	39.7	39.2
1.4	39.8	39.5	39.7	39.3

A_E = 0.25x8 μm²				
V_{CE}(V)	25˚C	0˚C	-25˚C	-50˚C
0.0	7.9	7.5	7.5	7.4
1.0	54.4	55.2	55.8	56.8
1.1	53.3	54.3	54.7	55.2
1.2	52.8	53.6	53.8	54.4
1.3	52.8	53.2	53.6	53.9
1.4	52.9	53.2	53.6	53.9

A_E = 0.40x6 μm²				
V_{CE}(V)	25˚C	0˚C	-25˚C	-50˚C
0.0	8.8	8.2	8.3	7.7
1.0	59.8	59.0	57.7	59.2
1.1	58.5	57.7	56.1	57.5
1.2	57.5	57.0	56.0	56.9
1.3	57.7	56.8	55.9	56.5
1.4	58.0	57.0	56.0	56.7

2.4.6 Delay Times (τ_{be}, τ_{bc}, $\tau_B+\tau_C$)

Applying the method described at the beginning of Section 2.4, plotting $1/2\pi f_T$ versus $1/I_C$ and extrapolating to the $1/I_C = 0$ condition, τ_{f0} is determined. Table 2-5 summarizes the values of τ_{f0} extracted for an A_E = 0.25x4 μm² and A_E = 0.40x4 μm² device over the available V_{CE} and T_{amb} values. The determination of τ_{f0} necessitates the use of *S*-parameter over a large range of I_C, but τ_{ec} and τ_{be} can be calculated at any number of frequencies and at any number of I_C. The values of τ_{ec} and τ_{be} shown in Table 2-5 are calculated from a complete frequency sweep measured at an I_C near peak f_T. The additional frequency points allow for a more accurate estimation of the transit times

($\tau_B+\tau_C$) and hence the average ensemble electron velocity, $v_{e,ave}$, through the base and collector. Table 2-5 also shows values for τ_{bc} resulting from the measured R_E in Section 2.4.2, measured C_{BC} in Section 2.4.4, and the estimated R_C in Section 2.4.3. The measured temperature dependencies of R_E and C_{BC} are small, and R_C is expected to have an equally small variation in temperature. The result is a τ_{bc} with 5 fs or less variation over the T_{amb} range for any given device and V_{CE}. Therefore, any change in τ_{f0} over T_{amb} can be assumed to be a result of the temperature dependence of $\tau_B+\tau_C$.

Table 2-5: Partitioning of delay times between the base-emitter charging time (τ_{be}), base-collector charging time (τ_{bc}), and the transit times (τ_B+τ_C) determined from a complete frequency sweep at a single forced I_B and various T_{amb} and V_{CE}.

A_E = 0.25x4 μm^2							
V_{CE} (V)	T_{amb}	τ_{ec} (fs)	τ_{f0} (fs)	τ_{be} (fs)	τ_{bc} (fs)	τ_b+τ_c (fs)	$v_{e,ave}$ (x10^7 cm/s)
1.0	+25	397	300	97	65	235	6.61
	0	394	293	101	64	229	6.77
	-25	379	282	97	63	220	7.06
	-50	374	281	93	61	220	7.05
1.1	+25	385	298	87	61	237	6.53
	0	379	289	90	60	230	6.75
	-25	368	278	90	58	220	7.04
	-50	363	281	82	58	223	6.96
1.2	+25	385	299	86	59	240	6.46
	0	376	292	84	57	236	6.58
	-25	365	281	84	56	226	6.86
	-50	357	277	80	56	221	7.01
1.3	+25	385	300	85	57	243	6.37
	0	375	292	83	56	237	6.55
	-25	363	281	82	54	227	6.82
	-50	355	278	77	54	225	6.90
1.4	+25	388	302	86	56	245	6.32
	0	375	294	81	54	240	6.47
	-25	359	283	76	53	230	6.74
	-50	355	278	77	53	225	6.88

A_E = 0.40x4 μm^2							
V_{CE} (V)	T_{amb}	τ_{ec} (fs)	τ_{f0} (fs)	τ_{be} (fs)	τ_{bc} (fs)	τ_b+τ_c (fs)	$v_{e,ave}$ (x10^7 cm/s)
1.0	+25	381	284	97	70	214	7.25
	0	368	281	87	69	213	7.28
	-25	363	273	90	70	203	7.64
	-50	352	265	87	69	196	7.91
1.1	+25	370	288	82	64	224	6.93
	0	359	279	80	64	216	7.18
	-25	351	272	79	63	209	7.42
	-50	342	265	77	62	203	7.63
1.2	+25	368	285	83	61	224	6.93
	0	356	280	76	60	220	7.04
	-25	348	269	79	60	209	7.40
	-50	341	267	74	58	209	7.42
1.3	+25	369	287	82	59	228	6.81
	0	356	281	75	58	223	6.96
	-25	348	272	76	58	214	7.24
	-50	338	267	71	56	211	7.36
1.4	+25	371	291	80	59	232	6.68
	0	361	283	78	57	226	6.86
	-25	346	274	72	56	218	7.10
	-50	337	270	67	55	215	7.22

$v_{e,ave}$ can be calculated from the $\tau_B+\tau_C$ values in Table 2-5 and the combined thickness of the base and collector of 155 nm given in Section 2.2. It may be noted that the estimates of $v_{e,ave}$ are significantly higher than the steady state saturation velocity of InP and $In_{0.53}Ga_{0.47}As$, which is approximately $1x10^7$ cm/s for both materials. Due to the aggressive base grade and the high peak electron velocity at low electric field of InGaAs alloys, there is a significant drift component of the electron transport across the base. It is expected that τ_B is reduced significantly compared to a non-graded base, and τ_B does not dominate the total transit time. For a given V_{CE} and decreasing T_{amb}, there is a general decrease in the transit times and hence an increase in $v_{e,ave}$. This is consistent with reduced scattering mechanisms and higher overall mobility at reduced temperatures. In the presence of a 25 kV/cm electric field, the steady-state electron saturation velocity, $v_{e,sat}$, of InP is expected to increase $1.3x10^6$ cm/s for a 75 K reduction in T_{amb} [2-7]. For the same 75 K T_{amb} reduction in $In_{0.53}Ga_{0.47}As$, $v_{e,sat}$ is only expected to increase by $0.4x10^6$ cm/s [2-7]. According to Table 2-5, a 4.3-5.5$x10^6$ cm/s and a 4.9-7.0$x10^6$ cm/s increase is observed for the A_E = 0.25x4 μm^2 and A_E = 0.40x4 μm^2 device, respectively. Compared to the published temperature dependence of $v_{e,sat}$ in InP and $In_{0.53}Ga_{0.47}As$, the extracted $v_{e,ave}$ has a significantly greater dependence on temperature. Since $v_{e,ave}$ is significantly greater than $v_{e.sat}$, non-equilibrium transport (velocity overshoot and ballistic carriers) is expected to play a prominent role in these devices, and the temperature dependence of $v_{e,ave}$ is not expected to correlate well to $v_{e.sat}$. Comparing the $v_{e,ave}$ values for the different emitter geometries, the W_E = 400 nm devices exhibit a larger change over T_{amb}, highlighting the potential impact of self-heating on the wider W_E devices.

Higher absolute values of $v_{e,ave}$ are also observed for the W_E = 400 nm devices. The narrower W_E devices suffer from increased I_C spreading, which increases the effective distance traveled by an electron crossing the collector and decreases the perceived $v_{e,ave}$ [2-6]. A less pronounced trend of increasing transit times with increasing V_{CE} for a given T_{amb} is observed, which is consistent with the negative differential mobility exhibited by many compound semiconductors as well as with expectations from self-heating.

Figure 2-7 and Figure 2-8 show the T_{amb} and V_{CE} dependencies of τ_{f0} and τ_{be} for an A_E = 0.25x4 μm^2 and A_E = 0.40x4 μm^2 device, respectively, biased at peak f_T. Since the data in these two figures is determined from single frequency point f_T extrapolations, some measurement variation is expected and the more subtle trends may not be observed. For τ_{f0}, the approximate 20 fs reduction with decreasing T_{amb} is apparent for both devices, and the transit times have been previously shown to be responsible for this behavior. At the same time, τ_{be} shows an 8-17 fs reduction with increasing V_{CE} and a 2-10 fs reduction with decreasing T_{amb}. A portion of the τ_{be} reduction with increasing V_{CE} can be attributed to the 15-20% reductions in C_{BC} with increased V_{CE} as shown in Table 2-3, but it is weighted against the larger values of C_{BE} shown in Table 2-4. The majority of the τ_{be} reduction with increasing V_{CE} is a result of the 8-35% increase in I_C at peak f_T, which is offset by a smaller increase in T_j as a result of the increased P_{diss}. The reader may note that the τ_{be} of the A_E = 0.40x4 μm^2 device shows a larger variation with T_{amb} than the A_E = 0.25x4 μm^2 device. For both devices, the position of peak f_T with respect to I_C is unchanged over T_{amb}, and the C_{BE}+C_{BC} sum has been shown to be unchanged over T_{amb}. Therefore, the greater variation of τ_{be} = (ηkT/qI_C)*(C_{BE}+C_{BC}) observed with the A_E =

0.40x4 μm^2 device is attributed to a greater difference in temperature experienced by that device. The only source of this temperature difference is the difference in self-heating between the narrower A_E = 0.25x4 μm^2 device and the wider A_E = 0.40x4 μm^2 device. When comparing the τ_{be} of a single device over T_{amb}, the fractional decrease in τ_{be} should equal the ratio of T_{amb}, (273+25)/(273-50) or ~1.34, but the fractional decrease observed from Figure 2-7 and Figure 2-8 is less than 1.16. This behavior is a result of the collector current ideality factor, η, dependence on T_{amb}. Numerical analysis of the forward Gummels in Figure 2-1 show that η increases with decreasing T_{amb}. Since the InP/InGaAs base-emitter junction is described as abrupt in Section 2.2, barrier tunneling is expected to be significant and the resulting increase in η with decreasing T_{amb} is sufficient to moderate the change in τ_{be}.

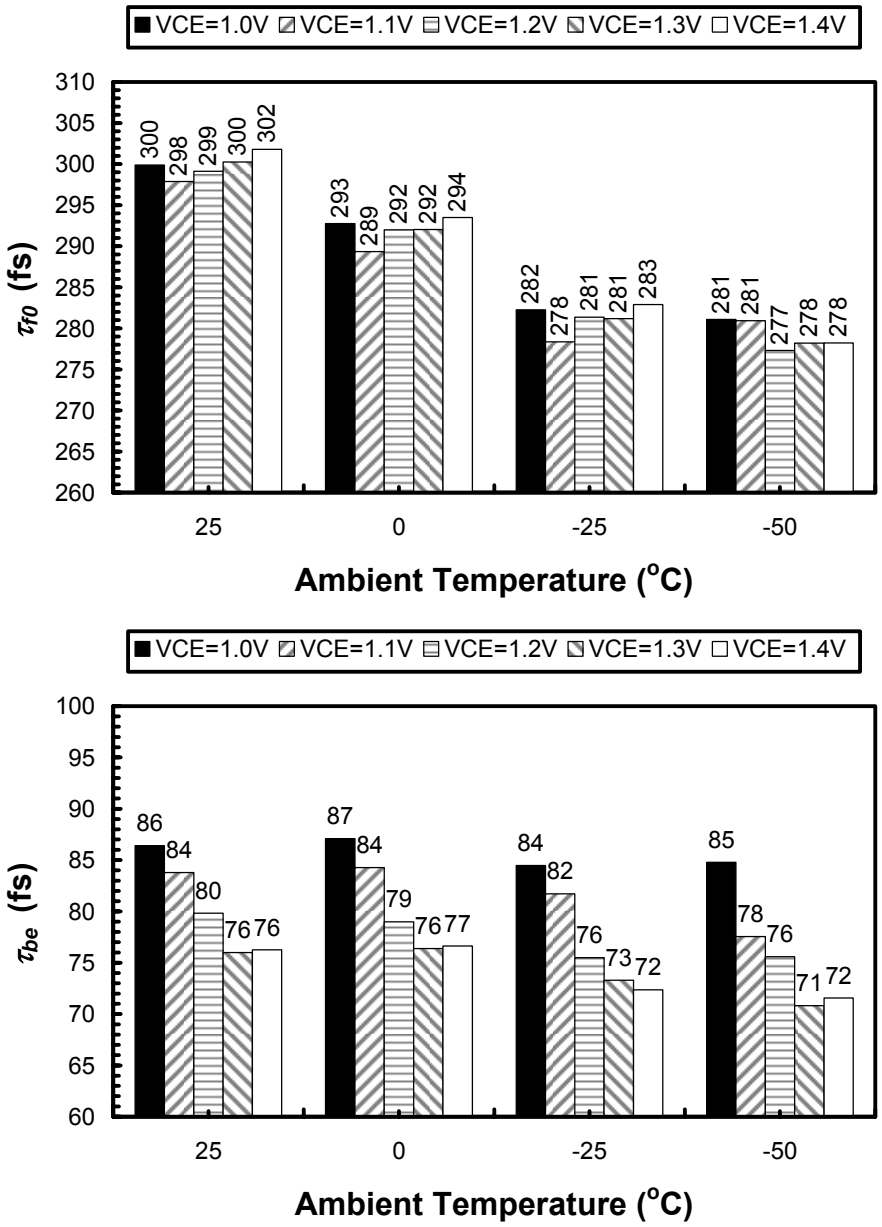

Figure 2-7: Extrapolated forward transit time (τ_{f0}) and base-emitter charging time (τ_{be}) dependence on V_{CE} and T_{amb} for an A_E = 0.25x4 μm^2 biased at peak f_T.

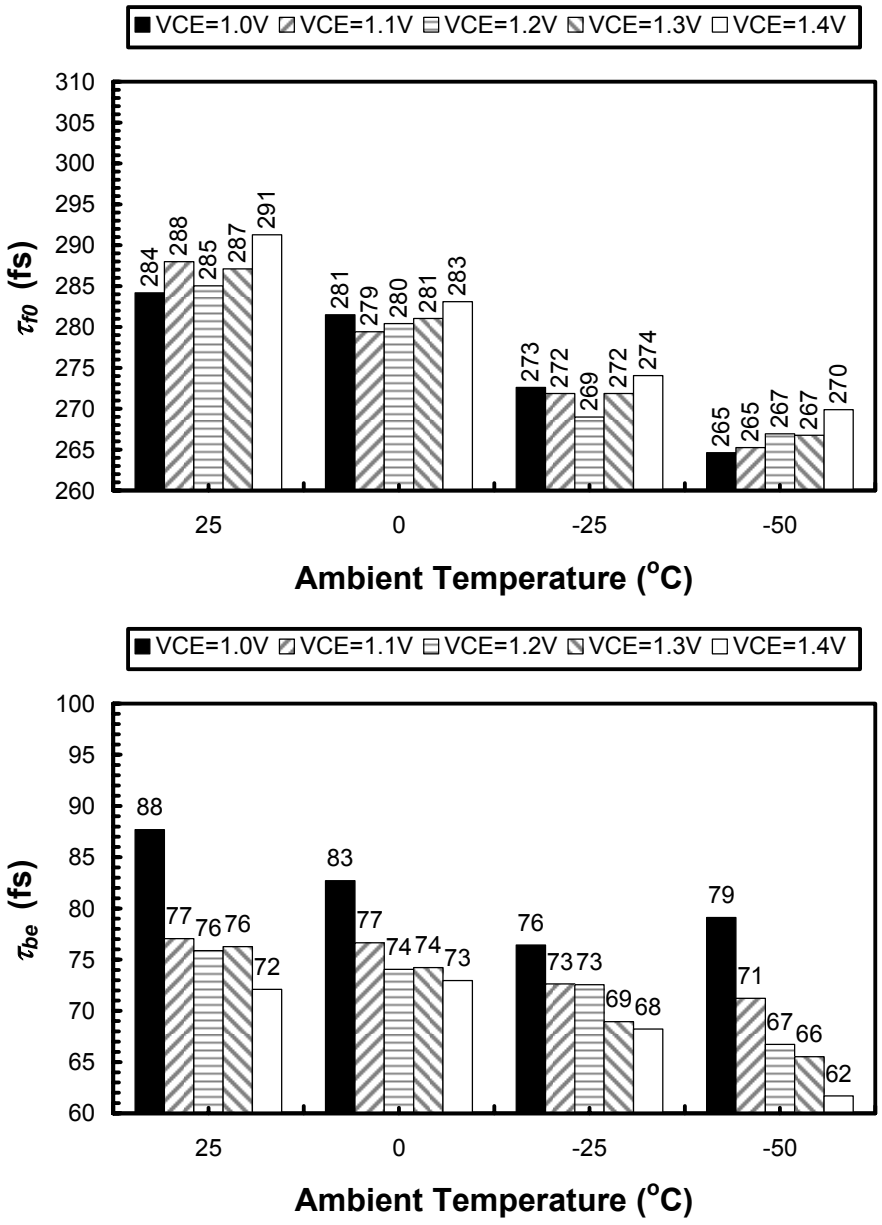

Figure 2-8: Extrapolated forward transit time (τ_{f0}) and base-emitter charging time (τ_{be}) dependence on V_{CE} and T_{amb} for an A_E = 0.40x4 μm^2 biased at peak f_T.

In order to examine the impact of both W_E and L_E on the delay time components, the geometry independent terms, τ_{f0}- τ_{bc} = τ_B+τ_C and $\tau_{be,}$ are plotted in Figure 2-9 for all six devices under investigation over all measured T_{amb}. The highest V_{CE} value of 1.4 V is selected to highlight the impact of self-heating, and all data shown is extracted from a

forced I_B condition near peak f_T. In general, the larger L_E and W_E devices suffer from a larger variation of transit times over T_{amb} which can be attributed to self-heating. The extracted values for τ_{be}, shown in the bottom of Figure 2-9, show a less obvious trend over L_E and W_E. Device to device comparisons are complicated by the less favorable intrinsic to extrinsic capacitance ratio of the smaller W_E and L_E devices. The larger W_E and L_E devices have a marginally greater variation in τ_{be} over T_{amb}. However, the direct comparison of τ_{be} of various different devices at the same T_{amb} is difficult due to the small variation, as little as 1.0 fs, that separates many of the devices.

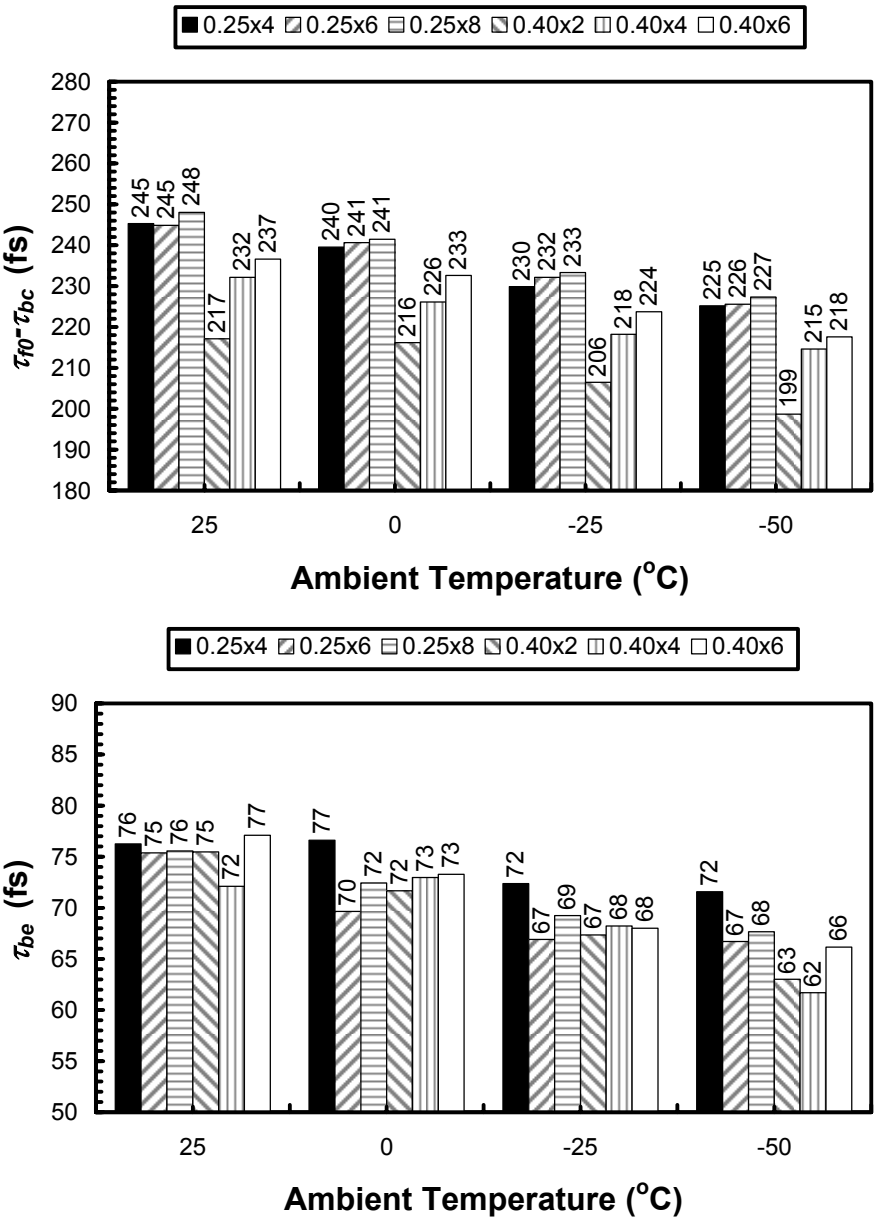

Figure 2-9: Temperature dependence of τ_{f0}-$\tau_{bc,max}$ and τ_{be} for all six HBTs under investigation at a V_{CE} = 1.4 V.

2.4.7 Thermal Resistance (R_{TH})

In order to explain many of the phenomena observed in the DC and RF measurements, any differences in self-heating among the six devices under investigation must be identified. Measured R_{TH} values for the devices under investigation, obtained

using the V_{BE} method of Dawson et al [2-16] at a J_C = 1 mA/μm^2, have already been presented in [2-11] and are summarized in Table 2-6. Since the measurement method does not allow for the determination of R_{TH} at high J_C (near or at peak f_T) and the thermal conductivity of materials is known to decrease with increasing temperature, it is expected that the measured R_{TH} values represent a lower limit to the actual R_{TH} at higher J_C. In addition, the measured R_{TH} also includes the beneficial heat spreading properties of large RF probe pads, which would otherwise not be present in a dense IC. A 3-D thermal model has been used to predict R_{TH} at higher J_C and to thermally de-embed the pad thermal impedance [2-11]. For the purposes of this investigation, the measured R_{TH} values are adequate to establish trends in T_j.

To illustrate the greatest degree of self-heating, P_{diss} values corresponding to I_C values at peak f_T and a V_{CE} = 1.4 V are shown in Table 2-6. The lowest and highest ΔT_j are experienced by the A_E = 0.25x4 μm^2 and A_E = 0.40x6 μm^2 devices, respectively. Even the A_E = 0.40x4 μm^2 device shows 23 ˚C more self-heating than the A_E = 0.25x4 μm^2 device, illustrating the significant impact of W_E on T_j. Comparing the ΔT_j values in Table 2-6 with the τ_{f0}-τ_{bc} values in Figure 2-9, there is a direct correlation between ΔT_j and the transit time. At the same time, the non-linear increase of R_{TH} and hence T_j at higher P_{diss} and T_{amb} will magnify the changes in T_j for the larger devices, resulting in the greater variation of τ_{be} observed over T_{amb}. The behavior of f_T and f_{MAX} over temperature and across different A_E can be observed from Table 2-1, and further discussion on the trends can be found in [2-11]. However, the net impact is an 8-10% increase in peak f_T for a 75 ˚C reduction in T_{amb}. Such a large reduction in T_{amb} may have seemed

unreasonable, but the smallest ΔT_j shown in Table 2-6 is 77 ˚C. Therefore, the f_T improvement observed in this investigation is a realistic estimate of the performance to be recovered with improved device design and thermal management resulting in reduced T_j. In addition, the observed f_T improvement with reduced T_{amb} is comparable to the results obtained by additional vertical or lateral scaling of the device geometry. Readers are encouraged to refer to [2-10] for a detailed discussion of the thermal design of InP HBTs.

Table 2-6: Summary of measured R_{TH} and other self-heating related values at T_{amb} = +25 ˚C and V_{CE} = 1.4 V.

W_E (nm)	L_E (μm)	R_{TH} (˚C/mW)	$I_{C,Peak}$ (mA)	P_{diss} (mW)	ΔT_j (˚C)
250	4	6.3*	8.7	12.2	77
	6	4.9*	13.9	19.5	96
	8	4.1*	17.8	24.9	102
400	2	8.5*	7.5	10.5	89
	4	5.7*	12.5	17.5	100
	6	4.5*	18.4	25.8	116
* Denotes values taken from [2-11]					

2.5 Summary

Recent efforts to aggressively scale the device dimensions [2-1],[2-2],[2-3],[2-4] have produced sub-micron 400+ GHz InP HBTs, but scaling has not limited or reduced the power density. In order to assess the impact of increasing power density, six different A_E devices with f_T greater than 400 GHz were characterized, and it was found that peak f_T could be increased by 8-10% for a 75 ºC reduction in T_{amb}. Subsequent analysis of the RF data indicate that the peak f_T improvement is due to reductions in transit times (τ_B+τ_C) and the base-emitter charging time (τ_{be}), but the balance between these two time delays depends on the particular device. When the R_{TH} and hence T_j is considered, the wider W_E and longer L_E devices experience significantly more self-heating. The significant

variation in $\tau_B+\tau_C$ across devices and T_{amb} was found to be directly correlated to T_j. However, τ_{be} showed a weaker dependence on T_{amb}, but a much stronger V_{CE} dependence due to variations in I_C and C_{BC} at peak f_T. The estimated amount of self-heating ranges from 77 ˚C to 116 ˚C across all six devices at a V_{CE} = 1.4 V and T_{amb} = +25 ˚C. Therefore, the 8-10% peak f_T improvement over a 75 ˚C change in T_{amb} is a realistic estimate of the performance that could be recovered with reduced T_j, emphasizing the importance of minimizing T_j in device design.

2.6 Acknowledgements

This chapter, in full, has been submitted for publication in Solid State Electronics, 2006. The contributions from the co-authors Tahir Hussain, Donald A. Hitko, Yakov Royter, Charles H. Fields, Ivan Milosavljevic, Stephen Thomas III, Rajesh D. Rajavel, and Marko Sokolich of HRL Laboratories, L.L.C., and Peter M. Asbeck of UCSD are appreciated. The author of this dissertation was the primary investigator and primary author of this publication. This work was sponsored by the Defense Advanced Research Projects Agency (DARPA) through AFRL Contract F33615-02-1286 (TFAST). The authors would like to thank Mark Banbrook, Cristian Cismaru, and Peter J. Zampardi of Skyworks Solutions, Inc. for their assistance with low temperature *S*-parameter measurements.

2.7 References

[2-1] W. Hafez and M. Feng, "Lateral scaling of 0.25 μm InP/InGaAs SHBTs with InAs emitter cap," *Electronics Letters*, vol. 40, no. 18, pp.1151-3, Sept 2004.

[2-2] W. Hafez, J. W. Lai, M. Feng, "InP/InGaAs SHBTs with 75 nm collector and $f_T >$ 500 GHz," *Electronics Letters*, vol. 39, no. 20, pp.1475-6, Oct 2003.

[2-3] Z. Griffith, M. Dahlström, M. Urteaga, M. J. W. Rodwell, X.-M. Fang, D. Lubyshev, Y. Wu, J. M. Fastenau, and W. K. Liu, "InGaAs/InP mesa DHBTs with simultaneously high f_t and f_{max} , and low $C_{cb} = I_c$ ratio," *IEEE Electron Device Lett.*, vol. 25, pp. 250–252, 2004.

[2-4] T. Hussain, Y. Royter, D. Hitko, M. Montes, I. Milosavljevic, R. Rajavel, S. Thomas, M. Antcliffe, A. Arthur, Y. Boegeman, J. Li, and M. Sokolich, "First demonstration of sub-0.25 μm-width emitter InP-DHBTs with >400 GHz f_t and >400 GHz f_{max}," in 2004 *IEDM Technical Digest*.

[2-5] M. J.W. Rodwell, M. Urteaga, T. Mathew, D. Scott, D. Mensa, Q. Lee, J. Guthrie, Y. Betser, S. C.Martin, R. P. Smith, S. Jaganathan, S. Krishnan, S. I. Long, R. Pullela, B. Agarwal, U. Bhattacharya, L. Samoska, and M. Dahlstrom, "Submicrometer scaling of heterojunction bipolar transistors," *IEEE Transactions on Electron Devices*, vol. 48, pp. 2606–2624, Dec. 2001.

[2-6] P. J. Zampardi, "A Study of New Base Pushout Effect in Modern Bipolar Transistors," *UCLA Ph.D. Thesis*, 1997.

[2-7] http://www.ioffe.rssi.ru/SVA/NSM/Semicond/

[2-8] S. Thomas III, J.A. Foschaar, C.H. Fields, M.M. Madhav, M. Sokolich, R.D. Rajavel, and B. Shi, "Effects of device design on InP-based HBT thermal resistance", *IEEE Transactions on Device and Materials Reliability*, vol. 1, no. 4, pp. 185-189, Dec. 2001.

[2-9] C.H. Fields, J. Foschaar, and S. Thomas III, "Thermal resistance characterization of 200 GHz F_t InGaAs/InAlAs HBTs", in 2002 *IPRM Technical Digest*, pp. 79-82.

[2-10] J. C. Li, P. M. Asbeck, M. Sokolich, T. Hussain, D. Hitko, and C. Fields, "Effects of device design on the thermal properties of InP-based HBTs," in 2003 *ISCS Post-Conference Proceedings*, pp. 138-143.

[2-11] J.C. Li, T. Hussain, D.A. Hitko, P.M. Asbeck, and M. Sokolich, "Characterization and Modeling of Thermal Effects in Sub-Micron InP DHBTs", in 2005 *CSIC Symposium Technical Digest*, pp. 65-68.

[2-12] P. J. Van Wijnen, "On the Characterization and Optimization of High-Speed Silicon Bipolar Transistors," Cascade Microtech, Inc., Beaverton, OR, 1995.

[2-13] W. Liu, *Handbook of III-V Heterojunction Bipolar Transistors*, New York, USA: John Wiley & Sons, 1998, pp. 724-728.

[2-14] D.R. Pelke and D. Pavlidis, "Evaluation of the Factors Determining HBT High-Frequency Performance by Direct Analysis *S*-Parameter Data", *IEEE Trans. On Microwave Theory and Techniques*, vol. 40, no. 12, pp. 2367-2373, Dec. 1992.

[2-15] S.J. Spiegel, D. Ritter, R.A. Hamm, A. Feygenson, and P.R. Smith, "Extraction of the InP/GaInAs Heterojunction Bipolar Transistor Small-Signal Equivalent Circuit", *IEEE Trans. On Elec. Dev.*, vol. 42, no. 6, pp. 1059-1064, June 1995.

[2-16] D. E. Dawson, A. K. Gupta, and M. L. Salib, "CW Measurement of Thermal Resistance," *IEEE Trans. Electron Devices*, vol. 39, no. 10, pp. 2235-9, Oct. 1992.

3. EFFECTS OF DEVICE DESIGN ON THE THERMAL PROPERTIES OF INP-BASED HBTS

3.0 Abstract

Thermal management is of critical concern in high performance InP-based HBTs, because enhancements in RF performance are typically obtained with increased current density and aggressive device scaling. The resulting increase in junction temperature can degrade carrier transport and negatively affect overall device reliability. This paper reports an investigation of thermal resistance in InP-based HBTs with various vertical and lateral designs. Three-dimensional simulations and experimental results illustrate that significant differences in thermal resistance can arise with relatively small changes in device structure.

3.1 Introduction

Device designers have focused their efforts on two primary methods of improving the RF performance of InP-based HBTs: (1) delaying the onset of Kirk effect and (2) reducing parasitic resistances and capacitances. The onset of Kirk effect can be tailored to the technology specification by altering the collector doping profile [3-1]. However, in order to improve RF performance, Kirk effect must be delayed, and the HBT must be allowed to operate at greater current densities. Today, InP-based HBTs are being operated at current densities exceeding 5 $mA/\mu m^2$ [3-2],[3-3]. Although this method is effective at increasing RF performance, it dramatically increases the power dissipated by the HBT.

In order to counteract the increasing current density, the emitter area must be scaled proportionally to maintain constant or reduced total power dissipation. Simultaneously, the remainder of the device must be scaled in order to maintain or increase RF performance [3-4]. However, device scaling generally degrades the thermal resistance (R_{TH}). Scaling without regard to R_{TH} may neither yield the desired RF performance, due to degraded carrier transport, nor the necessary device lifetime, due to high junction temperatures (T_j). Since aggressive scaling of InP-based HBTs has only recently been explored [3-5], much of the thermal design considerations are not yet known. Utilizing existing device data, this paper investigates the trade-off between device scaling and the device R_{TH} for next generation InP-based HBTs.

3.2 Simulations and Model Setup

The ISE TCAD v8.5 software simulation suite are used to simulate the thermal properties of InP-based HBTs. Due to aggressive scaling and an increasingly complex fabrication process, a 3-D mesh is required to accurately represent next generation InP-based HBTs. Using the TCL scripting language interface to the MDRAW structure generation tool, the mesh can be defined parametrically, allowing the user considerable freedom in altering the device geometry, materials, and bias conditions. Despite the computational burden of 3-D simulations, high performance Intel Pentium 4 based workstations running Redhat Linux 9.0 were able to complete the majority of simulations under one hour.

In order to ease the computational burden, three simplifications were utilized. First, due to geometric symmetry along the XZ and YZ planes, only a quarter of each HBT was simulated. This simplification allows the number of vertices to be limited to 50,000. Figure 3-1 shows a typical HBT structure generated for thermal simulations. Second, a Laplacian model is used to model bulk heat transport, but heat transport due to mobile carriers and other phenomena are ignored. Dissipated power is injected into the device structure through a plane, whose footprint is equal to that of the intrinsic base-emitter junction area, located in the collector. The Z-axis position of the heat generation plane is placed at a location that best represents the electrical bias condition. Finally, the thermal conductivity of each material is assumed to be constant versus temperature.

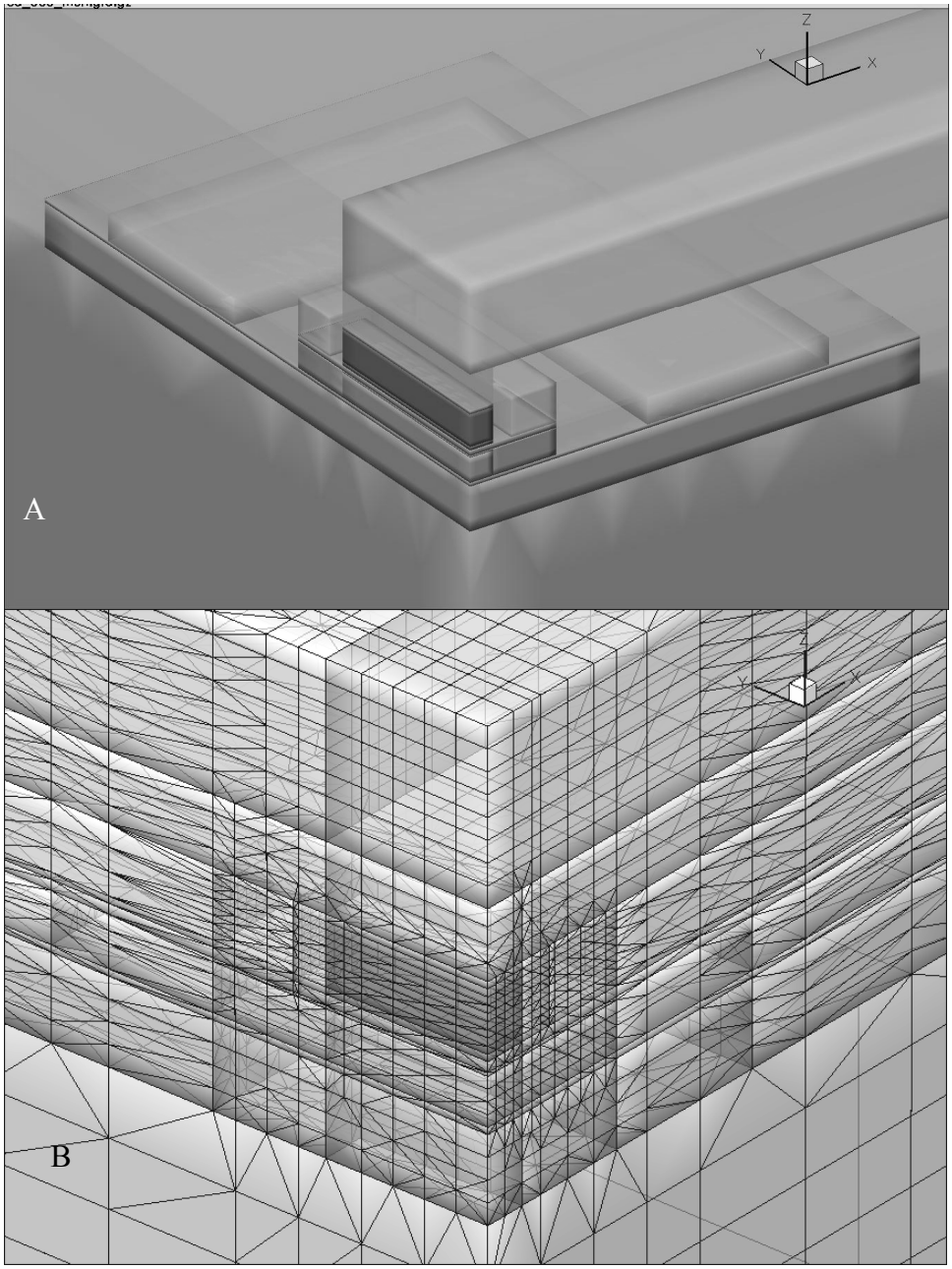

Figure 3-1: (A) The HBT structure is composed of various cuboids, and (B) a wire-frame image shows the mesh and vertices configuration.

In addition to the device, the InP substrate and surrounding Inter-Level Dielectric (ILD) play critical roles during simulation. For an isolated device, a 50 μm cube of InP is placed under the device to simulate the substrate. The four XZ and YZ faces of this cube

are perfect reflecting boundaries, while the bottom XY plane is treated as an ideal thermal contact to an isothermal 300 K heat sink. Devices with substrate cubes as large as 200 μm were simulated; however, the simulated lattice temperatures and calculated R_{TH} deviated less than 1% from the 50 μm substrate cube case. The ILD material is used to fill all volume up to the top surface of the emitter metallization. The top surface of the emitter metallization and ILD is a perfect reflecting boundary. Additional cases where the above assumptions are not adequate are explored in later sections.

3.3 R_{TH} Calculation and Model Calibration

Since the HBT lattice temperature is expected to vary considerably over its 3-D volume, shown in Figure 3-2A, the determination of T_j will have considerable impact on the R_{TH} calculation. In order to correlate experimental and simulated R_{TH} values, T_j was calculated from five candidate locations. They are the point of maximum temperature; center point of the planar heat source; center point of the base-collector junction; center point of the base-emitter junction; and a planar average of the base-emitter junction. Figure 3-2B shows the variation of R_{TH} from the five calculated T_j values. In order to determine which R_{TH} calculation method best correlates to measurement, the simulated R_{TH} is compared to published R_{TH} values [3-6],[3-7]. It is determined that a planar average of the base-emitter junction temperature correlates best to the measured data. Figure 3-3 show the reasonable model to hardware correlation.

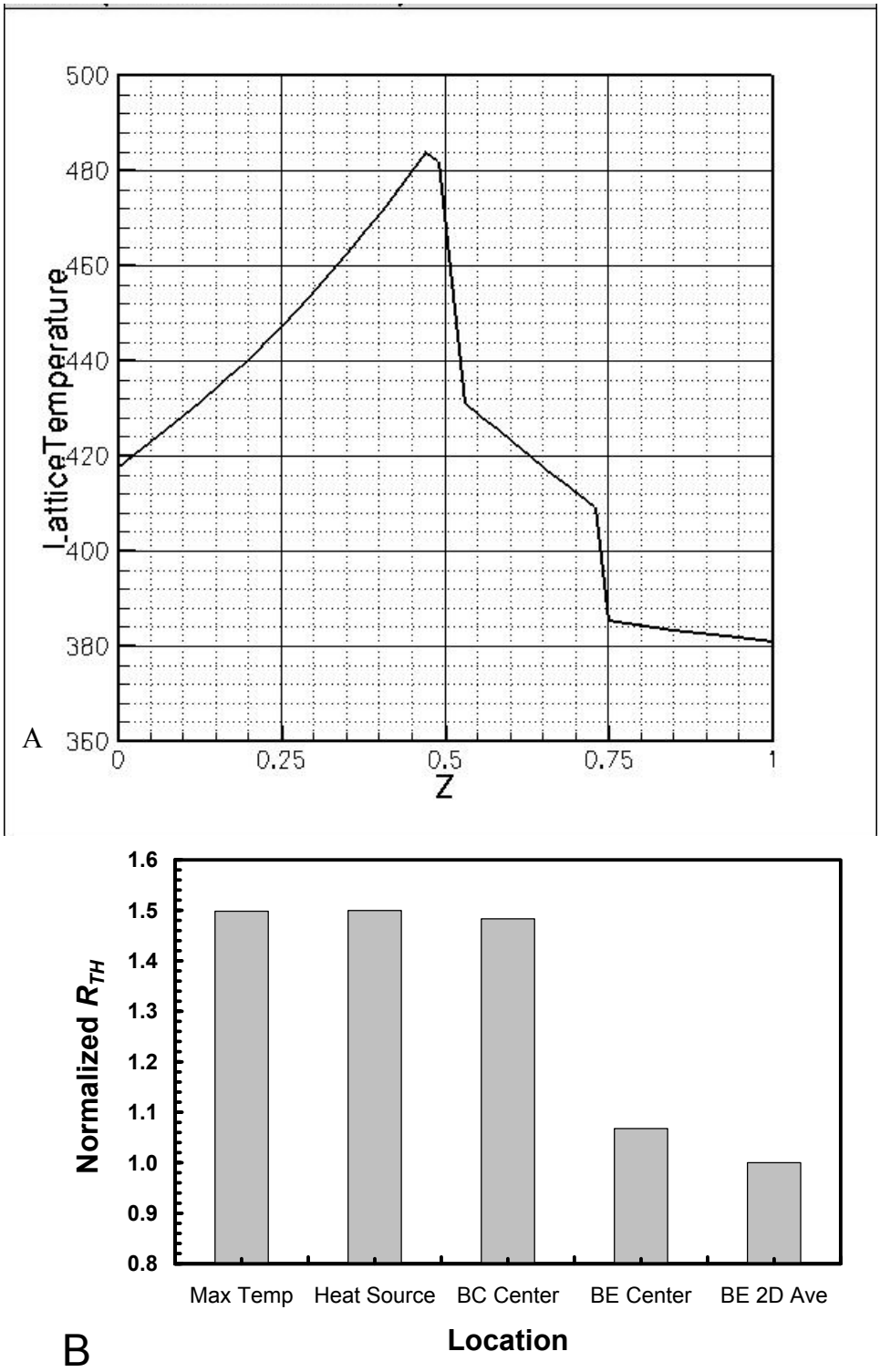

Figure 3-2: (A) The Z-axis temperature variation from sub-collector at left to emitter at right, and (B) R_{TH} values from various T_j extraction methods.

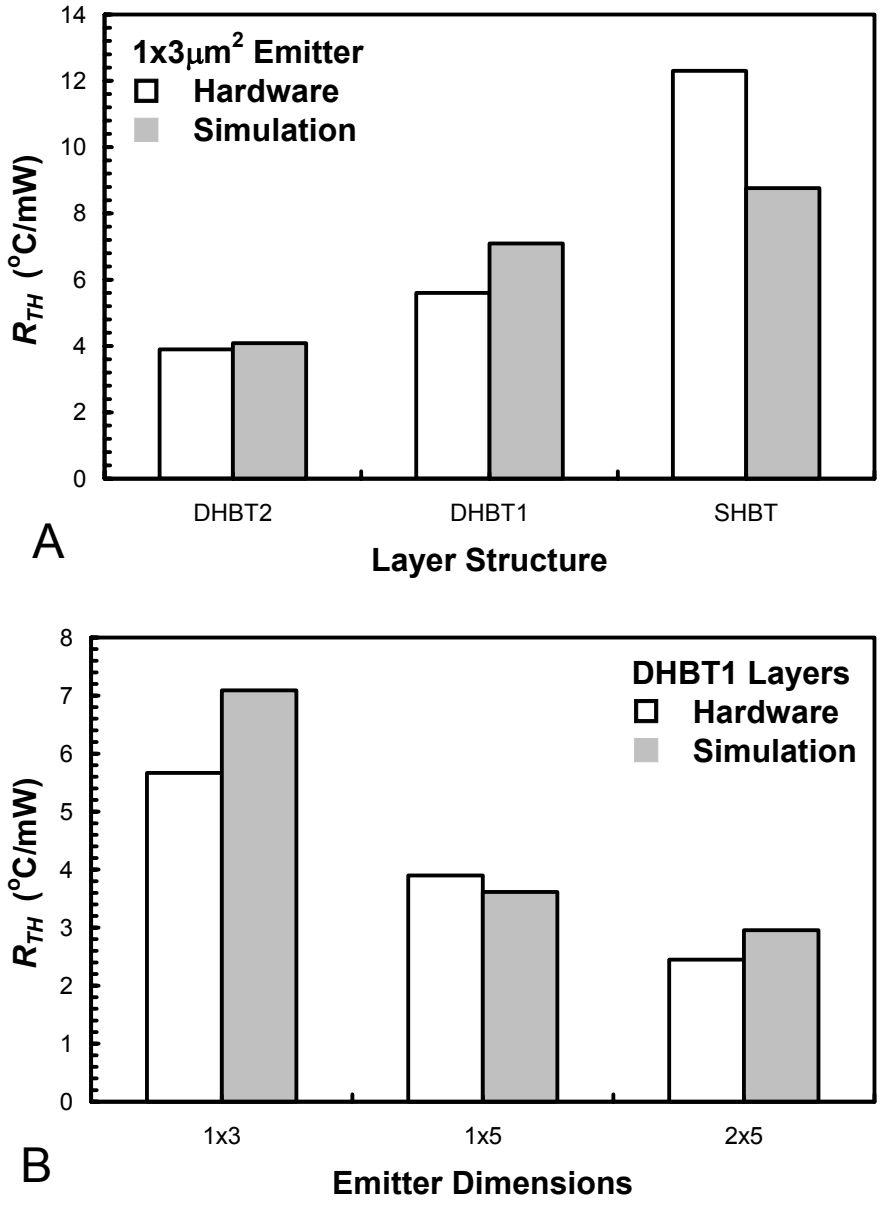

Figure 3-3: The model to hardware correlation is shown for (A) various layer structures and (B) various emitter dimensions.

3.4 Simulation Results

This section outlines several variations in device materials, device geometry, and thermal management strategies that have been considered for high performance InP-based HBTs.

3.4.1 Material Variations

Both InP and InGaAs are commonly used in HBT design; however, their use in the collector and sub-collector plays a critical role in determining both the RF performance and R_{TH}. InP is preferred due to its over 10X advantage in thermal conductivity; nearly 2X advantage in bandgap; and larger inter-valley energy spacing when compared to InGaAs. However, inferior electron mobility and a large conduction band offset to an InGaAs base balance out these benefits. Due to its poor thermal conductivity, an InGaAs collector can significantly increase the collector temperature beyond T_j. A high collector temperature can potentially increase the base-collector diode leakage; increase the HBT offset voltage; and degrade the HBT reliability. It is also important to note that thinner, 20 nm or less, layers of InGaAs can be used as etch stops, but less severely impact R_{TH}. Figure 3-4 illustrates the effects of InP and InGaAs in both the collector and sub-collector.

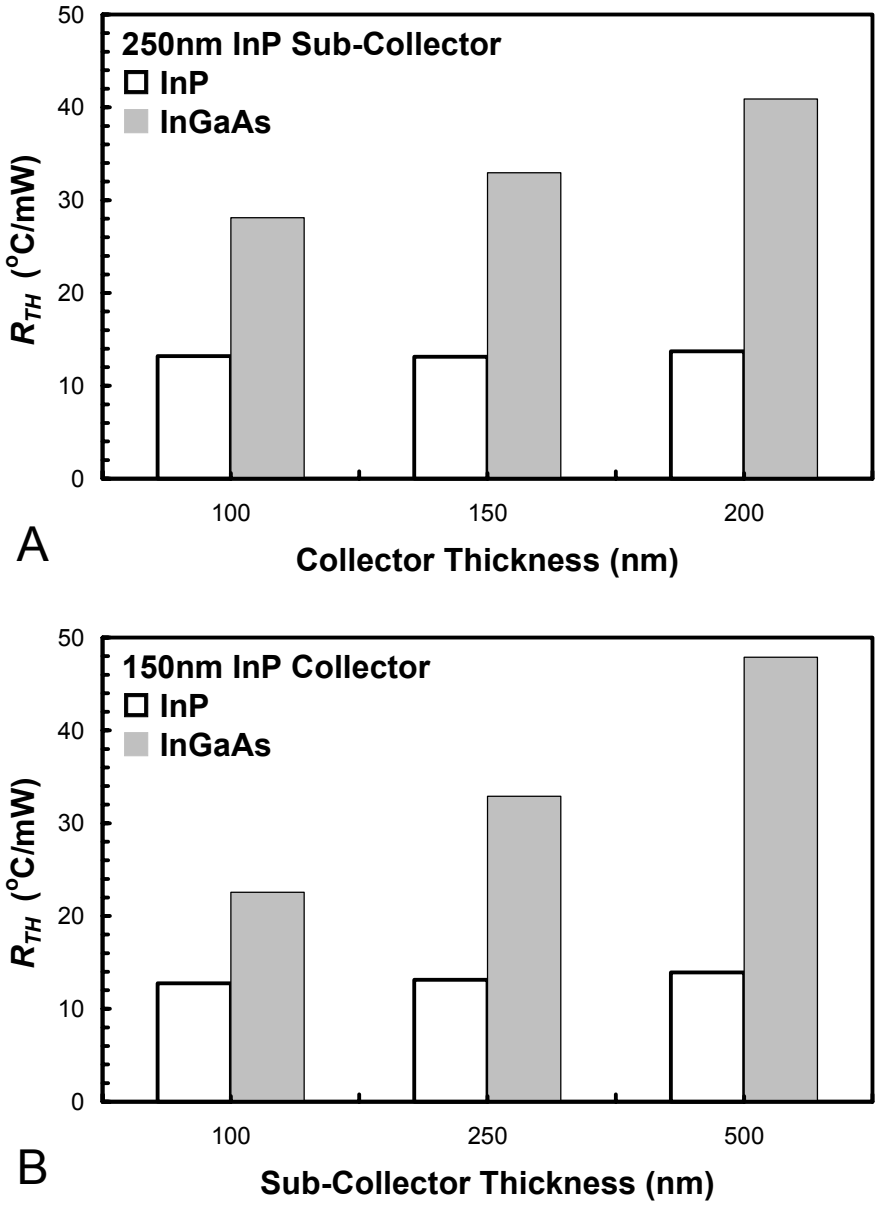

Figure 3-4: R_{TH} values for a 0.25x2.00 μm^2 emitter HBT are shown with (A) 250 nm InP sub-collector, and (B) 150 nm InP collector.

3.4.2 Device Layout

In the past, the triple mesa HBT structure has allowed base-collector capacitance reduction through various etching methods. From left to right, the first four cases shown in Figure 3-5A show the effect of gradually increasing the collector under-cut. The *Field C* value represents the un-etched collector case, while the *Full C Undercut* value represents the case where the extrinsic collector has been completely removed and replaced with the ILD material. The final two values, *Field SC* and *Partial SC Undercut*, represent the un-etched sub-collector, but etched collector case, and the over-etched sub-collector case, respectively. In addition, the spacing and width of the base and collector metals play a role in the R_{TH}. Figure 3-5B shows the effects of the base metal. Variations in the collector metal are not shown, but have less of an impact than the base metal.

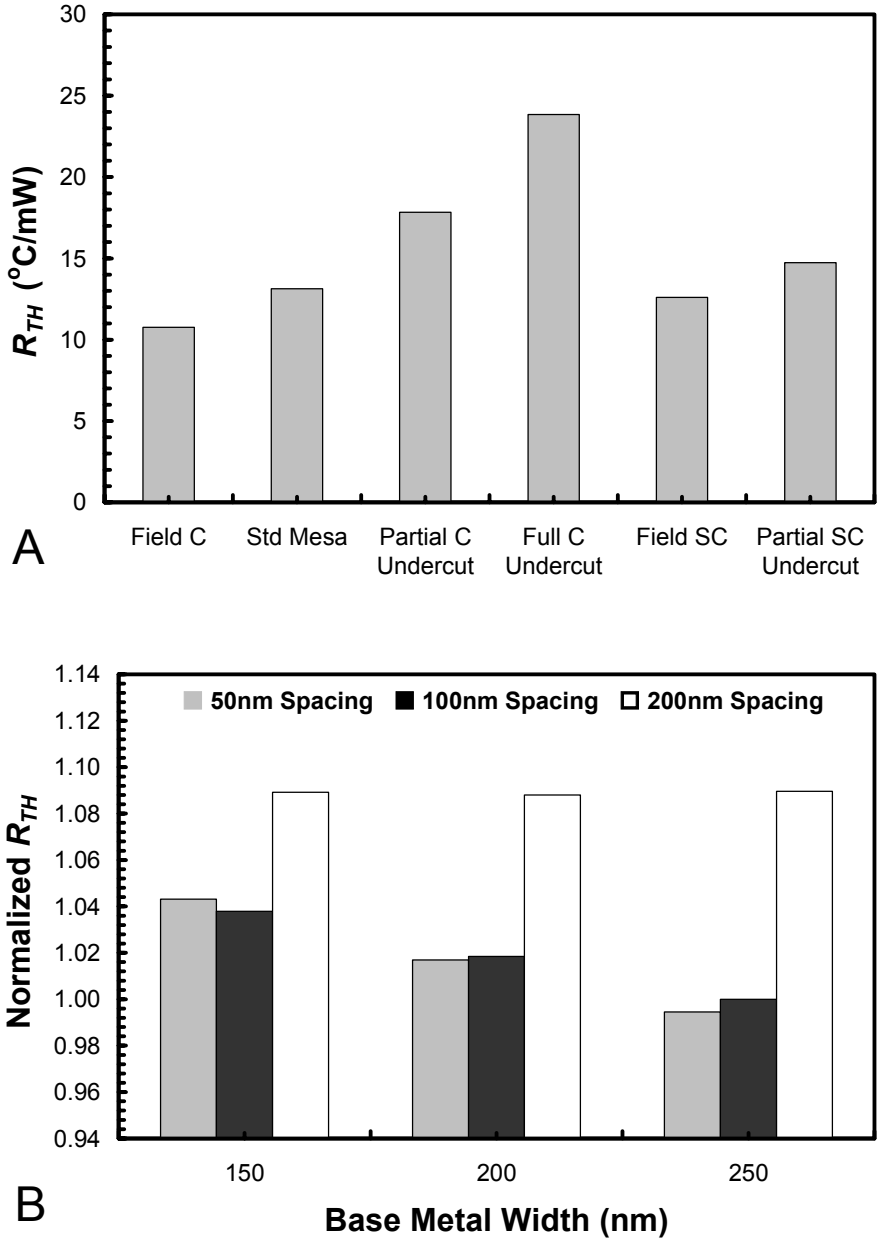

Figure 3-5: The impact of (A) collector and sub-collector etching, and (B) base metal spacing and width are shown on a HBT with a 0.25x2.00 μm^2 emitter, 150 nm InP collector, and 250 nm InP sub-collector.

3.4.3 Thermal Management

Although R_{TH} can be minimized through device design, methods external to the HBT should not be neglected. InP and InGaAs layers in the collector and sub-collector impact substrate heat conduction, but emitter metallization and ILD affect the top-side heat conduction. Figure 3-6A shows the effects of a *M1 bar*, a 10 μm Metal 1 extension of the emitter metal; *Heat Shunt*, a gold via from the emitter metal through a Metal 1 bar to the InP substrate spaced 2 μm from the device edge; and *Heat Spreader*, a large 50 μm square Metal 1 plate connected to the emitter metal. Although Metal 1 is an effective means of reducing R_{TH}, variations in the Metal 1 placement and size significantly affect the R_{TH}.

A more effective way of minimizing R_{TH} is the replacement of BCB, Polyimide, and other traditional dielectrics with a high thermal conductivity ILD like Diamond Like Carbon (DLC). Figure 3-6A also shows the effect of replacing BCB with DLC for various Metal 1 configurations. The use of a high thermal conductivity ILD negates any of the metallization dependence of R_{TH} present with BCB. However, a high quality DLC is not required to reduce R_{TH}. Figure 3-6B shows that once the ILD thermal conductivity becomes comparable to that of the HBT, heat generated within the HBT can preferentially exit the device, and significant reductions in R_{TH} can be realized.

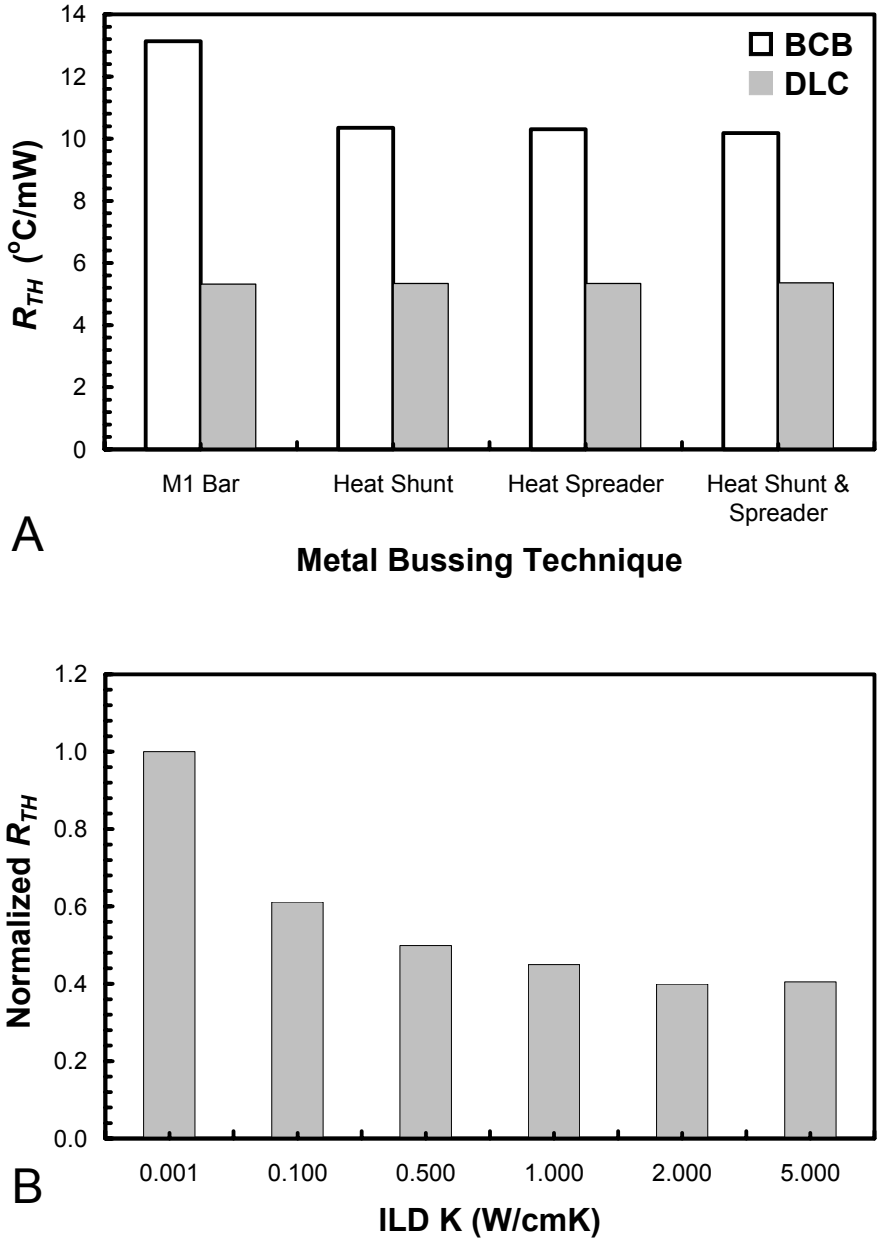

Figure 3-6: The impact of (A) emitter metallization and ILD material, and (B) ILD thermal conductivity are shown on a HBT with a 0.25x2.00 μm^2 emitter, 150 nm InP collector, and 250 nm InP sub-collector.

3.4.4 Transistor Density

Although the previous scenarios provide valuable insight, thermal simulations of an isolated device are not an accurate indication of acceptable T_j or R_{TH} in a circuit. In order to reproduce the thermal environment in a circuit, the substrate geometry is altered from a cube to a column. Symmetric reduction of the X and Y extents represents a regular 2-D array of devices, but an asymmetric reduction corresponds to a row or column of devices. By moving the reflecting boundary conditions of the XZ and YZ planes closer to the intrinsic device, heat generated by the HBT is reflected back into the device. This serves to mimic the heat contribution from devices directly adjacent to the original device. Although this method is computationally favorable, it can only assess the case where all devices in the densely packed array, column, or row are both structurally and operationally identical. Figure 3-7A shows the effects of device spacing and substrate thickness for a regular 2-D array of HBTs.

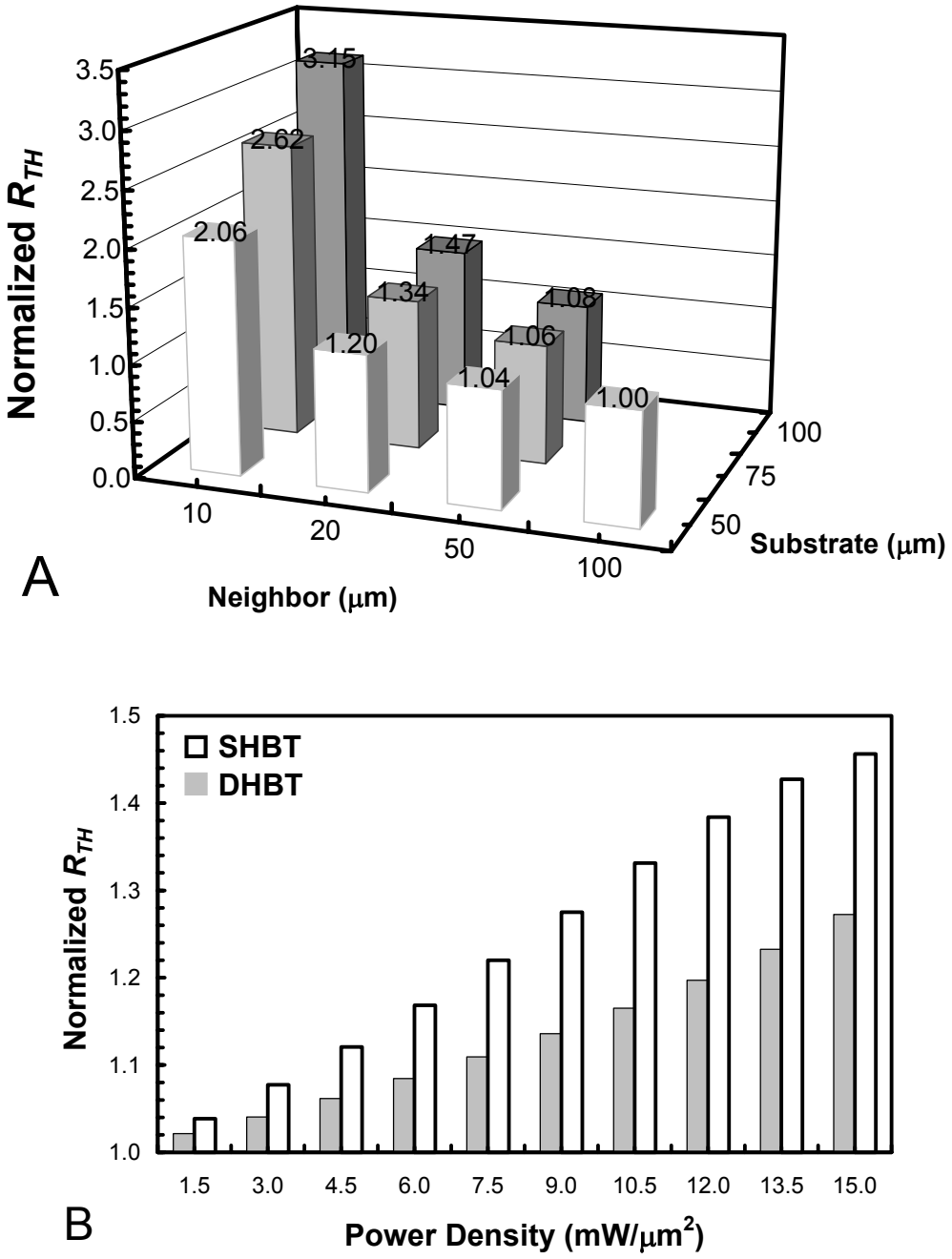

Figure 3-7: The impact of (A) 2-D densely packed transistor array and (B) temperature dependent thermal conductivity are shown on a HBT with a 0.25x2.00 μm^2 emitter, 150 nm InP collector, and 250 nm InP sub-collector.

3.4.5 Temperature Dependence

The final refinement to the thermal model of InP-based HBTs is the temperature dependence of thermal conductivity. For computational simplicity, the majority of simulations ignored this phenomenon, but some cases require a more rigorous thermal conductivity model. As expected, Figure 3-7B shows the increasing deviation between temperature independent and dependent with increasing dissipated power.

3.5 Summary

A 3-D thermal model was developed and calibrated for InP-based HBTs with the ISE TCAD simulation suite. This model allows for the accurate estimation of R_{TH} values for aggressively scaled, next generation HBTs. The effects of device design, materials, and thermal management are explored. Figure 3-8 contrast the temperature profile of a poorly and properly designed HBT, respectively.

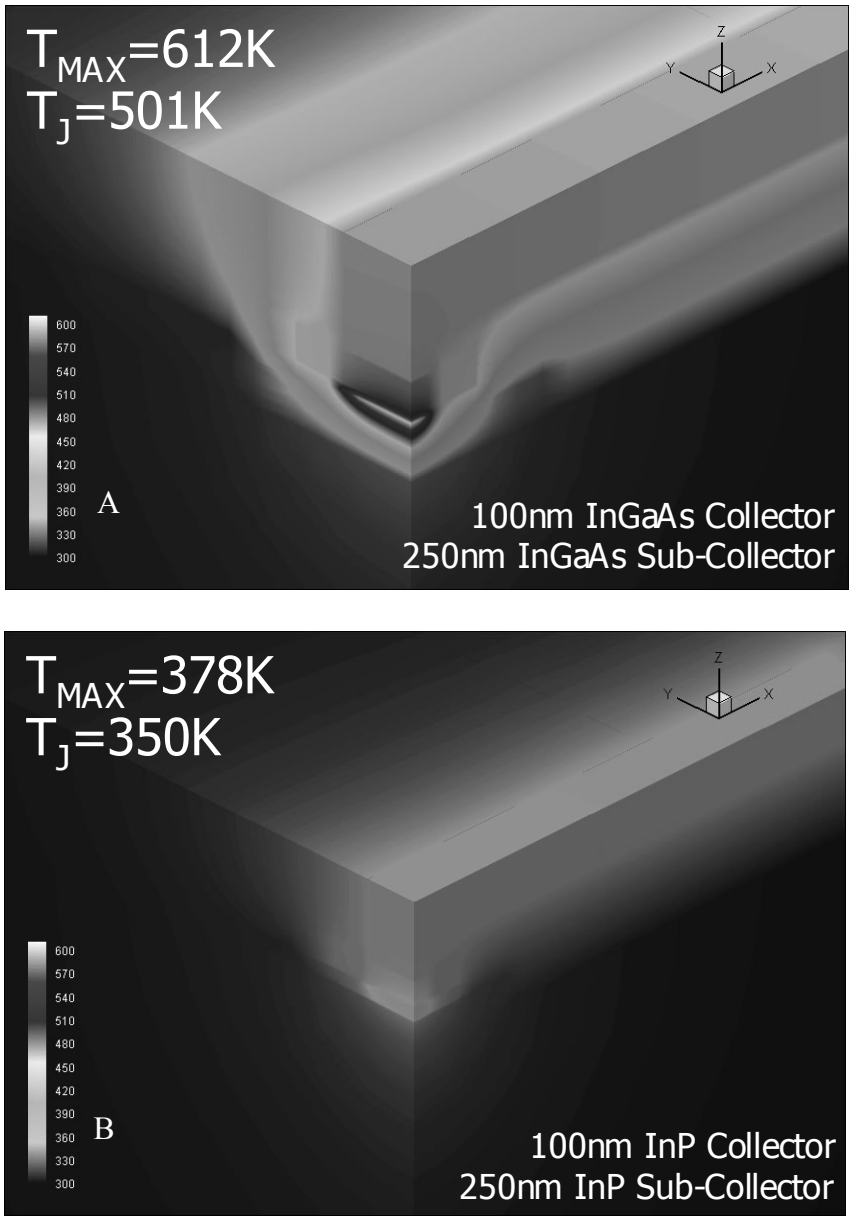

Figure 3-8: The lattice temperature is shown for a (A) poorly and (B) properly thermal designed HBT with a 0.25x2.00 μm^2 emitter.

3.6 Acknowledgements

This chapter, in full, is a reprint as it appears in the Proceedings of the 2003 International Symposium on Compound Semiconductors. The contributions from the co-authors Tahir Hussain, Donald A. Hitko, Charles H. Fields, and Marko Sokolich of HRL Laboratories, L.L.C., and Peter M. Asbeck of UCSD are appreciated. The author of this dissertation was the primary investigator and primary author of this publication. This work was sponsored by the Defense Advanced Research Projects Agency (DARPA) through AFRL Contract F33615-02-1286 (TFAST). The authors would like to thank John Zolper of DARPA, and John King and Mark Pacer of AFRL for their support. In addition, the donation of simulation software and technical support from ISE Inc. is greatly appreciated.

3.7 References

[3-1] P. J. Zampardi, "A Study of New Base Pushout Effect in Modern Bipolar Transistors," *UCLA Ph.D. Thesis*, 1997.

[3-2] M. Ida, K. Kurishima, N. Watanabe, "Over 300 GHz f_T and f_{max} InP/InGaAs double heterojunction bipolar transistors with a thin pseudomorphic base", *IEEE Electron Device Letters*, vol.23, no.12, pp. 694-6, Dec. 2002.

[3-3] W. Hafez, J.W. Lai, M. Feng, "Record f_T and f_T+f_{MAX} performance of InP/InGaAs single heterojunction bipolar transistors", *Electronics Letters*, vol. 39, no. 10, pp. 811-13, May 2003.

[3-4] M. J.W. Rodwell, M. Urteaga, T. Mathew, D. Scott, D. Mensa, Q. Lee, J. Guthrie, Y. Betser, S. C.Martin, R. P. Smith, S. Jaganathan, S. Krishnan, S. I. Long, R. Pullela, B. Agarwal, U. Bhattacharya, L. Samoska, and M. Dahlstrom, "Submicrometer scaling of heterojunction bipolar transistors," *IEEE Transactions on. Electron Devices*, vol. 48, pp. 2606–2624, Dec. 2001.

[3-5] J. Zolper, 2003 GaAs MANTECH, pp. 7-10.

[3-6] C.H. Fields, J. Foschaar, and S. Thomas III, "Thermal resistance characterization of 200 GHz F_t InGaAs/InAlAs HBTs", in 2002 *IPRM Technical Digest*, pp. 79-82.

[3-7] S. Thomas III, J.A. Foschaar, C.H. Fields, M.M. Madhav, M. Sokolich, R.D. Rajavel, and B. Shi, "Effects of device design on InP-based HBT thermal resistance", *IEEE Transactions on Device and Materials Reliability*, vol. 1, no. 4, pp. 185-189, Dec. 2001.

4. CHARACTERIZATION AND MODELING OF THERMAL EFFECTS IN SUB-MICRON INP DHBTS

4.0 Abstract

S-parameter measurements performed on 400 GHz InP DHBTs, with 250 nm and 400 nm wide emitters, show that an 8-10% increase in peak f_T can be achieved when the ambient temperature is reduced from +25 ºC to -50 ºC. This strong temperature dependence of device performance indicates that thermal modeling will play a critical role in device and circuit design. Using the Synopsys® DESSIS simulator, a 3D thermal model was calibrated to these sub-micron 400 GHz InP DHBTs for use in technology development. The 3D model is sufficiently complex to allow the thermal de-embedding of pads; projection of R_{TH} to higher dissipated powers; and estimates of cooperative heating. These three features allow the 3D model to go beyond the data that can be acquired by direct measurement, and lead to a more accurate value of R_{TH} for compact models.

4.1 Introduction

Several groups have reported InP DHBTs with f_T and f_{MAX} values that exceed 400 GHz [4-1],[4-2],[4-3]. To achieve this level of performance, the device geometry has been scaled aggressively into the sub-micron regime and collector current density, J_C, has been increased by delaying the onset of Kirk effect [4-4]. Associated with these changes has been a substantial increase in the power density, P_D, since the collector-emitter voltage, V_{CE}, has not been scaled down sufficiently. Furthermore, due to the bandgaps and conduction band offsets of materials in the InP system, it is unlikely that V_{CE} will scale below 1.0 V if maximum small signal RF performance is to be obtained. At the same time, the actual scaling of the emitter area, A_E, has not kept pace with the increase in P_D leading to an increase in the overall power per transistor. Scaling also causes increased device mismatch due to local and global process variations [4-5], and the thermal mismatch due to device placement; metal routing; and process variations will only magnify mismatch concerns [4-6]. As a result, the junction temperature, T_j, rise associated with the increase in P_D and mismatch can be expected to be a significant issue in sub-micron InP DHBTs.

By quantifying the T_j rise in sub-micron InP DHBTs and illustrating its effect on device performance, the data presented in this paper indicates that the increasing P_D and hence T_j is becoming an increasing barrier to higher performance devices. Comprehensive 3D thermal modeling has been used to capture and predict the thermal properties of sub-micron InP DHBTs. These simulated thermal properties can then be represented in compact models and aid in the IC design process.

4.2 RF Measurements at Reduced T_{AMB}

The rise of T_j over the ambient temperature, T_{amb}, can be defined as the product of the thermal resistance, R_{TH}, and the dissipated power, P_{diss}, as shown in (4-1). P_{diss} is defined as the sum of the products of the terminal currents and voltages, as shown in (4-2).

$$T_j = R_{TH} P_{diss} + T_{amb} \tag{4-1}$$

$$P_{diss} = I_C V_{CE} + I_B V_{BE} \tag{4-2}$$

To demonstrate the effect of self-heating on device performance, InP DHBTs, whose emitter widths are 250 nm and 400 nm and emitter lengths are 2, 4, 6, and 8 μm, were characterized from a T_{amb} of -50 ºC to +25 ºC. Using a HP8510C network analyzer, *S*-parameter measurements were taken over a frequency range from 400 MHz to 40.4 GHz. The frequency of unity current gain and power gain, f_T and f_{MAX}, are determined from –20 dB/dec extrapolations of the small signal current gain, $|h_{21}|$, and Mason's gain, U, respectively. A Short-Open-Load-Thru (SOLT) off wafer calibration was first used, and on-wafer open and short pad structures, whose dimensions are identical to the device under test (DUT), were used to de-embed the associated pad parasitics from the DUT measurement. Figure 4-1 shows the de-embedded $|h_{21}|$ and U curves at peak f_T and a T_{amb} = +25 ºC, corresponding to an I_C = 8.3 mA and V_{CE} = 1.4 V, for an A_E = 0.25x4.0 μm^2 device. Figure 4-2 shows the f_T versus I_C at various T_{amb}. Over this 75 ºC range, the peak f_T increases from 421 GHz to 455 GHz, a full 8% increase from T_{amb} = +25 ºC. Figure 4-3 and Figure 4-4 show how the peak f_T evolves for the 250 nm and 400 nm wide emitter DHBTs with various emitter lengths and V_{CE} values, respectively [4-7]. By

comparing peak f_T values of a variety of emitter widths and lengths, we find that proper thermal design could improve RF performance by as much as 10%. When examining the peak f_T with increasing V_{CE}, the reduced T_{amb} not only increases the absolute peak f_T value, but also allows peak f_T to continue to increase with higher V_{CE}. The additional performance gained through lowering T_j can be used to reduce the demands of scaling. The net impact of similar devices in digital circuits can be gauged by the temperature dependence of ring oscillator stage delay previously published in [4-8].

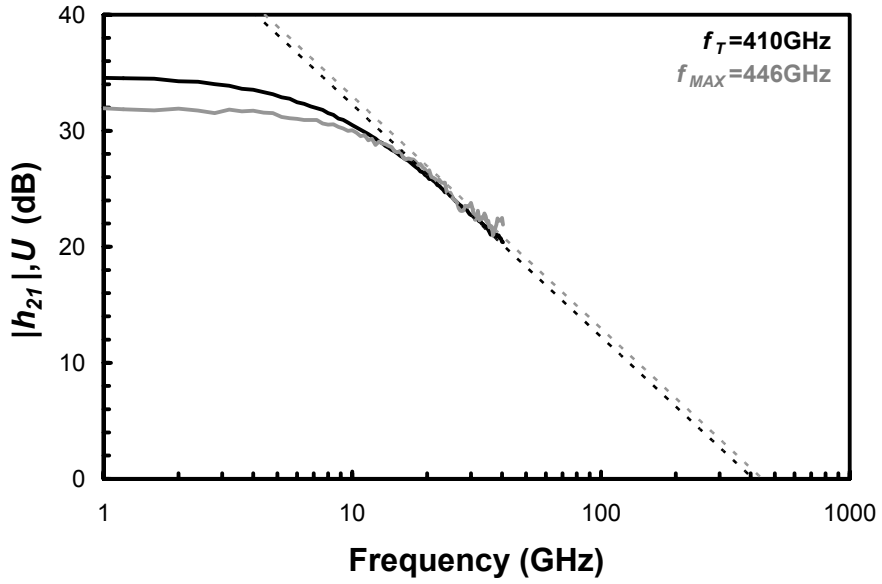

Figure 4-1: Small signal current gain, $|h_{21}|$, and Mason's gain, U, curves for an A_E = 0.25x4.0 μm^2 InP DHBT at I_C = 8.3 mA, V_{CE} = 1.4 V, and T_{amb} = +25 ºC.

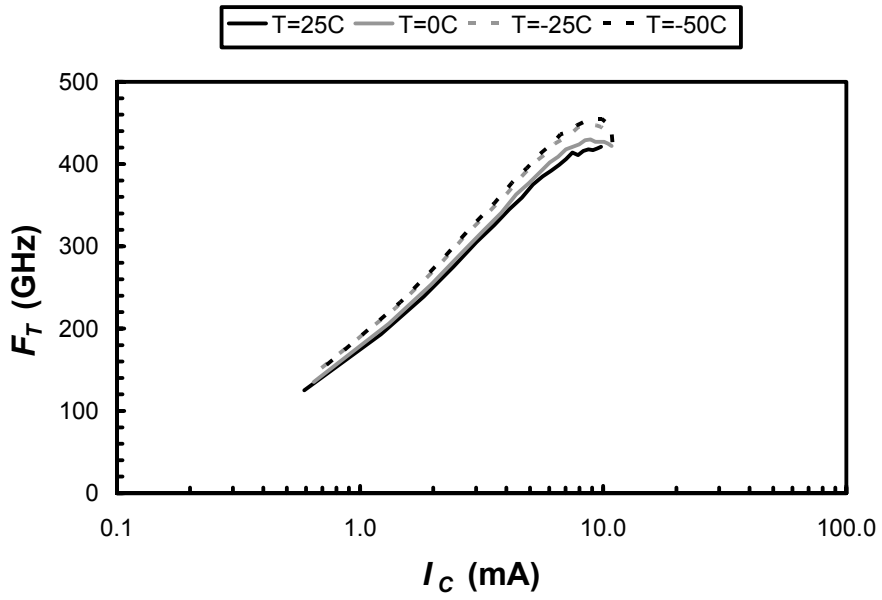

Figure 4-2: Unity current gain frequency, f_T, versus collector current, I_C, curves over a T_{amb} range from –50 ºC to +25 ºC for an A_E = 0.25x4.0 μm^2 InP DHBT.

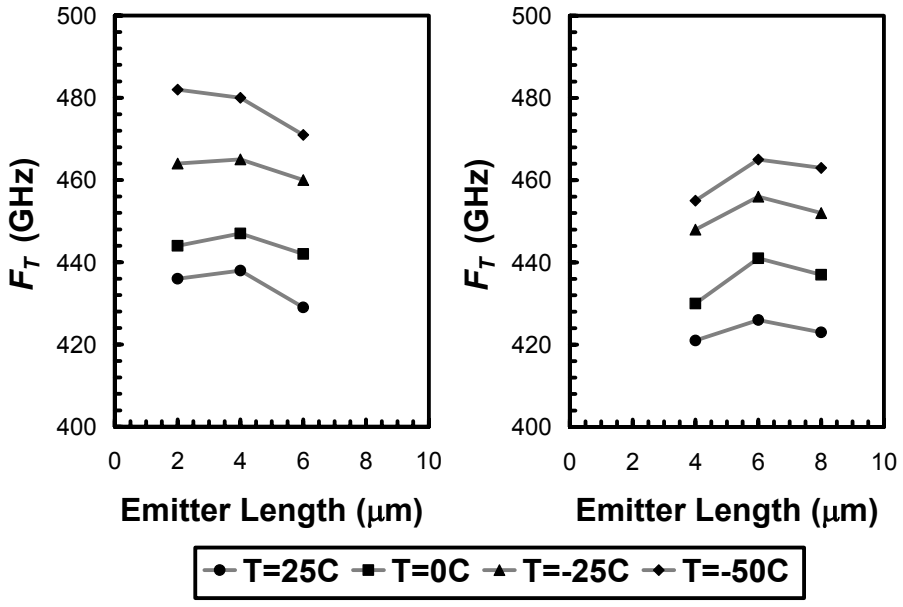

Figure 4-3: Peak f_T of 400 nm wide emitter (left) and 250 nm wide emitter (right) DHBTs with various emitter lengths and at various T_{amb}.

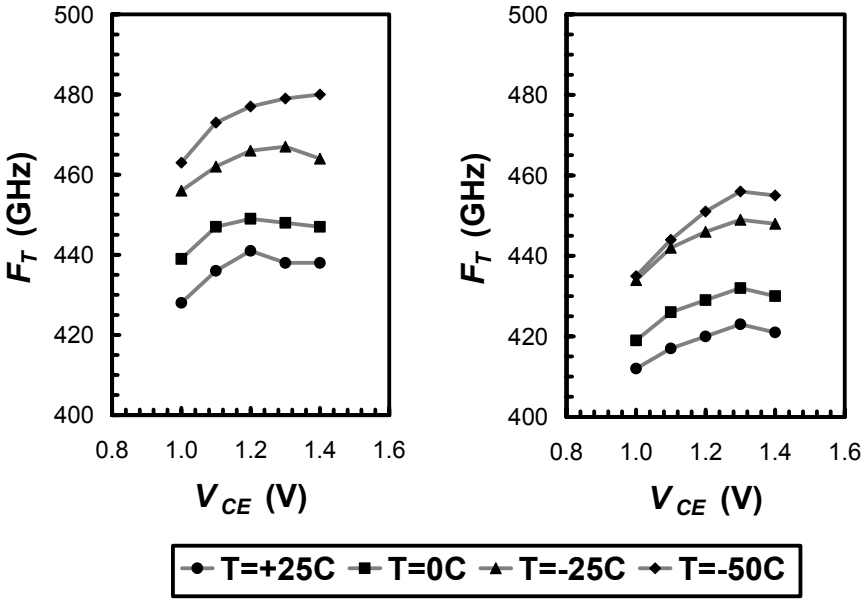

Figure 4-4: Peak f_T for an A_E = 0.4x4.0 μm² DHBT (left) and an A_E = 0.25x4.0 μm² (right) DHBT at various V_{CE} and T_{amb}.

4.3 R_{TH} Measurements

T_{amb} can be varied to produce relative changes in T_j, but values of R_{TH} are required to determine the absolute change in T_j. Using the base-emitter voltage, V_{BE}, method of Dawson et al [4-9], the R_{TH} was measured for InP DHBTs with 250 nm and 400 nm wide and 2, 4, 6, and 8 μm long emitters. Figure 4-5 shows the measured R_{TH} for 250 nm and 400 nm wide emitters at J_C = 1 mA/μm² and a T_{amb} of 25 ºC [4-7]. At the bias condition of maximum f_T, it is estimated that there is an 80-110 ºC increase in T_j with respect to T_{amb}. Therefore, the selection of T_{amb} in Section 4.2 was reasonable, and it can be inferred that a 75 ºC increase in T_j due to self-heating results in approximately 40 GHz reduction in peak f_T. It is important to note that R_{TH} is temperature dependent and hence, a power dependent parameter. Since the V_{BE} method of Dawson et al must be performed at low J_C to avoid the influence of series resistances and hetero-interfaces, the measured

R_{TH} may not be representative of the R_{TH} at peak f_T. It is expected that R_{TH} will increase with increasing P_D, because of the increase in material thermal resistivities. Therefore, the measured R_{TH} should be viewed as a lower bound of the high power R_{TH}.

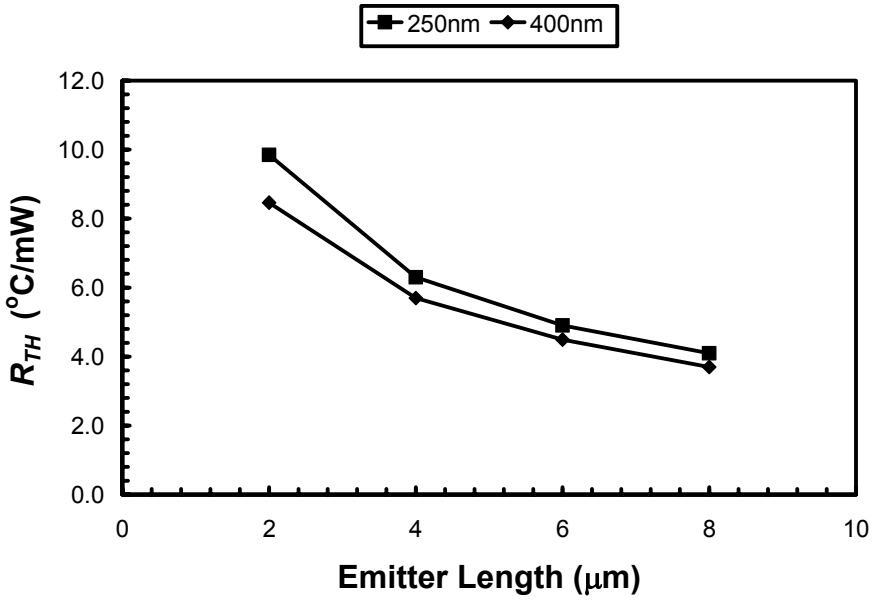

Figure 4-5: Measured R_{TH} versus emitter length for 250 nm (squares) and 400 nm (diamonds) wide emitter InP DHBTs.

4.4 3D Thermal Model

Using the Synopsys® tool, DESSIS, a 3D thermal model of sub-micron DHBTs was constructed. Due to the computational demands of a 3D electro-thermal simulation, only the heat equation was solved to produce the temperature distribution throughout the lattice. Further reductions in computational demands were achieved by using device symmetry, simulating a quarter of the whole HBT, to reduce the mesh complexity. Figure 4-6 shows the layers of the canonical HBT structure. The numerous device layers are essential to properly model the various epitaxial layers that allow >400 GHz peak f_T; device layout schemes; process variations; and heat source locations. To simulate heat

transport out of the top of the HBT, the first metal level and surrounding dielectric was also included. Likewise, to simulate heat transport out of the bottom of the HBT, no less than 50 μm per side cube of InP was used to represent the substrate. The temperature dependence of the thermal conductivity is included for materials used in the 3D thermal model. The results of an earlier version of this model have been previously published in [4-6] and allowed the initial examination of material and device design on the thermal properties of sub-micron InP DHBTs. The enhanced 3D thermal model presented in this work accounts for the details associated with sub-micron devices.

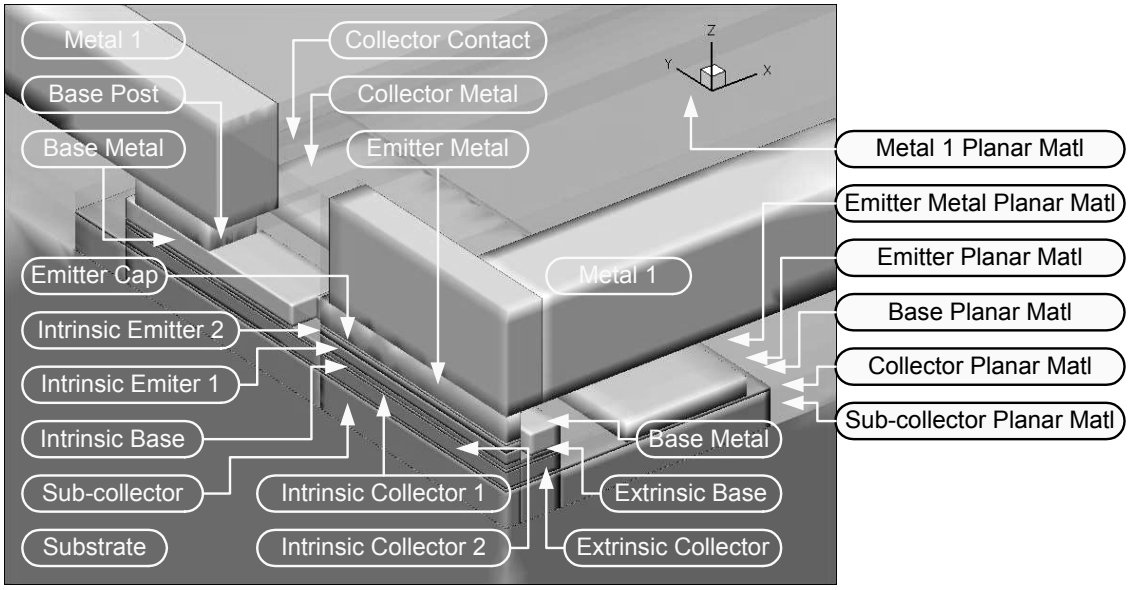

Figure 4-6: Canonical HBT representation in the 3D thermal model.

Figure 4-7 and Figure 4-8 show the reasonable correlation between measured and simulated R_{TH} for 400 nm and 250 nm wide emitter devices, respectively, at a constant P_D = 1.5 mW/μm^2. Process variations can also impact R_{TH}, and as an example, Figure 4-8 also shows the measured and simulated R_{TH} of 250 nm wide emitter DHBTs, where some emitters were reproduced as drawn and some had been undercut by 1 μm. The 8.0 μm long DHBT suffers a ~40% increase in R_{TH}, but the shortest, 2.0 μm DHBT suffers a

~70% increase in R_{TH}. Based on previous simulations [4-6], variations in epitaxial layers; collector mesa etching; and base metal width and spacing are also expected to produce significant R_{TH} variations.

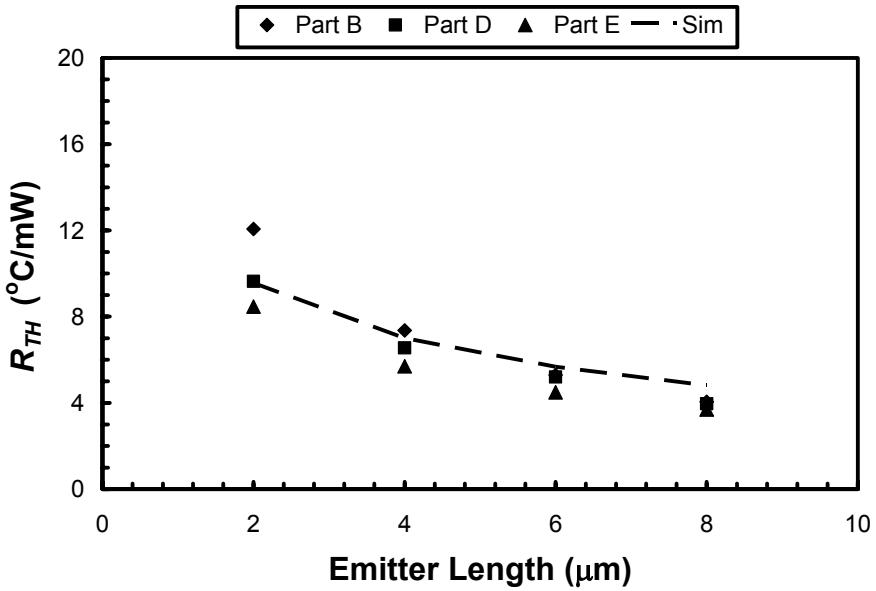

Figure 4-7: Measured (Part B, Part D, Part E) and simulated (Sim) R_{TH} for 400 nm wide emitter InP DHBTs.

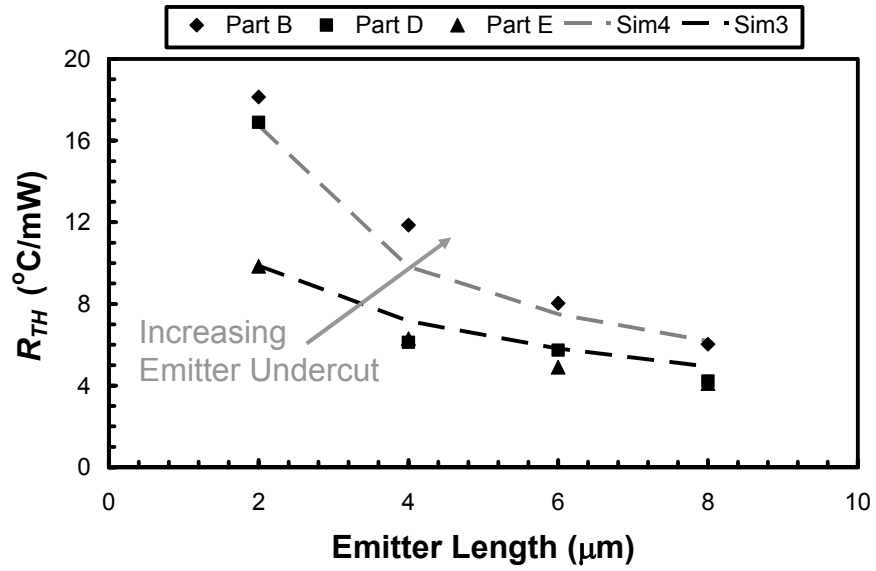

Figure 4-8: Measured (Part B, Part D, Part E) and simulated R_{TH} for 250 nm wide emitter DHBTs with (Sim4) and without (Sim3) a 1 μm emitter undercut.

4.5 Compact Modeling

The 3D thermal model is a flexible tool that can also predict how R_{TH} depends on the IC environment. For example, the measurement of R_{TH} requires large probe pads that make both low impedance electrical and thermal contact to a relatively high impedance device. When the HBT is placed into an IC, only a small mass of metal remains attached to the emitter. Figure 4-9 shows the effect of thermally de-embedding the probe pads from the measured R_{TH} of 250 nm wide emitter DHBTs. The relatively large A_E = 0.25x8.0 μm^2 DHBT suffers a 14% increase, but as the emitter length is scaled to 2.0 μm, a 25% increase in R_{TH}, over the measured R_{TH}, is observed. The impact of thermal de-embedding is analogous to the electrical de-embedding required to remove pad parasitics for an *S*-parameter measurement.

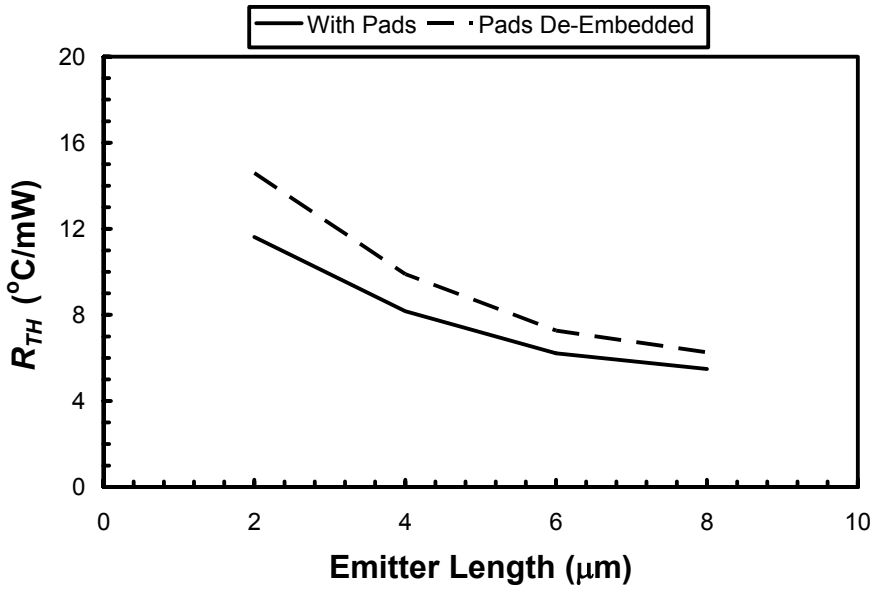

Figure 4-9: Simulated R_{TH} for 250 nm wide emitter InP DHBTs of various emitter lengths with (solid) and without (dashed) probe pads.

The large differences in measured and de-embedded R_{TH} values would indicate significant heat removal through the emitter. Using Fourier's Law and a parallel network

of R_{TH} values, it is estimated that 12-20% of the total P_{diss} is removed through the emitter of the 250 nm wide DHBTs, while the remainder is removed through the sub-collector. Variations in the metals attached to the emitter, not only the emitter (Figure 4-8), are expected to produce variations in effective R_{TH}.

In addition to the thermal de-embedding of the pads, the R_{TH} measurement requires a relatively low J_C, as described in Section 4.3. As a result, the R_{TH} measurement bias condition is unlike the actual IC operating conditions. Simulation can be used to predict R_{TH} at higher J_E and hence P_D. Figure 4-10 shows an A_E = 0.25x4.0 μm^2 DHBT with and without thermal de-embedding over a large range of P_D. Thermal de-embedding has not only increased the absolute value of R_{TH}, but it has changed the P_D dependence. At P_D = 12 mW/μm^2, the bias condition at peak f_T, R_{TH} has increased by 30% over the P_D = 1.5 mW/μm^2 condition of the R_{TH} measurement.

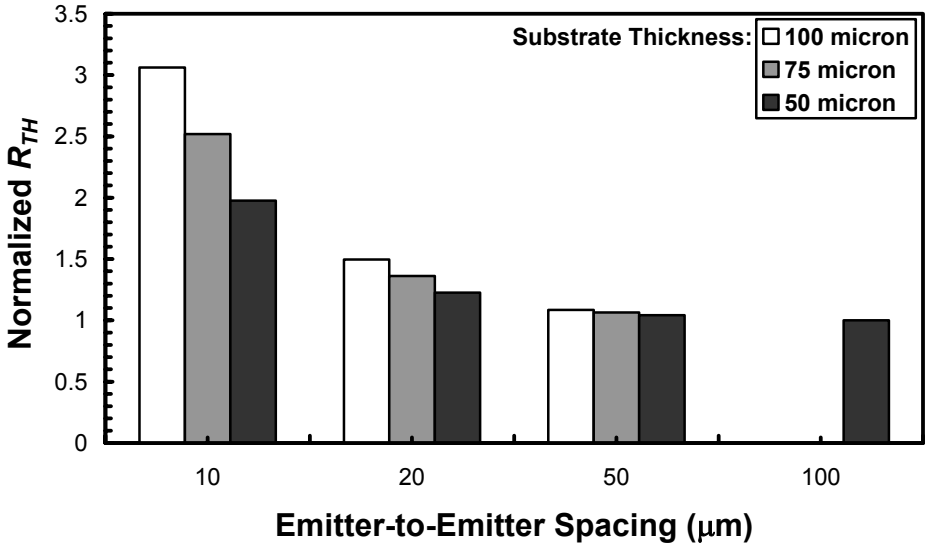

Figure 4-10: Simulated power density dependence of R_{TH} for an A_E = 0.25x4.0 μm^2 InP DHBT with (solid) and without (dashed) probe pads.

The third condition that cannot be easily measured is the increase in effective R_{TH} due to cooperative heating. By altering the substrate, metallization, and dielectric boundaries, the 3D thermal model can be used to predict the temperature profile of a uniformly spaced 1D or 2D array of identical HBTs. Figure 4-11 shows the effective increase in R_{TH}, normalized to the isolated HBT case, with respect to emitter-to-emitter spacing and substrate thickness. For a 2D array of A_E = 0.25x2.0 μm^2 DHBTs, with a 10 μm emitter-to-emitter spacing and a 100 μm thick substrate, simulations predict a 3X increase in effective R_{TH}. Although a 2D array of identical devices is unlikely to be used, the results provide a reasonable guideline for the layout of large transistor count ICs.

These three aspects of the 3D model, thermal de-embedding, P_D dependence, and cooperative heating, provide a distinct advantage over R_{TH} measurements alone. A more representative value of R_{TH} can be selected for use in a compact model, such as VBIC or HICUM. Given the large variations in peak f_T shown in Section 4.2, the improved accuracy of R_{TH} will be imperative to achieving first pass design success for high performance InP based ICs.

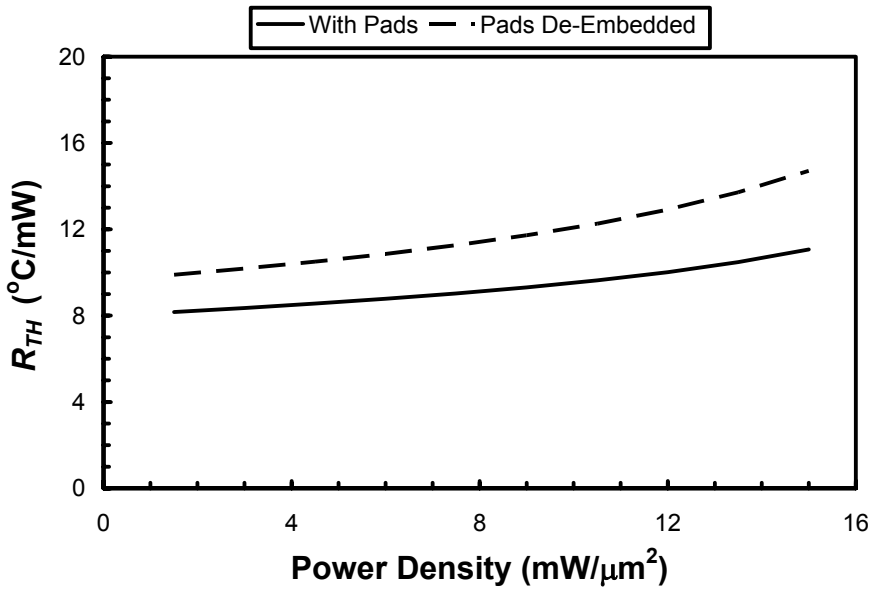

Figure 4-11: R_{TH} increase for an A_E = 0.25x2.0 μm² InP DHBT, normalized to the isolated DHBT case, as a function of emitter spacing and substrate thickness.

4.6 Conclusions

An 8-10% increase in peak f_T can be achieved for a 75 ºC reduction in T_{amb}, demonstrating the strong temperature dependence of these 400+ GHz InP DHBTs and the potential for improved device thermal design. A refined model, calibrated to this new generation of sub-micron 400 GHz InP DHBTs, is used to investigate the impact of process variations. An important benefit of this 3D model is that it can be extended beyond technology development and correlation to R_{TH} measurements. The 3D model is also used to thermally de-embed the pads from the measured R_{TH}; predict the P_D dependence of R_{TH}; and predict the effective increase of R_{TH} due to cooperative heating. All three of these capabilities improve the accuracy of the R_{TH} compact model parameter and hence, improve the accuracy of circuit simulations.

4.7 Acknowledgements

This chapter, in full, is a reprint as it appears in the Technical Digest of the 2005 Compound Semiconductors IC Symposium. The contributions from the co-authors Tahir Hussain, Donald A. Hitko, and Marko Sokolich of HRL Laboratories, L.L.C., and Peter M. Asbeck of UCSD are appreciated. The author of this dissertation was the primary investigator and primary author of this publication. This work was sponsored by the Defense Advanced Research Projects Agency (DARPA) through AFRL Contract F33615-02-1286 (TFAST). We thank Dr. John Zolper and Dr. Stephen Pappert of DARPA, and Mr. Mark Pacer and Dr. Charles Cerny of AFRL for their support. We also thank the many contributors to the TFAST effort at HRL, and especially members of HRL's High Speed Circuits Laboratory for wafer fabrication.

4.8 References

[4-1] Z. Griffith, M. J. W. Rodwell, X.-M. Fang, D. Loubychev, Y. Wu, J. M. Fastenau, and A. W. K. Liu, "InGaAs/InP DHBTs With 120 nm Collector Having Simultaneously High f_T, f_{max} > 450 GHz", *IEEE Electron Device Letters*, vol. 26, no. 8, pp. 530-532, August 2005.

[4-2] Z. Griffith, M. Dahlstrom, M. Urteaga, M. J. W. Rodwell, X.-M. Fang, D. Lubychev, Y. Wu, J. M. Fastenau, and W. K. Liu, "InGaAs/InP mesa DHBTs with simultaneously high f_t and f_{max}, and low C_{cb} = I_c ratio", *IEEE Electron Device Letters*, vol. 25, no. 5, pp. 250–252, May 2004.

[4-3] T. Hussain, Y. Royter, D. Hitko, M. Montes, M. Madhav, I. Milosavljevic, R. Rajavel, S. Thomas, M. Antcliffe, A. Arthur, Y. Boegeman, M. Sokolich; J. Li, and P. Asbeck, "First demonstration of sub-0.25 μm-width emitter InP-DHBTs with >400 GHz f_t and >400 GHz f_{max}", IEDM Technical Digest, pp. 553-556, December 2004.

[4-4] M. J.W. Rodwell, M. Urteaga, T. Mathew, D. Scott, D. Mensa, Q. Lee, J. Guthrie, Y. Betser, S. C. Martin, R. P. Smith, S. Jaganathan, S. Krishnan, S. I. Long, R. Pullela, B. Agarwal, U. Bhattacharya, L. Samoska, and M. Dahlstrom, "Submicrometer scaling of HBTs", *IEEE Transactions on Electron Devices*, vol. 48, no. 11, pp. 2606–2624, November 2001.

[4-5] H. P. Tuinhout, "Improving BiCMOS technologies using BJT parametric mismatch characterization", *IEEE BCTM Proceedings*, pp. 163-170, September 2003.

[4-6] J. C. Li, P. M. Asbeck, T. Hussain, D. Hitko, C. Fields, and M. Sokolich, "Effects of device design on the thermal properties of InP-based HBTs", *ISCS Post-Conference Proceedings*, pp. 138-143, August 2003.

[4-7] J. C. Li, T. Hussain, D. A. Hitko, Y. Royter, C. H. Fields, I. Milosavljevic, S. Thomas III, R. D. Rajavel, P. M. Asbeck, and M. Sokolich, "Reduced Temperature *S*-Parameter Measurements of 400+ GHz Sub-Micron InP DHBTs", *Solid State Electronics*, In Review.

[4-8] D.A. Hitko, T. Hussain, J. F. Jensen, Y. Royter, S. L. Morton, D. S. Matthews, R. D. Rajavel, I. Milosavljevic, C. H. Fields, S. Thomas III, A. Kurdoghlian, Z. Lao, K. Elliott, and M. Sokolich, "A low power (45 mW/latch) static 150 GHz CML Divider", *IEEE CSICS Digest*, pp. 167-170, October 2004.

[4-9] D. E. Dawson, A. K. Gupta, and M. L. Salib, "CW Measurement of Thermal Resistance", *IEEE Transactions on Electron Devices*, vol. 39, no. 10, pp. 2235-2239, October 1992.

5. EXPERIMENTAL METHOD TO THERMALLY DE-EMBED PADS FROM R_{TH} MEASUREMENTS

5.0 Abstract

Both compound semiconductor and silicon-based BJTs or HBTs require the efficient removal of heat in order to achieve a maximum level of performance and reliability. In order to satisfy both of these criteria, the electro-thermal behavior of each device must be captured in a compact model. The model parameter that determines the junction temperature is R_{TH}, the thermal resistance. Experimental methods to determine R_{TH} often require a relatively small device with a large R_{TH} to be attached to a set of relatively large metal pads with a low R_{TH}. The pads act as a thermal shunt to the substrate and artificially lower the measured R_{TH}. In order to obtain a suitable R_{TH} value for a device located in an IC, the pads must be de-embedded from the measured data, much like pad de-embedding for an *S*-parameter measurement. Test structures with various width metal traces between the emitter pad and device's emitter have been fabricated in a 200 GHz InP DHBT process. A method of using the measured R_{TH} of these structures and a simple resistive network model to de-embed the pads is presented. It is shown that de-embedded values can be as much as 30% higher than the measured R_{TH}.

5.1 Introduction

The efficient removal of heat from compound semiconductor HBTs is imperative to achieve the performance and reliability needed for ICs. In the past, thermal management has typically been focused on large signal applications such as power amplifiers [5-1]. However, recent advances in SiGe and InP HBTs have pushed f_T and f_{MAX} past 400 GHz and simultaneously, the dissipated power density past 10 mW/μm^2 [5-2],[5-3],[5-4], making thermal management also important for digital applications. For either application, it is imperative to capture the electro-thermal behavior resulting from self-heating and temperature variations in a compact model. One of the critical parameters needed for such a compact model is the thermal resistance (R_{TH}). For compound semiconductors, whose thermal conductivities can be significantly lower than that of silicon, the R_{TH} parameter is particularly crucial.

Although the vast majority of the heat is generated in the collector, it is the average temperature at the base-emitter junction (T_j) which is indirectly observable through DC electrical measurements. Most methods to experimentally determine R_{TH} rely on the shift of the base-emitter voltage, V_{BE}, with respect to ambient temperature (T_{amb}) and dissipated power (P_{diss}) [5-5],[5-6]. All of the methods involve the electrical connection of large plates of metal to the emitter, base, and collector of an individual device. Given the high thermal conductivity of most metals compared to compound semiconductors and passivation dielectrics, the metals contacting the device could in principle, serve as a low thermal impedance path to thermal ground. In particular, the close proximity of the emitter metal to the base-emitter junction may serve as an effective heat sink. Previous

work on heat shunts [5-1],[5-7] have indicated that proper heat sinking of the emitter can be beneficial to power devices. In addition, 3D thermal simulation results quantifying the impact of pads on the effective R_{TH}, have been previously presented [5-8],[5-9]. Therefore, the measured value of R_{TH} would likely represent a lower limit to the actual R_{TH} of the individual device.

This paper presents an experimental method to quantify and de-embed the impact of emitter metallization on measured R_{TH} values. R_{TH} measurements are described here for a series of identical InP DHBTs, optimized for microwave power amplifiers and with different emitter metal contact schemes. A lumped element model is then presented and used to gain insight into the partitioning of the various thermal resistances of the system. Despite the selection of InP power devices for this work, the described method can be applied to any compound semiconductor HBT or silicon BJT with the proper test structures. To the authors' knowledge, this is the first study of the thermal de-embedding of pads from R_{TH} measurements.

5.2 HBTs and Test Structures

The necessary test structures are fabricated in a 200 GHz InP DHBT technology using Selectively Implanted Buried Sub-Collector (SIBS) optimized for power amplifier applications, previously presented in [5-10]. The increased collector current (I_C) and hence dissipated power at peak f_T and f_{MAX} offered by SIBS technology makes it a particularly good candidate for this method. The fabricated DHBTs are symmetric about the emitter length's centerline, and a half cross-section of a DHBT using SIBS technology is shown (Figure 5-1 bottom). Electrical and thermal contact to the DHBT

emitter is made through the first level of global interconnect, designated as *M1* (Figure 5-1 top). The gold plate labeled *M1 BAR* in Figure 5-1 completely covers the emitter metal and serves to connect the emitter to the generic pad structure shown in Figure 5-2. The emitter, base, and collector pads shown in Figure 5-2 utilize both levels of global interconnect and are designed for Ground-Signal-Ground (GSG) RF probes with a 100 μm probe pitch. The majority of the area under these pads is also in intimate contact with the semi-insulating InP substrate, and the emitter pad alone has over $3x10^4$ μm^2 of metal-substrate contact area. Therefore, it can be assumed that these pads have a large thermal mass and a low thermal resistance to the substrate.

Several DHBTs with a constant emitter area (A_E) of 1x10 μm^2, but with five *M1 BAR* widths of 1 μm, 3 μm, 5 μm, 8 μm, and 10 μm, were used for all the measurements presented in Sections 5.3 and 5.5. The *M1 BAR* width is taken to be in the *y*-axis dimension shown in Figure 5-1 and Figure 5-2. By decreasing the width of the *M1 BAR* from the full emitter length of 10 μm to the minimum allowed *M1* width of 1 μm, heat flow from the DHBT emitter through the *M1 BAR* to the emitter pads can be greatly reduced. This should result in an increased measured R_{TH} and an increase in magnitude of other self-heating effects. The 625 μm thick wafer on which the DHBTs have been fabricated has not been thinned or scribed.

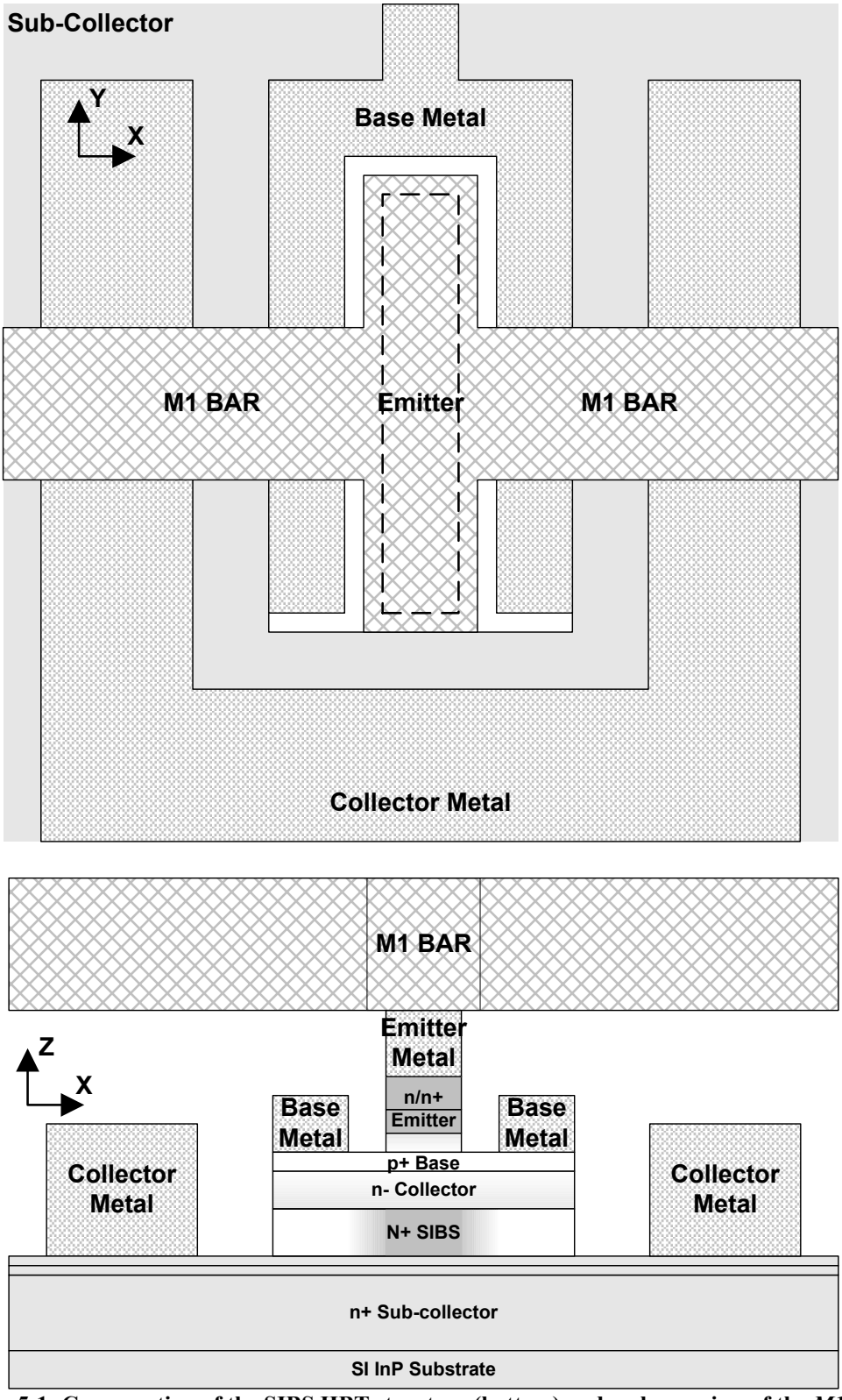

Figure 5-1: Cross-section of the SIBS HBT structure (bottom) and a planar view of the *M1 BAR* placement and contact to the emitter (top).

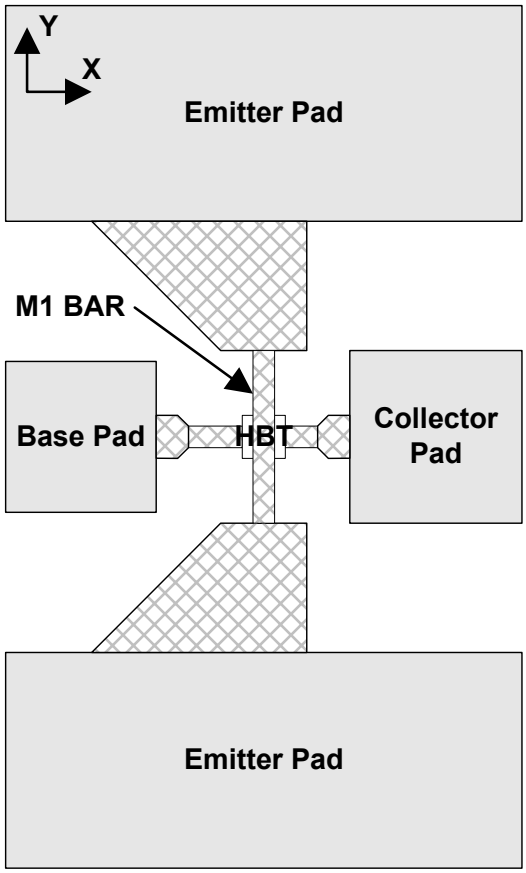

Figure 5-2: Diagram of the generic pad structure used for DHBT measurements.

5.3 R_{TH} Measurements

To perform electrical measurements at various T_{amb}, a Cascade Summit 12K wafer prober with a 200 mm nickel plated chuck surface and TP3010B thermal chuck system was used. Device oscillation was suppressed using GSG RF probes and high frequency bias networks. A HP4142B mainframe with a HP41421B medium power SMU driving the base and a HP41422A high current SMU driving the collector were used for all DC measurements. A test procedure similar to the V_{BE} method of Dawson et al [5-6] was used to measure the R_{TH} of the structures described in Section 5.2. For each structure, a forward Gummel curve where the base emitter voltage (V_{BE}) is swept from 0.2 V to 0.9 V

in 2 mV steps, and the collector-emitter voltage (V_{CE}) is swept from 0.8 V to 1.6 V in 200 mV steps. This large quantity of data exceeds that required for the R_{TH} measurement alone and allows a more general investigation of self-heating and temperature on these DHBTs. These measurements are then repeated at a T_{amb} of 25 ˚C, 35 ˚C, 45 ˚C, 55 ˚C, and 65 ˚C with a minimum of 15 minutes soak time at each temperature to ensure that the chuck and wafer reach thermal equilibrium.

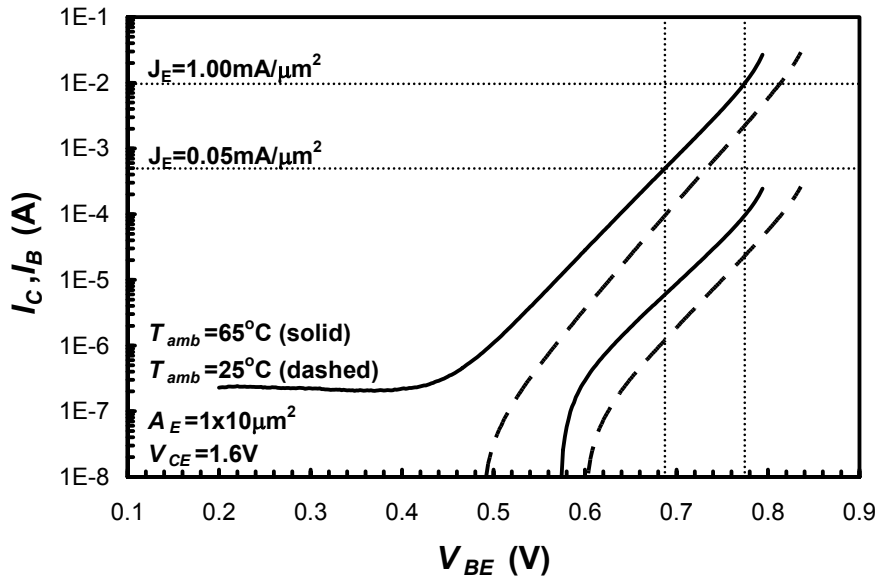

Figure 5-3: Forward Gummel curves of an A_E = 1x10 μm^2 DHBT with a 10 μm wide *M1 BAR* at T_{amb} = 25 ˚C (dashed) and 65 ˚C (solid).

In order to determine R_{TH}, an emitter current density (J_E) must be selected such that the V_{BE} shift is indicative of the intrinsic base-emitter junction and linear versus P_{diss} and T_{amb}. The J_E must be high enough to avoid the influences of leakage or recombination, but J_E must be low enough to avoid the influence of any series resistance or heterojunctions in the emitter cap. Figure 5-3 shows the forward Gummel of an A_E = 1x10 μm^2 DHBT with a 10 μm wide *M1 BAR* at T_{amb} = 25 ˚C and 65 ˚C. Since a wide range of V_{CE} values are required to provide sufficient variation in P_{diss}, the higher V_{CE}

values does result in some base-collector junction leakage current driving the base current, I_B, negative at low V_{BE} where V_{CB} is at its maximum. The effects of leakage current can be observed even at V_{BE} values as high as 0.6 V. At J_E = 0.05 mA/μm^2, the V_{BE} shift is influenced by a non-ideal I_B component attributed to recombination. While at J_E greater than 1.00 mA/μm^2, a rapid increase in both I_C and I_B is observed which could be the result of both conventional self-heating and an effective decrease in the emitter resistance due to a heterojunction in the emitter cap. A complete discussion of both the low and high current effects is beyond the scope of this work. Figure 5-4 shows the measured R_{TH} for an A_E = 1x10 μm^2 DHBT with a 10 μm wide *M1 BAR* at various T_{amb} and biased at various J_E. For the purposes of R_{TH} determination and subsequent discussions, both low V_{BE} and high I_C regions should be avoided, and the measured R_{TH} values at a J_E = 0.5 mA/μm^2 has been used for this work. Figure 5-5 shows the measured R_{TH} values for the five *M1 BAR* widths at the five T_{amb} for DHBTs with an A_E = 1x10 μm^2 biased at a J_E = 0.5 mA/μm^2. Figure 5-6 shows the same R_{TH} data as Figure 5-5 plotted against the inverse of the *M1 BAR* width. The significance of the *M1 BAR* width and hence the heat sinking capabilities of the emitter pads is clearly shown in both Figure 5-5 and Figure 5-6.

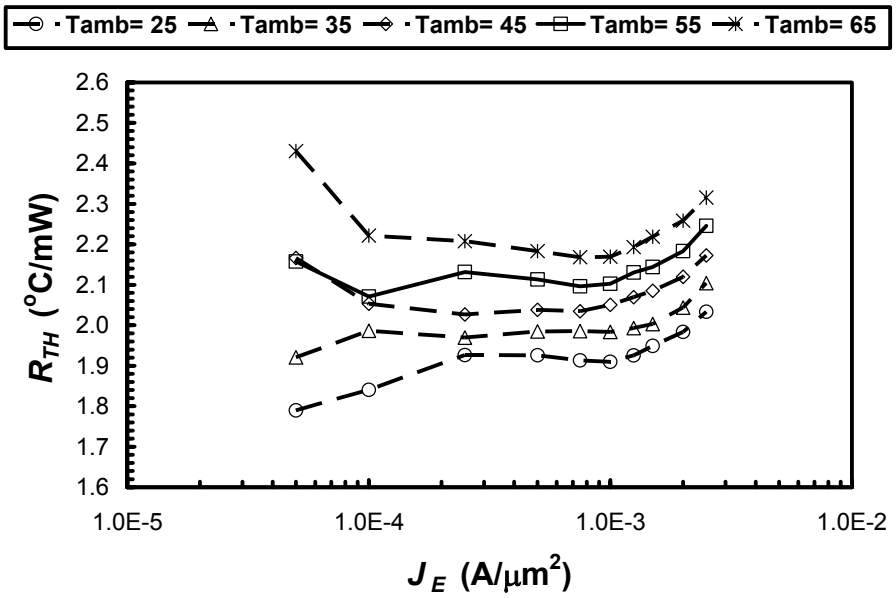

Figure 5-4: Measured R_{TH} values of an A_E = 1x10 μm² DHBT with a 10 μm wide *M1 BAR* at various T_{amb} and biased at various J_E.

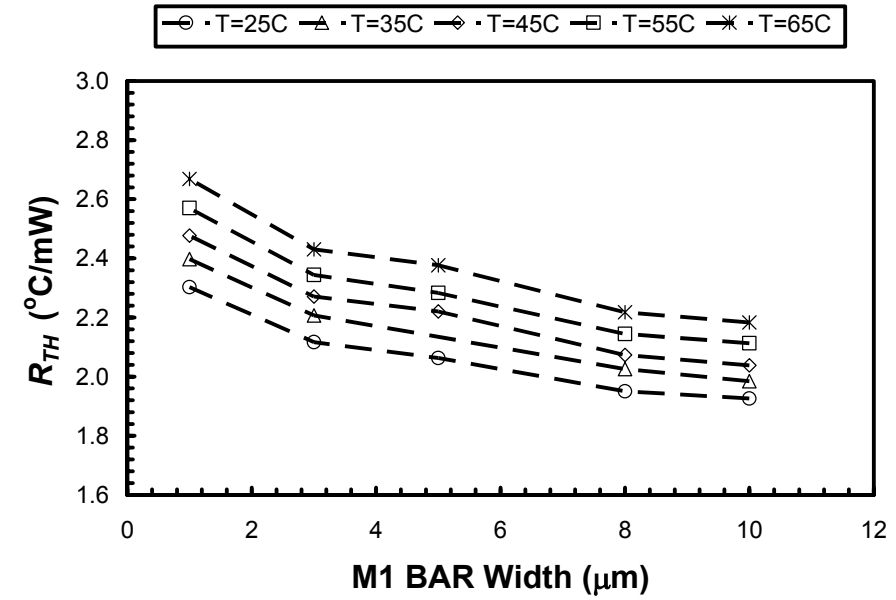

Figure 5-5: Measured R_{TH} values at various *M1 BAR* widths and T_{amb} for DHBTs with an A_E = 1x10 μm² and biased at J_E = 0.5 mA/μm².

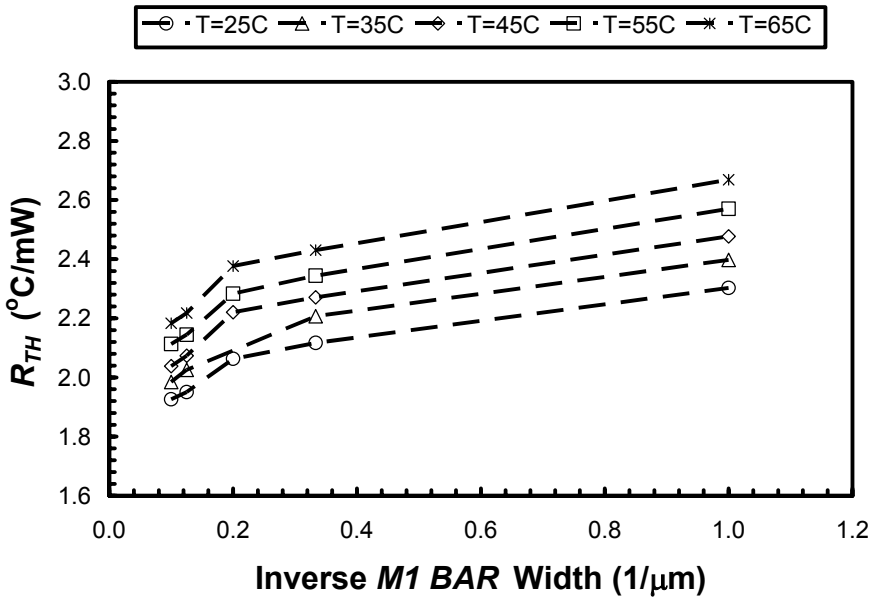

Figure 5-6: Measured R_{TH} values at various inverse *M1 BAR* widths and T_{amb} for DHBTs with an A_E = 1x10 μm^2 and biased at J_E = 0.5 mA/μm^2.

5.4 Lumped Element Model

In order understand the components that comprise the total measured R_{TH}, the lumped element model shown in Figure 5-7 is used. The DC current source with magnitude P_{diss} represents the total power dissipated by the DHBT and is computed from the terminal current-voltage product of the base and collector. The node *B* represents the base-emitter junction, and the voltage computed at this node represents T_j. The resistor $R_{TH,SX}$ is the component of the total R_{TH} that represents heat dissipation through the substrate. In the absence of any heat sinking through the emitter, $R_{TH,SX}$ represents the only means of heat dissipation for the DHBT and the maximum obtainable R_{TH}. The resistor $R_{TH,E}$ represents the vertical R_{TH} component through the emitter, emitter cap, and emitter metal of the DHBT. $R_{TH,E}$ is likely to be large compared to the remaining components, because of the small cross-sectional area equal to A_E and the high thermal

resistivities of the ternaries, $In_{0.53}Ga_{0.47}As$ and $In_{0.52}Al_{0.48}As$. Accurate estimations of $R_{TH,E}$ are difficult due to the lack of published data concerning the thermal properties of $In_{1-x}Al_xAs$ alloys, which comprise a large portion of the emitter and emitter cap of these DHBTs. Finally, $R_{TH,BAR}$ and $R_{TH,PAD}$ represents the R_{TH} components due to the *M1 BAR* and emitter pads, respectively. It is assumed that the passivation and inter-level dielectrics that surround the DHBT have such a low thermal conductivity that they negligibly reduce the measured R_{TH}. The ground terminal shown in Figure 5-7 represents the isothermal boundary condition maintained by the thermal chuck top surface.

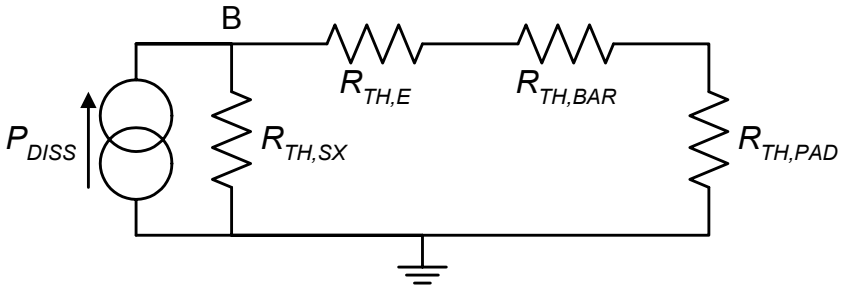

Figure 5-7: Lumped element R_{TH} model for the DHBT and pad system.

It may be noted that sufficient experimental data does not exist to uniquely determine all four R_{TH} components. Since various *M1 BAR* widths exist, the dependence of $R_{TH,BAR}$ on *M1 BAR* width ($dR_{TH,BAR}/dW$) can be determined uniquely. Under the condition when $R_{TH,BAR}$ becomes infinite i.e. the *M1 BAR* width goes to zero, $R_{TH,SX}$ can be determined uniquely and represents the fully de-embedded R_{TH} for the DHBT. At the other extreme where $R_{TH,BAR}$ becomes zero i.e. the *M1 BAR* width goes to infinity, the parallel combination of $R_{TH,SX}$ with the series combination $R_{TH,E}$ and $R_{TH,PAD}$ can be determined. However, only the sum of $R_{TH,E}$ and $R_{TH,PAD}$ can be determined uniquely once $R_{TH,SX}$ is known. Given the high thermal conductivity of gold, the relatively large size of the emitter pads, and the large contact area of the pads with the substrate, it is

reasonable to assume that $R_{TH,PAD}$ is small compared to $R_{TH,E}$. If the DHBT is to be used in sparsely packed MMIC with ample heat sinking, any one of the measured R_{TH} values, which includes heat sinking from the pads, may be a reasonable value to use in a compact model. However, $R_{TH,SX}$ is likely to be the best compact model value to use if the DHBT is to be placed in a densely packed digital IC. The inclusion of the layout dependence of R_{TH} in compact modeling will become increasingly practical as more compact models offer a user accessible thermal node.

Although five *M1 BAR* widths were measured, there are still an insufficient quantity of *M1 BAR* widths near zero and infinity in order to directly extrapolate $R_{TH,SX}$ from Figure 5-5 and $R_{TH,E}$+$R_{TH,PAD}$ from Figure 5-6. Using the measured R_{TH} values presented in Figure 5-5 and a least squares fit to the lumped R_{TH} model, parameter values of $R_{TH,SX}$, $R_{TH,BAR}$, and $R_{TH,E}$+$R_{TH,PAD}$ can be calculated for each T_{amb}. Table 5-1 summarizes the parameter values obtained, and the fitted model is plotted against the measured data in Figure 5-8. The calculated values of $R_{TH,SX}$ are well behaved and monotonically increase with increasing T_{amb}, but there is less well behaved variation in $dR_{TH,BAR}/dW$ and $R_{TH,E}$+$R_{TH,PAD}$. The fully de-embedded value, $R_{TH,SX}$, represents as much as a 30% increase over the measured R_{TH} values, corresponding to a 30% increase in T_j for a given P_{diss}. Using a thermal conductivity value of 250 W/m·K for a 1.0 μm thick gold thin film [5-11], a two sided *M1 BAR* of approximately 17 μm in length would have a theoretical $dR_{TH,BAR}/dW$ value of 34.0 mW/°C·μm. When compared to the experimental data, the fitted model parameters which range from 32.6 mW/°C·μm to 42.8 mW/°C·μm appear to be reasonable. The variation in $dR_{TH,BAR}/dW$ is likely to decrease if

a large number of *M1 BAR* widths are available for test. Concerning the variation of the $R_{TH,E}$+$R_{TH,PAD}$ values, the existing method does not allow for the separation of these two terms so the source of the variation will require further study.

Table 5-1: Summary of measured R_{TH} values and extracted parameter values for the lumped R_{TH} model.

T_{amb}	$R_{TH,SX}$ (˚C/mW)	$dR_{TH,BAR}/dW$ (˚C/mW·μm)	$R_{TH,E}$+$R_{TH,PAD}$ (˚C/mW)	Measured R_{TH} (˚C/mW)
25˚C	2.45	32.57	5.79	1.93-2.30
35˚C	2.53	38.87	5.38	1.98-2.40
45˚C	2.61	42.80	5.08	2.04-2.48
55˚C	2.74	34.46	5.79	2.11-2.57
65˚C	2.83	39.11	5.65	2.18-2.67

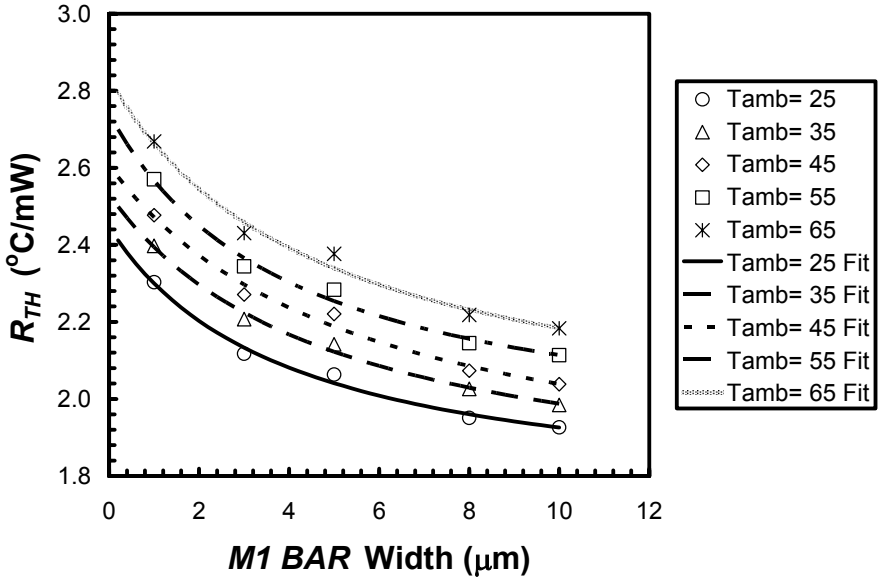

Figure 5-8: Measured R_{TH} plotted against a fitted lumped element model for various T_{amb}.

5.5 Other Manifestations of Self-Heating

The variation of R_{TH} as the *M1 BAR* width is varied has a direct impact on several HBT characteristics. From Figure 5-5, there is a 16% reduction in measured R_{TH} when the *M1 BAR* width is increased from 1 μm to 10 μm at a T_{amb} = 25 ˚C. For a V_{CE} = 2.0 V and an I_C = 25 mA at peak f_T, the 50 mW of total dissipated power results in an

approximate T_j difference of 19 ˚C between *M1 BAR* widths of 1 μm and 10 μm. Figure 5-9 shows the high I_C regime of the forward Gummels at a constant V_{CE} = 1.6 V and the increased self-heating due to narrower *M1 BAR* widths is significant. Similarly, Figure 5-10 shows the common emitter I-V curves for a forced V_{BE} = 0.83 V. Both figures show that with decreasing *M1 BAR* width, there is a corresponding increase in I_C despite increasing emitter pad resistance.

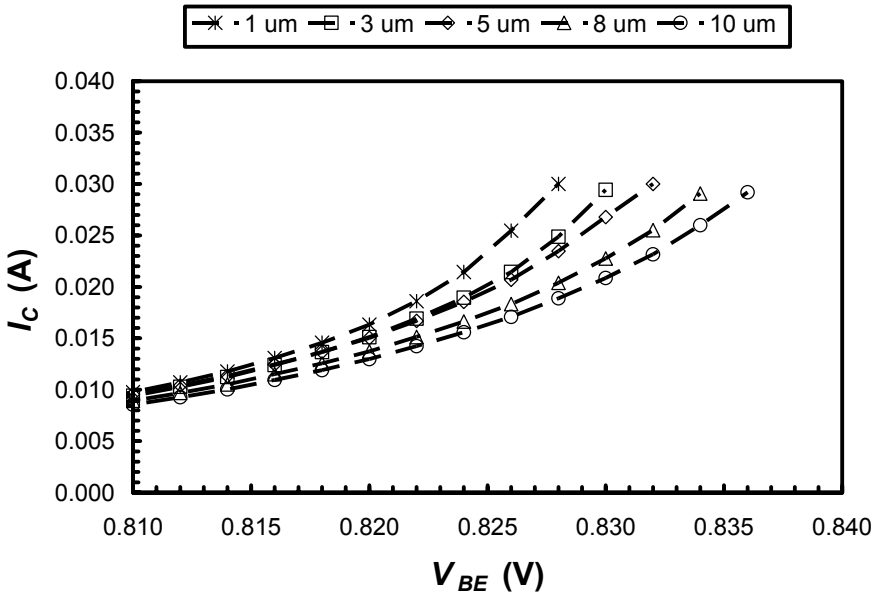

Figure 5-9: High current behavior of forward Gummels at a constant V_{CE} = 1.6 V showing the increased self-heating for narrower *M1 BAR* widths.

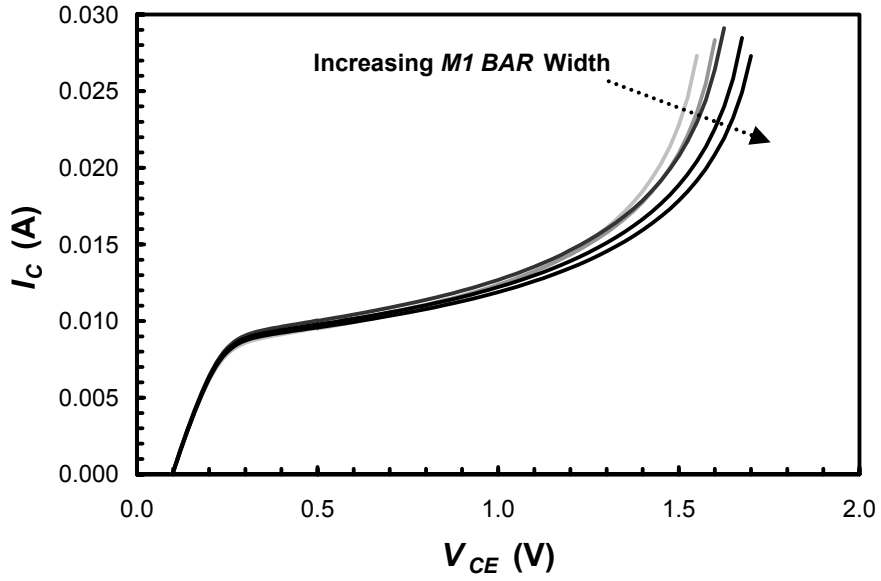

Figure 5-10: Common emitter I-V curves at a forced V_{BE} = 0.83 V for *M1 BAR* widths of 1 μm to 10 μm.

5.6 Summary

Test structures with 1 μm, 3 μm, 5 μm, 8 μm, and 10 μm wide *M1 BAR*, gold traces that connect the DHBT emitter to the emitter pad, were fabricated in a 200 GHz InP DHBT process using SIBS. The R_{TH} of each of these structures was measured using the Dawson V_{BE} method at a T_{amb} from 25 ˚C to 65 ˚C. It was found that there was a significant increase, 16% at a T_{amb} = 25 ˚C, in measured R_{TH} with decreasing *M1 BAR* width. The change in measured R_{TH} is attributed to the change in the heat flow through the *M1 BAR* to the emitter pads, which act as a heat sink or shunt to the substrate. A simple model consisting of a resistor network is used to explain the various components of the measured R_{TH}. Using the measured R_{TH} values from these test structures, values for the various model components have been determined, and the fully de-embedded R_{TH} value, $R_{TH,SX}$, was obtained.

5.7 Acknowledgements

This chapter, in full, has been submitted for publication to the IEEE Transactions on Electron Devices. The contributions from the co-authors Donald A. Hitko and Marko Sokolich of HRL Laboratories, L.L.C., and Peter M. Asbeck of UCSD are appreciated. The author of this dissertation was the primary investigator and primary author of this publication.

5.8 References

[5-1] C. Bozoda, C. Cerny, G. de Salvo, R. Dettmer, J. Ebel, J. Gillespie, C. Havasy, T. Jenkins, C. Ito, K. Nakano, C. Pettiford, T. Quach, J. Sewell, G.D. Via, and R. Anholt, "Thermal Management of Microwave Power Heterojuncion Bipolar Transistors", *Solid State Electronics*, vol. 41, no. 10, pp. 1667-1673, 1997.

[5-2] J-S. Rieh, B. Jagannathan, D.R. Greenberg, M. Meghelli, A. Rylyakov, F. Guarin, Z. Yang, D.C. Ahlgren, G. Freeman, P. Cotrrell, and D. Harame, "SiGe Heterojunction Bipolar Transistors and Circuits Towards Terahertz Communication Applications", *IEEE Transactions On MTT*, vol. 52, no.10, pp. 2390-2408, Oct. 2004.

[5-3] T. Hussain, Y. Royter, M. Montes, D. Hitko, M. Madhav, I. Milosavljevic, R. Rajavel, S. Thomas, M. Antcliffe, A. Arthur, Y. Boegeman, J. Li, and M. Sokolich, "First Demonstration of Sub-0.25 μm-width Emitter InP-DHBTs with >400 GHz f_T and >400 GHz f_{MAX}," in *IEEE IEDM Technical Digest*, 2004.

[5-4] Z. Griffith, M.J.W. Rodwell, Xiao-Ming Fang, D. Loubychev, Ying Wu; J.M. Fastenau, and A.W.K. Liu, "InGaAs/InP DHBTs with 120-nm collector having simultaneously high f_τ, $f_{max} \geq 450$ GHz", *IEEE Electron Device Letters*, vol. 26, no. 8, pp. 530-532, Aug. 2005.

[5-5] W. Liu, "Handbook of III-V Heterojunction Bipolar Transistors", pp. 362-368, J. Wiley and Sons, New York, 1998.

[5-6] D.E. Dawson, A.K. Gupta, and M.L. Salib, "CW Measurements of HBT Thermal Resistance", *IEEE Transactions On Electron Devices*, vol. 39, no. 10, pp. 2235-2239, Oct. 1992.

[5-7] L.L. Liou, B. Bayraktaroglu, C.I. Huang, and J. Barrette, "The Effect of Thermal Shunt on the Current Instability of Multiple-Emitter-Finger Heterojunction Bipolar Transistors" in *IEEE BCTM Proceedings*, pp. 253-256, 1993.

[5-8] J.C. Li, P.M. Asbeck, T. Hussain, D. A. Hitko, C. H. Fields, and M. Sokolich, "Effects of Device Design on the Thermal Properties of InP HBTs" in *IEEE ISCS Proceedings*, 2003.

[5-9] J.C. Li, T. Hussain, D.A. Hitko, P.M. Asbeck, and M. Sokolich, "Characterization and Modeling of Thermal Effects in Sub-Micron InP DHBTs" in *IEEE CSICS Proceedings*, 2005.

[5-10] J.C. Li, M.Y. Chen, Z. Lao, R.D. Rajavel, S. Thomas III, B. Shi, S.S. Bui, K.V. Guinn, J.R. Duvall, D.A. Hitko, D.H. Chow, and M. Sokolich, "200 GHz InP DHBT Technology using Selectively Implanted Buried Sub-Collector (SIBS) for Broadband Amplifers", *IEEE Electron Device Letters*, In Review.

[5-11] G. Langer, J. Hartmann, and M. Reichling, "Thermal conductivity of thin metallic films measured by photothermal profile analysis", *Rev. Sci. Instrum*., vol. 68, no.3, pp. 1510-1513, March 1997.

6. INVESTIGATION OF BALLISTIC CARRIER TRANSPORT IN 400 GHZ INP DHBTS

6.0 Abstract

The physical phenomena of velocity overshoot have been observed in InP HBTs with f_T as low as 100 GHz. With the aggressive scaling currently being untaken to develop 400 GHz InP HBTs, velocity overshoot and ballistic transport are expected to play a key role in device engineering. This work investigates the numerical simulation of these two phenomena using the commercial device simulator, DESSIS, by Synopsys™. Negative differential mobility, characteristic of many compound semiconductors, is modeled using the built-in transferred-electron high-field mobility model, and reasonable agreement to published data is achieved. Velocity overshoot is simulated using the hydro-dynamic transport equations. The energy relaxation time and the Peltier coefficient are energy dependent and can be calibrated to existing Monte Carlo simulation results. However, liberal use of the Boltzmann form of the Einstein relation to interchange diffusivity and mobility proves to be the greatest limitation to the existing implementation. Under ballistic conditions, the diffusive terms are significantly over-estimated, resulting in a DC current gain under-estimated by 65%. The anisotropic mobility models are found to provide a limited correction to this deficiency, and the resulting simulations agree reasonably with measured data.

6.1 Introduction

The long energy and momentum relaxation times associated with many compound semiconductors such as GaAs, InGaAs alloys, and InP allow for the physical phenomena of velocity overshoot to occur. Velocity overshoot is the condition when a free-carrier, most commonly electrons, exceeds the steady-state carrier saturation velocity, $v_{sat}(E)$. Due to differences in phonon scattering processes, compound semiconductors do not exhibit velocity overshoot until electrons transfer into the higher m_e* satellite valleys [6-1]. This requires an applied electric field that is above a minimum threshold value, E_{TH}, which corresponds to the electric field required to achieve peak $v_{sat}(E)$ and the onset of negative differential mobility. The initial overshoot of $v_{sat}(E)$ is governed by the momentum relaxation time, τ_m, but the return to $v_{sat}(E)$ is controlled by the energy relaxation time, τ_e. For InP, it has been speculated that the average electron drift velocity, $v_e(E)$, can approach 1.13×10^8 cm/s if the electric field undergoes a sufficiently large transient in either space or time [6-2]. Even a moderate 25 kV/cm electric field can produce $v_e(E)$ values exceeding 4×10^7 cm/s over a 250 nm distance [6-1]. If the traversed distances are sufficiently short, a significant fraction of the overshot electrons may not relax to $v_{sat}(E)$, leading to quasi-ballistic transport [6-3]. Compared to the peak $v_{sat}(E)$ of $\sim 2.5 \times 10^7$ cm/s, the $v_e(E)$ under velocity overshoot or quasi-ballistic conditions can be extra-ordinarily high and the resulting transit time is significantly reduced. For GaAs and InP HBTs, the result is a reduced collector transit time, τ_C, and even a reduced base transit time, τ_B, if the device is properly engineered [6-4]. The reduced τ_c and τ_b can be

observed through the small signal figures of merit, f_T and f_{MAX}, and the DC current gain, β.

The development of InP HBTs whose f_T and f_{MAX} both exceed 400 GHz will not only rely on device scaling [6-5], but also an understanding on how to maximize velocity overshoot and even ballistic transport [6-4]. These phenomena have already been observed in InP/InGaAs single-HBTs with a 400 nm collector and a 50 nm thick base yielding a f_T and f_{MAX} of 100 GHz and 83 GHz, respectively [6-6]. If this generation of devices is already impacted, velocity overshoot will be a critical aspect of device design at 400 GHz. This work is not intended as a rigorous discussion on the theoretical basis of these transport mechanisms, but more as a guide to simulate the advanced transport properties of InP HBTs. The calibration of a high field mobility model which includes negative differential mobility and the transport equations which include velocity overshoot is presented. All simulations are performed in an industry-standard device simulator, Synopsys DESSIS, without modification. Although some aspects of the implementation are expected to be DESSIS specific, most concepts will be portable to any other device simulator with similar capabilities.

6.2 Simulation Environment

Several commercial, off-the-shelf device simulators are available to the device engineer to aid in the design of high-performance InP HBTs. Many of these simulators were originally designed for use with silicon and its derivative technologies, but do have extensions to support compound semiconductor technologies. Direct support for ternaries and quaternaries, hetero-interfaces, negative differential mobility, and velocity

overshot are features that are particularly useful when dealing with compound semiconductors. One such simulator with these features is the product called DESSIS, now supported by Synopsys. Support for ternaries and quaternaries are provided through a series of bowing parameters based on Vegard's Law. Numerical provisions have been added to allow mesh generation for abrupt hetero-interfaces. An additional non-local mesh can be specified for the computation of barrier tunneling and thermionic emission. The model parameters for barrier tunneling and thermionic emission are straight forward and can be determined from various published works [6-7],[6-8],[6-9],[6-10]. The remaining two features of compound semiconductors, negative differential mobility and velocity overshoot, are the focus of this investigation. Negative differential mobility will be discussed here, but the calibration of the relevant materials i.e. InP and InGaAs are discussed in the following sections. The DESSIS implementation of the Hydrodynamic transport equations used for the simulation of velocity overshoot is discussed in Appendix D.

In the steady state, most compound semiconductors e.g. GaAs and InP exhibit negative differential mobility when electrons transfer from the relatively low m_e* Γ-valley to a relatively high m_e* satellite valley. The resulting non-monotonic behavior of the v_{sat} versus electric field characteristic, shown in Figure 6-1, can pose a numerical challenge for device simulators. Proper selection of model parameters to ensure consistency between the steady-state mobility and velocity overshoot models will produce more realistic results and improved convergence. In DESSIS, the Transferred Electron high field mobility model is defined as

$$\mu = \frac{\mu_{low} + \left(\frac{v_{sat}}{F}\right)\left(\frac{F}{E_0}\right)^4}{1 + \left(\frac{F}{E_0}\right)^4} \tag{6-1}$$

where μ_{low} is the low field mobility; F is the driving force; v_{sat} is the steady-state saturation velocity; and E_0 is a user defined parameter.

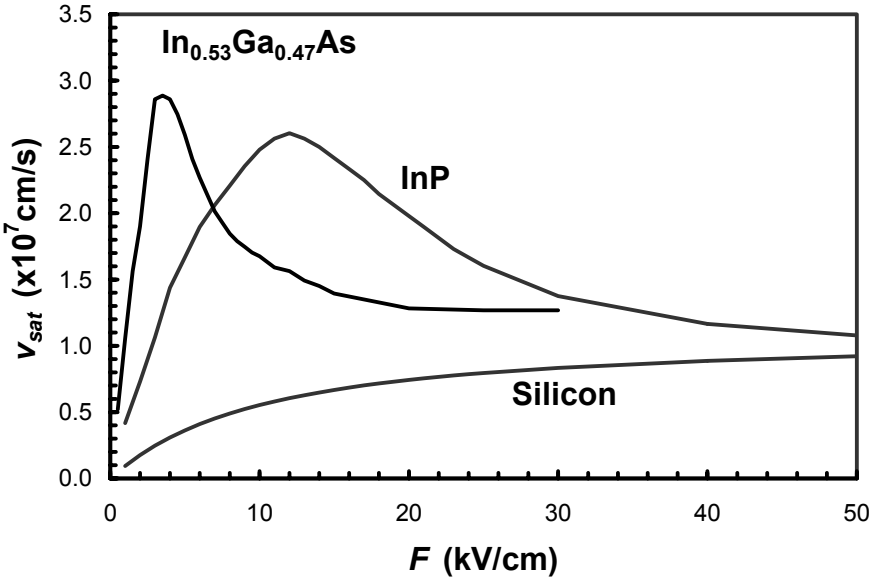

Figure 6-1: The dependencies of steady-state electron saturation velocity (v_{sat}) on the electric field (F) for InP, $In_{0.53}Ga_{0.47}As$, and Si. InP and $In_{0.53}Ga_{0.47}As$ both exhibit negative differential mobility resulting from electron transfer from the Γ-valley into a lower m_e* satellite valley.

The Arora mobility model is used to represent the doping dependence under low electric field, and the model parameters can be determined from various published works [6-7],[6-8],[6-9],[6-11]. The definition of F in Equation (6-1) varies based on the set of transport equations selected by the user. For conventional drift-diffusion transport, F is related to the electric field or the quasi-fermi level gradient. For Hydrodynamic transport, the carrier specific F is based on the carrier temperature,

$$F_C = \sqrt{\frac{w_C - w_0}{\tau_{e,c} q \mu}} \tag{6-2}$$

where w_c and w_0 are the average carrier thermal energy and equilibrium thermal energy, respectively. The determination of the energy relaxation time, $\tau_{e,c}$, is discussed in Section 6.3.1. The quantity, v_{sat}, in Equation (6-1) is determined by the *Type 2* velocity saturation model,

$$v_{sat} = A_{vsat} - B_{vsat}\left(\frac{T}{T_0}\right) \qquad \text{for } v_{sat} > v_{sat,min} \tag{6-3}$$

Limited temperature dependent data is available [6-8] for InP and $In_{0.53}Ga_{0.47}As$ and the calibrated values are summarized in Table 6-1. The remaining parameter, E_0, approximates the location of v_{max}, the maximum $v_{sat}(F)$. Figure 6-2 shows a comparison between the experimental data taken from [6-8] and the DESSIS transferred electron model. A least squares fit is used to ensure the resulting model parameters yield the least total error over the complete range in F shown. Optimization near v_{max} alone is not sufficient due to the large range in F experienced throughout the HBT. DESSIS does allow the user specify a more generic form of the high field mobility, but the limited quantity of data and other uncertainties discussed in Section 6.3 do not warrant a more complex model. The transferred electron model is adequate to capture of the phenomena of negative differential mobility. An additional parameter, K_{smooth}, is used to split the curve resulting from Equation (6-1) and widen the v_{max} region. F_{vmax} is defined as the point in F where v_{sat} is at its maximum, and K_{smooth} is defined as a unit-less factor where the following region in F space, $F_{vmax} < F < K_{smooth} F_{vmax}$, is held at v_{max}. Additional computation is performed internal to DESSIS to ensure that derivatives are continuous

and convergence is not severely impacted by the use of K_{smooth}. The widening of the peak v_{sat} region is evident from Figure 6-2, and the dashed lines show the two instances of Equation (6-1) with $K_{smooth} = 1$ that are combined to form the final curve.

Table 6-1: Summary of parameters used in the Transferred Electron and *Type 2* v_{sat} models.

Parameter	Units	InP	$In_{0.53}Ga_{0.47}As$
E_0	kV/cm	8.8	3.5
K_{smooth}	---	2.13	1.33
Avsat	x10^7 cm/s	1.250	1.415
Bvsat	x10^7 cm/s	0.250	0.165
Vsat,min	x10^7 cm/s	0.500	0.500

Table 6-2 lists the models supported by DESSIS and calibrated in this work for the two-dimensional electro-thermal simulations used in this investigation. Since velocity overshoot can affect β, C_{BC}, and f_T, the generation/recombination, dielectric constant, and mobility models must also be properly calibrated. The implementation of these models and the experimental data required for calibration has been previously published and will not be discussed here.

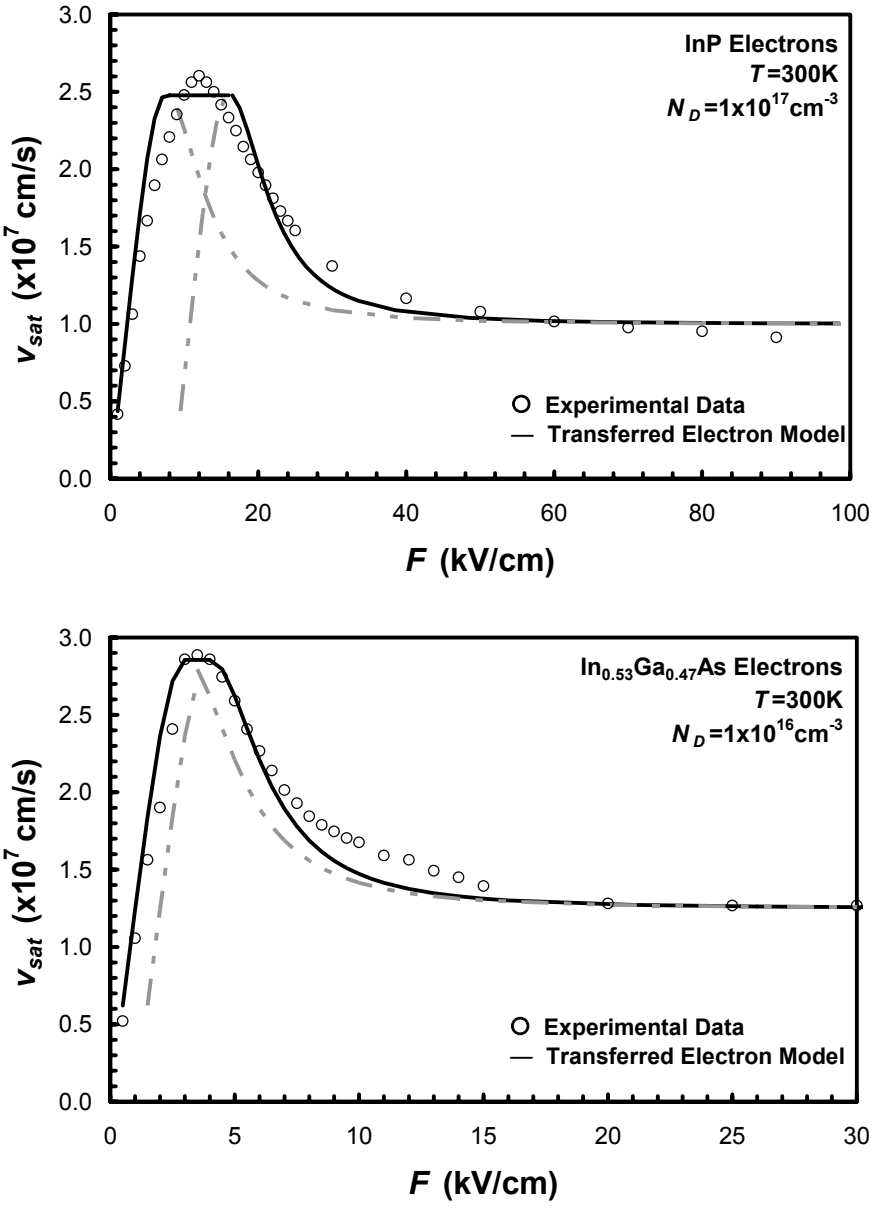

Figure 6-2: Comparison of experimental data taken from [6-8] and the DESSIS transferred electron model.

Table 6-2: Summary of calibrated models for InP and $In_{0.53}Ga_{0.47}As$.

Category	Model	InP	$In_{1-x}Ga_xAs$
General	• Dielectric Constant	Y	Y^{11}
	• Refractive Index	D	D
Thermal	• Heat Capacity	Y^{1}	$Y^{1,11}$
	• Conductivity	Y^{1}	$Y^{1,11}$
Hydrodynamic (Electron, Hole)	• Energy relaxation time	Y^{2},D^{2}	$Y^{2,12}$,$D^{2,12}$
	• Energy flux	Y^{3},Y^{3}	$Y^{3,12}$,$Y^{3,12}$
	• Thermal diffusion	Y^{3},Y^{3}	$Y^{3,12}$,$Y^{3,12}$
	• Heat flux	Y^{2},D^{2}	$Y^{2,12}$,$D^{2,12}$
	• Avalanche	D,D	D,D
Impurities (Donor, Acceptor)	• Binding energy	Y,Y	Y^{12},Y^{12}
	• Mott transition	Y,Y	Y^{12},Y^{12}
Band Structure (Electron, Hole)	• Bandgap	Y,Y	Y^{11},Y^{11}
	• Electron affinity	Y,Y	Y^{11},Y^{11}
	• Temperature dependence	Y,Y	Y^{11},Y^{11}
	• BGN	$Y^{4,5}$,$Y^{4,5}$	$Y^{4,5,12}$,$Y^{4,5,12}$
	• Doping dependence	Y,Y	Y^{12},Y^{12}
	• DOS	Y^{6},Y^{6}	Y^{6},Y^{6}
Interfaces (Electron, Hole)	• Schroedinger	Y,Y	Y^{11},Y^{11}
	• Thermionic Emission	D,D	D,D
	• Barrier Tunneling	Y,Y	Y,Y
Mobility (Electron, Hole)	• Constant	Y,Y	Y^{11},Y^{11}
	• Low Field	$Y^{1,7}$,$Y^{1,7}$	$Y^{1,7,11}$,$Y^{1,7,11}$
	• High Field	$Y^{1,8}$,$Y^{1,8}$	$Y^{1,8,12}$,$Y^{1,8,12}$
	• Anisotropy	Y^{9},Y^{9}	Y^{9},Y^{9}
Generation/ Recombination (Electron, Hole)	• Auger	Y,Y	Y^{12},Y^{12}
	• Poole-Frenkel	D,D	D,D
	• Impact Ionization	Y^{10},Y^{10}	$Y^{10,12}$,$Y^{10,12}$
	• Radiative	Y,Y	Y^{12},Y^{12}
	• SRH	Y,Y	$Y^{12,13}$,$Y^{12,13}$

Y Published values or DESSIS model fit to published values used
N No published data exists and no ISE default exists
D DESSIS default values used

Notes:

1 Temperature dependence supported and parameters calibrated
2 Energy dependence supported and parameters calibrated
3 DESSIS does not support an energy dependence of particular parameter
4 Limited experimental data and parameters based on theoretical values
5 Table based model
6 Isotropic energy band model (Formula = 2 in DESSIS)
7 Arora model
8 Inter-valley scattering model (Transferred electron in DESSIS)
9 Anisotropic model and parameters is set identical to isotropic axis model and parameters
10 Van Over-Straeten/de Man model
11 Composition dependent model
12 Customized for x = 0.47
13 Doping dependence supported and calibrated

6.3 HTE Parameter Extraction

Appendix D describes the DESSIS implementation of the Hydrodynamic transport equations and the model variables discussed here. The four user specified pre-factors (r, f^{td}, f^{hf}, τ_e) for each carrier allows the activation and de-activation of certain physical effects. The r and f^{td} parameters are constants, but the f^{hf} and τ_e parameters are energy dependent quantities. To maintain generality, the ratio of two polynomials of the form below,

$$G(w,s) = f\frac{((\sum a_i w^{p_i}) + d_n s)^{g_n}}{((\sum a_j w^{p_j}) + d_d s)^{g_d}} \tag{6-4}$$

where w is the carrier energy and s is an additional fitting variable, is used to define these two energy dependent quantities. For silicon, the use of constant values for all four pre-factors is sufficient, but for compound semiconductors, this energy dependence is critical to the proper modeling of carrier transport. Further flexibility could be introduced into the simulator by making the pre-factors doping or carrier concentration dependent, but the additional complexity would make the parameter definition cumbersome and numerical simulation prohibitive. Little theoretical or experimental data exists for compound semiconductors concerning these four pre-factors, so any additional complexity would likely go unused. The HTE pre-factors for the two materials of interest, InP and $In_{0.53}Ga_{0.47}As$, will be determined from two sources of Monte Carlo simulations [6-12],[6-13]. This section will discuss the determination of the four HTE pre-factors from published Monte Carlo, *MC*, data and its implementation into the DESSIS device simulator.

6.3.1 Energy Relaxation Times (τ_{en}, τ_{ep})

Of the four pairs of HTE parameters, the energy relaxation times are the most straight-forward and can be determined directly from published works. From [6-1], τ_{en} is described as the time constant governing a carrier's relaxation from the velocity overshot condition to steady state condition. The energy dependent τ_e is defined in the following rational form,

$$\tau(w) = \tau_W^0 \frac{((\sum a_i w^{p_i}))^{g_n}}{((\sum a_j w^{p_j}))^{g_d}} \tag{6-5}$$

where w is the unit carrier kinetic energy, $3kT_{n,p}/2q$. A least squares fit to Equation (6-5), where i and j are a maximum of 4 and $g_n = g_d = 1.0$, produces a reasonable fit to the tabular data presented in [6-12] for $In_{0.53}Ga_{0.47}As$ and [6-13] for InP. Higher order terms to Equation (24) can be used, but the added complexity provides little marginal reduction in the fitting error. Figure 6-3 shows the resulting $\tau_e(w)$ from the DESSIS fitting function compared to the *MC* simulation data, and Table 6-3 lists the calculated parameters.

Table 6-3: Summary of DESSIS fitting function parameters for the energy dependent relaxation time for electrons, $\tau_{en}(w)$, of InP and $In_{0.53}Ga_{0.47}As$.

Parameter	InP	$In_{0.53}Ga_{0.47}As$
τ_w^0	1.375	0.943
$a_{i=0}/p_{i=0}$	$2.7578x10^2$ / 0.0	$1.66482x10^2$ / 0.0
$a_{i=1}/p_{i=1}$	$3.0020x10^5$ / 1.0	$2.71631x10^5$ / 1.0
$a_{i=2}/p_{i=2}$	$-9.7452x10^5$ / 2.0	$-8.34331x10^5$ / 2.0
$a_{i=3}/p_{i=3}$	$8.1832x10^5$ / 3.0	$3.15625x10^5$ / 3.0
$a_{i=4}/p_{i=4}$	$1.2412x10^5$ / 4.0	$7.09082x10^5$ / 4.0
$a_{j=0}/p_{j=0}$	$1.0355 x10^5$ / 1.0	$2.51050x10^4$ / 0.0
$a_{j=1}/p_{j=1}$	$-3.2074 x10^5$ / 2.0	$-1.29157x10^5$ / 1.0
$a_{j=2}/p_{j=2}$	$3.6242 x10^5$ / 3.0	$4.28248x10^5$ / 2.0
$a_{j=3}/p_{j=3}$	$-6.0943 x10^5$ / 4.0	$-1.00000x10^6$ / 3.0
$a_{j=4}/p_{j=4}$	$9.6878 x10^5$ / 5.0	$9.73743x10^5$ / 4.0
g_n	1.0	1.0
g_d	1.0	1.0

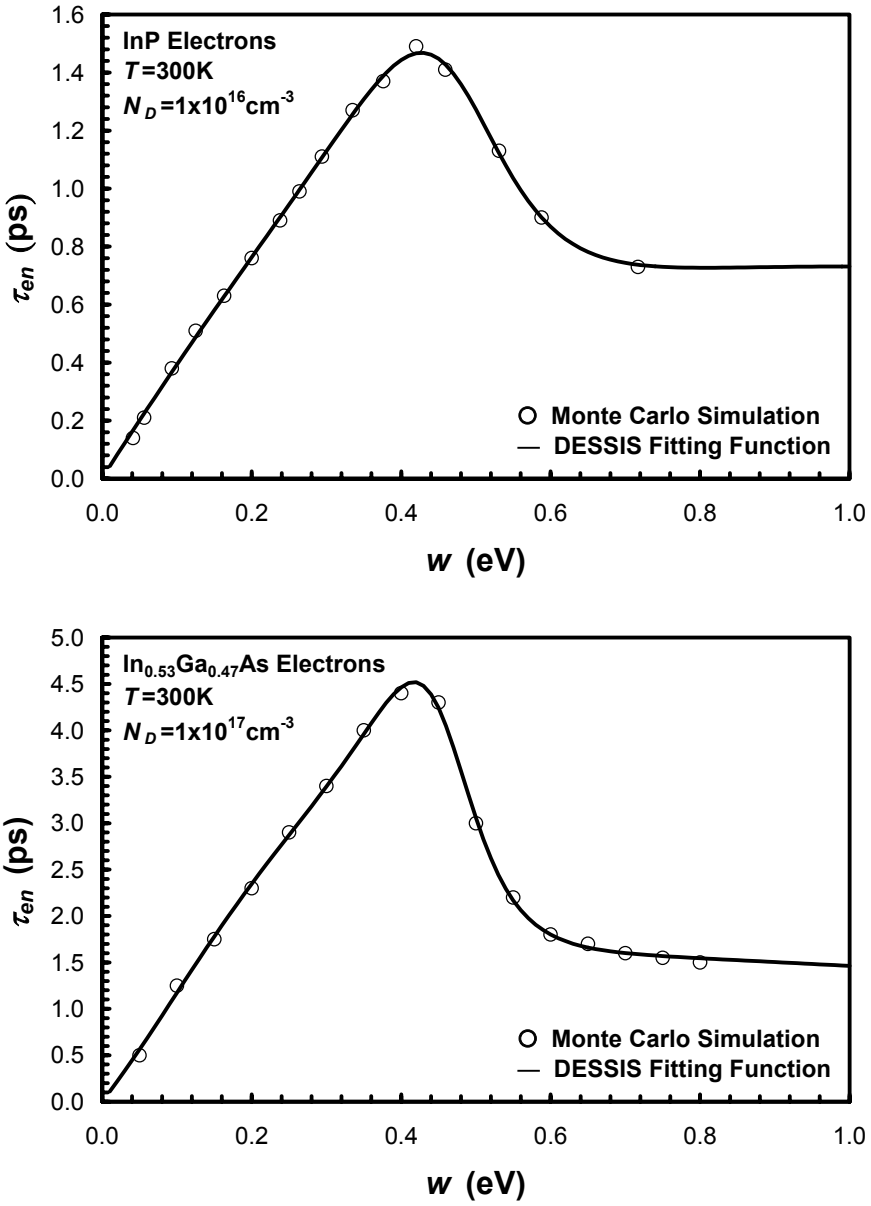

Figure 6-3: Electron energy relaxation times, τ_{en}, for InP (top) and $In_{0.53}Ga_{0.47}As$ (bottom) from published Monte Carlo simulations [6-12],[6-13] and the DESSIS fitting function.

6.3.2 Energy Flux Pre-factor (r_n,r_p)

Both the energy flux pre-factor and the Peltier coefficients are derived from the momentum relaxation time, τ_m [6-12], and it is this time constant that governs the degree of velocity overshoot that occurs in a semiconductor. The presence of an additional

factor of 2.5 and the impact on the Peltier coefficients, shown in Equations (D-11) and (D-12), must be considered in the determination of r_n and r_p. However, the limitations of DESSIS only allow a constant value to be assigned despite the significant energy dependence observed in [6-12]. For InP, the $2.5r_n$ product varies from less than 2.0 at w>0.45 eV and greater than 4.0 at w~0.8 eV. Similar behavior is observed from Monte Carlo simulations of $In_{0.53}Ga_{0.47}As$. The spatial variations of the electric field throughout a high-performance InP HBT [6-4] are sufficient to induce considerable velocity overshoot, resulting in a wide range of T_n and w. The selection of a single constant value of r_n that will accurately represent carrier transport is unlikely, but a single reasonable value that allows simulations to converge and the use of other model parameters for optimization is likely.

Figure 6-4 shows the band diagram and the electron energy, w_e, for a representative InP DHBT similar to those described in [6-14]. The InGaAs base and the InP collector are the two regions where velocity overshot is expected to occur. Since the acceptor concentration, N_A, is $3x10^{19}$ cm^{-3} in the base, base width modulation is negligible and the electric fields are not expected to change over bias. For the narrow range of w_e from 150 meV to 200 meV, the $2.5r_n$ product ranges from 2.5 to 3.0 for $In_{0.53}Ga_{0.47}As$ [6-12]. This allows a static value of r_n to more accurately represent the transport properties in the base. The low donor concentrations, N_D, and the large variations in V_{CE} will produce a much larger range of electric fields in the collector. For the wide range of w_e from 200 meV to 480 meV, the $2.5r_n$ product ranges from 2.0 to 3.0 in InP. In the absence of an energy dependent model and a means to decouple it from the energy dependent Peltier coefficients, r_n = 1.0 is a reasonable choice for the base and collector regions. The

parameters associated with the high field mobility and velocity saturation models are then used as fitting parameters to best match the experimental data. The behavior of r_n for compound semiconductors is significantly different than the nearly constant value of r_n = 1.0 over a 400 meV carrier energy range for silicon. Since the high field transport properties of holes are not considered for this n-type device, r_p remains at its default value of one.

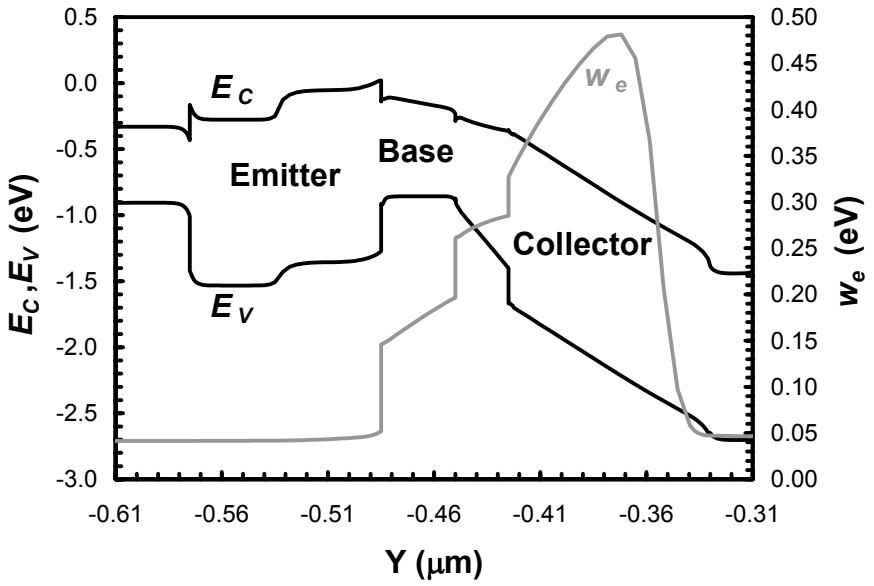

Figure 6-4: Representative band diagram of a high-performance InP DHBT showing the spatial variation of the electron energy, w_e.

6.3.3 Peltier Coefficient

Similar to τ_{en} and τ_{ep}, the Peltier coefficients can be defined as energy dependent parameters, but unlike τ_{en} and τ_{ep}, the form of the Peltier coeffcients depends on a greater set of parameters. The previously determined r_n and r_p pre-factors and the new Peltier pre-factors, f_n^{hf} and f_p^{hf} serve as coefficients to the energy dependent term, based on Equation (6-5). The resulting expression

$$PC_n(w) = \frac{5}{2} r_n \left(f_n^{hf}(w) \right) = \frac{5}{2} r_n \left(f_{n0}^{hf} \left(1 + f \frac{((\sum a_i w^{p_i}))^{g_n}}{((\sum a_j w^{p_j}))^{g_d}} \right) \right) \tag{6-6}$$

is designated as the energy dependent Peltier coefficient. The energy dependent Peltier pre-factor, $f_n^{hf}(w)$, shown in Equation (6-6) replaces the constant f_n^{hf} pre-factor shown in Equation (D-11). The same least squares fitting methodology presented for τ_{en} and τ_{ep} is used to fit Equation (6-6) to the Monte Carlo simulation data presented in [6-12]. With a maximum $i = j = 4$, Figure 6-5 highlights the limits of Equation (6-6) and the highly peaked nature of $PC_n(\mathrm{w_e})$. If i and j are allowed to increase to larger values, the required a_i and a_j coefficients are extremely large ($>10^6$) and further degrade computational performance. It is not clear that additional accuracy is needed given the limited quantity of Monte Carlo simulation data available for comparison. Table 6-4 summarizes the fitting parameters used in Figure 6-5.

Table 6-4: Summary of DESSIS fitting function parameters for the energy dependent Peltier Coefficients for electrons, $PC_n(w)$, of InP and $In_{0.53}Ga_{0.47}As$.

Parameter	InP	$In_{0.53}Ga_{0.47}As$
r_n	1.0	1.0
f_{n0}^{hf}	1.0	1.0
f	1.971	1.311
$a_{i=0}/p_{i=0}$	-1.0435×10^{3} / 0.0	-1.4694×10^{3} / 0.0
$a_{i=1}/p_{i=1}$	1.0836×10^{5} / 1.0	1.0906×10^{5} / 1.0
$a_{i=2}/p_{i=2}$	-5.4963×10^{5} / 2.0	-7.1013×10^{5} / 2.0
$a_{i=3}/p_{i=3}$	-1.8183×10^{-4} / 3.0	-1.8183×10^{-4} / 3.0
$a_{i=4}/p_{i=4}$	5.8585×10^{-3} / 4.0	5.8585×10^{-3} / 4.0
$a_{j=0}/p_{j=0}$	5.2740×10^{3} / 0.0	6.5856×10^{3} / 0.0
$a_{j=1}/p_{j=1}$	-1.0987×10^{5} / 1.0	-1.2911×10^{5} / 1.0
$a_{j=2}/p_{j=2}$	1.0000×10^{6} / 2.0	9.5325×10^{5} / 2.0
$a_{j=3}/p_{j=3}$	-3.3315×10^{-4} / 3.0	-3.3315×10^{-4} / 3.0
$a_{j=4}/p_{j=4}$	4.2542×10^{-3} / 4.0	4.0584×10^{-3} / 4.0
g_n	1.0	1.0
g_d	1.0	1.0

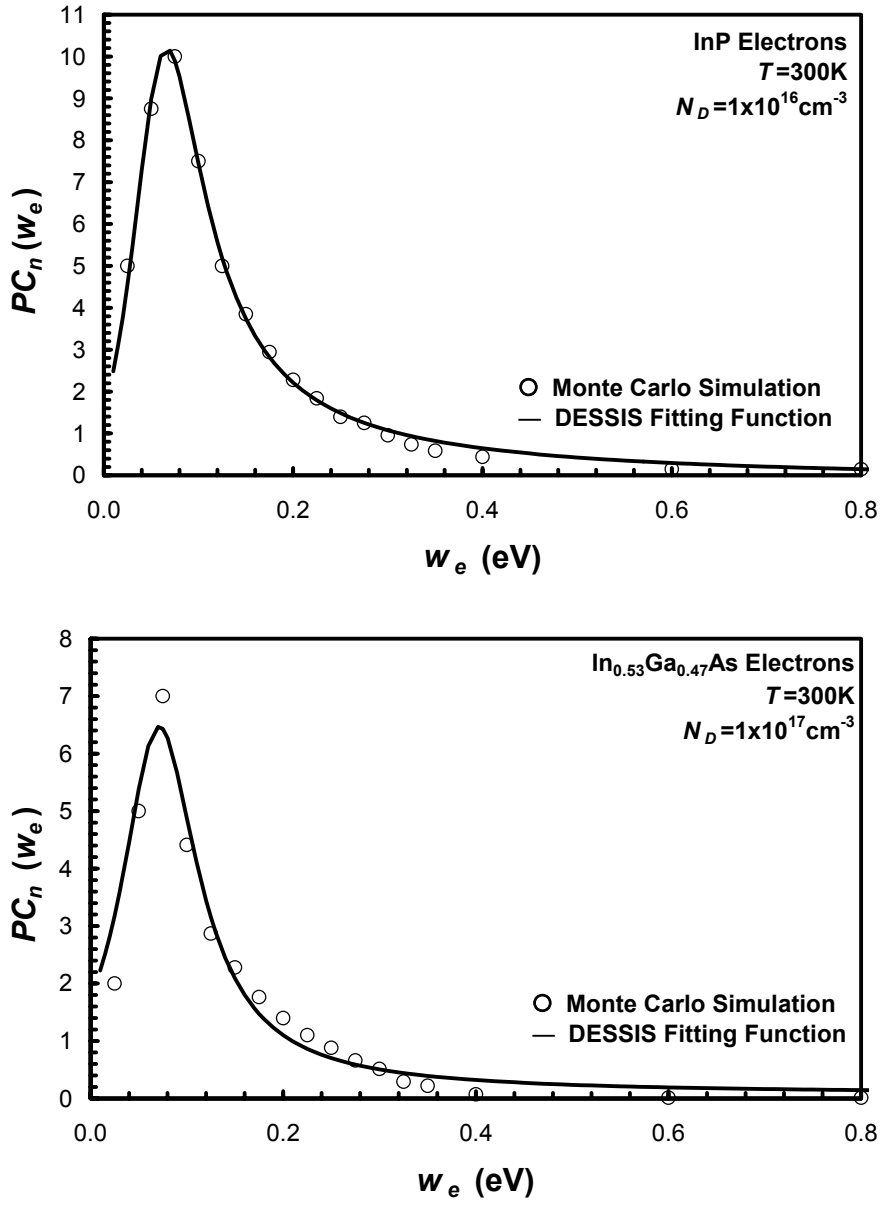

Figure 6-5: Peltier coefficient, τ_e, for InP (top) and $In_{0.53}Ga_{0.47}As$ (bottom) from published Monte Carlo simulations [6-12] and the DESSIS fitting function.

6.3.4 Thermal Diffusion Pre-Factor

The remaining f_n^{td} and f_p^{td} pre-factors define the contribution of thermal carrier diffusion in the Equations (D-1) and (D-2). $D_{e,h}$ has been removed from the current equations by using Equation (D-3), but when T_n and T_p diverge from T_L significantly, this

expression no longer holds. If velocity overshot or ballistic transport does occur within the device, the selection of f_n^{td} and f_p^{td} can be based on the *MC* computations of [6-12], but the fundamental construct of Equation (D-1) and (D-2) must be revisited. The following section will discuss the greater role of thermal carrier diffusion in the current equations and the modifications necessary for high-performance InP HBTs. In order to decouple the electro-thermal diffusion term from other modifications, f_n^{td} is initially set to one for all regions. The impact of f_n^{td} on regions where $T_n >> T_L$ is discussed in Section 6.5. For the n-type InP HBT under investigation, holes are not expected to be very energetic (T_p comparable to T_L) and f_p^{td} is also set to one for all regions.

6.4 Ballistic Transport Modifications

The previous sections have described the assumptions and some of the limitations associated with the HTE implementation in DESSIS. In most cases, the default implementation is adequate to represent InP HBTs where electrons experience a limited degree of velocity overshoot. If the base and collector thicknesses are scaled sufficiently, a large number of electrons will not have the time to relax to v_{sat} [6-3]. If a carrier traverses a region without any phonon, carrier, and/or lattice interactions, that carrier can be termed "ballistic". Qualitatively, the carrier is similar to bullet traveling relatively unimpeded through the lattice. This is believed to be case with many InP HBTs whose f_T exceeds 300 GHz and certainly true for HBTs whose f_T exceeds 400 GHz [6-4]. The modifications required to model ballistic transport are centered on Equations (D-1) and (D-2), and their use of Equation (D-3). By using Equation (D-3), the effective $D_{e,h}$ used for the carrier concentration diffusive term and thermal carrier diffusive term are coupled

to $\mu_{e,h}$ and $T_{n,p}$. In regions where $T_{n,p}$ are high, the diffusion of ballistic carriers in a direction perpendicular to its velocity vector can be over-estimated significantly. This is a result of the scalar property of $T_{n,p}$ and the over-estimation of $\mu_{e,h}$. Without the scattering events necessary to randomize a carrier's motion, the effective diffusivity is not an isotropic quantity. The high value of $T_{n,p}$ only represents the properties of a ballistic carrier along its velocity vector, not perpendicular to its velocity vector. Simulation of ballistic transport would require $T_{n,p}$ to be vectorized, but this would require a significant modification to the device simulator. Such a change in the HTE could not be implemented by any end-user of a commercial device simulator. The coupling of the diffusive terms to $\mu_{e,h}$ also presents a problem. Velocity overshoot and ballistic transport serve to inflate $\mu_{e,h}$ and delay the onset of negative differential mobility. With an over-estimation of $\mu_{e,h}$, the effective diffusivity is further over-estimated. This also requires that $\mu_{e,h}$ be defined as an anisotropic quantity, but unlike the $T_{n,p}$ problem, most device simulators do provide a solution.

These two combined effects have a significant impact on HBT simulations. Figure 6-6 shows a simulated peak $\beta = 11$, which is much smaller than the measured β values that exceed 70 in [6-15]. The over-estimation of the diffusive term allows an erroneously large fraction of electrons entering the base from the emitter to laterally diffuse toward the base contact. The high recombination velocity of the base contact captures these electrons and prevents them from entering the collector, resulting in the lower β. The aggressively scaled dimensions present in 400 GHz InP DHBTs [6-15] have further exacerbated the problem by reducing the base contact to emitter spacing to 150 nm or

less. From Equation (D-1) and (D-2), the drift and spatial composition terms are negligible compared to the two diffusive terms. If the InGaAs base was grown by MBE or MOCVD, there is no doping or compositional variation in the axis parallel to wafer surface. This eliminates the spatial composition term, because the spatial variation of $m_{e,h}$ is zero. In the absence of doping and compositional variations, the only band bending results from the base resistance, R_B, but this is negligible in a high f_{MAX} device where R_B is minimized. Similar arguments can be applied to the base-collector grade and the drift collector regions of traditional mesa HBTs. Therefore, any corrections to Equations (D-1) and (D-2) will be focused on the diffusive terms and neglect the impact on the drift and composition terms. A complication arises with the introduction of SIBS [6-16] where the drift term can no longer be considered negligible due to the large x-axis doping gradients at the SIBS periphery. However, proper definition of regions and model parameters will allow simulation of such a device.

To simulate ballistic transport in DESSIS, a common factor must be identified in the two diffusive terms, and this factor must allow anisotropic behavior to be user-defined. The carrier mobility is just such a factor, and the anisotropic mobility models can be utilized to correct for the scalar properties of $T_{n,p}$ and the over-estimation of $\mu_{e,h}$. A major axis can be defined in any one axis direction that would be unaffected by the anisotropic mobility model, and the minor axis or axes are defined as the remaining directions that would be de-rated by the anisotropic mobility model. The user has the choice of three different means to define the major and minor axis $m_{e,h}$: 1) constant anisotropy pre-factor; 2) constant anisotropy pre-factor with modified driving force; and 3) independent mobility models in the major and minor axis. The logical choice would

be to define separate and independent mobility models for the major and minor axis, but computational and numerical demands cause the third method to fail often. Therefore, the second method is the only reasonable choice. The definition of the constant anisotropy factor, AF, can be taken as the average $T_{n,p}$ normalized to T_L. The large spatial variation of $T_{n,p}$ and the over-estimatation of $\mu_{e,h}$ require some flexibility in the definition of AF in order to match experimental data. Figure 6-6 shows the 3X improvement in β at V_{BE} = 1.0 V resulting from setting AF = 5 in the InGaAs base and base-collector grade. The significant increase in β at low V_{BE} is due to the under-estimation of the diffusive terms when $T_{n,p}$ are comparable to T_L. Other recombination mechanisms can be used to alter the base current, I_B, at low V_{BE} to better match the β dependence on V_{BE} and I_C. The use of a constant AF is a limited means to simulate ballistic transport, and a more comprehensive correction to the device simulator is still required.

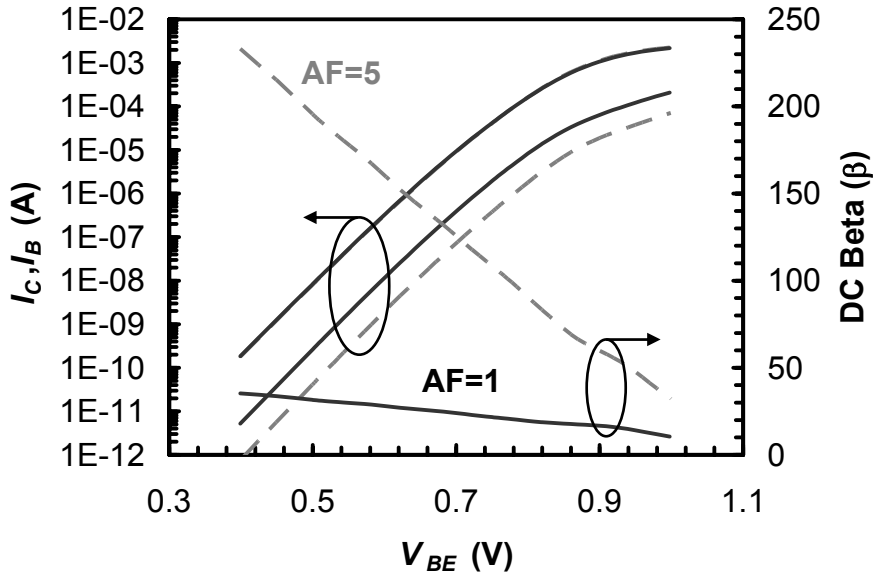

Figure 6-6: Impact of the anisotropy factor, *AF*, on the forward Gummel characteristics of a high performance InP DHBT.

6.5 Simulation Results

Figure 6-8 and Figure 6-8 shows the forward Gummel and the f_T versus I_C curves, respectively, that result using the parameters discussed in this investigation. Also shown are the measured data of an A_E = 0.25x4.0 μm^2 InP DHBT of identical structure and fabrication as those presented in [6-15]. There is reasonable agreement between the measured and simulated results, but several key differences exist. The curvature of the forward Gummel is reasonably matched indicating the proper calibration of the conduction band structure, but the currents diverge as low V_{CE}. The higher currents observed in the experimental data is a result of a leakage path in the pad structure used to probe the HBT, and this path was not included in the simulation. The curvature of the simulated and measured f_T curves is also reasonably matched, but the simulated f_T is 10-20 GHz higher at low I_C and the onset of Kirk effect is pre-mature.

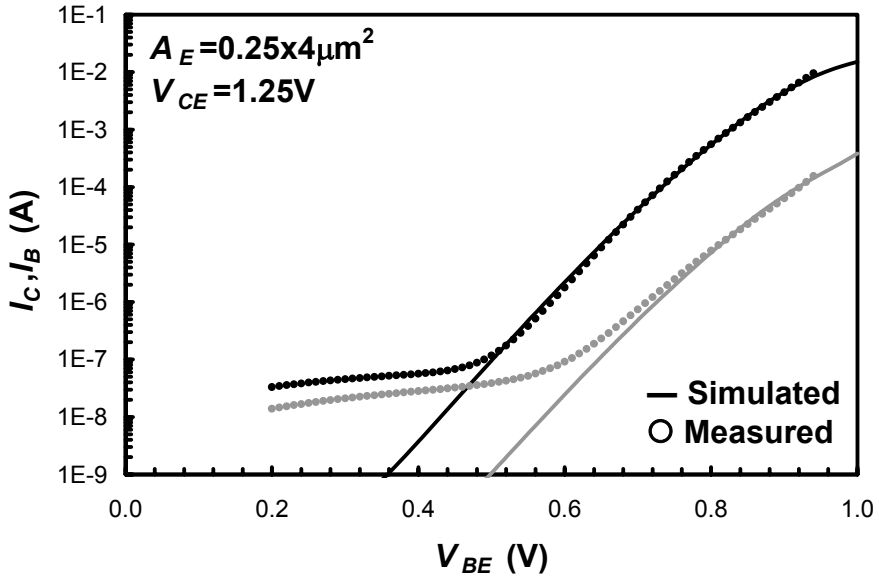

Figure 6-7: Forward Gummel curves showing measured results from an A_E = 0.25x4.0 μm^2 InP DHBT similar to those presented in [6-15] and the simulated results from this investigation.

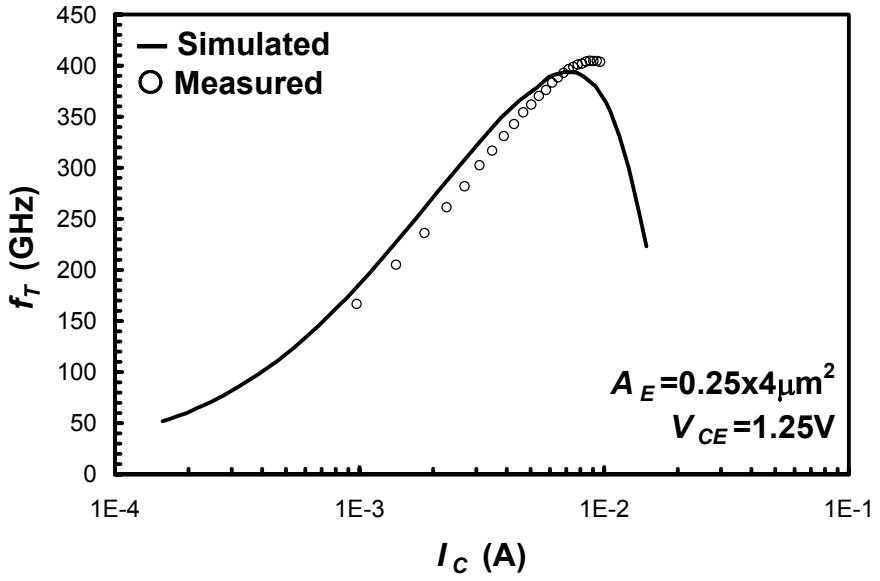

Figure 6-8: f_T versus I_C curves showing measured results from an A_E = 0.25x4.0 μm^2 InP DHBT similar to those presented in [6-15] and the simulated results from this investigation.

Analysis of the simulated *Y*-parameters indicates that the degree of velocity overshoot is over-estimated at low I_C yielding a lower than expected C_{BC}. At higher I_C, the degree of velocity overshoot is under-estimated leading to an electron concentration increase in the base-collector grade and the pre-mature onset of Kirk effect. Figure 6-9 shows the I_C dependence of both the measured and simulated C_{BC} and illustrates the impact of velocity overshoot. The C_{BC} reduction at higher I_C is due to the screening of the base-collector space charge by the free electrons transiting the collector depletion region. This can be observed in Figure 6-10 where the free electron population, *n*, exceeds the ionized donor concentration, N_D^+, of 5x10^{16} cm^{-3} is a large portion of the collector. Since no published data on the high-field transport properties of the base-collector grade material exist, it is not unexpected that velocity overshoot is not well predicted in this region. Further optimization of the model parameters may yield insight into the properties of the base-collector grade material.

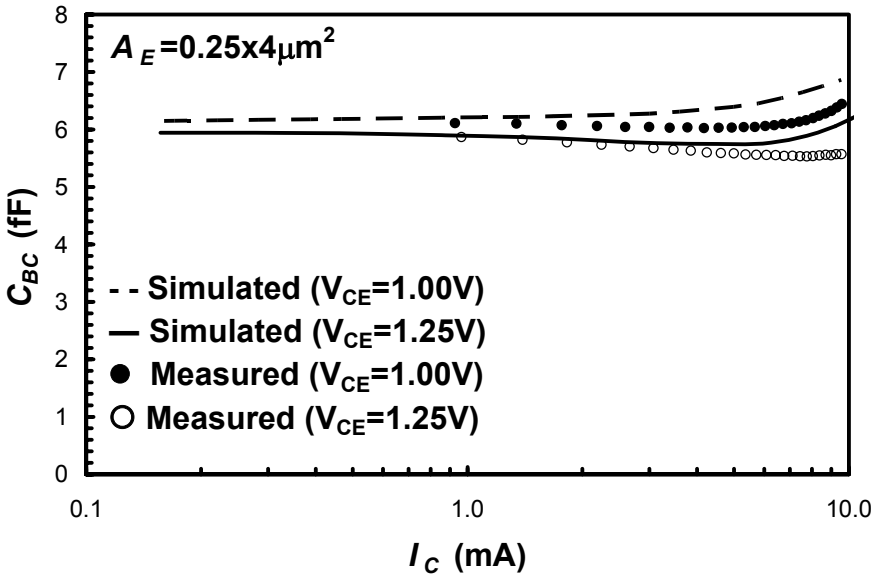

Figure 6-9: The collector current, I_C, dependence on the measured and simulated C_{BC} for two V_{CE} values, 1.00 V and 1.25 V.

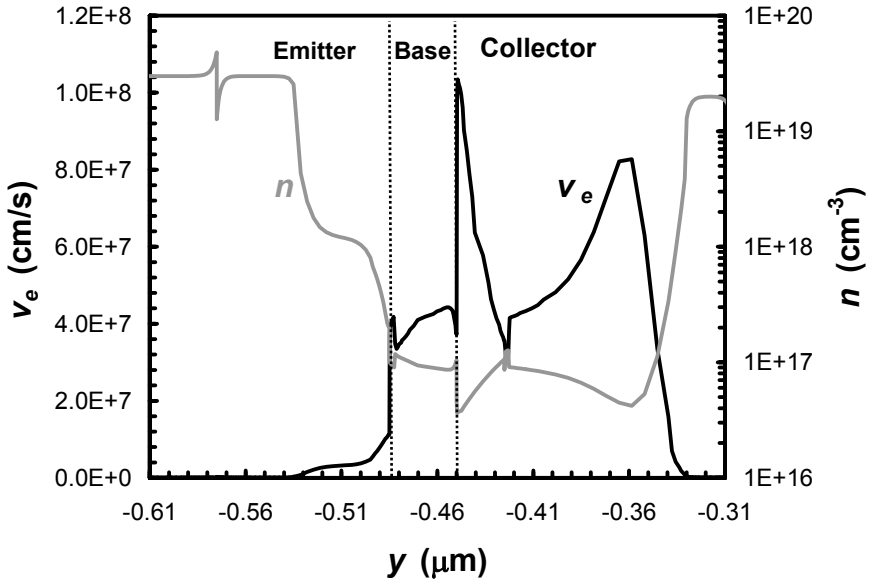

Figure 6-10: Simulated electron velocity, v_e, and electron population, n, through the y-axis centerline of an A_E = 0.25x4.0 μm^2 InP DHBT biased at V_{CE} = 1.25 V and I_C = 6.4 mA.

Figure 6-10 also shows a v_e spike at y = -0.36μm, near the transition from the n-InP collector into the n+ InP sub-collector, but it is questionable if this spike actually occurs in the device. For regions where T_n>>T_L and T_n shows significant spatial variation

e.g. the n- InP collector, the f_n^{td} parameter does have a significant effect on the simulated v_e profile. A f_n^{td} value of 0.6, corresponding to a w_e of approximately 0.40 eV [6-12], produced the 8.27x10^7 cm/s v_e spike observed in Figure 6-10. If f_n^{td} is increased to 1.0 in the n- InP collector to match the rest of the device, a sharper 1.16x10^8 cm/s v_e spike is produced at the same location. Unfortunately, the w_e independent nature of f_n^{td} does not allow for a more refined calibration of the InP model parameters required for more accurate simulations. The Hydrodynamic implementation of the Boltzmann Transport Equation (BTE) is also known to generate spurious velocity overshoot spikes in n-type ballistic diodes. The collector structure of these HBTs is not dissimilar to a ballistic diode. Others have devised alternative formulations that are not susceptible to the same problem and implemented them in custom simulation code [6-17]. Such a fundamental change in the treatment of carrier transport cannot be applied to a commercial simulator by the end user.

Even with the v_e spike present, the overall device behavior is captured by the present model. This can be explained by the modified collector transit time formulation,

$$\tau_C' = \int_0^{t_C} \frac{dy}{v(y)}\left(1 - \frac{y}{t_C}\right) \tag{6-7}$$

derived by [6-18] where $v(y)$ is the position dependent electron velocity and t_C is the collector thickness. The spatial variable, y, is equal to zero at the metallurgical base-collector junction and equal to t_C at the sub-collector interface. The extra weighting factor, $(1-y/t_C)$, in Equation (6-7) is required to correct for a spatially non-uniform carrier velocity and places greater importance on $v(y)$ values near the base-collector junction.

Therefore, the high-field transport properties of the collector grade have a greater impact on device performance than the anomalous v_e spikes deep in the collector.

6.6 Summary

With the aggressive scaling currently being untaken to develop 400 GHz InP HBTs, velocity overshoot and ballistic transport are expected to play a key role in device engineering. Negative differential mobility, characteristic of many compound semiconductors, is modeled using the transferred-electron mobility model, and reasonable agreement to published data is achieved. Velocity overshoot is modeling using the Hydrodynamic transport equations. Previously published Monte Carlo simulations are used to calibrate the energy dependence of $\tau_{en,p}(w)$ and $PC_{n,p}(w)$, two of the four sets of material-specific parameters. However, the remaining two sets are static quantities leading a rough approximation of the actual value. The liberal use of the Boltzmann form of the Einstein relation to interchange diffusivity and mobility proves to be the greatest limitation to the existing implementation. Under ballistic conditions, the diffusive terms are significantly over-estimated, resulting in a third lower DC current gain. The anisotropic mobility models are found to provide a limited correction to this deficiency. The resulting simulations agree reasonably with the measured data, but the ultimate simulation error is dominated by a limited understanding of the materials.

6.7 References

[6-1] T.J. Maloney and J. Frey, "Transient and steady-state electron transport properties of GaAs and InP", *Journal of Applied Physics*, vol. 48, no. 2, pp. 781-787, Feb. 1977.

[6-2] H. Kroemer, "Hot-Electron Relaxation Effects in Devices", *Solid State Electronics*, vol. 21, no. 1, pp. 61-67, 1978.

[6-3] S. Krishnamurthy, M.A. Berding, and A. Sher, "Ballistic transport in semiconductor alloys", *Journal of Applied Physics*, vol. 63, no. 9, pp. 4540-4547, May 1988.

[6-4] T. Ishibashi, "Nonequilibrium Electron Transport in HBTs", *IEEE Transactions on Electron Devices*, vol. 48, no. 11, pp. 2595-2605, Nov. 2001.

[6-5] M. J.W. Rodwell, M. Urteaga, T. Mathew, D. Scott, D. Mensa, Q. Lee, J. Guthrie, Y. Betser, S. C.Martin, R. P. Smith, S. Jaganathan, S. Krishnan, S. I. Long, R. Pullela, B. Agarwal, U. Bhattacharya, L. Samoska, and M. Dahlstrom, "Submicrometer scaling of heterojunction bipolar transistors," *IEEE Transactions on Electron Devices*, vol. 48, pp. 2606–2624, Dec. 2001.

[6-6] Y. Betser and D. Ritter, "Reduction of the Base-Collector Capacitance in InP/InGaAs Heterojunction Bipolar Transistors Due to Electron Velocity Modulation", *IEEE Transactions On Electron Devices*, vol. 46, no. 4, pp. 628-633, April 1999.

[6-7] O. Madelung, "Semiconductors – Basic Data", 2nd revised edition, Springer-Verlag, 1996.

[6-8] http://www.ioffe.ru/SVA/NSM/Semicond/

[6-9] M. Levinshtein, S. Rumyantsev, and M. Shur, "Handbook Series on Semiconductor Parameters", vol.2, World Scientific, 1999.

[6-10] I. Vurgaftman, J.R. Meyer, and L.R. Ram-Mohan, "Band Parameters for III-V compound semiconductors and their alloys", *Journal of Applied Physics*, vol. 89, no. 11, pp. 5815-5875, June 2001.

[6-11] M. Sotoodeh, A.H. Khalid, and A. A. Rezazadeh, "Empirical low-field mobility model for III-V compounds application to device simulation codes", *Journal of Applied Physics*, vol. 87, no. 6, pp. 2890-2900, March 2000.

[6-12] J.M. Ruiz-Palmero, I. Schnyder, and Heinz Jäckel, "Hydrodynamic 2D Simulation of InP/InGaAs DHBT", *Proceedings of the 2004 BCTM*, pp. 152-155.

[6-13] G.B. Tait and C.M. Krowne, "Determination of Transport Parameters for InP Device Simulation in n+ nn+ Structures", *Solid State Electronics*, vol. 30, no. 12, pp. 1317-1322, 1987.

[6-14] J.C. Li, M. Sokolich, T. Hussain, and P.M. Asbeck, "Physical Modeling of Degenerately Doped Compound Semiconductors for High-Performance HBT Design", *Solid State Electronics*, Accepted for publication.

[6-15] J.C. Li, T. Hussain, D.A. Hitko, Y. Royter, C.H. Fields, I. Milosavljevic, S. Thomas III, R. D. Rajavel, P.M. Asbeck, and M. Sokolich, "Reduced Temperature *S*-Parameter Measurements of 400+ GHz Sub-Micron InP DHBTs", *Solid State Electronics*, In Review.

[6-16] J.C. Li, M. Chen, D.A. Hitko, C.H. Fields, B. Shi, R. Rajavel, P.M. Asbeck, and M. Sokolich, "A submicrometer 252 GHz f_T and 283 GHz f_{MAX} InP DHBT with reduced C_{BC} using Selectively Implanted Buried Subcollector (SIBS)", *IEEE Electron Device Letters*, vol. 26, no. 3, pp. 136-138, March 2005.

[6-17] D. Chen, E.C. Kan, U. Ravaioli, C.-W. Shu, and R.W. Dutton, "An Improved Energy Transport Model Including Nonparabolicity and Non-Maxwellian Distribution Effects", *IEEE Electron Device Letters*, vol. 13, no. 1, pp. 26-28, Jan. 1992.

[6-18] S.E. Laux and W. Lee, "Collector Signal Delay in the Presence of Velocity Overshoot", *IEEE Electron Device Letters*, vol. 11, no. 4, pp. 174-176, April 1990.

7. A SUB-MICRON 252 GHZ F_T AND 283 GHZ F_{MAX} INP DHBT WITH REDUCED C_{BC} USING SELECTIVELY IMPLANTED BURIED SUB-COLLECTOR (SIBS)

7.0 Abstract

The Selectively Implanted Buried Sub-collector (SIBS) is a method to decouple the intrinsic and extrinsic C_{BC} of InP-based DHBTs. Similar to the Selectively Implanted Collector (SIC) used in Si-based BJTs and HBTs, ion implantation is used to create a N+ region in the collector directly under the emitter. By moving the sub-collector boundary closer to the BC junction, SIBS allows the intrinsic collector to be thin, reducing τ_C, while simultaneously allowing the extrinsic collector to be thick, reducing C_{BC}. For a 0.35x6 μm^2 emitter InP-based DHBT with a SIBS, 6 fF total C_{BC} and >6 V BV_{CBO} were obtained with a 110 nm intrinsic collector thickness. A maximum f_T of 252 GHz and f_{MAX} of 283 GHz were obtained at a V_{CE} of 1.6 V and I_C of 7.52 mA. Despite ion implantation and materials re-growth during device fabrication, a base and collector current ideality factor of ~2.0 and ~1.4, respectively, at an I_C of 100 μA, and a peak β of 36 were measured.

7.1 Introduction

InP-based Heterojunction Bipolar Transistors (HBTs) can be used in a wide variety of digital and analog applications whose operating frequency exceeds 40 GHz. In the past, researchers working with III-V semiconductors have relied on material properties and bandgap engineering to achieve high breakdown and performance. As applications whose clock frequency approached 100 GHz emerged, researchers have pushed the small signal performance of InP-based HBTs to over 350 GHz [7-1],[7-2]. However, the rapid progress of SiGe HBTs threatens to displace InP-based HBTs in many markets [7-3],[7-4]. Although the electron transport properties of InP and InGaAs are superior to Si and SiGe, SiGe HBTs leverage the enormous knowledge base and infrastructure of silicon CMOS and BJT technologies to effectively compete against the incumbent III-V technologies.

In particular, SiGe HBTs utilize ion implantation to decouple the intrinsic and extrinsic base-collector capacitances, C_{BCI} and C_{BCX}, respectively. This is accomplished by growing a relatively thick n- epitaxial collector and selectively ion implanting a n+ region, called a Selectively Implanted Collector (SIC), directly beneath the emitter [7-5]. The SIC allows the intrinsic collector doping to be increased, thereby delaying the onset of Kirk effect and minimizing the BC space charge region. Although the high collector doping causes C_{BCI} to increase, the corresponding reduction in τ_C still yields an improvement in device performance. Since the SIC only defines the intrinsic collector, the extrinsic collector remains at the as-deposited doping level. If the extrinsic collector thickness and doping are properly matched, C_{BCX} should be both small and voltage

invariant when compared to C_{BCI} [7-6]. By decoupling C_{BCI} and C_{BCX}, the collector can be optimized to yield higher f_T and f_{MAX}.

In the case of mesa InP-based HBTs, both the intrinsic and extrinsic collector layers are grown simultaneously; therefore, C_{BCX} can be only be reduced by laterally scaling the collector mesa [7-7],[7-8]. However, all of these lateral scaling methods will magnify the effects of process variation and increase the device R_{TH} [7-9]. Since InP-based HBTs require a lower processing temperature, the implant damage associated with the formation of a SIC would cause irreparable damage to the BC junction. In order to incorporate the benefits of a SIC-like structure, the selectively implanted region is formed before any intrinsic device layers are grown and buried further beneath the intrinsic collector. Instead of defining the intrinsic collector properties, the implanted region serves as a vertical extension of the sub-collector. The intrinsic collector, base, and emitter layers are then grown normally, without regard to the implanted region. Since the implanted region does not define the intrinsic collector, this variant of the SIC concept is called the Selectively Implanted Buried Sub-collector (SIBS). Although a SIBS has been previously demonstrated with InP DHBTs [7-10], this is the first demonstration of the SIBS technique where RF performance comparable to more conventional mesa devices [7-11] has been achieved.

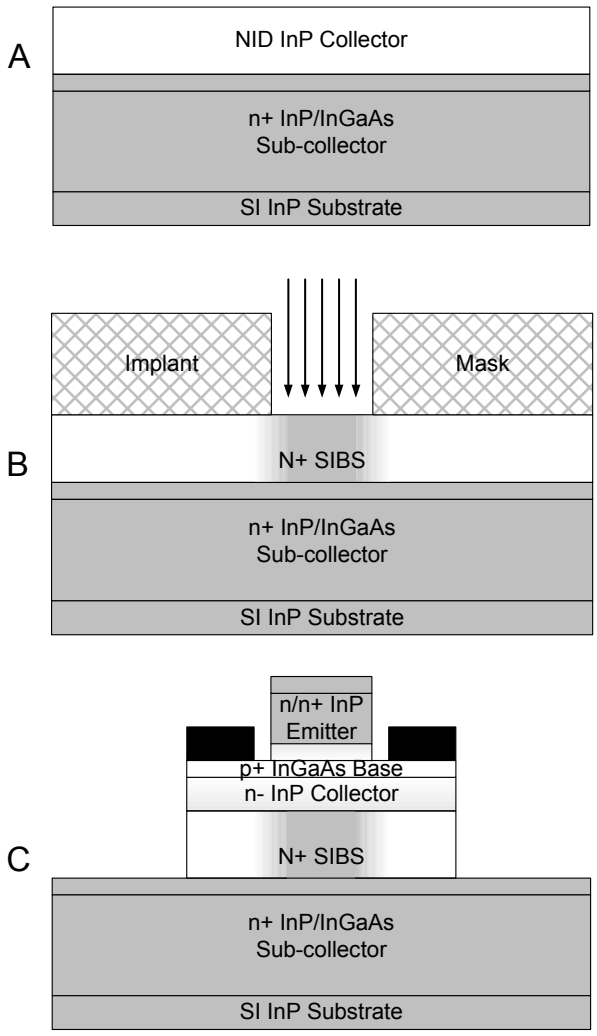

Figure 7-1: Cross-section of (A) initial layers prior to SIBS formation, (B) SIBS formation, and (C) final device.

7.2 Device Structure and Fabrication

Figure 7-1 shows a schematic cross-section of the SIBS fabrication process. Molecular Beam Epitaxy (MBE) is used to grow a 100 nm / 100 nm n+ InP/InGaAs sub-collector and a 200 nm undoped InP collector on a (100) semi-insulating InP substrate. An implant mask is then deposited and patterned to form the openings for the SIBS. At an elevated temperature of 200 $^{\circ}$C, a 2.5x10^{14} cm^{-2} dose of Si^{+} ions at 120 keV is implanted into the wafer. The dose and ion energy were selected to yield a 5x10^{18} cm^{-3}

Si concentration near the top of the SIBS. The implant mask is stripped, and the wafer is then annealed at elevated temperature under Phosphine over-pressure. Subsequently, a 110 nm n- InP collector and grade, 35 nm p+ InGaAs base, 145 nm n/n+ InP emitter, and 110 nm n+ InGaAs emitter cap were grown with MBE. The device layers are then patterned and etched to form the emitter, collector, and sub-collector mesas. The emitter, base, and collector contacts are composed of a Ti/Pt/Au metal stack deposited in a non-self-aligned method with lift-off. Additional information on the material growth, ion implantation, and device fabrication are discussed in [7-12],[7-13],[7-14],[7-15],[7-16].

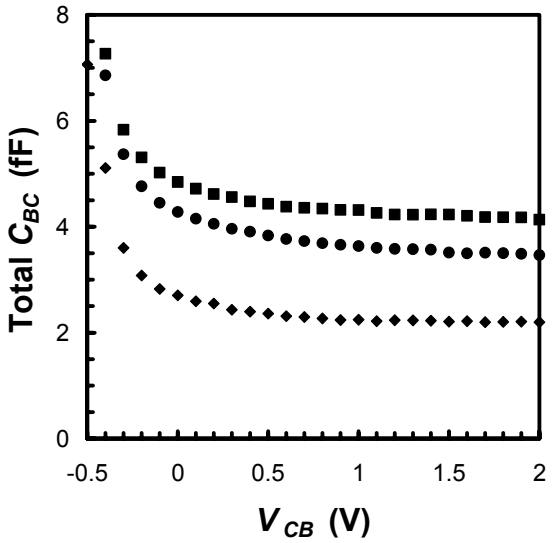

Figure 7-2: Total C_{BC} versus V_{CB} for a 0.35x3 μm^2 device with (♦) no SIBS, (●) 0.35 μm wide SIBS, and (■) 1.35 μm wide SIBS.

7.3 Device Measurements

Due to the small geometries of sub-micron devices, *S*-parameter measurements at 5 GHz were used to study the capacitance of various SIBS structures. Figure 7-2 shows the total zero bias C_{BC} versus V_{CB} for a 0.35x3 μm^2 device with a 1.35 μm wide collector mesa without a SIBS, with a 0.35x3.45 μm^2 SIBS, and with a 1.35x3.45 μm^2 SIBS. The

largest structure corresponds to a SIBS which encompasses the entire collector mesa. The stated dimensions for the device and the SIBS refer to the drawn dimensions of the base-emitter junction and the implant mask window, respectively. Figure 7-3 shows the evolution of C_{BC} and BV_{CBO} with the drawn SIBS width for a 0.35x3 μm^2 device with a fixed collector mesa width of 1.35 μm and fixed SIBS length of 3.45 μm. The lateral straggle from ion implantation and diffusion from annealing increase the actual SIBS width approximately 100 nm. Despite the increase in C_{BC}, the additional SIBS width is necessary for the proper collection of electrons [7-17]. Although B_{VCBO} appears to decrease as the intrinsic collector, located above the SIBS, occupies a larger fraction of the total collector mesa area, its precise dependence on SIBS geometry is not yet well understood.

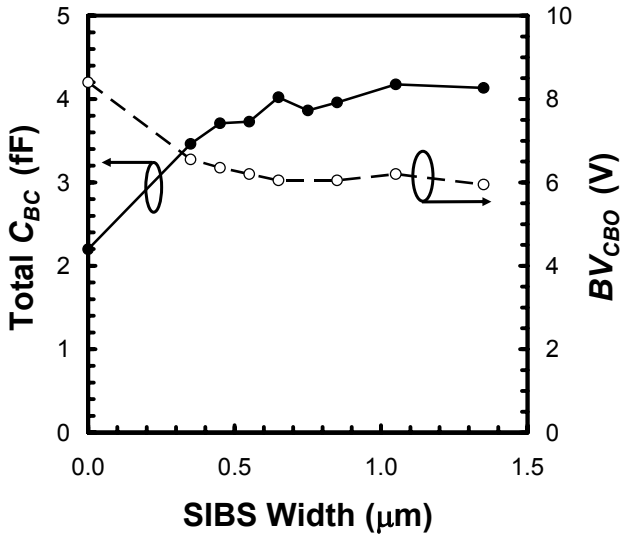

Figure 7-3: Total zero bias C_{BC} and 5 μA BV_{CBO} versus SIBS drawn width for a 0.35x3 μm^2 device with a fixed 1.35 μm collector mesa width and a fixed 3.45 μm length SIBS.

Figure 7-4 and Figure 7-5 show the forward I-V curve of the base-collector diode and the common emitter I-V curves under forced I_B values from 40 μA to 360 μA at 40

μA steps for a 0.35x6 μm^2 device, with a 0.35x6.45 μm^2 SIBS. The higher emitter resistance (R_E) and collector resistance (R_C) resulting from emitter over-etch, which reduced the emitter length by a factor of two, and small area collector contact, placed perpendicular to the emitter finger, contribute to the high R_{ON} in the saturation region, respectively. A forward Gummel curve, where V_{CB} = 0.0 V, is superimposed on Figure 7-5 as a qualitative method to partition the impact of R_C and R_E. *S*-parameters from 2 GHz to 110 GHz were measured on this device to assess its small signal performance. A simultaneous peak f_T of 252 GHz and f_{MAX} of 283 GHz were obtained at an I_C of 7.52 mA resulting from a forced V_{BE} of 0.975 V and V_{CE} of 1.6 V. Figure 7-6 shows both f_T and f_{MAX} as determined from -20 dB/dec extrapolations of h_{21} and U, respectively. The measured f_T and f_{MAX} were lower than expected due to the high R_C from sub-optimal collector contact placement and the less than favorable A_E:A_C ratio from the emitter over-etch.

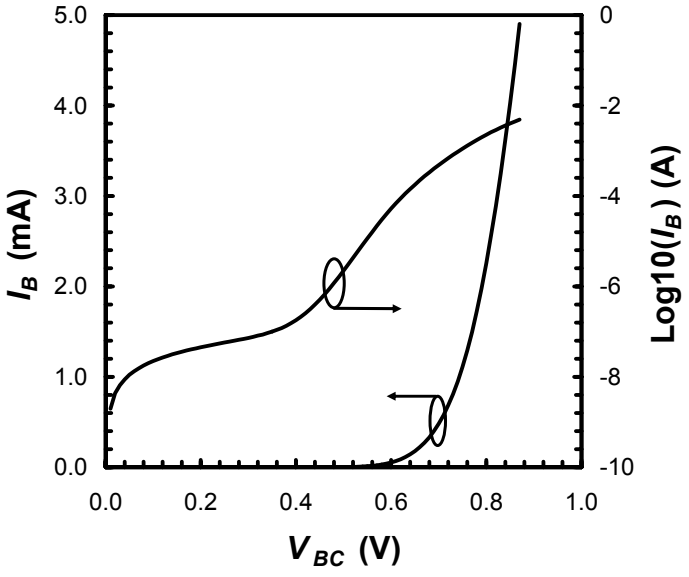

Figure 7-4: Forward I-V curves of the Base-Collector diode for a 0.35x6 μm^2 device with a 0.35x6.45 μm^2 SIBS and 1.35 μm wide collector mesa.

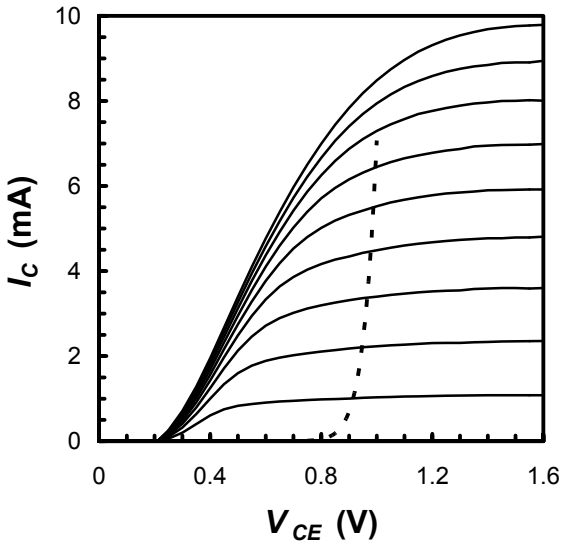

Figure 7-5: Solid lines show the common emitter I-V curves (I_B = 40 μA to 360 μA, 40 μA steps) for a 0.35x6 μm² device with a 0.35x6.45 μm² SIBS and 1.35 μm wide collector mesa. Dashed line shows the forward Gummel curve of the same device at a fixed V_{CB} = 0.0 V.

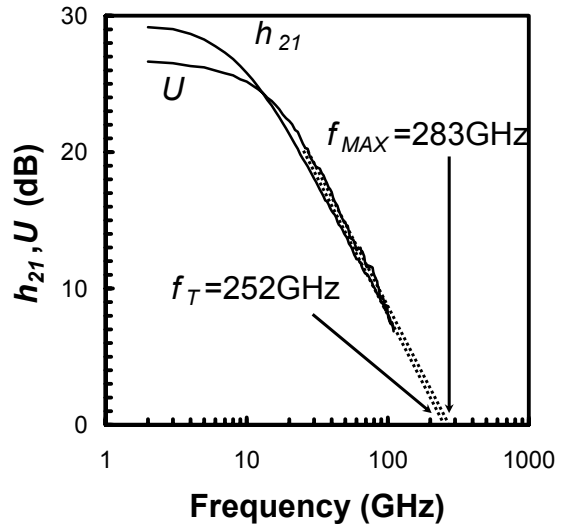

Figure 7-6: RF gains versus frequency for 0.35x6 μm² device with a 0.35x6.45 μm² SIBS at V_{CE} = 1.6 V and V_{BE} = 0.975 V.

The SIBS concept has shown to successfully reduce C_{BC}, but more importantly, it is the first method to successfully decouple C_{BCI} and C_{BCX} in an InP-based HBT. To date, this work has shown the best small signal performance of an InP-based HBT using a SIBS structure. Further optimization of the SIBS fabrication process will yield even faster devices in the near future.

7.4 Acknowledgements

This chapter, in full, is a reprint as it appears in the IEEE Electron Device Letters, vol. 26, no, 3, pp. 136-138, March 2005. The contributions from the co-authors Mary Chen, Donald A. Hitko, Charles H. Fields, Binqiang Shi, Rajesh Rajavel, and Marko Sokolich of HRL Laboratories, L.L.C., and Peter M. Asbeck of UCSD are appreciated. The author of this dissertation was the primary investigator and primary author of this publication. This work was sponsored by the Defense Advanced Research Projects Agency (DARPA) through AFRL Contract F33615-02-1286 (TFAST).

7.5 References

[7-1] Z. Griffith, M. Dahlström, M. Urteaga, M. J. W. Rodwell, X.-M. Fang, D. Lubyshev, Y. Wu, J. M. Fastenau, and W. K. Liu, "InGaAs/InP mesa DHBTs with simultaneously high f_t and f_{max} , and low $C_{cb} = I_c$ ratio", *IEEE Electron Device Letters*, vol. 25, pp. 250–252, May 2004.

[7-2] T. Hussain, Y. Royter, M. Montes, D. Hitko, M. Madhav, I. Milosavljevic, R. Rajavel, S. Thomas, M. Antcliffe, A. Arthur, Y. Boegeman, J. Li, and M. Sokolich, "First Demonstration of Sub-0.25 μm-width Emitter InP-DHBTs with >400 GHz f_T and >400 GHz f_{MAX}", in *IEEE IEDM Technical Digest*, 2004.

[7-3] J.-S. Rieh, B. Jagannathan, H. Chen, K. T. Schonenberg, D. Angell, A. Chinthakindi, J. Florkey, F. Golan, D. Greenberg, S.-J. Jeng, M. Khater, F. Pagette, C. Schnabel, P. Smith, A. Stricker, K. Vaed, R. Volant, D. Ahlgren, G. Freeman, K. K. Stein, and S. Subbanna, "SiGe HBTs with cut-off frequency of 350 GHz", in *IEDM Technical Digest*, 2002, pp. 771–774.

[7-4] A. Rylyakov, L. Klapproth, B. Jagannathan, and G. Freeman, "100 GHz dynamic frequency divider in SiGe bipolar technology", *Electronics Letters*, vol. 39, no. 2, pp. 217-218, Jan. 2003.

[7-5] M. Liang and M. E. Law, "Influence of a selectively ion-implanted collector on bipolar transistor electrical characteristics", *Solid State Electronics*, vol. 35, no. 7, pp. 1017-1018, July 1992.

[7-6] Y. Tuar and T. H. Ning, "Fundamentals of Modern VLSI Devices," Cambridge, UK: Cambridge University Press, 1998, pp. 351-413.

[7-7] Y. Miyamoto, J. M. M. Rios, A. G. Dentai, and S. Chandrasekhar, "Reduction of base-collector capacitance by undercutting the collector and subcollector in GaInAs/InP DHBTs", *IEEE Electron Device Letters*, vol. 17, no. 3, pp. 97-99, Mar. 1996.

[7-8] M. J.W. Rodwell, M. Urteaga, T. Mathew, D. Scott, D. Mensa, Q. Lee, J. Guthrie, Y. Betser, S. C.Martin, R. P. Smith, S. Jaganathan, S. Krishnan, S. I. Long, R. Pullela, B. Agarwal, U. Bhattacharya, L. Samoska, and M. Dahlstrom, "Submicrometer scaling of heterojunction bipolar transistors", *IEEE Transactions on Electron Devices*, vol. 48, pp. 2606–2624, Dec. 2001.

[7-9] J. C. Li, P. M. Asbeck, M. Sokolich, T. Hussain, D. Hitko, and C. Fields, "Effects of device design on the thermal properties of InP-based HBTs", in *ISCS Technical Digest*, 2003, pp.205-206.

[7-10] Y. Dong, Y. Wei, Z. Griffith, M. Urteaga, M. Dahlstrom, and M. J. W. Rodwell, "InP heterojunction bipolar transistor with a selectively implanted collector", *Solid State Electronics*, vol. 48, pp. 1699-1702, Oct. 2004.

[7-11] M. Moktari, C. Fields, R. D. Rajavel, M. Sokolich, J. F. Jensen, W. E. Stanchina, "100+ GHz Static Divide-by-2 Circuit in InP-DHBT Technology", *IEEE Journal of Solid-State Circuits*, vol. 38, no. 9, pp. 1540-1544, Sept. 2003.

[7-12] M. Sokolich, M. Y. Chen, D. H. Chow, Y. Royter, S. Thomas III, C. H. Fields, D. A. Hitko, B. Shi, M. Montes, S. S. Bui, Y. K. Boegeman, A. Arthur, J. Duvall, R. Martinez, T. Hussain, R. D. Rajavel, J. C. Li, K. Elliott, and J. D. Thompson, "InP HBT integrated circuit technology with selectively implanted subcollector and regrown device layers", in *Gallium Arsenide IC Symposium Technical Digest*, 2003, pp. 219–222.

[7-13] C.H. Fields, M. Sokolich, D. Chow, R. Rajavel, M. Chen, D. Hitko, Y. Royter, and S. Thomas III, "Advanced InP Heterojunction Bipolar Transistors with Implanted Subcollector", in *GaAs MANTECH Technical Digest*, 2004, pp. 333-336.

[7-14] M. Chen, M. Sokolich, D. Chow, B. Shi, R. Rajavel, S. Bui, Y. Royter, S. Thomas III, and C. Fields, "High Performance InP /InGaAs/InP DHBTs with Patterned Subcollector Fabricated by Elevated Temperature N+ Implant", in *Lester Eastman Conference Technical Digest*, 2004, pp. 5-8.

[7-15] M. Y. Chen, M. Sokolich, D. H. Chow, S. Bui, Y. Royter, D. Hitko, S. Thomas III, C. H. Fields, R. D. Rajavel, and B. Shi, "Patterned n Implant Into InP Substrate for HBT Subcollector", *IEEE Transactions on Electron Devices*, vol. 51, pp. 1736-1739, Oct. 2004.

[7-16] M. Sokolich, M. Y. Chen, R. D. Rajavel, D. H. Chow, Y. Royter, S. Thomas III, C. H. Fields, B. Shi, S. S. Bui, J. C. Li, D. A. Hitko, and K. R. Elliot, "InP HBT Integrated Technology, With Selectively Implanted Subcollector and Regrown Device Layers", *IEEE Journal of Solid-State Circuits*, vol. 39, pp.1615-1621, Oct. 2004.

[7-17] P. J. Zampardi, "A Study of New Base Pushout Effect in Modern Bipolar Transistors", *UCLA Ph.D. Thesis*, 1997.

8. INVESTIGATION INTO THE SCALABILITY OF SELECTIVELY IMPLANTED BURIED SUB-COLLECTOR (SIBS) FOR SUB-MICRON INP DHBTS

8.0 Abstract

Recent attempts to achieve 400 GHz or higher f_T and f_{MAX} with InP HBTs have resulted in aggressive scaling into the deep sub-micron regime. In order to alleviate some of the traditional mesa scaling rules, several groups have explored Selectively Implanted Buried Sub-collectors (SIBS) as a means to decouple the intrinsic collector and extrinsic collector design. This allows τ_C to be minimized without incurring a large total C_{BC} increase and hence a net improvement in f_T and f_{MAX} is achieved. This work represents the first investigation into the series resistance and capacitance characteristics of sub-micron width SIBS regions (as narrow as 350 nm) for InP DHBTs. Although the SIBS resistance is higher than that of epitaxially grown layers, the SIBS concept is able to provide good dopant activation and a significant decrease in C_{BC}. RF measurements are presented to clarify the impact of SIBS geometry variations, caused by both intentional device design and process variations, on f_T and f_{MAX}. Parasitic resistances and high background doping limit the f_T improvement, but the C_{BC} reduction is sufficient to demonstrate a 30% increase in f_{MAX}. Results indicate that further improvements in f_T and f_{MAX} using the SIBS concept will be possible.

8.1 Introduction

In order to break the 400 GHz barrier with InP HBTs, critical dimensions and spacings must be aggressively scaled into the deep sub-micron regime [8-1]. Several research groups have fabricated devices whose performance exceeds 400 GHz [8-2],[8-3],[8-4], but the demands on device fabrication are intensive. Device dimensions such as the emitter width, base contact width, and base contact to emitter spacing have been reduced to 250 nm or less. Such dimensions have been common in the silicon industry for a number of years, but are relatively new to the compound semiconductor industry. This exacerbates existing concerns about process control and device consistency in a market with limited IC volumes to date. The rapid progress of SiGe HBTs also threatens to displace InP-based HBTs in many markets [8-5],[8-6], and it is clear that InP-based HBT technologies can no longer rely solely on their device performance. Any device structure or processing method to alleviate the scaling demands on InP HBTs and improve both process control and performance is critical to future technology insertions.

A fundamental difference between InP and SiGe HBTs is the extensive use of ion implantation in the latter. Due to the electron mobility, saturation velocity, and bandgap engineering advantages of compound semiconductors, InP HBTs have not been forced to widely adopt ion implantation as a means to improve device performance. The challenges of implantation damage and materials re-growth have also slowed its introduction into the compound semiconductor industry. As a result, InP DHBTs have traditionally used a mesa device structure where the intrinsic and extrinsic collectors share the same thicknesses and doping profile. This forces a trade-off between the total

base-collector capacitance, C_{BC}; collector transit time, τ_C; and breakdown. However, the Selective Implanted Collector (SIC) concept allows the intrinsic and extrinsic collector design to be the decoupled. Such a device structure has been used for decades in the silicon industry [8-7],[8-8]. A similar concept for InP DHBTs, called the Selectively Implanted Buried Sub-collector (SIBS), has been reported recently by several research groups [8-9],[8-10].

In order to better understand the SIBS concept as applied to InP DHBTs, this work represents the first investigation into the scalability of the SIBS concept to geometries as small as 350 nm in sub-micron InP DHBTs. Using a series of base-collector diodes with different implant widths, the evolution of C_{BC} and the collector resistance, R_C, has been observed. The sensitivity of device performance to implant geometry (length, width, and mis-alignment) was also investigated with a series of DHBTs with an emitter area, A_E, of 0.35x3 μm^2. Analysis of the measured series resistances show that the conductivity of the SIBS region is not yet comparable to that of epitaxially grown layers, but capacitance measurements show the SIBS concept does succeed in lowering the total C_{BC}. Capacitance measurements are also used to determine the vertical doping profile and dopant activation near the re-growth interface and SIBS boundaries. Measurements show modest f_T values for the various SIBS geometries investigated, which are limited by parasitic resistances and high background doping. However, significant improvements in f_{MAX} are achieved by reducing the SIBS length. Continued development is required to reduce parasitic resistances and optimize the implanted doping profile to reap the full benefit of SIBS.

8.2 Device Fabrication

In order to investigate the geometric scalability of the SIBS region as well as the SIBS geometry impact on the HBT electrical characteristics, two different samples were used. The first sample, designated as *Sample A*, has a comprehensive set of base-collector diodes with which to investigate the series resistance, junction capacitance, and breakdown properties of SIBS. The second sample, designated as *Sample B*, has a comprehensive set of HBTs with various SIBS widths, lengths, and misalignments with which to investigate the DC and RF characteristics of HBTs using SIBS technology. Although the fundamental process is identical to the one used to fabricate *Sample A* [8-10], several differences do exist and are discussed below.

Molecular Beam Epitaxy (MBE) is used to grow a thicker 330 nm n+ InP/InGaAs sub-collector for *Sample B*, compared to the 200 nm n+ InP/InGaAs sub-collector for *Sample A*. Both *Sample A* and *Sample B* have a 200 nm Not Intentionally Doped (NID) InP collector region where the SIBS region is formed. After the implant mask is deposited and patterned, an identical 2.5×10^{14} cm^{-2} dose of Si+ ions at 120 keV is implanted into *Sample A* and *Sample B*, but the implant is carried out at an elevated temperature of 300 °C for *Sample B* and 200 ˚C for *Sample A*. After the damage recovery anneals, MBE was used to grow a 130 nm n- InP collector and grade; 35 nm p+ InGaAs base with compositional grade; 90 nm n/n+ InP emitter; and 75 nm n+ InGaAs/InAs emitter cap on *Sample B*. Compared to *Sample A*, the re-grown collector is 20 nm longer and the total emitter stack was thinned by 90 nm. Device fabrication for both *Sample A* and *Sample B* were consistent with common methods used in a triple mesa process,

except *Sample B* utilized Electron Beam Lithography (EBL) to produce smaller device geometries as described in [8-2]. Additional information on the material growth, ion implantation, and device fabrication are discussed in [8-11],[8-12],[8-13],[8-14].

8.3 Base-Collector Diode I-V Measurements

By comparing the series resistance, current drive, and junction capacitance, the electrical properties and ultimate scalability of sub-micron SIBS geometries can be assessed. First, the current-voltage (I-V) characteristics of a series of base-collector diodes with various SIBS geometries were measured using a HP4155B semiconductor parameter analyzer and DC needle probes. The access resistances associated with the cabling, probe, and probe contact were determined by using an on-wafer short structure and subtracted from the raw measurement data. The conventional diode equation is modified to include the diode series resistance (R_S),

$$I_B = I_S \exp\{-\frac{q}{nkT}(V_B - I_B R_S)\} \tag{8-1}$$

where I_B is the base current; I_S is the saturation current; V_B is the base voltage; and n is the ideality factor. The first order derivative with respect to the applied voltage (V_D),

$$\left[\frac{dI_B}{dV_B}\right]^{-1} = \frac{nkT}{qI_B} + R_S \tag{8-2}$$

is used to determine R_S from measurement. For the majority of the SIBS diodes, V_B is forward biased from 0.0 V to 1.0 V while the collector voltage (V_C) is grounded, and R_S is determined by taking the value of dI_B/dV_B at or near V_B = 1.0 V. Figure 8-1 shows the measured R_S versus the inverse drawn SIBS width (W_{SIBS}) for a fixed drawn SIBS length

(L_{SIBS}) of 3.45 μm and a total base-collector area (A_{BC}) of 6.5 μm^2. The definition of W_{SIBS} is shown in the Figure 8-1 inset, and L_{SIBS} extends into the page and can be seen in the Figure 8-12 inset. Using linear regression, the W_{SIBS} dependent and independent portions of R_S, labeled as dR_S/dW_{SIBS}^{-1} and R_{S0}, respectively, can be determined.

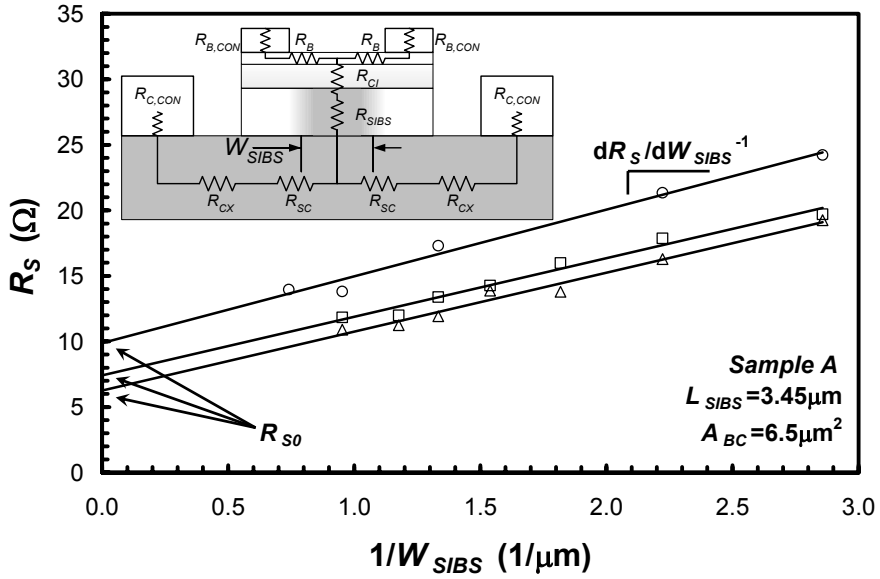

Figure 8-1: Base-Collector diode series resistances (R_S) plotted against the inverse drawn SIBS width (1/W_{SIBS}) for three die on *Sample A*.

The Figure 8-1 inset shows a schematic cross-section of the base-collector diode and the various resistance components of the measured R_S. These components are related to R_S through the following expression,

$$R_S = R_{B,CON} + R_B + R_{CI} + R_{SIBS} + R_{SC} + R_{CX} + R_{C,CON} \tag{8-3}$$

The base contact resistance and any resistance due to the 35 nm thick p+ base are represented by the components, $R_{B,CON}$ and R_B, respectively. R_{CI} represents the vertical resistance resulting from the un-depleted portion of the 110 nm thick re-grown InP collector, and R_{SIBS} is the vertical resistance resulting from the implanted region. Since the diode is forward biased, R_{CI} is expected to be non-zero and comparable to R_{SIBS} due to

the low $7x10^{16}$ cm^{-3} donor concentration. The resistance contributions due to the sub-collector under the implanted region and collector mesa (R_{SC}); the remaining sub-collector between the collector mesa and collector contact (R_{CX}); and collector contact ($R_{C,CON}$) are also visible in the inset. It is expected that R_{SIBS} and R_{SC} will be dependent on W_{SIBS}, and are aggregated into the fitted value, dR_S/dW_{SIBS}^{-1}. Subsequent resistance estimates and discussions on current scaling indicate that R_B and R_{CI} are more likely to be W_{SIBS} independent. R_B, R_{CI}, and the remaining W_{SIBS} independent terms, $R_{B,CON}$, $R_{C,CON}$, R_B, R_{CI}, and R_{CX}, are lumped into the y-intercept, R_{S0}.

Table 8-1: R_S scaling parameters for L_{SIBS} = 3.45 μm and A_{BC} = 6.5 μm² diodes on *Sample A*.

		Die Number				
Parameter	**Units**	**1**	**2**	**3**	**4**	**5**
dR_S/dW_{SIBS}^{-1}	Ω·μm	5.1	4.4	4.5	4.4	4.6
R_{S0}	Ω	9.9	7.8	6.2	7.5	7.3
r^2	---	0.984	0.965	0.977	0.983	0.981
L_{SIBS}	μm	3.45	3.45	3.45	3.45	3.45
t_{SIBS}	μm	0.20	0.20	0.20	0.20	0.20
$\mu_e \cdot n$	$(V \cdot s \cdot cm)^{-1}$	$7.1x10^{20}$	$8.2x10^{20}$	$8.1x10^{20}$	$8.3x10^{20}$	$8.0x10^{20}$

The fitted values of five different die on *Sample A* are shown in Table 8-1. Although the extrapolated R_{S0} values, ranging from 6.2 Ω to 9.9 Ω, appear to be high, they are reasonable given the small footprint of the base and collector contacts. Large-area TLMs and split-collector test structures indicate that the sub-collector has a nominal sheet resistance ($R_{SC,SH}$) of 12 Ω/□ and specific contact resistance (R_{CC}) of 20 Ω·μm². Large-area TLMs indicate that the nominal intrinsic base sheet resistance ($R_{B,SH}$) is 770 Ω/□ and the specific contact resistance (R_{BC}) is 30 Ω·μm². The absence of a R_{BC} value determined from a sub-micron, split-base structure may result in an over-estimation of R_{BC} and R_{S0}. For a base contact area ($A_{B,CON}$) of 4.2 μm² and sub-collector contact area ($A_{C,CON}$) of 7.0 μm², $R_{B,CON}$ and $R_{C,CON}$ would approximately be 7.1 Ω and 2.9 Ω,

respectively. From the as-drawn geometries, R_{CX} is expected to contribute less than 0.3 Ω. Assuming an electron mobility (μ_e) of 3600 $cm^2/V{\cdot}s$ [8-15] for a uniform $7x10^{16}$ cm^{-3} electron concentration (n) in the 110 nm thick re-grown InP collector, R_{CI} would contribute no more than 4.2 Ω. The vertical resistance through the p+ InGaAs base is not expected to contribute significantly to R_{S0}. These estimated resistance values are summarized in Table 8-2 and result in a total estimated R_{S0} of 10 Ω to 15 Ω.

Table 8-2: Estimated values of R_{S0} resistance components and dR_S/dW_{SIBS}^{-1} for L_{SIBS} = 3.45 μm and A_{BC} = 6.5 μm^2 on *Sample A* and L_{SIBS} = 3.00 μm and A_{BC} = 5.4 μm^2 on *Sample B*.

R_S Component	Units	*Sample A*	*Sample B*
$R_{B,CON}$	Ω	7.1	7.6
R_B	Ω	<1	<1
R_{CI}	Ω	<4.2	<7.9
dR_{SC}/dW_{SIBS}^{-1}	Ω·μm	≤1	≤1
R_{CX}	Ω	<0.3	1.4
$R_{C,CON}$	Ω	2.9	5.1

In order to extract R_{SIBS} from dR_S/dW_{SIBS}^{-1}, the R_{SC} component must first be removed. The general form of R_{SC},

$$R_{SC} = \frac{1}{3}R_{SC,SH}\left(\frac{W_{SIBS}}{4L_{SIBS}}\right) + R_{SC,SH}\left(\frac{W_{BC}-W_{SIBS}}{4L_{SIBS}}\right) = R_{SC,SH}\left(\frac{W_{BC}}{4L_{SIBS}}\right) - \frac{2}{3}R_{SC,SH}\left(\frac{W_{SIBS}}{4L_{SIBS}}\right) \tag{8-4}$$

where the first term is the resistance component directly under the SIBS region and the second term is the resistance component not under the SIBS region. The contribution of Equation (8-4) to dR_S/dW_{SIBS}^{-1} is

$$\frac{dR_{SC}}{dW_{SIBS}^{-1}} = \frac{2}{3}R_{SC,SH}\left(\frac{W_{SIBS}^2}{4L_{SIBS}}\right) \tag{8-5}$$

The quantity, W_{BC}, represents the width of the entire base-collector diode. This expression assumes current injection from the un-implanted region into the sub-collector

is negligible compared to the current injected from the SIBS region. For a $R_{SC,SH}$ = 12 Ω/□ and L_{SIBS} = 3.45 μm, dR_{SC}/dW_{SIBS}^{-1} is found to be only 1 Ω·μm when W_{SIBS} is at its maximum value of W_{BC} = 1.35 μm. From Table 8-1, all values of dR_S/dW_{SIBS}^{-1} exceed 4.4 Ω·μm; therefore, R_{SIBS} is significantly greater than R_{SC}. If the R_{SC} component is assumed to be zero, an upper bound to R_{SIBS} can be determined. Table 8-1 shows the minimum $\mu_e \cdot n$ product for the SIBS region, but the measurement does not permit μ_e and n to be determined independently. Values of the $\mu_e \cdot n$ product are lower than would be expected for complete implant activation and crystal recovery. For $\mu_e \cdot n = 8.3 \times 10^{20}$ $V^{-1} \cdot cm^{-1} \cdot s^{-1}$, the inferred value of μ_e would only be 166 $cm^2/V \cdot s$ for $n = 5 \times 10^{18}$ cm^{-3}, but if μ_e = 1400 $cm^2/V \cdot s$, the inferred value of n would only be 5.9×10^{17} cm^{-3}. If the $n = 5 \times 10^{18}$ cm^{-3} target is simultaneously achieved with a MBE quality μ_e = 1400 $cm^2/V \cdot s$, the $\mu_e \cdot n$ product would be 7×10^{21} $V^{-1} \cdot cm^{-1} \cdot s^{-1}$.

In addition to the examination of R_S, the total base-collector diode current also provides insight into the electrical properties of SIBS. Figure 8-2 shows the I-V characteristics of three diodes with no implanted region (W_{SIBS} = 0.00 μm); implanted region coincident with the emitter width (W_{SIBS} = 0.35μm); and an implanted region much wider than the emitter width (W_{SIBS} = 1.05μm). The total implanted area changes significantly in Figure 8-2 yet no change in the diode ideality factor, approximately 1.15 or 69 mV/dec, or the base current at low V_{BE} are observed. This indicates that the fundamental aspects of current transport across the base-collector junction are unchanged by the presence or size of the SIBS region. This is expected, since the re-grown InP n-collector should be uniform across implanted and not implanted regions, and it is the

subsequent re-grown layers that define the metallurgical base-collector junction. This supports the assumption made above that R_B and R_{CI} are independent of W_{SIBS}. Differences between the diodes shown in Figure 8-2 are only visible at high V_{BE}, where R_S plays a greater role in the I-V characteristics.

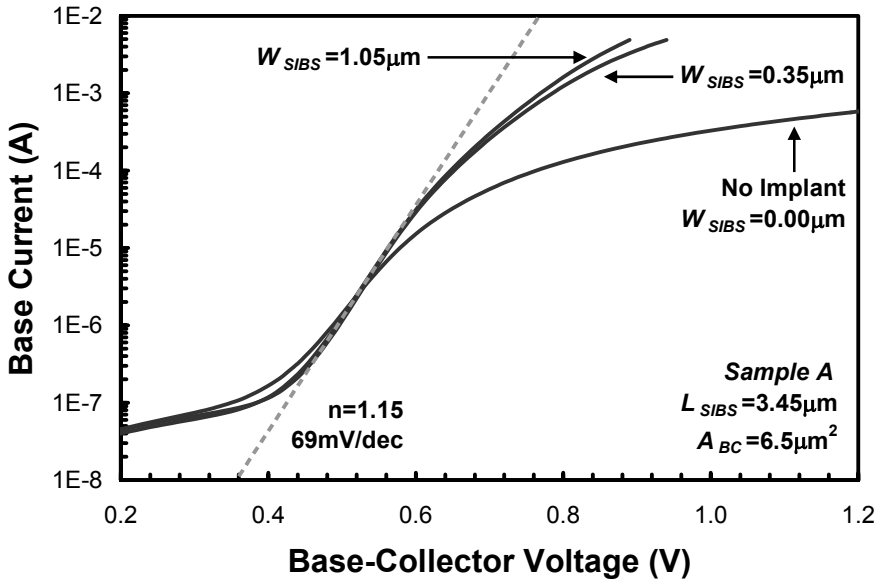

Figure 8-2 Forward I-V characteristics of base-collector diodes with drawn SIBS width, W_{SIBS}, of 0.00 µm, 0.35 µm, and 1.05 µm and a 69 mV/dec reference line on *Sample A*

Another means to observe the current scaling is shown in Figure 8-3, where I_B was sampled at four discrete V_{BC} values. A significant difference in I_B is observed between the no implant case, W_{SIBS} = 0.0 µm, and even the narrowest case, W_{SIBS} = 0.35 µm. Continued SIBS development will improve the conductivity of the SIBS region and exaggerate this difference, but it is unlikely to reduce the conductivity in the non-implanted regions. At larger values of W_{SIBS}, I_B is observed to reach an asymptotic limit, and this is a result of three factors. First, the expected change in R_S is only 1.0 Ω compared to the total measured R_S of 10 Ω to 20 Ω using a nominal dR_S/dW_{SIBS}^{-1} = 4.5 Ω·µm. Such a small change in R_S is within the observed measurement variation in Figure

8-1. Second, the exact dimensions of the base-collector diode are not known, but a finite quantity of mesa under-cut is determined from capacitance measurements and will be discussed in the following section. If W_{BC} is smaller than the drawn dimension of 1.35 μm, the measured R_S will reach an asymptotic value at a lower W_{SIBS}. Third, lateral diffusion of the implanted species during the damage recovery anneals will result in a deviation of the actual SIBS width from the as drawn dimension, W_{SIBS}. This also results in R_S reaching an asymptotic value at a lower W_{SIBS}.

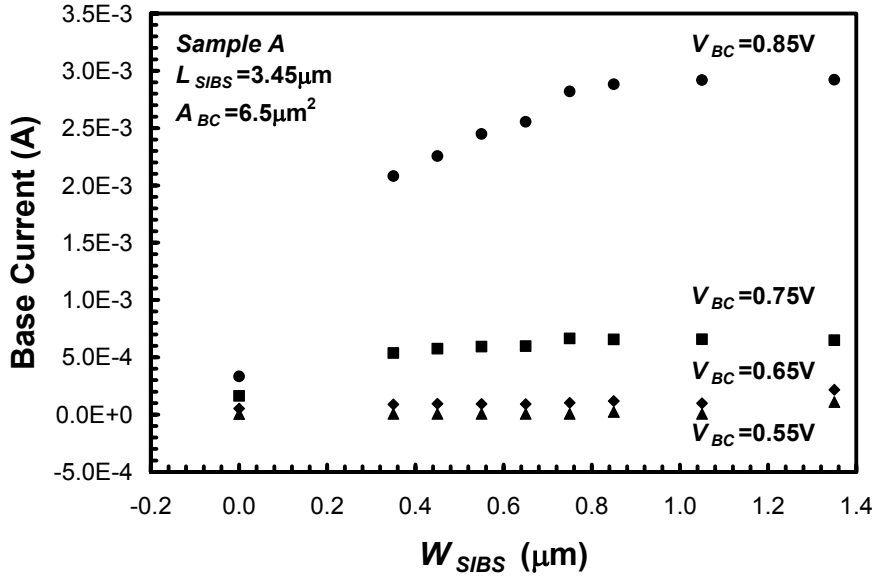

Figure 8-3: Scaling of base current with drawn SIBS width, W_{SIBS}, at selected V_{BC} values and a fixed L_{SIBS} = 3.45 μm on *Sample A*.

Additional confirmation of R_{SIBS} can be derived from *Sample B*, which has a series of HBTs whose base-collector junctions and SIBS areas are comparable to those on *Sample A*. The 200 nm NID InP collector, implant dose, implant energy, and hence, target doping profile and SIBS conductivity have remained identical between *Sample A* and *Sample B*. However, *Sample B* does have differences in the layer structure, device geometry, and fabrication that result in substantial differences in the electrical properties

of both the diodes and the HBTs themselves. Figure 8-4 shows the measured R_S for various *Sample B* diodes versus $1/W_{SIBS}$, similar to Figure 8-1. The *Sample B* R_{S0} value of 9.4 Ω is similar to that of *Sample A*, but the fitted dR_S/dW_{SIBS}^{-1} value of 3.3 Ω·μm is 25% smaller. TLM test structures indicate that $R_{B,SH}$ = 778 Ω/□; R_{BC} = 25 Ω·μm^2; $R_{SC,SH}$ = 17 Ω/□; and R_{CC} = 75 Ω·μm^2 for *Sample B* At the same time, the doping concentration in the 130 nm re-grown collector was decreased to 5x10^{16} cm^{-3} compared to the 7x10^{16} cm^{-3} in the 110 nm re-grown collector of *Sample A*. The more aggressive device geometries in *Sample B* have decreased $A_{B,CON}$ to 3.3 μm^2 and A_{BC} to 5.4 μm^2, resulting in an increase in $R_{B,CON}$ to 7.6 Ω and R_{CI} to 7.9 Ω (μ_e = 3800 cm^2/V·s from [8-15]). The increased $R_{SC,SH}$ and R_{CC} result in an increase of $R_{C,CON}$ to 5.1 Ω for $A_{C,CON}$ = 14.8 μm^2 and R_{CX} to 1.4 Ω. The estimated values for *Sample B* are summarized in Table 8-2 and suffer from the same over-estimate of $R_{B,CON}$ as *Sample A*. Despite the increase in $R_{SC,SH}$, the estimated value of dR_{SC}/dW_{SIBS}^{-1} remains approximately 1 Ω·μm due to reductions in maximum W_{SIBS} from 1.35 μm to 1.1 μm and L_{SIBS} from 3.45 μm to 3.00 μm. If the most pessimistic case is assumed (dR_{SC}/dW_{SIBS}^{-1} = 0 Ω·μm), then *Sample B* shows a significant decrease in normalized resistance, $L_{SIBS}\cdot dR_S/dW_{SIBS}^{-1}$, from a minimum value of 14.5 Ω·μm^2 on *Sample A* to 9.9 Ω·μm^2 on *Sample B*. This corresponds to a $\mu_e \cdot n$ product of 12.5x10^{20} V^{-1}·s^{-1}·cm^{-1} on *Sample B* compared to 8.3x10^{20} V^{-1}·s^{-1}·cm^{-1}, a 51% increase over the best case on *Sample A*. The increase in the $\mu_e \cdot n$ product is expected since the implant temperature was increased from 200 ˚C for *Sample A* to 300 ˚C for *Sample B*.

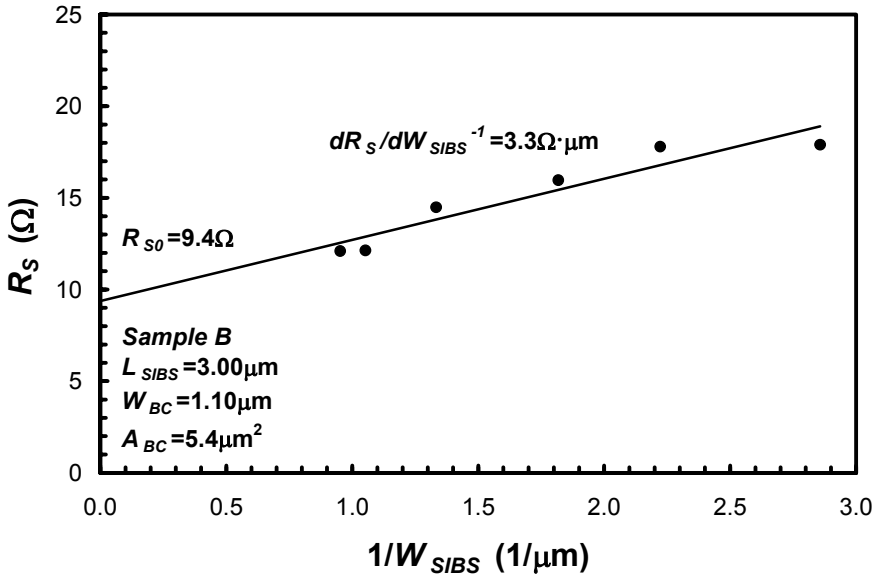

Figure 8-4: Base-Collector diode series resistances (R_S) plotted against the inverse drawn SIBS width ($1/W_{SIBS}$) for a single die on *Sample B*.

8.4 Base-Collector C-V Measurements

The capacitance was measured for the diode variations on *Sample A* using a HP8510C network analyzer and Ground-Signal-Ground (GSG) RF probes, which provided greater accuracy than a LCR meter for the small devices involved. After a Short-Open-Load-Thru (SOLT) off-wafer calibration, an on-wafer open is used to de-embed the pad parasitic capacitance from the *S*-parameter measurements. The base-collector capacitance (C_{BC}) is then determined from -Imag$\{Y_{12}\}/\omega$ at a test frequency of 5 GHz. Representative zero bias C_{BC} values and select C_{BC} versus V_{BC} curves for the *Sample A* diodes discussed in Section 8.3 have already been presented in [8-10]. Similar capacitance data are used here to examine the effective doping in the NID layer and capacitance partitioning within the collector.

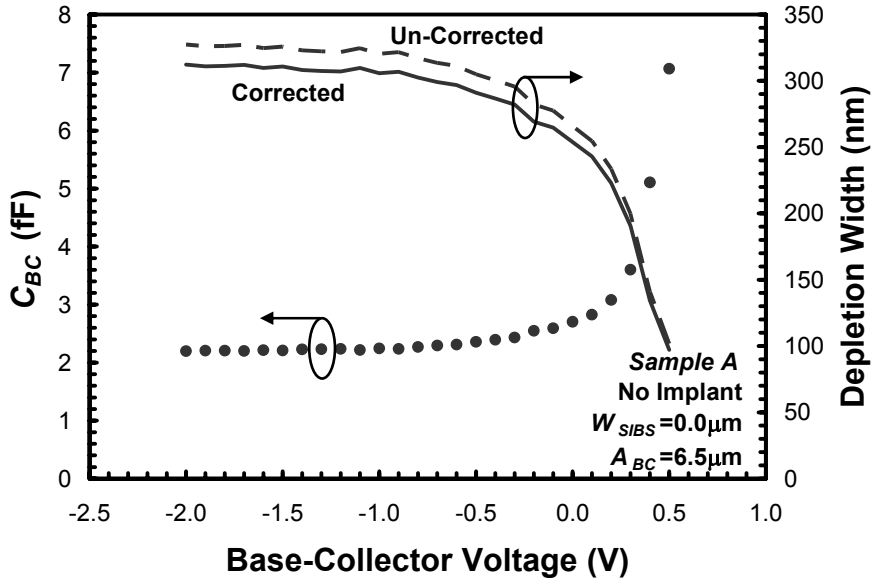

Figure 8-5: Representative C-V curve and the corresponding depletion width with and without A_{BC} correction of a non-implanted (W_{SIBS} = 0.0 μm) diode on *Sample A*.

Sample A contains several W_{SIBS} = 0.0 μm diodes, the non-implanted or NOI case, that allows the examination of the 200 nm NID InP collector. Figure 8-5 shows the representative C-V characteristics of a non-implanted diode, W_{SIBS} = 0.0 μm, and the calculated depletion region thickness, t_{Cd}. The effective base-collector junction area,

$$A_{BC,eff} = \frac{C_{BC,\min}}{\varepsilon_C / t_C} \tag{8-6}$$

where the collector is assumed to be a uniform layer of InP ($\varepsilon_c = 12.5\varepsilon_o$) and the nominal thickness (t_c = 310 nm), is found to be 6.2 μm^2. Better agreement between the diode's t_{Cd} and t_c is achieved with $A_{BC,eff}$ = 6.2 μm^2 instead of the drawn area of 6.5 μm^2. The deviation between A_{BC} and $A_{BC,eff}$ is small in this case and therefore, unlikely to impact the current scaling behavior discussed in Section 8.3. Both the corrected and un-corrected t_{Cd} values are shown in Figure 8-5. Although a C_{BC} reduction was shown in [8-

10] at zero bias, the diode still requires a reverse bias of approximately 1.0 V in order to fully deplete the 200 nm NID collector.

The effective doping profile can be obtained from the differential capacitance expression,

$$N_D = \frac{2}{q\varepsilon_s}\left[-\frac{d}{dV}\frac{1}{C^2}\right]^{-1} \tag{8-7}$$

which is described in [8-16]. If the 200 nm NID collector has the anticipated $1x10^{16}$ cm^{-3} or less background impurity concentration, then the diode should be fully depleted at zero-bias. Figure 8-6 shows the effective doping concentration, N_D, calculated from the measured C-V data, shown as the dotted curve, and from smoothed data, shown as the dashed curve. N_D is approximately $1x10^{16}$ cm^{-3} near the interface between the NID collector and the re-grown collector, but N_D increases to approximately $1x10^{17}$ cm^{-3} before reaching the n+ sub-collector. A tail of dopant is observed at the NID collector and sub-collector boundary indicating some quantity of dopant diffusion from the n+ sub-collector. The diffusion is likely to have occurred during the damage recovery anneals, but may not be detrimental to the overall device performance. Silicon BJTs have utilized and currently utilize the Gaussian and Gaussian-like doping profiles characteristic of ion implantation and diffusion in order to reduce the electric fields between low and high doped regions to improve breakdown characteristics while maintaining low series resistance [8-17],[8-18]. Smoothly varying doping profiles are possible with MOCVD growth techniques, but generally impose an impractical level of complexity for traditional MBE growth techniques. The observed doping diffusion tail in Figure 8-6 may be

viewed as a secondary benefit of SIBS, and continued development of SIBS may allow its optimization.

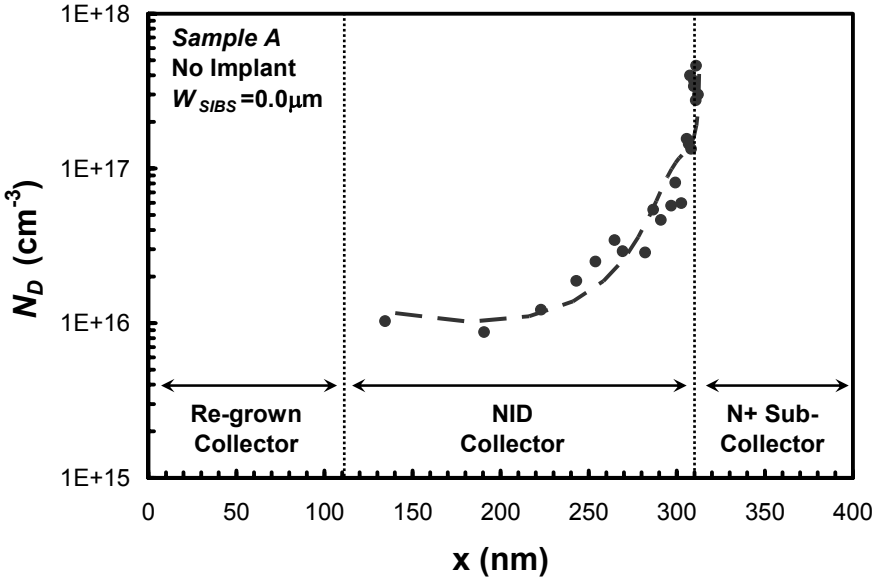

Figure 8-6: Effective doping, N_D, profile calculated from measured C-V data (dots) and smoothed C-V data (dash) for base-collector with no implant (W_{SIBS} = 0.0 μm) on *Sample A*.

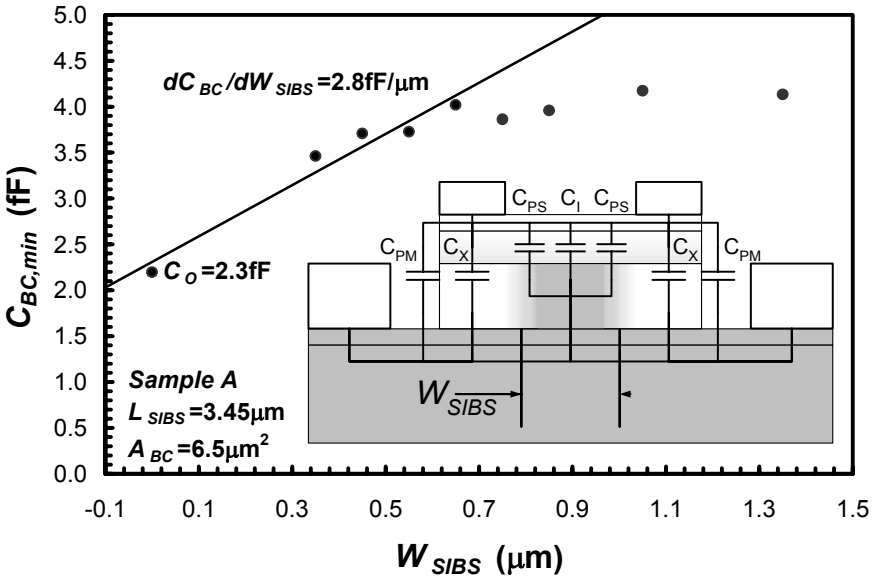

Figure 8-7: W_{SIBS} dependence of punch-through capacitance, $C_{BC,min}$, of base-collector diode with a drawn L_{SIBS} = 3.45 μm and A_{BC} = 6.5 μm^2 for *Sample A*.

The capacitance characteristics of the implanted regions can also be determined from a single diode. However, the $W_{SIBS} = W_{BC} = 1.35$ μm diode does have an implant that covers the entire width of the diode, but not the entire length. A series of diodes and a partitioning exercise similar to R_S will allow the determination of the SIBS region unit capacitance. Equation (8-8) shows the general form of the fully depleted junction capacitance, $C_{BC,min}$, and is pictorially represented in the Figure 8-7 inset.

$$C_{BC,\min} = C_I + C_X + C_{PS} + C_{PM} + C_{BP} \tag{8-8}$$

C_{PM} and C_{BP} are the W_{SIBS} independent terms that represent the perimeter capacitance of the base-collector mesa and the base contact area not in the Figure 8-7 inset cross-sectional plane, respectively. C_{PS} is the perimeter capacitance of the SIBS implant, but it is composed of both a W_{SIBS} dependent and independent component. Using the unit length capacitance, C_{PS}', the C_{PS} contribution to the W_{SIBS} dependent portion of $C_{BC,min}$ is included. C_I and C_X are the W_{SIBS} dependent capacitance components resulting from the thin, intrinsic collector above SIBS and the thick, extrinsic collector without SIBS, respectively. C_{PS}, C_{PM}, and C_{BP} are lumped into the fitted parameter, C_O, determined from extrapolation of $C_{BC,min}$ to $W_{SIBS} = 0.0$ μm. The W_{SIBS} dependent components, C_I, C_X, and C_{PS}, can be expressed as

$$C_{BC,\min}(W_{SIBS}) = \frac{\varepsilon_I}{t_I} L_{SIBS} W_{SIBS} + \frac{\varepsilon_X}{t_X} L_{SIBS}(W_{BC} - W_{SIBS}) + 2C_{PS}'(W_{SIBS} + L_{SIBS}) \tag{8-9}$$

and its first order derivative yields the fitted parameter,

$$\frac{dC_{BC}}{dW_{SIBS}} = \left(\frac{\varepsilon_I}{t_I} - \frac{\varepsilon_X}{t_X}\right) L_{SIBS} + 2C_{PS}' \tag{8-10}$$

Figure 8-7 shows the representative $C_{BC,min}$ values at V_{BC} = -2.0 V for various W_{SIBS} on *Sample A* and the fitted values of 2.3 fF and 2.8 fF/μm for C_O and dC_{BC}/dW_{SIBS}, respectively. The reader may note that the fitted values are determined only from $C_{BC,min}$ values where W_{SIBS} = 0.0 μm to W_{SIBS} = 0.65 μm. For W_{SIBS} > 0.65 μm, the measured $C_{BC,min}$ begins to converge to the W_{SIBS} = 1.35 μm value. This behavior is the result of lateral diffusion of the implanted species during processing, leading to a larger W_{SIBS} than the drawn value, and an electric blurring between C_I and C_X, leading to a breakdown of Equation (8-9). If there was a significant deviation of W_{BC} from its drawn value, then it too would contribute to this behavior.

With fitted values of C_O and dC_{BC}/dW_{SIBS}, the analysis of the various C_{BC} components can begin. Assuming an extrinsic collector thickness, t_X, of 310 nm and a uniform InP composition, $\varepsilon_X = 12.5\varepsilon_O$, the estimated value of C_{BP} is 0.7 fF, based on a unit capacitance of 0.36 fF/μm^2 and an as drawn area of 1.8 μm^2. An insufficient number of diodes with significantly different area to perimeters ratios exist on *Sample A* to experimentally determine a unit value of C_{PM}. However, a reasonable estimate can be calculated using a dielectric constant of $2.8\varepsilon_O$; base to collector contact spacing of 0.15 μm; and a sidewall height of 0.15 μm. Based on a unit capacitance of 25 aF/μm and a mesa periphery of 13 μm, the estimated value of C_{PM} is 0.3 fF. From the remaining 1.3 fF of C_O and 6.9 μm of W_{SIBS} independent SIBS periphery, C_{PS}' would be approximately 0.2 fF/μm, and this would result in a non-negligible 0.5 fF variation over the complete range of W_{SIBS}. Another interpretation of C_{PS}' is the additional capacitance introduced by lateral diffusion of the implant species during processing. If we assume an intrinsic

collector unit capacitance of 1.0 fF/μm^2, estimated from the nominal 110 nm thick InP re-grown collector, a C_{PS}'=0.2 fF/μm corresponds to 200 nm of lateral increase in W_{SIBS}. Since this estimate is derived from electrical data, it is likely to be greater than the lateral diffusion determined from metallurgical analysis. Using the fitted value of dC_{BC}/dW_{SIBS} and the derived value of C_{PS}', C_I has a calculated value of 1.1 fF/μm^2 from Equation (8-10), which corresponds to an intrinsic collector thickness, t_I, of 105 nm if a uniform InP composition, $\varepsilon_I = 12.5\varepsilon_O$, is assumed. This calculated value is in good agreement with the intended 110 nm thickness of the regrown InP collector and grade. The values of the various C_{BC} components determined in this analysis are summarized in Table 8-3.

Table 8-3: Summary of estimated and fitted values of C_{BC} scaling components for diodes with L_{SIBS} = 3.45 μm and A_{BC} = 6.5 μm^2 on *Sample A*.

C_{BC} Component	Units	Value
C_{PM}	fF	0.3
C_{PS}	fF	1.3
C_{PS}'	fF	0.2
C_{BP}	fF	0.7
ε_X	ε_O	12.5
t_X	nm	310
ε_S	ε_O	12.5
t_S	nm	105
C_O	fF	2.3
dC_{BC}/dW_{SIBS}	fF/μm	2.8

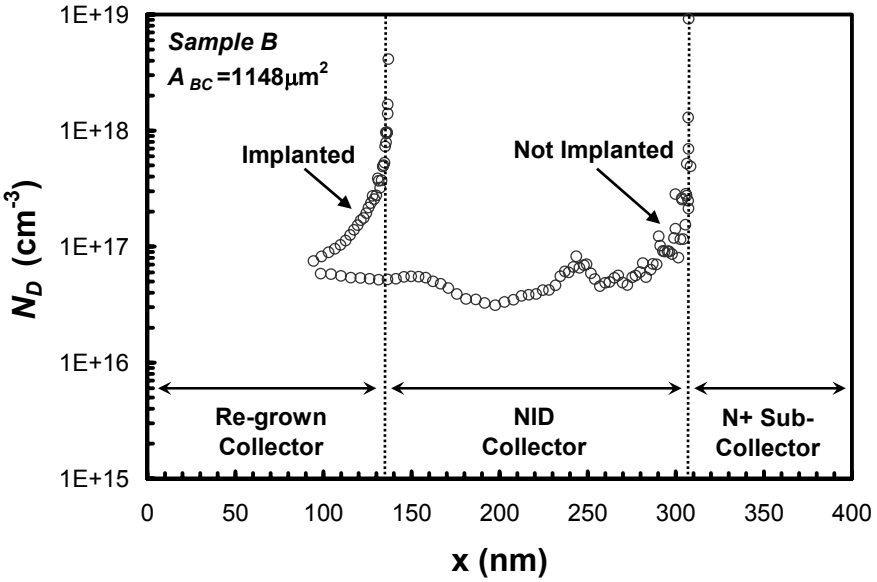

Figure 8-8: Effective doping profile calculated from C-V profiles for *Sample B* large area diodes with and without the SIBS implant.

In addition to small area devices, *Sample B* has large area diodes (A_{BC} = 1148 μm^2) with which to perform C-V profiling. Structures with such a large capacitance and overall size cannot be tested at high frequencies so a HP4284 C-V meter and a 1 MHz test frequency are used. Figure 8-8 shows the calculated N_D obtained from C-V profiles of an implanted and non-implanted (NOI) large area diode. Due to the absolute size of these diodes, the impact of any dimensional bias associated with fabrication can be neglected, and a more accurate representation of the N_D profile can be acquired. Assuming a uniform InP collector ($\varepsilon_X = \varepsilon_I = 12.5\varepsilon_O$), t_I and t_X are approximately 135 nm and 305 nm, respectively. The value of t_I is consistent with the specified thickness of 130 nm and the difference is within the error computational margin of this investigation, but t_X is only 305 nm, significantly lower than the specified thickness of 330 nm for *Sample B*. A dopant tail is observed for the NOI diode, but additional reverse bias quickly sweeps through the tail region to the abrupt transition into the n+ sub-collector. Since the

collector/sub-collector interface is visible in the data, the reduced t_X obtained from C-V profile is unlikely to be caused by up-diffusion from the sub-collector. In addition, a high background N_D = 5x10^{16} cm^{-3} is observed in the NID collector region, a value comparable to the re-grown collector. Compared to the N_D = 1x10^{16} cm^{-3} obtained on *Sample A*, this high background N_D will require the HBT to be biased at a higher V_{CE} in order to fully deplete the HBT collector and achieve maximum f_{MAX}. A similar dopant tail and abrupt transition is observed for the implanted diode, indicating that the activated donor concentration in the SIBS region meet or exceed the 5x10^{18} cm^{-3} target value. Therefore, any shortcomings in the $\mu_e \cdot n$ product reported in Section 8.3 are more likely to be caused by poor μ_e than low N_D.

8.5 DHBT Electrical Behavior

The DC and RF electrical characteristics of a representative DHBT with $A_E = A_{SIBS}$ = 0.35x6.0 μm^2 from *Sample B* is shown in Figure 8-9 and Figure 8-10. A peak DC current gain (β) of 112 and ideality factors of 1.6 and 1.4 for the base current (I_B) and collector current (I_C), respectively, are observed from the forward Gummel in Figure 8-9. The common-emitter I-V curves exhibit high turn-on resistance (R_{ON}) and a soft knee. From the measurement of Re$\{Y_{21}\}^{-1}$ versus I_C^{-1} at a test frequency of 2 GHz, the extracted emitter resistance (R_E) is only 4.3 Ω. Therefore, the bulk of R_{ON} is collector resistance (R_C) and is consistent with the estimated values discussed in Section 8.3. At the same time, the high background N_D discussed in Section 8.4 results in both a C_{BC} and R_C with a strong V_{CE} dependence. The V_{CE} dependent R_C manifests itself as quasi-saturation and the soft knee observed in Figure 8-9. Further evidence of the high background N_D can be

observed in the V_{CE} dependence of f_{MAX} in Figure 8-10. The high background doping in the NID layer also prevents f_T from improving at low V_{CE}, where the intrinsic collector material structure has been optimized.

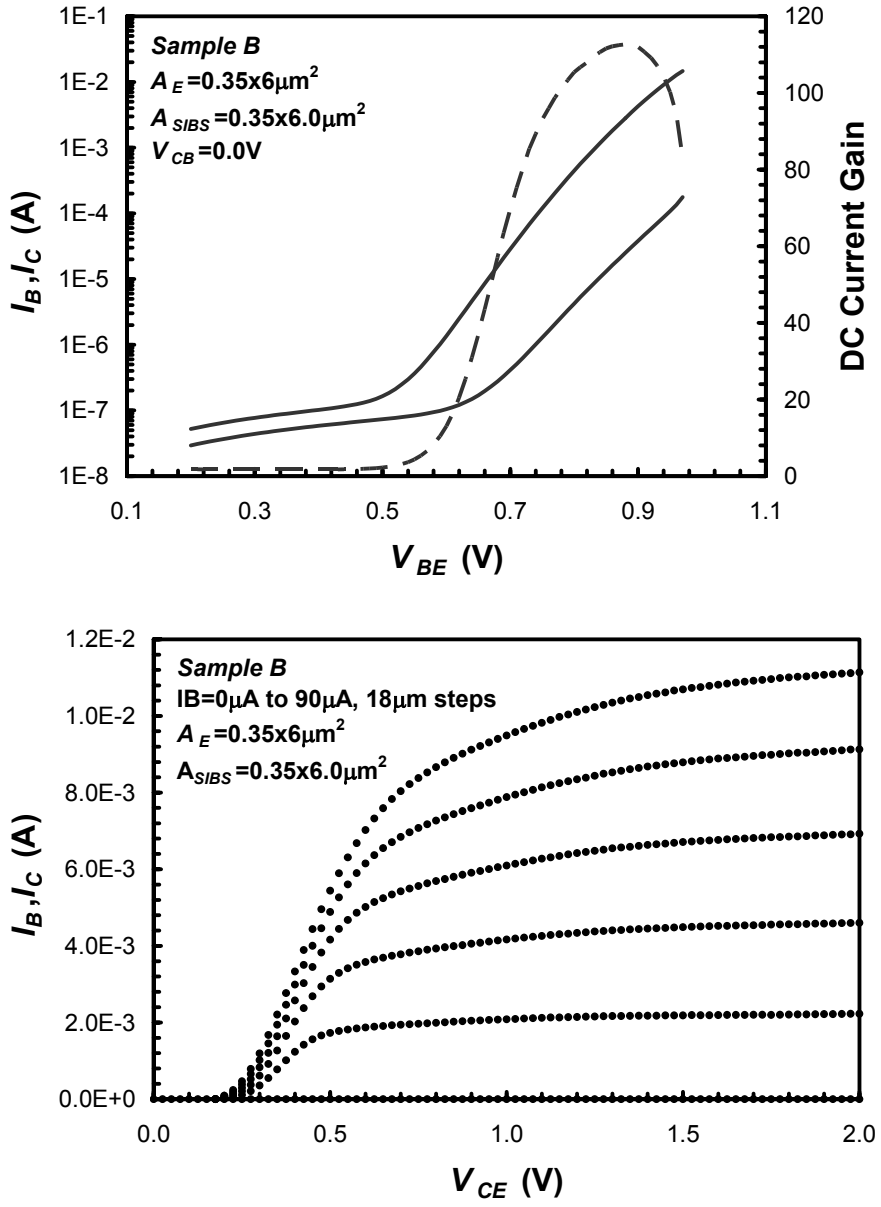

Figure 8-9: Forward Gummel (top) and common emitter I-V curves (bottom) of an A_E = 0.35x6 μm² DHBT on *Sample B* with an A_{SIBS} = 0.35x6 μm².

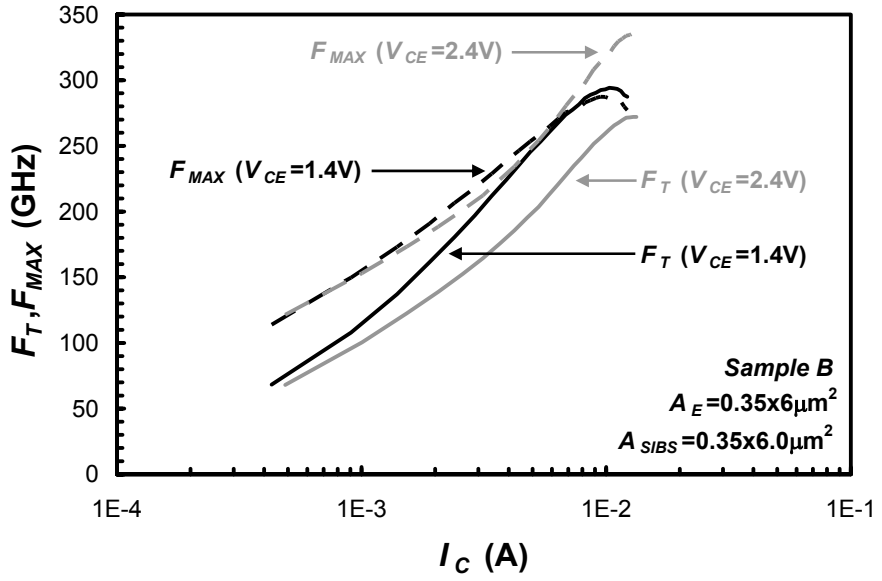

Figure 8-10: I_C dependence of f_T and f_{MAX} at two V_{CE} values, 1.4 V and 2.4 V, for an A_E = 0.35x6 μm^2 DHBT on *Sample B* with an A_{SIBS} = 0.35x6 μm^2.

8.6 Process Sensitivity

The insertion of SIBS introduces two additional parameters (W_{SIBS} and L_{SIBS}) with which to tune the device for a given circuit application. However, these parameters are subject to process variation, and it is important to quantify the sensitivity of device performance on these parameters. Using a fixed A_E = 0.35x3 μm^2 DHBT, the impact of W_{SIBS}, L_{SIBS}, and SIBS mis-alignment on the small signal performance (f_T and f_{MAX}) is presented. Figure 8-11 shows the dependence of maximum f_T and the corresponding I_C, but the high background N_D and high total R_C significantly impact the trend. The maximum f_T is determined by sweeping I_C to determine the peak f_T at a fixed V_{CE} and then V_{CE} from 1.4 V to 2.2 V in 0.2 V steps. If the NID collector were fully depleted at a V_{CE} = 1.6 V, the increasing C_{BC} with increasing W_{SIBS} would decrease f_T. However, it is the decreasing R_C with increasing W_{SIBS} that dominates the f_T trend. The increasing I_C at

maximum f_T with increasing W_{SIBS} is an indicator of collector current-crowding [8-19]. The benefits of SIBS can be observed in Figure 8-12 where the maximum f_T and f_{MAX} dependence on L_{SIBS} are shown. Maximum f_{MAX} is determined in the same manner as maximum f_T. With decreasing L_{SIBS}, f_T is relatively unchanged, but f_{MAX} increases significantly, reflecting the reduced C_{BC}. The changes in L_{SIBS} exceed any measure of lateral diffusion presented in Section 8.4 (approximately 0.2 μm), and the emitter undercut determined from the zero bias C_{BE} is no more than a 0.2 μm. Therefore, the reduction in L_{SIBS} can overcome more than just the process variation and enable true f_{MAX} improvement. Finally, a series of test structures where the SIBS region is intentionally offset from the emitter centerline is used to determine sensitivity to misalignment. Figure 8-13 defines the intentional offset in the inset and shows a less than 5% decrease in maximum f_T for a 100 nm intentional offset and approximately a 10% decrease for a 200 nm intentional offset. Perhaps a stronger indicator of the mis-alignment is the corresponding I_C at which maximum f_T occurs. Maintaining a mis-alignment of 100 nm or less is possible with existing optical lithography tools.

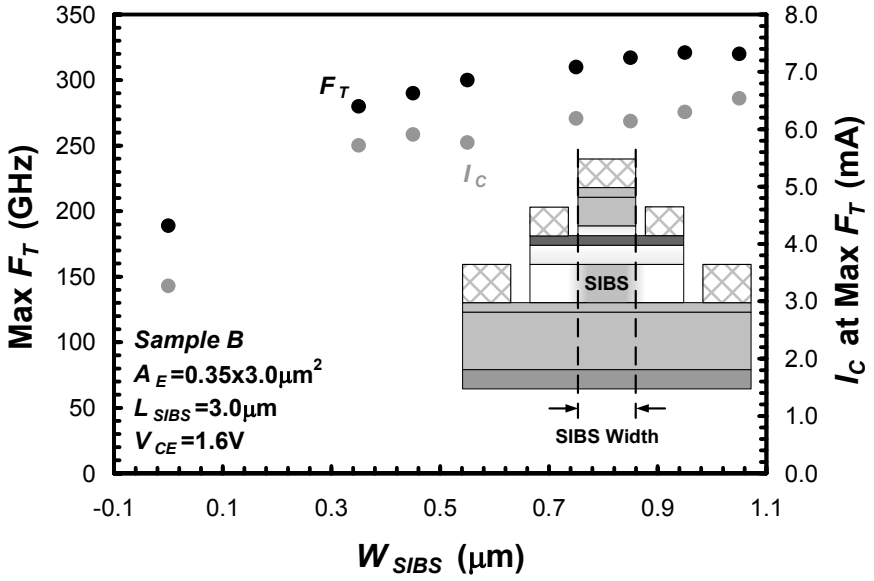

Figure 8-11: Maximum f_T and the I_C at maximum f_T dependence on W_{SIBS} for an A_E = 0.35x3 μm^2 DHBT, with a fixed L_{SIBS} = 3.0 μm and V_{CE} = 1.6 V on *Sample B*. The definition of W_{SIBS} is shown in the inset.

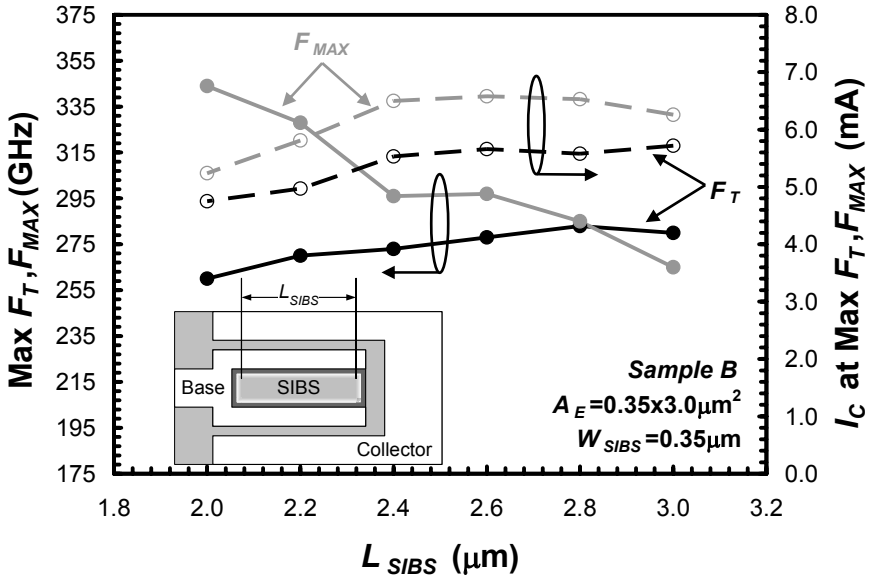

Figure 8-12: Maximum f_T (solid black), maximum f_{MAX} (solid gray), and their corresponding I_C at maximum f_T (dashed black) and maximum f_{MAX} (dashed gray) dependence on L_{SIBS} for an A_E = 0.35x3 μm^2 DHBT with a fixed W_{SIBS} = 0.35 μm on *Sample B*. The definition of L_{SIBS} is shown in the inset.

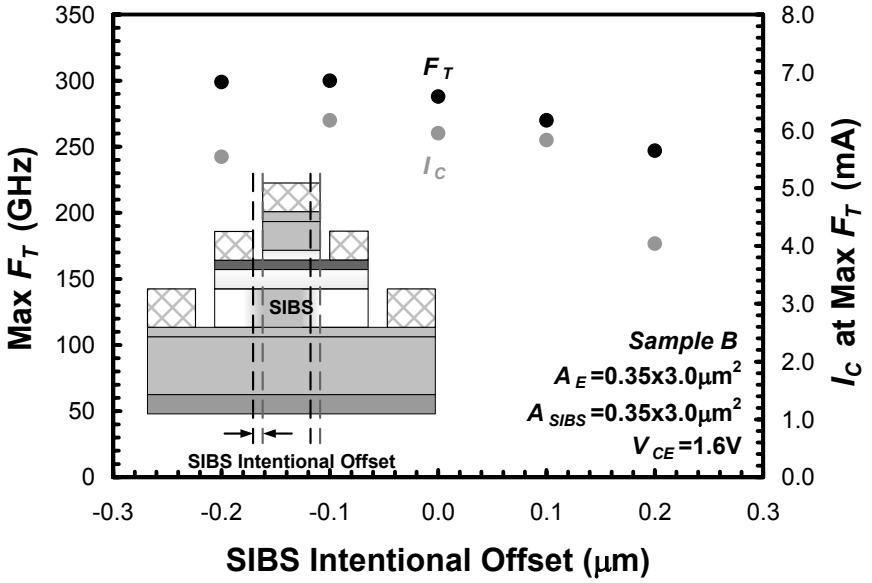

Figure 8-13: The sensitivity of f_T on the mis-alignment of the SIBS region to the emitter for an A_E = 0.35x3 μm² device with a fixed A_{SIBS} = 0.35x3 μm² and V_{CE} = 1.6 V on *Sample B*. The misalignment is achieved through a series of test structures where the implant is intentionally offset from the emitter (inset).

8.7 Summary

The scaling of the SIBS concept down to 350 nm has been investigated in InP DHBTs. Analysis of the base-collector diode series resistances enabled the determination of the SIBS resistance component and a best case $\mu_e \cdot n$ product of 12.5×10^{20} $V^{-1}s^{-1}cm^{-1}$. Additional development is required to improve the $\mu_e \cdot n$ product and NID collector background doping to ensure significant C_{BC} reduction at lower V_{CE}. RF measurements show f_T to have a weak dependence on W_{SIBS}, but this is limited by high background doping and parasitic resistances. The C_{BC} reduction offered by SIBS produces a 30% increase in f_{MAX} for reduced L_{SIBS}. Furthermore, a 100 nm mis-alignment between the SIBS region and emitter center line only reduces f_T by 5%. This investigation shows that

SIBS does require additional development, but is a practical means of improving device performance for InP DHBTs.

8.8 Acknowledgements

This chapter, in full, has been submitted for publication to the IEEE Transactions on Electron Devices. The contributions from the co-authors Yakov Royter, Tahir Hussain, Mary Y. Chen, Charles H. Fields, Rajesh D. Rajavel, Steven S. Bui, Binqiang Shi, Donald A. Hitko, David H. Chow, and Marko Sokolich of HRL Laboratories, L.L.C., and Peter M. Asbeck of UCSD are appreciated. The author of this dissertation was the primary investigator and primary author of this publication. This work was sponsored by the Defense Advanced Research Projects Agency (DARPA) through AFRL Contract F33615-02-1286 (TFAST).

8.9 References

[8-1] M. J.W. Rodwell, M. Urteaga, T. Mathew, D. Scott, D. Mensa, Q. Lee, J. Guthrie, Y. Betser, S. C.Martin, R. P. Smith, S. Jaganathan, S. Krishnan, S. I. Long, R. Pullela, B. Agarwal, U. Bhattacharya, L. Samoska, and M. Dahlstrom, "Submicrometer scaling of heterojunction bipolar transistors," *IEEE Transactions on Electron Devices*, vol. 48, pp. 2606–2624, Dec. 2001.

[8-2] T. Hussain, Y. Royter, D. Hitko, M. Montes, I. Milosavljevic, R. Rajavel, S. Thomas, M. Antcliffe, A. Arthur, Y. Boegeman, J. Li, and M. Sokolich, "First demonstration of sub-0.25 μm width emitter InP-DHBTs with >400 GHz f_t and >400 GHz f_{max}," in 2004 *IEEE IEDM Technical Digest*.

[8-3] Z. Griffith, M.J.W. Rodwell, Xiao-Ming Fang, D. Loubychev, Ying Wu; J.M. Fastenau, and A.W.K. Liu, "InGaAs/InP DHBTs with 120-nm collector having simultaneously high f_τ, $f_{max} \geq 450$ GHz", *IEEE Electron Device Letters*, vol. 26, no. 8, pp. 530-532, Aug. 2005.

[8-4] W. Hafez and M. Feng, "Lateral scaling of 0.25 μm InP/InGaAs SHBTs with InAs emitter cap", *Electronics Letters*, vol.40, no.18, 2 September 2004, pp.1151-1153.

[8-5] J.-S. Rieh et al., "SiGe HBTs with cut-off frequency of 350 GHz," in 2002 *IEEE IEDM Technical Digest*, pp. 771–774.

[8-6] A. Rylyakov, L. Klapproth, B. Jagannathan, and G. Freeman, "100 GHz dynamic frequency divider in SiGe bipolar technology," *Electron. Letters*, vol. 39, no. 2, pp. 217–218, Jan. 2003.

[8-7] H.N. Ghosh, K.G. Ashar, A.S. Oberai, and D. Dewitt, "Design and Development of an Ultralow-Capacitance, High Performance Pedastal Transistor", *IBM Journal of Research and Development*, vol. 15, pp. 436-441, 1971.

[8-8] M. Liang and M. E. Law, "Influence of a selectively ion-implanted collector on bipolar transistor electrical characteristics," *Solid State Electronics*, vol. 35, no. 7, pp. 1017-1018, July 1992.

[8-9] Y. Dong, Y. Wei, Z. Griffith, M. Urteaga, M. Dahlstrom, and M. J. W. Rodwell, "InP heterojunction bipolar transistor with a selectively implanted collector," *Solid State Electronics*, vol. 48, pp. 1699–1702, Oct. 2004.

[8-10] J.C. Li, M. Chen, D.A. Hitko, C.H. Fields, Binqiang Shi, R. Rajavel, P.M. Asbeck, and M. Sokolich, "A submicrometer 252 GHz f_T and 283 GHz f_{MAX} InP DHBT with reduced C_{BC} using selectively implanted buried subcollector (SIBS)", *IEEE Electron Device Letters*, vol.26, no.3, March 2005, pp.136-8.

[8-11] M. Sokolich, M. Y. Chen, R. D. Rajavel, D. H. Chow, Y. Royter, S. Thomas III, C. H. Fields, B. Shi, S. S. Bui, J. C. Li, D. A. Hitko, and K. R. Elliot, "InP HBT Integrated Technology, With Selectively Implanted Subcollector and Regrown Device Layers," *IEEE Journal of Solid-State Circuits*, vol. 39, pp.1615-1621, Oct. 2004.

[8-12] M. Chen, M. Sokolich, D. Chow, B. Shi, R. Rajavel, S. Bui, Y. Royter, S. Thomas III, and C. Fields, "High Performance InP /InGaAs/InP DHBTs with Patterned Subcollector Fabricated by Elevated Temperature N+ Implant," in 2004 *Lester Eastman Conference Technical Digest*, pp. 5-8.

[8-13] M.Y. Chen, M. Sokolich, D.H. Chow, S. Bui, Y. Royter, D. Hitko, S. Thomas III, C.H. Fields, R.D. Rajavel, and B. Shi, "Patterned n+ Implant Into InP Substrate for HBT Subcollector", *IEEE Transactions on Electron Devices*, vol. 51, no. 10, Oct 2004.

[8-14] C.H. Fields, M. Sokolich, D. Chow, R. Rajavel, M. Chen, D. Hitko, Y. Royter, and S. Thomas III, "Advanced InP Heterojunction Bipolar Transistors with Implanted Subcollector," in *GaAs MANTECH Technical Digest*, 2004, pp. 333-336.

[8-15] D.A. Anderson, N. Apsley, P. Davies, and P.L. Giles, "Compensation in heavily doped n-type InP and GaAs", *Journal of Applied Physics*, vol. 58, no. 8, pp. 3059-3067, Oct 1985.

[8-16] S.M. Sze, "Physics of Semiconductor Devices", Second Edition, J. Wiley and Sons, New York, 1981.

[8-17] C. Hu, "Optimum doping profile for minimum ohmic resistance and high-breakdown voltage", *IEEE Transactions on Electron Devices*, vol. 26, no. 3, pp. 243-244, Mar 1979.

[8-18] Y.C. Kao, "The Design of high-voltage high-power silicon junction rectifiers", *IEEE Electron Device Letters*, vol. 17, no. 9, pp. 657-660, Sept 1970.

[8-19] P. J. Zampardi, "A Study of New Base Pushout Effect in Modern Bipolar Transistors," UCLA Ph.D. Thesis, 1997.

9. CONCLUSIONS AND FUTURE WORK

9.0 Summary of Dissertation

The rapid growth of the internet and other communication systems has prompted strong interest and development of InP-based HBTs. The versatility of the InP material system has allowed it to be used for both high power and high data rate applications, but the emphasis has been on superior performance over cost and integration. The newest generations of devices with f_T and f_{MAX} values on the order of 400 GHz have aggressively scaled device geometries deep into the sub-micron regime, but A_E and V_{CE} scaling have not kept pace with the increase in J_C. The resulting rise in P_{diss} represents a potential barrier to the utilization of existing devices in ICs and the further improvement of device performance. This dissertation explored the performance limits through experiment and simulation and presented a set of guidelines for the design of 400 GHz InP-based HBTs.

DC and RF measurements presented in this dissertation illustrate the extra-ordinary performance of existing 400 GHz InP-based HBTs. Repetition of these measurements at reduced T_{amb} show an f_T increase of 8-10% can be obtained with a 75 ˚C decrease in T_{amb}. Estimates of the T_j rise over T_{amb} equal or more typically exceed 75 ˚C indicating that there is considerable room for f_T improvement if self-heating is minimized or eliminated. Parameter extraction and delay time analysis indicate that the average electron velocity exceeds $6x10^7$ cm/s, and it is the increase in the electron velocity and the corresponding decrease in the transit times that accounts for most of the f_T improvement at reduced T_{amb}.

In order to minimize R_{TH} and hence T_j, a 3-D thermal model was developed and calibrated to existing InP-based HBTs. The impact of various materials, device geometries, and thermal management strategies was investigated. It was found that the temperature gradients that exist within the device can be significantly greater than those outside the device. This indicates that thermal management within the device, through proper material selection and device layout, is important to achieving higher device performance while maintaining reliability. The 3-D thermal simulations also allow the power and environmental dependencies of R_{TH} to be explored, resulting in a more accurate R_{TH} value for compact models. In contrast, current experimental methods to determine R_{TH} employ probe pads that can significantly reduce the measured R_{TH}. They also use bias conditions lower than the actual circuit operating conditions, which also affects the measurement accuracy. The impact of the probe pad's heat sinking properties and vertical heat conduction through the emitter is illustrated with additional R_{TH} measurements, and a new method to thermally de-embed pads is presented.

A complete 2-D electro-thermal model was developed to investigate the role of non-equilibrium carrier transport on device performance. In order to simulate the degenerately doped materials used in the fabrication of 400 GHz InP-based HBTs, several modifications are required to properly model bandgap narrowing, the Mott transition, and band non-parabolicity. This ensures that the band diagram and free electron populations are correct prior to any carrier transport calculations. The calibration of several additional parameters, including the energy dependent energy relaxation times and Peltier coefficients, is discussed. Even with these modifications and calibrations, liberal use of the Boltzmann form of the Einstein relation results in

fundamental limitations with the DESSIS implementation of the Hydrodynamic transport equations. The anisotropic mobility model was used to overcome some of these limitations, and reasonable agreement between measured and simulated electrical characteristics was obtained.

As an alternative to aggressive scaling, an adaptation of the SIC structure used by silicon BJTs for InP-based HBTs is presented. The new device structure, designated as SIBS, allows for the simultaneous reduction of C_{BC} and τ_C without resorting to mesa undercutting or other planarization schemes that would otherwise increase R_{TH}. Analysis of the I-V and C-V data of base-collector diodes indicates that reasonable dopant activation is achieved, but the overall conductivity remains lower than similarly doped MBE grown layers due to the degraded electron mobility in the SIBS region. Even with this limitation, HBTs with reduced C_{BC} and f_T and f_{MAX} values on the order of 300 GHz are demonstrated. An extensive set of HBTs with various SIBS lengths and widths were used to explore the impact of SIBS on HBT electrical characteristics. The f_T improvement resulting from width scaling was modest, being limited by the high resistivity of the SIBS region. However, the performance improvement from reduced SIBS length resulted in a 30% increase in f_{MAX}. With further development, SIBS will have the potential to improve device performance beyond traditional mesa HBTs and offer additional flexibility to circuit designers.

The experiments and simulations presented in this dissertation have provided insight into the performance limitations and device design of 400 GHz InP-based HBTs. The greater importance of self-heating on device performance; the means to mitigate self-

heating; and alternatives to brute force scaling are all critical for the continued advancement of InP-based HBTs towards breaking the 500 GHz barrier.

9.1 Opportunities for Future Work

The measurements and simulations presented in this dissertation have revealed several limits to the current understanding of InP-based HBTs. However, these limits present others with challenges and opportunities to advance the understanding of semiconductor device physics. The following suggestions are presented to scientists and engineers as topics requiring additional investigation.

9.1.1 Thermal conductivity of degenerately doped semiconductors

Throughout Chapters 3 and 4, the interfacial thermal resistance (R_{THI}) is assumed to be insignificant and is neglected in all 3-D thermal simulations. Appendix B justifies this assumption by invoking the Weidemann-Franz law and attributing the negligible R_{THI} to a change in the heat transport mechanism in InGaAs compounds. It is proposed that the high free-electron population and high electron mobility in degenerately doped InGaAs compounds results in a significant electronic component to the thermal conductivity. Experimental evidence of a semiconductor-like material exhibiting a strong electronic component has already been observed in InAs and InSb films. Given the extensive use of InGaAs compounds in InP-based HBTs and opto-electronic devices, a series of experiments to quantify the doping dependence of the thermal conductivity would be of great benefit to the scientific community. If heavily doped InGaAs films can serve as a heat bridge between semiconductors and metals, the elimination of low thermal

conductivity InGaAs layers from electron devices cannot be absolute. In addition, any potential for thermal conductivity improvement through degenerate doping will provide additional guidelines for HBT design.

9.1.2 Carrier transport in III-V materials

The simulations presented in Chapter 6 highlight several deficiencies in commercial device simulators. As InP-based HBTs and other electron devices intentionally utilize velocity overshoot and ballistic transport to improve device performance, it is imperative that simulation tools adequately model these physical phenomena. Additional Monte Carlo simulations should be used to verify the validity of carrier velocity and temperature profiles throughout a set of well understood electron devices. Furthermore, the simulation of these phenomena requires numerous material specific parameters that are not yet available for the bulk of compound semiconductors. Numerous researchers should be commended for the existing collections of semiconductor material parameters, but there still remains much work to establish a complete set of parameters for Hydrodynamic transport simulations.

9.1.3 SIBS circuits

The introduction of the Selectively Implanted Buried Sub-collector (SIBS) technology to InP-based HBTs presents a milestone for compound semiconductor devices. For the first time, the ability to produce multiple devices with significantly different electrical characteristics exists for a III-V HBT technology. It provides a competitive feature to the Selective Implanted Collector (SIC) used in Silicon BJTs and

SiGe HBTs, but more importantly, SIBS allows circuit designers greater flexibility and performance. Although SIBS requires additional optimization before commercialization, the opportunity to explore the potential of circuits utilizing SIBS is at hand. A preliminary investigation of SIBS devices for broadband amplifiers has been presented in [9-1]. However, the use of HBTs with various SIBS geometries to maximize IC performance has yet to be explored.

9.2 References

[9-1] J.C. Li, M.Y. Chen, Z. Lao, R.D. Rajavel, S. Thomas III, S.S. Bui, B. Shi, K.V. Guinn, J.R. Duvall, D.A. Hitko, D.H. Chow, and M. Sokolich, "200 GHz InP DHBT Technology using Selectively Implanted Buried Sub-Collector (SIBS) for Broadband Amplifers", *IEEE Electron Device Letters*, In Review.

A. LIST OF SYMBOLS

Symbol	Units	Description
a_0	Å	Bohr radius
a_B^*	Å	Effective Bohr radius
E_A	eV	Acceptor binding energy
E_{A0}	eV	Acceptor binding energy at low doping
E_C	eV	Conduction band energy
E_D	eV	Donor binding energy
E_{D0}	eV	Donor binding energy at low doping
E_F	eV	Fermi-level
E_G	eV	Bandgap energy
f_{MAX}	Hz	Frequency of unity small signal power gain
f_T	Hz	Frequency of unity small signal current gain
J_C	A/μm^2	Collector current density
m^*	kg	Carrier effective mass
m_e^*	kg	Electron effective mass
m_{e0}^*	kg	Electron effective mass at conduction band minima
m_{ec}^*	kg	Conductivity effective mass for electrons
m_{hc}^*	kg	Conductivity effective mass for holes
n	cm^{-3}	Free-electron concentration
N_A	cm^{-3}	Acceptor concentration
N_A^-	cm^{-3}	Ionized acceptor concentration
N_{Acrit}	cm^{-3}	Critical acceptor concentration at which E_A=0
N_C	cm^{-3}	Conduction band density of states at band minima
N_D	cm^{-3}	Donor concentration
N_D^+	cm^{-3}	Ionized donor concentration
N_{Dcrit}	cm^{-3}	Critical donor concentration at which E_D=0
N_i	cm^{-3}	Total impurity concentration
N_V	cm^{-3}	Valence band density of states at band minima
p	cm^{-3}	Free-hole concentration
V_{BE}	V	Base-emitter voltage
V_{CE}	V	Collector-emitter voltage
v_{sat}	cm/s	Steady state carrier saturation velocity
ΔE_G	eV	Bandgap narrowing
α_A	eV·cm	Mott transition parameter for acceptors
α_D	eV·cm	Mott transition parameter for donors
ε_r	---	Relative dielectric constant
μ_e	cm^2/V·s	Low field electron mobility

B. THERMAL INTERFACE RESISTANCE

The 3-D thermal simulations presented in this dissertation do not consider the presence of an interfacial thermal resistance (R_{THI}) at any of the metal-semiconductor interfaces. At first, this assumption may appear to be invalid due to the different heat conduction methods present in metals and semiconductors. The heat transport through phonon scattering in a semiconductor would have to undergo a transition to the heat transport through the free electron gas of the contact metal. If contacts were made to InP or GaAs, materials where the electron mobility (μ_e) is relatively low and the thermal conductivity (K) is relatively high, R_{THI} could be significant. However, the contact metals are placed on degenerately doped InGaAs compounds or other narrow bandgap materials. These materials have relatively high μ_e compared to InP or GaAs, but have relatively low K. At the present time, experimental data on low doped films (N_A,N_D < 1x10^{17} cm^{-3}) are only available. One could expect K to increase with increasing doping concentration, but such a hypothesis assumes that phonons serve as the dominant means of heat conduction. Experimental data presented in [B-1] indicate that electrons, not phonons, are the dominant mechanism of heat conduction in high μ_e materials, such as InAs and InSb. It is important to note that experimental methods to determine K cannot identify the dominant mechanism of heat transport, but the dependence on doping concentration and temperature can be used to infer the dominant mechanism.

To assess the relative importance of electrons as a mechanism of heat transport, the Weidemann-Franz law,

$$\frac{\mathrm{K}}{q\mu n} = LT \tag{B-1}$$

is used to generate the following table. The quantities in Equation (B-1) are the carrier mobility, μ; carrier concentration, n; temperature, T; and the Lorenz factor, L. In the case of $In_{0.53}Ga_{0.47}As$ where K = 0.05 W/cm·K and μ_e = 3000 $cm^2/V{\cdot}s$, and a constant L = $2.45x10^{-8}$ $W{\cdot}\Omega/K^2$, $n > 1.5x10^{19}$ cm^{-3} would be adequate to match the measured K. For the devices measured and simulated in this dissertation, the contact metals are deposited on InGaAs layers which are all doped at $2x10^{19}$ cm^{-3} or higher. Therefore, the original assumption of negligible R_{THI} is reasonable.

Table B-2: Calculated thermal conductvitiy (K) values using the Weidemann-Franz law and a Lorentz factor of $2.45x10^{-8}$ $W{\cdot}\Omega/K^2$.

K (W/cmK)		μ (cm^2/Vs)							
		500	1000	1500	2000	2500	3000	3500	4000
n (cm^{-3})	1.00E+18	0.001	0.001	0.002	0.002	0.003	0.004	0.004	0.005
	2.00E+18	0.001	0.002	0.004	0.005	0.006	0.007	0.008	0.009
	3.00E+18	0.002	0.004	0.005	0.007	0.009	0.011	0.012	0.014
	4.00E+18	0.002	0.005	0.007	0.009	0.012	0.014	0.016	0.019
	5.00E+18	0.003	0.006	0.009	0.012	0.015	0.018	0.021	0.024
	6.00E+18	0.004	0.007	0.011	0.014	0.018	0.021	0.025	0.028
	7.00E+18	0.004	0.008	0.012	0.016	0.021	0.025	0.029	0.033
	8.00E+18	0.005	0.009	0.014	0.019	0.024	0.028	0.033	0.038
	9.00E+18	0.005	0.011	0.016	0.021	0.026	0.032	0.037	0.042
	1.00E+19	0.006	0.012	0.018	0.024	0.029	0.035	0.041	0.047
	2.00E+19	0.012	0.024	0.035	0.047	0.059	0.071	0.082	0.094
	3.00E+19	0.018	0.035	0.053	0.071	0.088	0.106	0.123	0.141
	4.00E+19	0.024	0.047	0.071	0.094	0.118	0.141	0.165	0.188
	5.00E+19	0.029	0.059	0.088	0.118	0.147	0.176	0.206	0.235
	6.00E+19	0.035	0.071	0.106	0.141	0.176	0.212	0.247	0.282
	7.00E+19	0.041	0.082	0.123	0.165	0.206	0.247	0.288	0.329
	8.00E+19	0.047	0.094	0.141	0.188	0.235	0.282	0.329	0.376
	9.00E+19	0.053	0.106	0.159	0.212	0.265	0.318	0.370	0.423
	1.00E+20	0.059	0.118	0.176	0.235	0.294	0.353	0.412	0.470

[B-1] E.F. Schubert, "Doping in III-V Semiconductors", Cambridge University Press, 1993.

C. PHYSICAL MODELING OF DEGENERATELY DOPED COMPOUND SEMICONDUCTORS FOR HIGH-PERFORMANCE HBT DESIGN

C.0 Abstract

Numerous research groups are currently developing high-performance InP HBTs with f_T and f_{MAX} greater than 400 GHz. However, the heavily degenerate doping concentrations used in these devices present new challenges to numerical device simulation. This work focuses on three physical phenomena in InP and $In_{0.53}Ga_{0.47}As$ and their implementation in physics based device simulators. First, the use of the parabolic band approximation yields a constant DOS effective mass, but this results in an erroneously deep Fermi-level under heavily degenerate donor concentrations. An empirical model is presented and shown to have good agreement with previously published simulations and experimental data. Second, bandgap narrowing parameters and a table based model are used as a more generic model for compound semiconductors. Third, calculated parameters to address the Mott Transition are used to obtain the proper free-carrier concentrations throughout the HBT. The improper calibration or neglect of these three physical phenomena is shown to alter HBT band profiles at thermal equilibrium by as much as 400 meV; the turn-on voltage by approximately 50 mV; and the f_T dependence on J_C by approximately 18%.

C.1 Introduction

In order to break the 400 GHz barrier with Heterojunction Bipolar Transistors (HBTs), device engineers have chosen to take advantage of the high electron mobility (μ_e), low electron effective mass (m_e*), and high electron saturation velocities (v_{sat}) of InP and InGaAs alloys [C-1],[C-2][C-3]. Consequently, the donor concentrations (N_D) of both the emitter and collector have been increased substantially, to greater than 10^{19} cm^{-3}, while maintaining μ_e equal to or greater than 1000 $cm^2/V{\cdot}s$. This has resulted in a net improvement in epitaxial layer conductivity, but raises a set of new device concerns. The doping dependent mobility has been explored previously [C-4],[C-5],[C-6],[C-7] and is routinely included in device simulation. However, the low m_e* prized by device designers also results in a lower conduction band density of states (N_C), approximately 10^{17} cm^{-3} to $5x10^{18}$ cm^{-3} for InP and InGaAs alloys, at the band edge. Therefore, the majority of n-type epitaxial layers are degenerately doped, and the breakdown of the parabolic band approximation and the impact of high doping effects must be considered. To construct an accurate physical model of the HBT for physics based simulation, it is imperative to properly determine the band structure and Fermi-level (E_F) of these degenerately doped layers. In particular, the dependence of N_C, bandgap-narrowing (BGN), and impurity ionization (N_D^+ and N_A^-) in the presence of degenerate levels of both donors and acceptors are critical quantities to be determined. If the appropriate values of N_C are not used or BGN is ignored, the resulting band diagram will be distorted and electron transport across critical potential barriers such as an abrupt InP/$In_{0.53}Ga_{0.47}As$ base-emitter junction cannot be accurately simulated. The change in the free-carrier

population resulting from the Mott Transition will distort the band diagram and also alter the carrier mobility and total resistance of various epitaxial layers. Consideration of all of these physical phenomena is required to determine the peak performance as well as bias dependence of high-performance HBTs.

State-of-the-art numerical simulators frequently generalize their implementation of semiconductor physics in order to improve simulation performance, but these generalizations can lead to erroneous results for high-performance HBTs. This work presents the necessary physical corrections and parameters necessary for the proper determination of the above quantities in degenerately doped compound semiconductors. It further emphasizes solutions that would allow a numerical simulator to operate over a wide range of impurity concentrations so that region specific modifications would be unnecessary. The physics based device simulator, DESSIS, from Synopsys is used to illustrate the effectiveness of these corrections, and some of the material presented is expected to be specific to DESSIS. However, the models discussed here should be applicable to other commercial simulators such as ATLAS from Silvaco and Medici from Synopsys.

C.2 Simulation Environment

One-dimensional structures composed of uniform compositions of InP and $In_{0.53}Ga_{0.47}As$ were constructed in DESSIS version 10 to demonstrate the impact of these physical phenomena on numerical simulation. The bulk structures are step graded with a shallow donor or acceptor to show the gradual onset of high doping effects. A representative structure is shown in Figure C-1, and such a structure easily allows the

dependence of carrier concentration, Fermi-level position, and energy bandgap on dopant concentration to be monitored. In all cases, incomplete ionization of impurities is used and a uniform lattice temperature of 300 K is maintained. Although the one-dimensional structures are simulated under thermal equilibrium conditions only, the physical models and material parameters are identical to the two-dimensional devices simulated under bias.

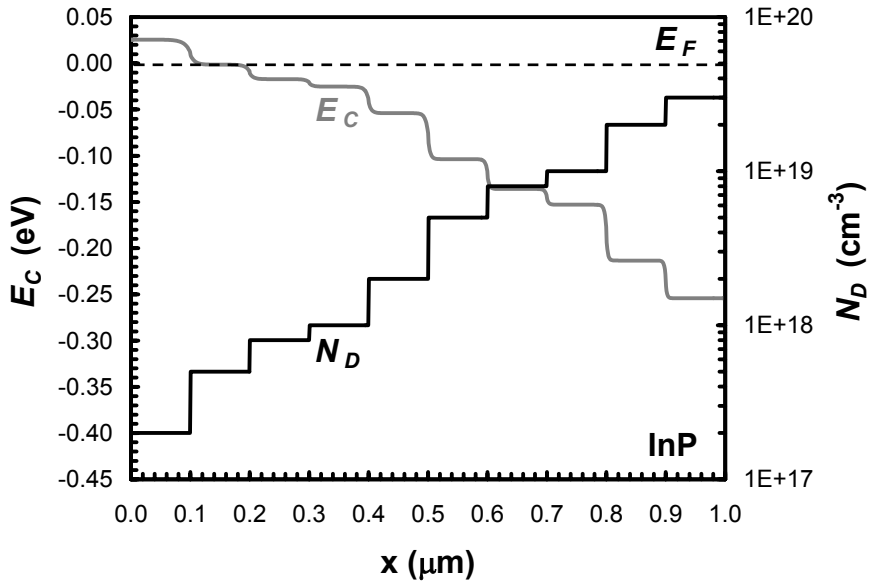

Figure C-1: Representative 1D structure in InP with stepped donor concentrations, N_D, used to monitor the effects of degenerate doping on the conduction band energy, E_C, with respect to the Fermi level, E_F.

The impact of high doping effects on the simulated electrical characteristics of an HBT, not bulk samples of InP and $In_{0.53}Ga_{0.47}As$, is more relevant to current device researchers. A two-dimensional Heterojunction Bipolar Transistor (HBT) structure, with a 250 nm wide emitter and fabricated using a triple mesa process, is used to simulate DC and small signal RF characteristics. The symmetry about the HBT longitudinal axis is utilized so that only half the device is required for simulation and computational demands

are reduced. Figure C-2 shows the physical structure of the half HBT, and Table C-1 shows the epitaxial layer structure of the generic HBT. Beyond the area shown in Figure C-2, the semi-insulating InP substrate extends 50 μm in both the x and y directions to ensure accurate representation of self-heating. Additional physical phenomena, which have been discussed in the literature extensively, are activated in the simulation in order to ensure a reasonably accurate representation of a high-performance HBT. For electron majority carrier characteristics, these include the use of hydrodynamic transport equations to account for velocity overshoot; the transferred electron mobility model to account for high field velocity saturation and negative differential mobility; and the Arora mobility model to account for doping dependent mobility under low field conditions. Carrier concentration dependent minority carrier lifetimes; Shockley-Read-Hall bulk recombination, surface recombination, Auger recombination, and radiative recombination are used to ensure the proper modeling of electron transport through the base. All of these physical phenomena, including the three under investigation in this work, are modeled simultaneously. The following sections will discuss a particular phenomenon and de-activate only one model at a time to illustrate its effects.

Table C-1: HBT layer structure used for model comparisons.

Description	Material	Thickness (nm)	Doping (cm^{-3})
Emitter Cap	$In_{0.53}Ga_{0.47}As$	75	$3x10^{19}$
	InP	40	$3x10^{19}$
Emitter	InP	50	$5x10^{17}$
Base	$In_{0.53}Ga_{0.47}As$	35	$3x10^{19}$
BC Grade	$In_{0.53}Ga_{0.47}As$ to InP	25	$4x10^{16}$
Collector	InP	95	$4x10^{16}$
Sub-Collector	InP	25	$2x10^{19}$
	$In_{0.53}Ga_{0.47}As$	25	$2x10^{19}$
	InP	280	$2x10^{19}$
Substrate	InP	50000	Semi-Insulating

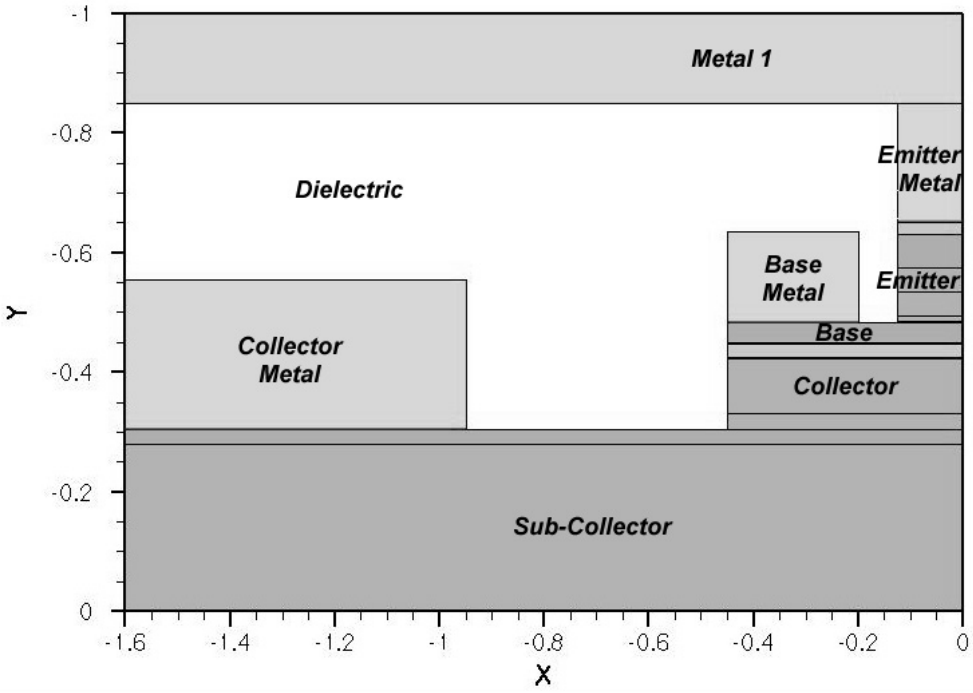

Figure C-2: Two-dimensional structure of the generic HBT used for device simulation. All dimensions are shown in microns.

The impact of high doping effects on E_F is evident from the thermal equilibrium band diagram, but this does not illustrate the effect on HBT performance. To represent the impact on steady state carrier transport, a forward Gummel curve, where the collector-emitter voltage (V_{CE}) is maintained at a constant 1.25 V and the base-emitter voltage (V_{BE}) is swept from 0.0 to 1.0 V, is simulated using the HBT described previously. Using the mixed mode capability in DESSIS, the small signal characteristics can be calculated simultaneously with the forward Gummel. Only a single frequency point at 50 GHz is simulated to minimize computation time, and the resulting Y-parameters are used to calculate the frequency of unity current gain (f_T).

C.3 DOS and effective mass

Physics based numerical device simulators like DESSIS use a simple parabolic band model, limiting the effective mass (m^*) and *DOS* to constant quantities despite N_D and N_A. However, this is only an accurate approximation near the conduction band minima or valence band maxima. If N_D and N_A become comparable or greater than the conduction band density of states (N_C) and valence band density of states (N_V), respectively, this has the effect of erroneously driving E_F deeper into the conduction or valence band. Regardless of the user's choice between Fermi-Dirac or Maxwell-Boltzman carrier statistics, the default condition of the numerical simulator cannot properly account for the non-idealities present in degenerately doped semiconductors.

Before continuing further, several generalizations can be made concerning the compound semiconductors of interest. The first generalization is that the majority of compound semiconductors used to produce electron devices are direct bandgap e.g. GaAs, $Al_{1-x}Ga_xAs$, $In_{1-x}Ga_xP$, InP, InAs, and $In_{1-x}Ga_xAs$. These semiconductors have cubic symmetry, so an isotropic, scalar value of m_e^* can be used to represent electron transport and N_C. The second generalization is that N_V is much greater than N_C in these semiconductors due to band degeneracy and curvature. Band degeneracy results from the light hole, heavy hole, and potentially the split-off band, all with a band maxima at $k = 0$, that can be occupied. The large values of the heavy hole mass (m_{hh}^*) compared to m_e^* and the light hole mass (m_{lh}^*) is indicative of the band curvature and the relative contribution of each band to N_V. The choice of N_A in the base is determined by a trade-off between the minority carrier lifetime which favors decreased N_A and lateral

conductivity which favors increased N_A. The optimal result is an N_A comparable or slightly higher than N_V. In contrast, some regions of the emitter and collector can have an N_D two orders of magnitude greater than N_C. Therefore, n++ regions in the emitter and collector can produce larger errors without the appropriate corrections. This work will focus on InP and $In_{0.53}Ga_{0.47}As$, but the corrections can be extended to other direct bandgap semiconductors.

To determine E_F within a semiconductor region, DESSIS uses an internally computed value of the *DOS* effective mass to determine N_C and N_V. DESSIS has two general formulations for the *DOS* and m^*. The first is designed for indirect bandgap semiconductors and in particular silicon (see Section 5.3.1.1 of [C-8]), and the second is designed for direct bandgap semiconductors (see Section 5.3.1.2 of [C-8]). However, neither formulation accounts for the non-parabolicity of the primary band when the carrier energy is significantly higher than the band minima. Metzger et al [C-9] have reported the free-electron density dependence of the electron effective mass (m_e^*). In this work, a third order polynomial,

$$m_e^*/m_o = A \cdot N_D^3 + B \cdot N_D^2 + C \cdot N_D + D \tag{C-1}$$

implemented with the DESSIS Physical Model Interface (PMI) and fitted to the experimental and theoretical data compiled in [C-9], is used to empirically represent the non-parabolicity of the gamma valley. It is important to note that limitations in the DESSIS device simulator prevent the use of the free-electron concentration (n) or the ionized donor concentration (N_D^+) within the PMI; therefore, the total donor concentration (N_D) is used. The use of N_D instead of n is expected to produce some error in regions with both high N_D and a space charge region, but should be adequate for quasi-

neutral regions. Figure C-3 shows a comparison between published data and the proposed empirical model (Poly3x). Table C-2 summarizes the parameters used for the two materials of interest. A second order polynomial was inadequate to represent this phenomena due to the rapid increase in m_e* with increasing N_D. However, the uneven nature of a third order polynomial almost guarantees the generation of zero or negative values of m* at sufficiently low N_D, which would be the source of convergence errors. To prevent this situation from occurring and since the variation in m_e* is only significant for high N_D, the model limits the value of m_e* to a lower limit, m_{e0}*, specified by the user, presumably m_e* at the band edge.

Table C-2: Summary of Poly3x model parameters.

Model Parameter	InP	$In_{0.53}Ga_{0.47}As$
A	6.0073×10^{-3}	7.8474×10^{-3}
B	-3.1698×10^{-2}	-4.1373×10^{-1}
C	5.5799	7.2756
D	-32.684	-42.629
m_{e0}*	0.080	0.041

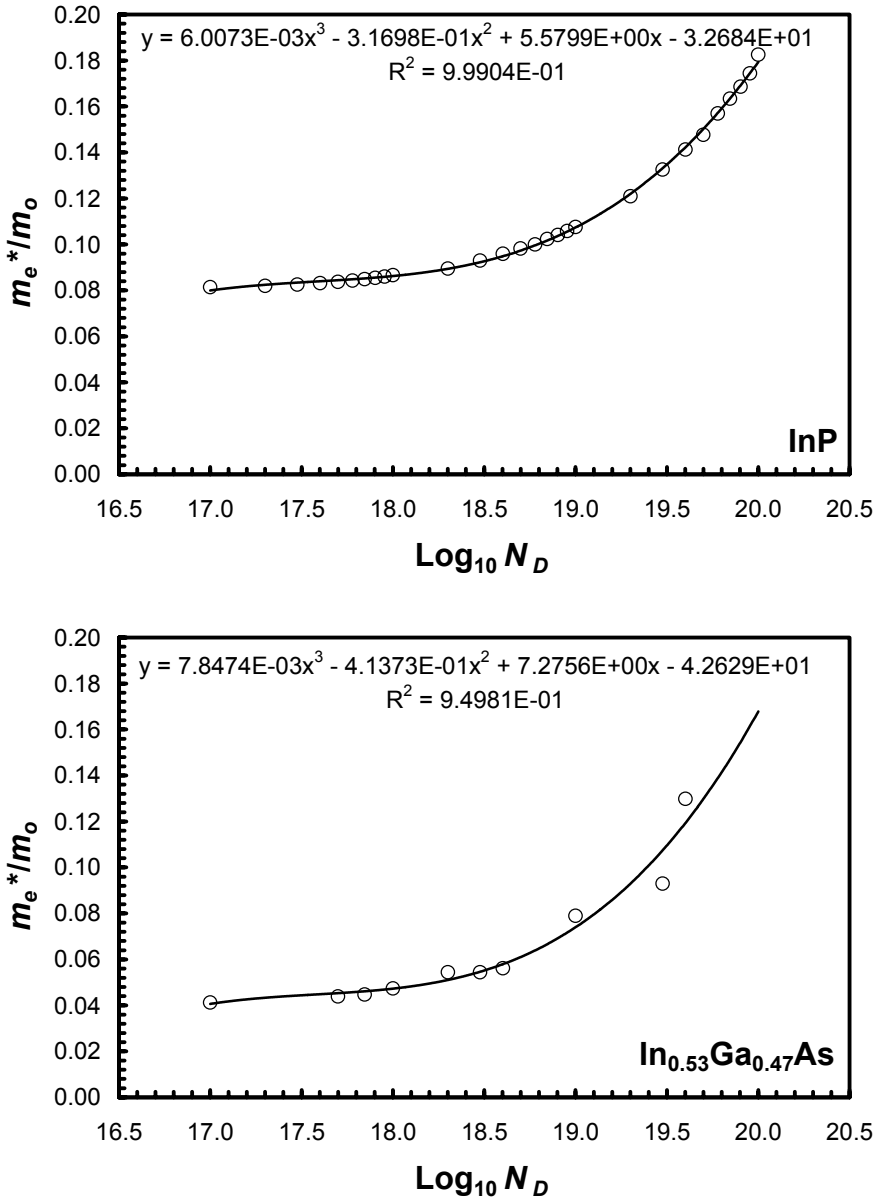

Figure C-3: Comparison of the normalized electron effective mass (m_e^*/m_o) dependence on donor concentration, N_D, from Metzger et al [C-9] (dot) and the Poly3x model (solid) for InP (top) and $In_{0.53}Ga_{0.47}As$ (bottom).

Without this correction to the effective mass, N_C would be constant even at high N_D levels and the resulting Fermi-level would be erroneously deep in the conduction band. Figure C-4 shows the shift in conduction band energy (E_C) with respect to E_F in InP and $In_{0.53}Ga_{0.47}As$ at various N_D for a constant m_e^* and the Poly3x model. For $N_D = 3x10^{19}$

cm^{-3}, a donor concentration level not uncommon for 400 GHz HBTs, the deviation between the constant m_e* and the Poly3x model exceeds 150 meV in InP and 400 meV in $In_{0.53}Ga_{0.47}As$. A Fermi-level change of this magnitude will significantly influence carrier transport calculations across hetero-interfaces, PN junctions, and contacts.

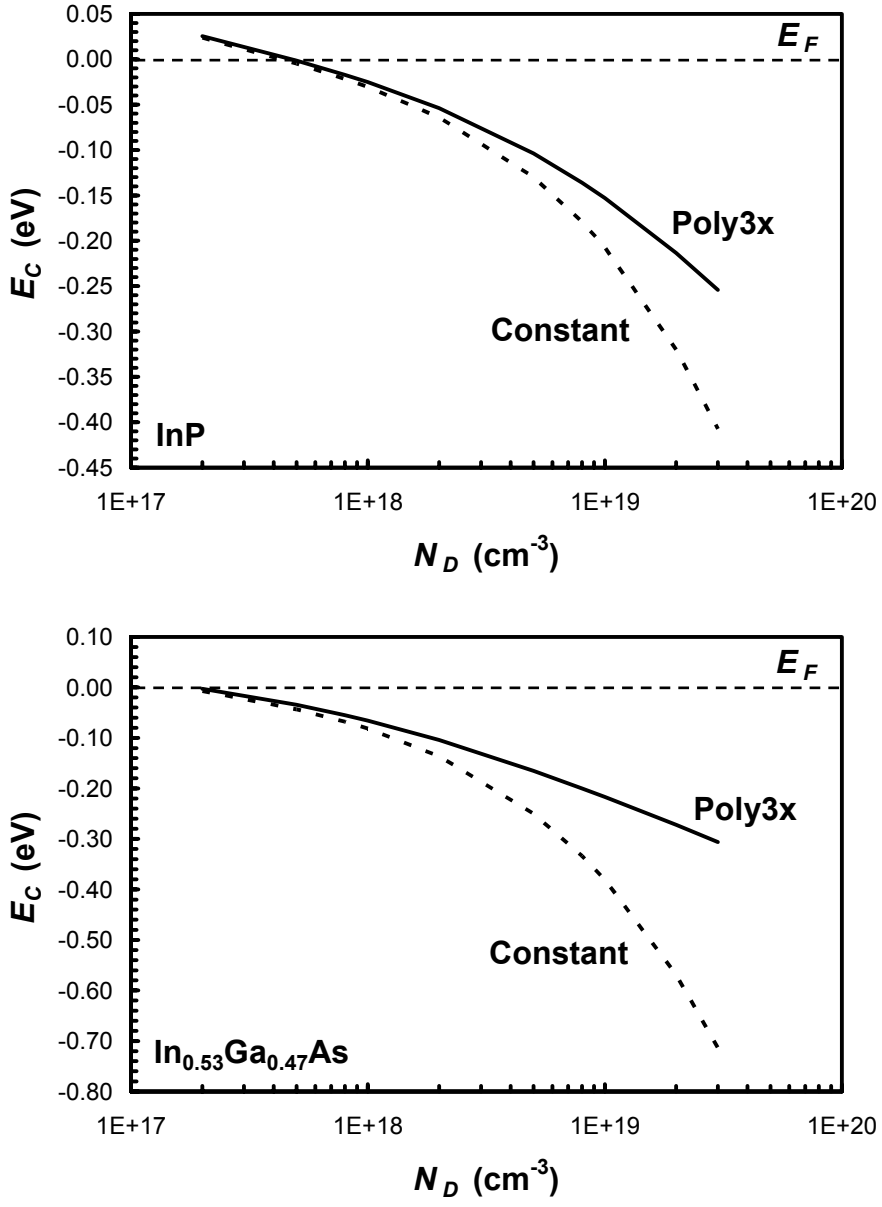

Figure C-4: Shift in conduction band energy, E_C, with respect to the Fermi-level, E_F, using a constant m_e* (dashed) and the Poly3x model (solid) for InP (top) and $In_{0.53}Ga_{0.47}As$ (bottom).

In order to demonstrate the impact on device simulation, Figure C-5 shows the conduction and valence bands generated with the Poly3x model and the constant m_e* model at thermal equilibrium. Since the m_e* is even lower in $In_{0.53}Ga_{0.47}As$, the effect of the Poly3x model is even more dramatic than InP. The erroneously high E_F-E_C in the n++ $In_{0.53}Ga_{0.47}As$ regions presents an artificially high barrier at InP/$In_{0.53}Ga_{0.47}As$ interfaces in the emitter cap and sub-collector. There is also greater band bending at the n/n++ interfaces between the emitter and emitter cap and between the collector and sub-collector. This band bending is equivalent to an additional 100-150 mV reverse bias across the base-emitter and base-collector junctions. However, electron transport through these regions is unaffected due to the deep E_F position within the conduction band, with or without the Poly3x model.

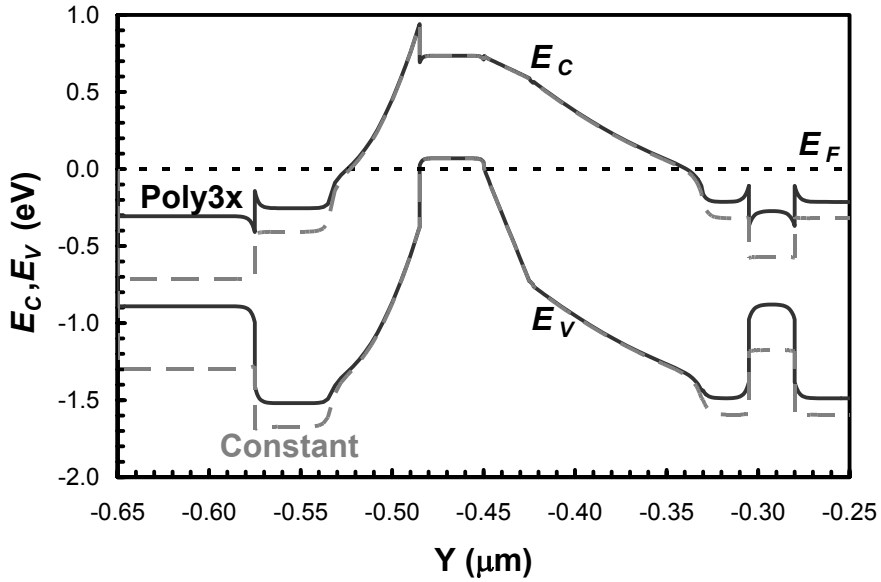

Figure C-5: HBT band diagram where the conduction and valence band energies, E_C and E_V, are plotted with respect to the Fermi-level, E_F, using the Poly3x model (solid) and the constant m_e* model (dashed) at thermal equilibrium.

Figure C-6 compares the simulated forward Gummel and f_T obtained from a constant m_e* and the Poly3x model. DESSIS was not able to converge upon a solution at higher V_{BE} and J_C with a constant m_e* despite the nearly identical behavior with the Poly3x model at low V_{BE} and J_C. The more realistic position of E_F provided by the Poly3x model is likely to improve convergence, resulting in a complete forward Gummel sweep. The value of N_C could be tuned in each region to produce the correct E_F position, but this would require considerable user customization on a case by case basis and prevent devices with a continual doping gradient e.g. SIBS HBTs [C-10] from being simulated accurately.

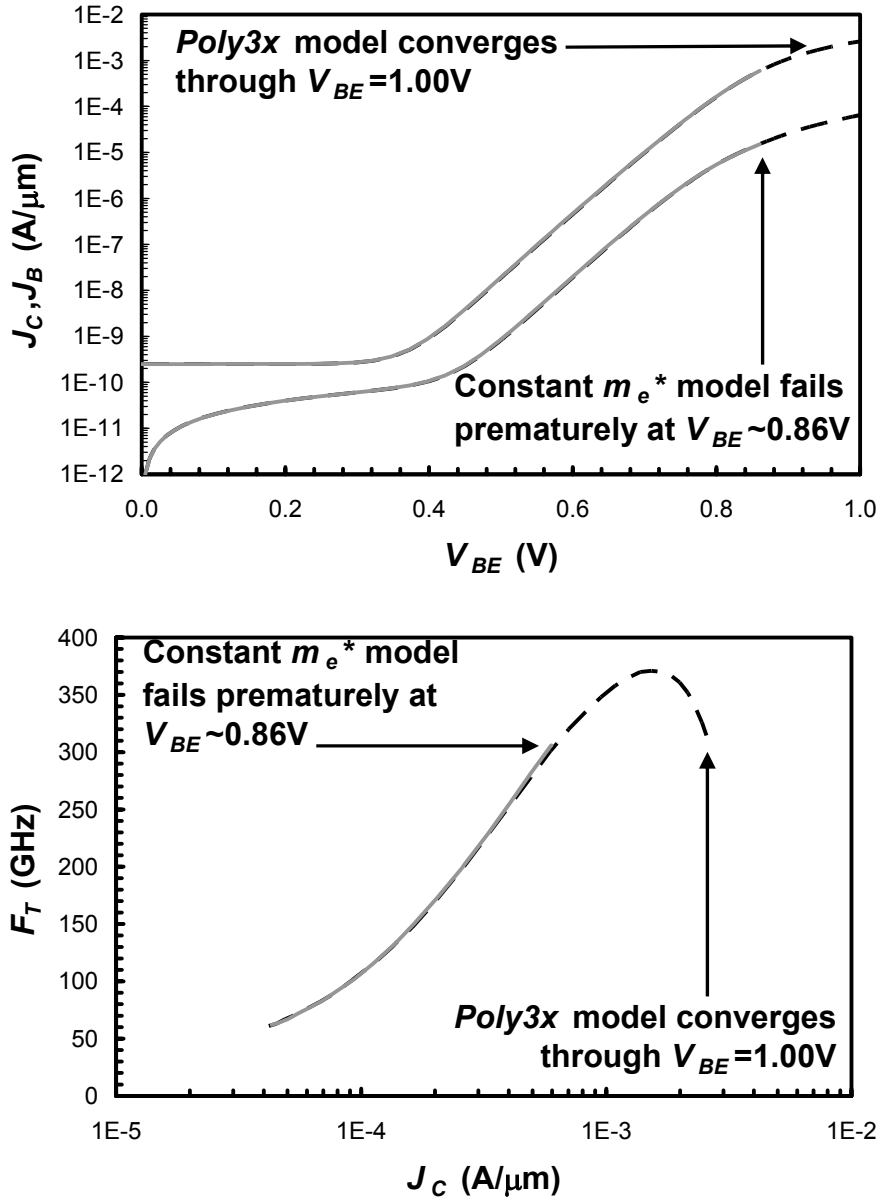

Figure C-6: Simulated forward Gummel (top) and f_T (bottom) with constant m_e* (solid) and Poly3x (dashed) models.

C.4 Band Gap Narrowing

As a result of increasing carrier-carrier interactions and carrier-impurity interactions with increasing impurity concentrations, the conduction band edge can be lowered or the valence band edge can be raised [C-11],[C-12]. The result is a net

reduction in the bandgap called Band Gap Narrowing (*BGN*). At low and moderate impurity concentrations, below 10^{16} cm^{-3} for most III-V semiconductors, the change in the bandgap is smaller than the thermal energy, ΔE_G = kT~26 meV. However, heavily degenerately doped semiconductors (10^{18} cm^{-3} and higher) may suffer as much as a 200 meV bandgap reduction. Unfortunately, the characterization of bandgap narrowing in InP and $In_{0.53}Ga_{0.47}As$ is not as complete as silicon or even GaAs; therefore, model parameters were based on theory [C-12], phenomenological expressions [C-13],[C-14],[C-15], and limited data [C-5],[C-6],[C-7]. The partitioning of the total bandgap reduction between the conduction and valence bands and the doping dependence of this partitioning is particularly important when simulating HBTs [C-16]. For $In_{0.53}Ga_{0.47}As$, the conduction band to valence band ratio ranges from 1:1 at N_A = $1x10^{18}$ cm^{-3} to approximately 1:2 at N_A = $1x10^{20}$ cm^{-3}. DESSIS supports a parameter (*Bgn2Chi*) that determines the partitioning of the total *BGN* between the conduction and valence bands, but it is constant and the PMI does not allow a user defined relationship for this parameter. Due to the limited quantities of experimental data and for the purposes of this work, the total *BGN* is evenly partitioned between the conduction and valence bands for both InP and $In_{0.53}Ga_{0.47}As$.

Most device simulators have implemented the models of Bennett and Wilson, Slotboom, and delAlamo, but all three of these models use the natural logarithm of the impurity concentration. In order to gain more flexibility, the general phenomenological expression presented by Jain et al [C-14] is used.

$$\Delta E_G = A \times N_{A,D}^{1/3} + B \times N_{A,D}^{1/4} + C \times N_{A,D}^{1/2} \tag{C-2}$$

Although Jain et al calculate the coefficients, *A*, *B*, and *C*, using material parameters, this work uses the expression as a fitting function for experimental data where it exists. Since Equation (C-2) is not implemented in the DESSIS simulator, it is used to compute entries in a table based model that does exist in the DESSIS simulator.

For InP, the expression presented in [C-5],

$$\Delta E_G = 2.25\times10^{-9} \bullet N_D^{1/3}(eV) \tag{C-3}$$

shows reasonable agreement with experimental data obtained up to donor concentrations of $1x10^{19}$ cm^{-3}. However, comparable experimental data for $In_{0.53}Ga_{0.47}As$ have not been reported. Since the *BGN* expressions derived by Jain et al [C-13], Abram et al [C-12], and Schubert [C-11] rely on the dielectric constant and effective mass of the particular material, the *BGN* parameters of a ternary compound are expected to fall between those of its constituent binary compounds. The *BGN* parameters used for InAs are extracted from a least squares fit to experimental data at moderate N_D ($2x10^{17}$ cm^{-3} to $2x10^{18}$ cm^{-3}) presented in [C-5]. A linear interpolation between the published *BGN* parameters for GaAs [C-15], which correlate well with published experimental data, and the previously discussed *BGN* parameters for InAs is expected to give a reasonable estimate. The inclusion of a bowing parameter corresponding to those of the dielectric constant and effective mass may yield a more accurate estimation, but in the absence of any experimental data, the linearly interpolated values are deemed sufficient. For all three materials, the phenomenological expressions derived by Jain et al [C-13],[C-14] are used to present the bandgap narrowing resulting from high N_A, because published experimental data could not be found. Since Jain et al have shown reasonable correlation between their calculated *BGN* parameters and published experimental data for p-type GaAs, Si, and

GaSb, it is expected that their *BGN* parameters for InP, InAs, and $In_{0.53}Ga_{0.47}As$ will be reasonable estimates. Table C-3 summarizes all the *BGN* parameters, both donor and acceptor, for the materials of interest, and Figure C-7 graphically shows the significant *BGN* that occurs for these degenerately doped semiconductors.

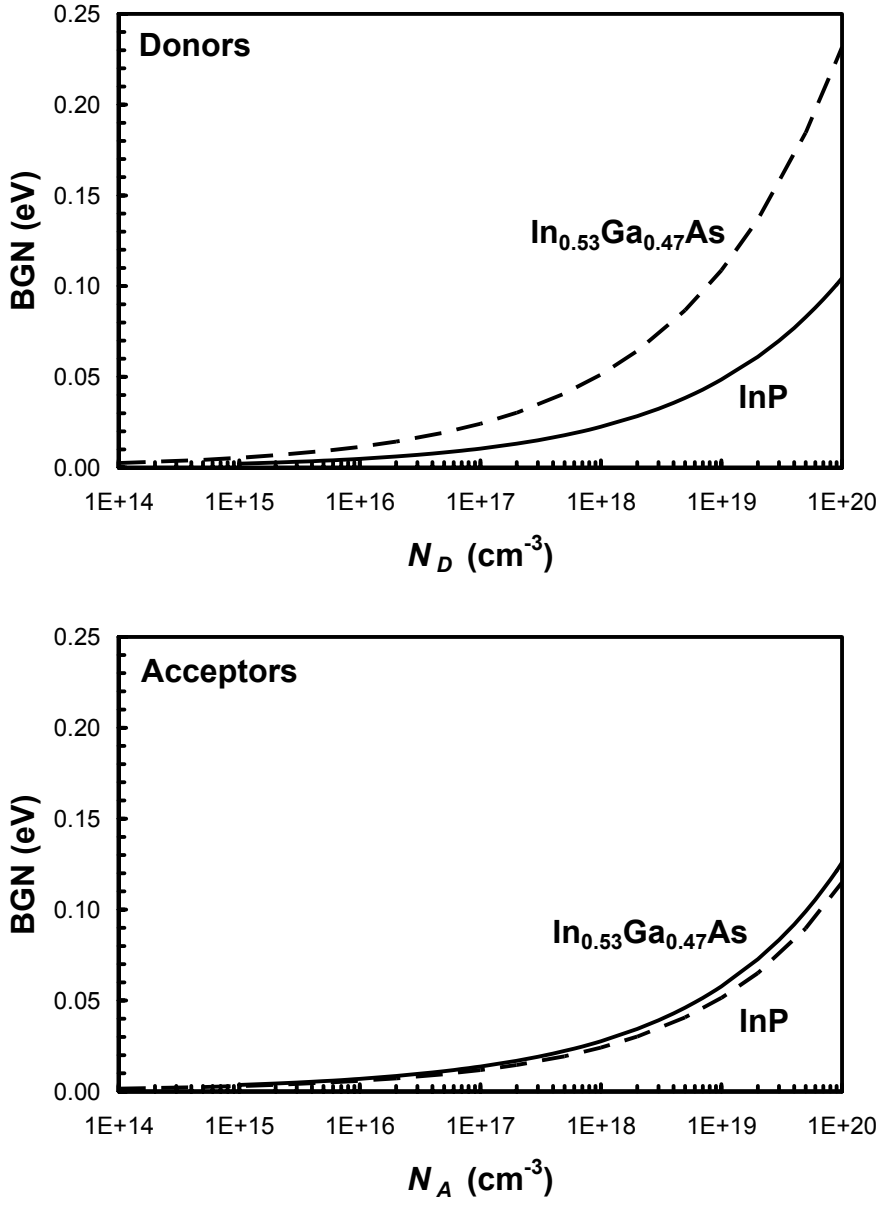

Figure C-7: Band gap narrowing, *BGN*, resulting from high donor (top) and acceptor (bottom) concentrations in InP (solid) and $In_{0.53}Ga_{0.47}As$ (dashed).

Table C-3: Summary of *BGN* parameters.

***BGN* Parameter**		**InP**	**$In_{0.53}Ga_{0.47}As$**	**InAs**
Donor	A	$2.25x10^{-8}$	$4.76x10^{-8}$	$3.06x10^{-8}$
	B	0	$9.99x10^{-8}$	0
	C	0	0	0
Acceptor	A	$1.03x10^{-8}$	$9.20x10^{-9}$	$8.34x10^{-9}$
	B	$4.43x10^{-7}$	$3.57x10^{-7}$	$2.91x10^{-7}$
	C	$3.38x10^{-12}$	$3.65x10^{-12}$	$4.53x10^{-12}$

Using the HBT whose layer structure is presented in Table C-1, the band diagram at thermal equilibrium illustrates the impact of *BGN* on device simulation. Figure C-8 clearly shows the impact to the n++ regions in the emitter and collector, but since the Fermi-level is pinned with respect to the conduction band energy, *BGN* does not affect electron transport in these regions. However, the effect is more significant in the p+ base where the Fermi-level is pinned with respect to the valence band. By ignoring *BGN*, the differences in the band diagram will impede electron transport across the base-emitter junction and result in a higher turn-on voltage. Figure C-9 illustrates the general increase in the turn-on voltage from the forward Gummel simulation and therefore, an increase in the voltage bias required to achieve a given J_C in the f_T simulation. The increase in V_{BE} also decreases the effective V_{BC} at a given V_{CE} which should result in an altered V_{CE} dependence of the f_T versus J_C curves. For this particular device structure, there is a relatively small change in peak f_T, 8 GHz or approximately 2% at a V_{CE} = 1.50 V.

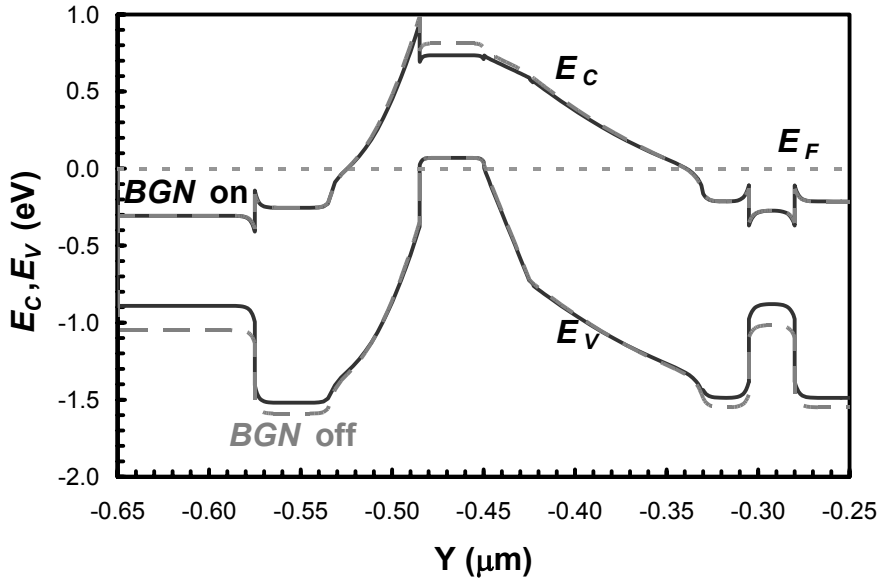

Figure C-8: HBT band diagram where the conduction and valence band energies, E_C and E_V, are plotted with respect to the Fermi-level, E_F, with the bandgap narrowing, *BGN*, model activated (solid) and de-activated (dashed) at thermal equilibrium.

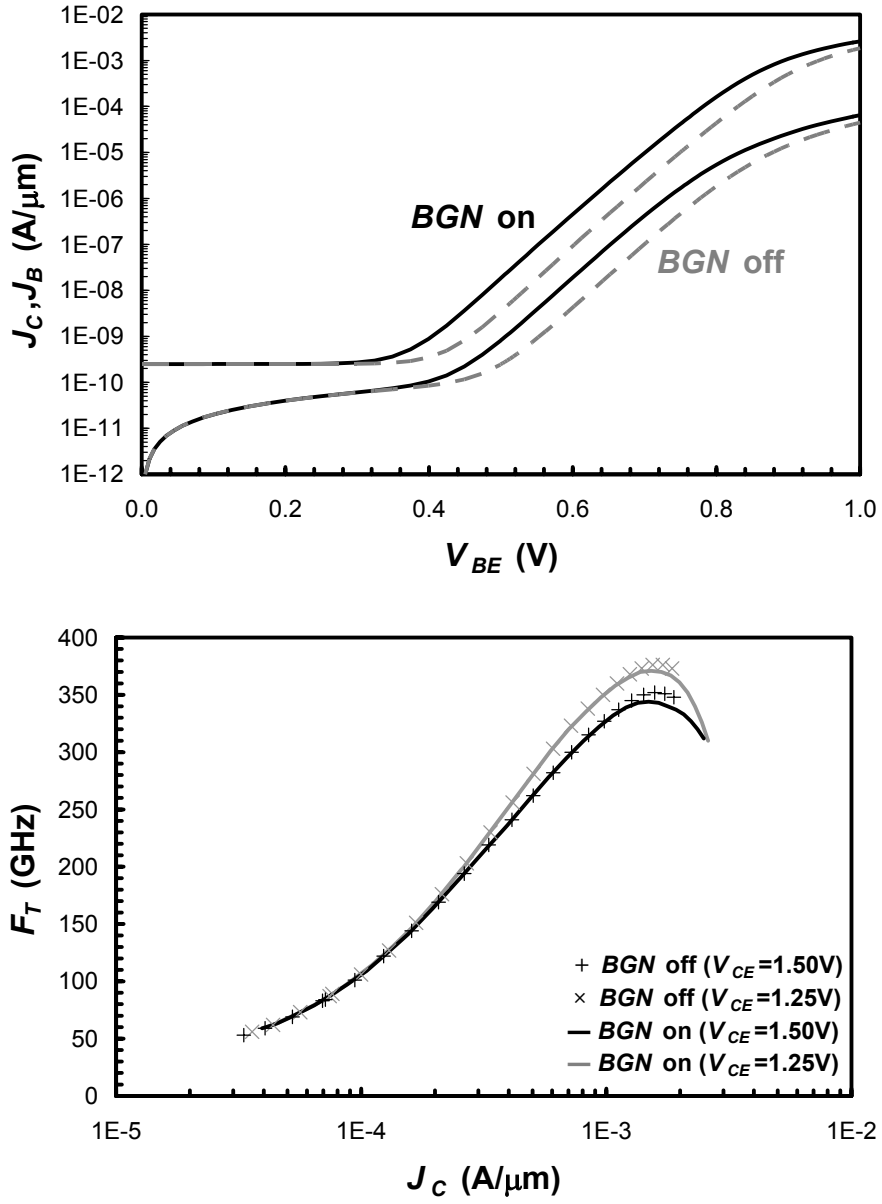

Figure C-9: Simulated forward Gummel (top) and f_T versus J_C (bottom) with bandgap narrowing, *BGN*, activated (solid) and de-activated (dashed).

C.5 Donor and Acceptor Activation Energy and the Mott Transition

As N_D or N_A increases, the semiconductor undergoes an insulator to metal transition, referred to as the Mott transition, but most simulators or their default material parameters do not accurately represent this phenomenon for compound semiconductors.

The mean spacing between impurities, either donors or acceptors, decreases as N_D or N_A increases resulting in a greater probability and amount of overlap of an impurity's Coulomb potential with others. As the amount of overlap increases, the effective impurity ionization energy (E_A or E_D) decreases. This reduction increases the probability of electrons transferring from any one impurity state to a state of an adjacent impurity by thermionic emission. In addition, the high free-carrier concentration serves to screen the impurity potentials, further reducing E_A or E_D and increasing the probability of electron transfer. Finally, the probability of electron transfer through tunneling is increased due to a net reduction of the barrier height as previously stated and the barrier thickness as the impurity separation decreases. The result is the gradual transition from insulator or semiconductor-like properties to those of a metal [C-11],[C-17],[C-18],[C-19].

Debye and Conwell [C-11] showed that the impurity concentration dependent ionization energy can be described by

$$E_{D,A} = E_{D,A0}\left[1 - \left(N_{D,A} \Big/ N_{D,Acrit}\right)^{1/3}\right] \tag{C-4}$$

where $E_{D,A0}$ is the low concentration donor or acceptor ionization energy; $N_{D,A}$ is the donor or acceptor concentration; and $N_{D,Acrit}$ is the Mott transition critical impurity concentration. The DESSIS implementation,

$$E_{D,A} = E_{D,A0} - \alpha_{D,A} N_i^{1/3} \tag{C-5}$$

is similar in form where N_i is the total impurity concentration, but requires the determination of the $\alpha_{D,A}$ model parameter. In order to represent this phenomenon for numerical simulation, the Mott Criterion [C-11],

$$a^*_{e,hB} N^{1/3}_{D,Acrit} = \frac{1}{4}\left(\frac{\pi}{3}\right)^{1/3} \tag{C-6}$$

is used to calculate the critical impurity concentration, $N_{D,Acrit}$, at which the Mott transition occurs, and $N_{D,Acrit}$ is expressed as a function of the effective Bohr radius,

$$a^*_{e,hB} = a_o \varepsilon_r \frac{m_o}{m^*_{e,hc}} \tag{C-7}$$

The relative dielectric constant, ε_r, and the Bohr radius, a_o, are easily obtained from the literature, but the conductivity effective mass, $m_{e,hc}$*, requires further discussion. For any semiconductor with spherical constant energy surfaces in *k*-space and no degeneracy other than spin, $m_{e,hc}$* is equal to the effective mass, m*, at the band minima. This accurately describes the conduction band for most compound semiconductors including InP and $In_{0.53}Ga_{0.47}As$, but not the valence band. Due to the anisotropy and degeneracy of the valence band, a simple compact expression does not exist to compute the value of m_{hc}*. However, there exists a tabular means to determine m_{hc}* for holes from the Luttinger parameters [C-22] of the target material, based on the work of Baldereschi and Lipari [C-20] and Schubert [C-21]. Table C-3 summarizes the values obtained for InP and $In_{0.53}Ga_{0.47}As$.

Figure C-10 shows the free-electron population, n, versus N_D in InP and free-hole population, p, versus N_A in $In_{0.53}Ga_{0.47}As$ for the default model parameters ($\alpha_{D,A}$ = 3.1x10^{-8} eV·cm and $N_{D.Acrit}$ = 1x10^{22} cm^{-3}) and those presented in Table (C-4). There is greater than a factor of two difference between the donor and electron concentrations even when the donor concentration is as low as 2x10^{18} cm^{-3}. The differences between acceptor and hole concentrations is less dramatic due to the higher N_V when compared to N_C, but no

less important to numerical simulation. The use of the previously described analytical expressions and table to determine the Mott transition is comparable with previously published experimental data for donors [C-23] and acceptors [C-24], respectively, in InP. Additional experimental data for $In_{0.53}Ga_{0.47}As$ were not available for comparison.

Table C-4: Summary of Mott transition parameters.

Parameter	Units	Symbol	InP	$In_{0.53}Ga_{0.47}As$
Relative dielectric constant	---	ε_r	12.4	14.1
Electron conductivity effective mass	m_o	m_{ec}*	0.080	0.041
Electron effective Bohr radius	Å	a_{eB}*	82.0	181.5
Donor critical doping	cm^{-3}	N_{Dcrit}	$2.965x10^{16}$	$2.735x10^{15}$
Shallow donor energy	meV	E_{D0}	5.7	6
Shallow donor parameter	eV·cm	α_D	$2.015x10^{-8}$	$4.647x10^{-8}$
Luttinger Parameters	---	$\gamma_1, \gamma_2, \gamma_3$	5.08,1.60,2.10	11.01,4.18,2.10
Spherical coupling parameter	---	μ	0.7480	0.5326
Baldereschi and Lipari function	---	$f(\mu)$	2.137	1.352
Hole conductivity effective mass	m_o	m_{hc}*	0.421	0.123
Hole effective Bohr radius	Å	a_{hB}*	15.6	60.6
Acceptor critical doping	cm^{-3}	N_{Acrit}	$4.314x10^{18}$	$7.345x10^{16}$
Shallow acceptor energy	meV	E_{A0}	40	20
Shallow Acceptor α Parameter	eV·cm	α_A	$2.4572x10^{-8}$	$4.7756x10^{-8}$

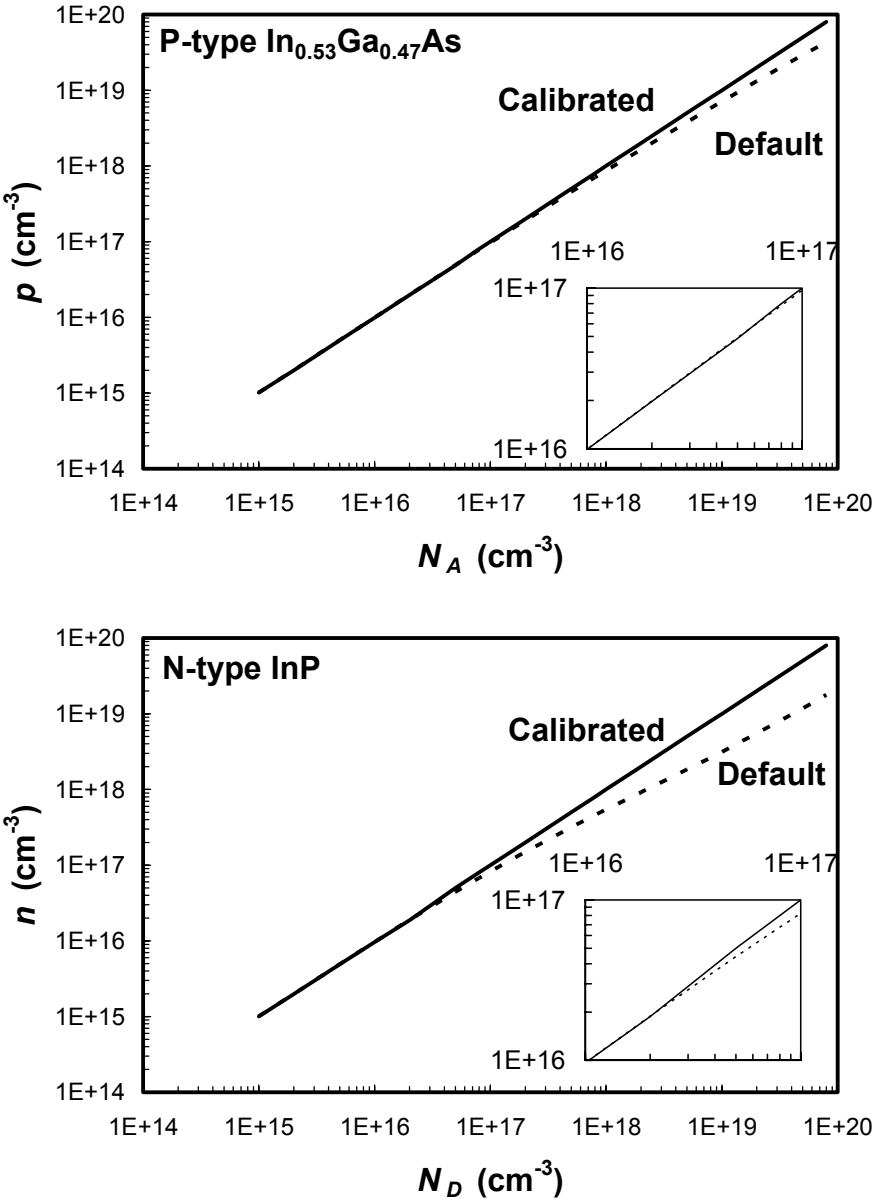

Figure C-10: Free-carrier concentrations, *n* and *p*, versus impurity concentration, N_D and N_A, resulting from DESSIS default parameters (dashed) and calibrated parameters (solid) for the Mott transition in n-type InP (top) and p-type $In_{0.53}Ga_{0.47}As$ (bottom). The insets show the behavior near the critical doping, $3.0x10^{16}$ cm^{-3} for n-type InP and $7.3x10^{16}$ cm^{-3} for p-type $In_{0.53}Ga_{0.47}As$.

Since the Mott transition occurs at fairly low donor concentrations, all impurities could be assumed to be fully ionized. However, for those electron devices where the impurity concentration varies by several orders of magnitude within the device, such as an III-V HBT, the inclusion of the Mott transition is recommended. Although the HBT

presented in Table C-1 does not utilize layers whose impurity concentration is both above and below N_{crit}, higher operating voltage HBTs (long collector) and optoelectronic HBTs and diodes will frequently utilize contact layers doped greater than 10^{19} cm^{-3} and collectors doped below $5x10^{15}$ cm^{-3}. It is possible to selectively activate this model for various regions within a device in an effort to improve computation time, but advances in computer processing power do not warrant the loss of generality.

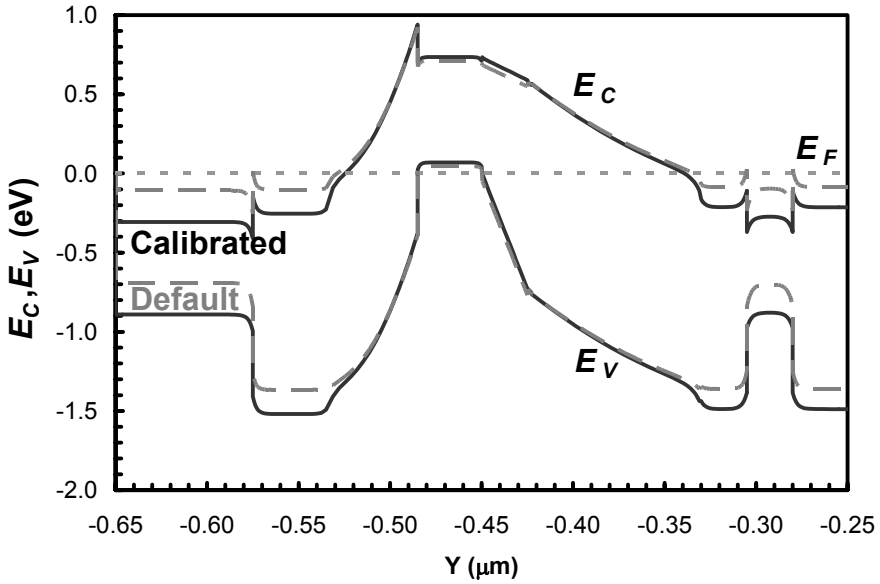

Figure C-11: HBT band diagram where the conduction and valence band energies, E_C and E_V, are plotted with respect to the Fermi-level, E_F, with default (dashed) and calibrated (solid) Mott Transition parameters and at thermal equilibrium.

The impact of the Mott Transition can also be observed from the band diagram, shown in Figure C-11, of the HBT presented in Table C-1 at thermal equilibrium. As in Figure C-10, the differences in free-electron population are most significant in the n++ regions of the emitter and collector, but no less important is the change in the free-hole population in the p+ base. This is observed in Figure C-11 by the change in the Fermi-level position with respect to the conduction and valence bands. The net effect is similar

to those discussed and observed in Section III and Figure C-5, but the Fermi-level is deeper, not shallower, into the corresponding band. The change in free-carrier population is also expected to cause a corresponding change in the carrier mobility and result in differences in the simulated base, emitter, and collector resistances. DESSIS and most other device simulators do not allow for the explicit definition of impurity band conduction, but sufficient experimental data concerning the carrier mobility of degenerately doped InP and $In_{0.53}Ga_{0.47}As$ are available [C-4],[C-5],[C-6],[C-7],[C-25]. These experimental mobility values represent all possible conduction mechanisms through the semiconductor including impurity band conduction. The doping dependent Arora model, fitted to these experimental data, is used to indirectly model the impurity band conduction for the simulations presented throughout this work. As a result, the apparent shift in turn-on voltage and high frequency performance can be observed in Figure C-12. The shift in peak f_T from 377 GHz to 371 GHz represents less than a 2% change, but the shift of peak f_T with respect to J_C from 1.25 mA/μm to 1.52 mA/μm represents an 18% under- estimation of J_C and hence the power consumed. Given the sensitivity of high-performance InP HBTs to self heating and temperature [C-26], the Mott Transition represents a critical aspect of device simulation.

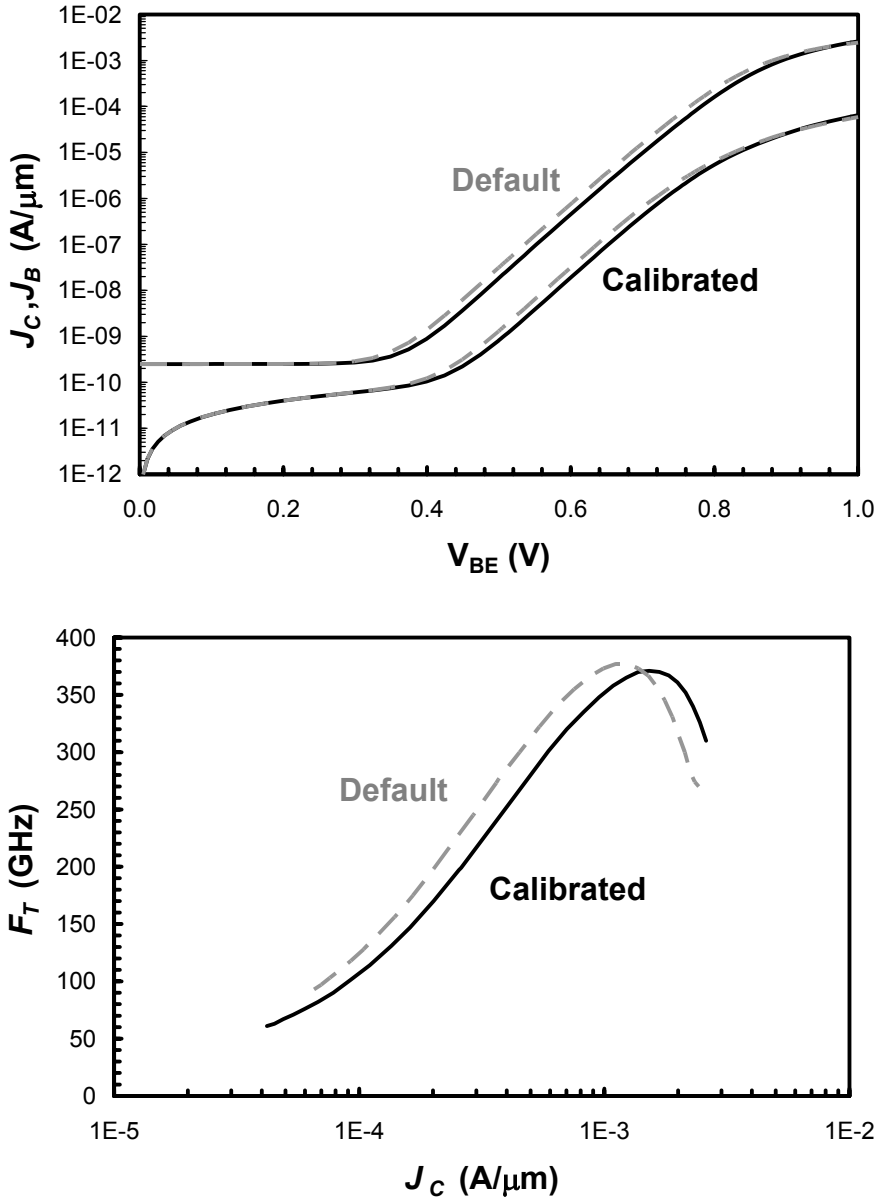

Figure C-12: Simulated forward Gummel (top) and f_T versus J_C (bottom) with default (dashed) and calibrated (solid) Mott Transition parameters.

C.6 Summary

Since high-performance InP HBTs require the use of degenerately doped semiconductors, it is imperative that phenomena associated with high impurity concentrations be properly modeled in device simulation. The models of three physical

phenomena: 1) doping dependent m_e* and hence energy band non-parabolicity; 2) *BGN*; and 3) the Mott transition are presented, and their implementations in the Synopsys device simulator, DESSIS, is discussed. For each phenomena, significant variation is observed in the band diagram (as large as 400 meV) and in the f_T dependence on J_C and V_{CE} of a representative high-performance InP HBT. Without an accurate representation of an HBT's band structure, transport, recombination, generation, and tunneling equations which rely on the band structure will neither correlate with experimental results nor allow the simulator to converge upon a solution.

C.7 Acknowledgements

This chapter, in full, is a reprint as it appears in Solid State Electronics, vol. 50, 2006. The contributions from the co-authors Tahir Hussain and Marko Sokolich of HRL Laboratories, L.L.C., and Peter M. Asbeck of UCSD are appreciated. The author of this dissertation was the primary investigator and primary author of this publication. This work was sponsored by the Defense Advanced Research Projects Agency (DARPA) through AFRL Contract F33615-02-1286 (TFAST). We also thank the many contributors to the TFAST effort at HRL, and especially members of HRL's High Speed Circuits Laboratory for wafer fabrication.

C.8 References

[C-1] T. Hussain, Y. Royter, D. Hitko, M. Montes, I. Milosavljevic, R. Rajavel, S. Thomas, M. Antcliffe, A. Arthur, Y. Boegeman, J. Li, and M. Sokolich, "First demonstration of sub-0.25 μm-width emitter InP-DHBTs with >400 GHz f_t and >400 GHz f_{max}," *2004 IEEE International Electron Devices Meeting Technical Digest*, pp. 553-556, Dec. 2004.

[C-2] Z. Griffith, M.J.W. Rodwell, F. Xiao-Ming, D. Loubychev, W. Ying, J.M. Fastenau, and A.W.K. Liu, "InGaAs/InP DHBTs with 120-nm collector having simultaneously high f_t, $f_{max} \geq 450$ GHz", *IEEE Electron Device Letters*, vol. 26, no, 8, pp. 530-532, Aug. 2005.

[C-3] M. J.W. Rodwell, M. Urteaga, T. Mathew, D. Scott, D. Mensa, Q. Lee, J. Guthrie, Y. Betser, S. C.Martin, R. P. Smith, S. Jaganathan, S. Krishnan, S. I. Long, R. Pullela, B. Agarwal, U. Bhattacharya, L. Samoska, and M. Dahlstrom, "Submicrometer scaling of heterojunction bipolar transistors," *IEEE Transactions on Electron Devices*, vol. 48, pp. 2606–2624, Dec. 2001.

[C-4] M. Sotoodeh, A.H. Khalid, and A. A. Rezazadeh, "Empirical low-field mobility model for III-V compounds application to device simulation codes", *Journal of Applied Physics*, vol. 87, no. 6, pp. 2890-2900, March 2000.

[C-5] http://www.ioffe.ru/SVA/NSM/Semicond/

[C-6] M. Levinshtein, S. Rumyantsev, and M. Shur, "Handbook Series on Semiconductor Parameters", vol.2, World Scientific, 1999.

[C-7] O. Madelung, "Semiconductors – Basic Data", 2nd revised edition, Springer-Verlag, 1996.

[C-8] ISE v10.0 DESSIS manual

[C-9] W. K. Metzger, M. W. Wanlass, L. M. Gedvilas, J. C. Verley, J. J. Carapella, and R. K. Ahrenkiel. "Effective electron mass and plasma filter characterization of n-type InGaAs and InAsP", *Journal of Applied Physics*, v.92, no. 7, pp. 3524-29, Oct 2002.

[C-10] J.C. Li, M. Chen, D.A. Hitko, C.H. Fields, B. Shi, R. Rajavel, P.M. Asbeck, and M. Sokolich, "A submicrometer 252 GHz f_T and 283 GHz f_{MAX} InP DHBT with reduced C_{BC} using selectively implanted buried subcollector (SIBS)", *IEEE Electron Device Letters*, vol. 26, no. 3, pp. 136-138, March 2005.

[C-11] E.F. Schubert, "Chapter 16-High Doping Effects", ECSE-6968 online course notes, http://www.rpi.edu/~schubert/.

[C-12] R.A. Abram, G.J. Rees, and B.L.H. Wilson, "Heavily doped semiconductors and devices", *Advances in Physics*, vol. 27, no. 6, pp. 799-892, 1978.

[C-13] S.C. Jain, J.M. McGregor, and D.J. Roulston, "Bandgap narrowing in novel III-V semiconductors", *Journal of Applied Physics*, vol. 68, no. 7, pp.3747-9, Oct 1990.

[C-14] S.C. Jain and D.J. Roulston, "A Simple Expression for Band Gap Narrowing (BGN) in Heavily Doped Si, Ge, GaAs, and Ge_xSi_{1-x} Strained Layers", *Solid State Electronics*, vol. 34, no. 5, pp. 453-465, 1991.

[C-15] S.C. Jain, J.M. McGregor, D.J. Roulston, and P. Balk, "Modified Simple Expression for Bandgap Narrowing in n-Type GaAs", *Solid State Electronics*, vol. 35, no. 5, pp. 639-642, 1992.

[C-16] J.M. Lopez-Gonzales and Lluis Prat, "The Importance of Bandgap Narrowing Distribution Between the Conduction and Valence Bands in Abrupt HBT's", *IEEE Transactions On Electron Devices*, vol. 44, no. 7, July 1997.

[C-17] N.F. Mott, "Metal-insulator transitions in non-crystalline systems", *Advance in Physics*, 1985.

[C-18] N.F. Mott, "Metals, non-metals and metal-non-metal transitions: some recollections", Rep. Prog. Phys. 1984.

[C-19] V.L. Bonch-Bruyevich, "The Electronic Theory of Heavily Doped Semiconductors", American Elsevier, 1966.

[C-20] A. Balderechi and N.O. Lipari, "Cubic contributions to the spherical model of shallow acceptor states", *Physical Review B*, vol. 9, no. 4, pp. 1525-1539, Feb. 1974.

[C-21] E.F. Schubert, "Doping in III-V Semiconductors", Cambridge University Press, 1993.

[C-22] I. Vurgaftman, J.R. Meyer, and L.R. Ram-Mohan, "Band Parameters for III-V compound semiconductors and their alloys", *Journal of Applied Physics*, vol. 89, no. 11, pp. 5815-5875, June 2001.

[C-23] Y. Morishita, M. Imaizumi, and M. Gotoda, "Electrical and Optical Properties of Silicon Doped InP Grown by Gas Source MBE", *Journal of Crystal Growth*, vol. 104, pp. 457-62, 1990.

[C-24] Y. Kawamura, H. Asahi, and H. Nagai, "Electrical and optical properties of Be-doped InP grown by molecular beam epitaxy", *Journal Applied Physics*, vol. 54, no. 2, pp. 841-846, Feb. 1983.

[C-25] D.A. Anderson, N. Apsley, P. Davies, and P.L. Giles, “Compensation in heavily doped n-type InP and GaAs”, *Journal Applied Physics*, vol. 58, no. 8, pp. 3059-3067, Oct 1985.

[C-26] J.C. Li, T. Hussain, D.A. Hitko, P.M. Asbeck, and M. Sokolich, “Characterization and modeling of thermal effects in sub-micron InP DHBTs”, *2005 IEEE Compound Semiconductor IC Symposium Technical Digest*, pp. 65-68, Nov. 2005.

D. DESSIS IMPLEMENTATION OF THE BOLTZMANN TRANSPORT EQUATION

D.0 Introduction

Conventional drift-diffusion transport equations, DDTE, and the Boltzmann statistics form of the Einstein relation are inadequate for the simulation of velocity overshoot and ballistic carrier transport. The primary deficiency with DDTE is the assumption that the carriers are in thermal equilibrium with the lattice. Electrons in state-of-the-art InP HBTs may be in thermal equilibrium with the lattice in regions such as the emitter cap and sub-collector, but the presence of an abrupt hetero-interface at the base-emitter junction and strong quasi-electric/electric fields in the base, base-collector grade, and collector allow carriers to accelerate beyond v_{sat}. The Hydrodynamic Transport Equations, HTE, form of the Boltzmann Transport Equation, BTE, is implemented as an extension of the drift-diffusion transport equations in DESSIS. The additional computational complexity introduced by the HTE generally limits device structures to one and two-dimensional cross-sections. Scientific computing is adequately advanced to produce solutions for three-dimensional device structures, but the marginal cost in time and capital is disproportionately greater than the scientific value of the simulation results.

D.1 Hydrodynamic Equations

The existing DESSIS implementation of the current, energy balance, and energy flux equations are summarized below. The BTE implementation within DESSIS version 10 is sufficiently general to cover a wide variety of materials and numerical treatments previously published in the literature [D-1],[D-2],[D-3].

The electron and hole currents,

$$\vec{J}_n = q\mu_n\left(n\nabla E_C + k_B T_n \nabla n + f_n^{td} k_B n \nabla T_n - \frac{3}{2} n k_B T_n \nabla \ln m_e \right) \tag{D-1}$$

$$\vec{J}_p = q\mu_p\left(p\nabla E_V + k_B T_p \nabla p + f_p^{td} k_B p \nabla T_p - \frac{3}{2} n k_B T_p \nabla \ln m_h \right) \tag{D-2}$$

respectively, are composed of conventional drift-diffusion and HTE terms. The first two terms of Equations (D-1) and (D-2) are the drift and diffusion terms similar to the conventional DDTE implementation, except the lattice temperature, T_L, has been replaced with the carrier temperatures, T_n and T_p. Since T_n and T_p are no longer equal to T_L, the third term is introduced to account for the diffusion of carriers due to gradients in the carrier temperature. The thermal diffusion pre-factors, f_n^{td} and f_p^{td}, are user specified parameters that allow the inclusion or exclusion of this phenomena. In the most general form, this pre-factor should be energy dependent and based on the generalized Einstein relation to exchange the carrier diffusivity, $D_{e,h}$, with the carrier mobility , $\mu_{e,h}$. The DESSIS implementation of f_n^{td} and f_p^{td} is of a static nature. In the "energy balance" method presented by Stratton [D-1], these pre-factors are zero, but for the method presented by Bløtekjær [D-2], these pre-factors are unity. Given the wide range in carrier

energies throughout the device and the static nature of these parameters, the values of f_n^{td} and f_p^{td} are set to one for the majority of simulations presented in this dissertation. The fourth and final term accounts for the spatial variation of the density of states (DOS) through the density of states effective mass, m_e and m_h. It is only valid for slow changes in composition and in regions where a localized m_e and m_h can be defined. Therefore, abrupt hetero-interfaces and quantum wells are not properly modeled by the fourth term. Aspects of carrier transport across the hetero-interface are considered in the DESSIS barrier tunneling and thermionic emission models [D-4]. Since Chirped Super Lattices are not employed in the HBTs discussed here, quantum wells are considered beyond the scope of this work. For a more rigorous treatment, the reader is referred to A.H. Marshak and K.M. van Vliet [D-5] and the works of Mark Lunstrom [D-4],[D-6],[D-7].

The computation of the band structure and carrier populations utilizes Fermi-Dirac statistics and a single, constant value of m_e and m_h. Therefore, the parabolic band approximation is enforced throughout all semiconductors regions. The necessary modifications to DESSIS in order to support degenerately doped materials and non-parabolicity have been previously discussed [D-8]. The Boltzmann statistics form of the Einstein relation

$$\frac{D_{e,h}}{\mu_{e,h}} = \frac{kT_{n,p}}{q} \tag{D-3}$$

is used to simplify many of the pre-factors shown in Equations (D-1) and (D-2). Since the generalized form of the Einstein relation

$$qD_{e,h} = \mu_{e,h} \left. \frac{\delta E_{fn,p}}{\delta Log(n)} \right|_{T_C} \tag{D-4}$$

is not used, it is assumed that carrier distributions are Maxwellian throughout all materials. The application of the Einstein relation has also coupled the carrier concentration diffusion term to the carrier temperature. These assumptions are reasonable for conventional electron devices, but for high performance HBTs and HEMTs, these assumptions fundamentally limit the simulation accuracy.

Although the current equations previously presented are modified for hydrodynamic simulations, it is the energy balance and energy flux equations that allow velocity overshoot to be modeled. The electron, hole, and lattice energy balance equations,

$$\frac{\partial W_n}{\partial t} + \nabla \cdot \vec{S}_n = \vec{J}_n \cdot \nabla E_C + \left. \frac{\partial W_n}{\partial t} \right|_{coll} \tag{D-5}$$

$$\frac{\partial W_p}{\partial t} + \nabla \cdot \vec{S}_p = \vec{J}_p \cdot \nabla E_V + \left. \frac{\partial W_p}{\partial t} \right|_{coll} \tag{D-6}$$

$$\frac{\partial W_L}{\partial t} + \nabla \cdot \vec{S}_L = \left. \frac{\partial W_L}{\partial t} \right|_{coll} \tag{D-7}$$

are represented in terms of the electron, hole, and lattice kinetic energy terms,

$$W_n = n\left(\frac{3}{2} k_B T_n\right) \tag{D-8}$$

$$W_P = p\left(\frac{3}{2} k_B T_p\right) \tag{D-9}$$

$$W_L = C_L T_n \tag{D-10}$$

and electron, hole, and lattice energy flux terms, S_n, S_p, and S_L, respectively. For Equations (D-5) and (D-6), the left hand side, LHS, of the energy balance equations represents the total potential and kinetic energy of the respective carrier, and the right hand side, RHS, represents the energy introduced to or removed from the system due to electric fields and carrier interactions with other carriers, phonons, or the lattice. For Equation (D-7), the energy balance equation is similar to that of the carriers, except the lattice does not have a current component.

On the LHS, the quantities of interest are the electron, hole, and lattice energy flux equations

$$\vec{S}_n = -\frac{5}{2} r_n \left(\frac{k_B T_n}{q} \vec{J}_n + f_n^{hf} \hat{\kappa}_n \nabla T_n \right) \tag{D-11}$$

$$\vec{S}_p = -\frac{5}{2} r_p \left(\frac{k_B T_p}{q} \vec{J}_p + f_p^{hf} \hat{\kappa}_p \nabla T_p \right) \tag{D-12}$$

$$\vec{S}_L = -\hat{\kappa}_L \nabla T_L \tag{D-13}$$

each carrier energy flux equation has two separate components, one for convection and one for diffusion. From Equations (D-11) and (D-12), the convective term is the first term on the RHS and the diffusive term is the second term on the RHS. The convective term has been discussed previously and is represented by Equations (D-1) and (D-2). The diffusive nature of the later term is hidden by the Einstein relation, which has been used to exchange $D_{e,h}$ with $\mu_{n,p}$ in

$$\hat{\kappa}_n = \frac{k_B^2}{q} n \mu_n T_n \tag{D-14}$$

$$\hat{\kappa}_p = \frac{k_B^2}{q} p \mu_p T_p \tag{D-15}$$

The diffusive term can also be referred to the Thomson-Peltier effect, and the pre-factors, f_n^{hf} and f_p^{hf}, can be viewed as fitting parameters for the Peltier coefficient. In DESSIS, the aforementioned pre-factors are energy dependent and allow the user considerable flexibility to tune the diffusive component of the energy flux. It is also important to note that additional constant pre-factors r_n and r_p, which allow corrections to the convective term, must be considered when calculating f_n^{hf} and f_p^{hf}. Although r_n and r_p should also be energy dependent, the current DESSIS implementation only allows them to be static quantities. The energy flux equation for the lattice is purely dependent on the material parameter, $\acute{\kappa}_L$, which is defined in the material or region specific parameter file.

On the RHS of Equations (D-5), (D-6), and (D-7) are the electric field and carrier interaction terms. The electric field component is straight forward and uses the previously discussed carrier current equations (D-1) and (D-2). The carrier interaction terms

$$\left.\frac{dW_n}{dt}\right|_{coll} = -H_n - \frac{W_n - W_{n0}}{\tau_{en}} \tag{D-16}$$

$$\left.\frac{dW_p}{dt}\right|_{coll} = -H_p - \frac{W_p - W_{p0}}{\tau_{ep}} \tag{D-17}$$

$$\left.\frac{dW_L}{dt}\right|_{coll} = H_L + \frac{W_n - W_{n0}}{\tau_{en}} + \frac{W_p - W_{p0}}{\tau_{ep}} \tag{D-18}$$

introduce the final pair of parameters critical to the simulation of velocity overshoot. The steady-state kinetic energies are defined as follows

$$W_{n0} = n\left(\frac{3}{2}k_B T_L\right) \tag{D-19}$$

$$W_{p0} = p\left(\frac{3}{2}k_B T_L\right) \tag{D-20}$$

For carrier-phonon interactions, the energy relaxation time approximation is used, and the relaxation time parameters, τ_{en} and τ_{ep}, are defined by the user. Just like the Thomson-Peltier fitting pre-factors, f_n^{hf} and f_p^{hf}, the energy relaxation times are an energy dependent quantity. All energy lost through these carrier-phonon interactions is assumed to be dissipated into the lattice eventually as described in Equation (D-18). For most compound semiconductors, the validity of this assumption is determined by the lifetime of polar optical phonons, but this behavior is lumped into the definition of τ_{en} and τ_{ep}. The H_n, H_p, and H_L are rates of energy gain or loss from generation-recombination (G-R) mechanisms.

D.2 References

[D-1] R. Stratton, “Diffusion of hot and cold electrons in semiconductor barriers,” *Physical Review,* vol. 126, no. 6, pp. 2002–2014, 1962.

[D-2] K. Bløtekjær, “Transport equations for electrons in two-valley semiconductors,” *IEEE Transactions on Electron Devices*, vol. ED-17, no. 1, pp. 38–47, 1970.

[D-3] ISE v10.0 DESSIS manual

[D-4] M.A. Stettler and M.S. Lundstrom, “A Detailed Investigation of Heterojunction Transport Using a Rigorous Solution to the Boltzman Equation”, *IEEE Trans. On Elec. Dev.*, vol. 41, no. 4, pp. 592-600, April 1994.

[D-5] A.H. Marshak and K.M. van Vliet, “Electrical Current in Solids with Position Dependent Band Structure”, *Solid State Electronics*, vol. 21, no. 2G, pp. 417-427, 1978.

[D-6] M.S. Lundstrom and R.J. Schuelke, “Numerical Analysis of Heterostructure Semiconductor Devices”, *IEEE Trans. On Elec. Dev.*, vol. 30, no. 9, pp. 1151-1159, Sept. 1983.

[D-7] M.S. Lundstrom, “Boundary Conditions for pn Heterojunctions”, *Solid State Electronics*, vol. 27, no. 5, pp. 491-496, 1984.

[D-8] J.C.Li, M. Sokolich, T. Hussain, and P.M. Asbeck, “Physical Modeling of Degenerately Doped Compound Semiconductor for High Performance HBT Design”, *Solid State Electronics*, Accepted for publication.

E. DESSIS MATERIAL PARAMETERS

E.0 Introduction

Physics-based device simulators are capable of modeling a wide variety of electron devices, but their accuracy is generally limited by the quality of various material parameters entered by the user. For compound semiconductors, many of necessary material parameters have not yet been investigated and require some crude estimation based on existing data. Due to this uncertainty, this section presents a listing of the material files used to represent InP and $In_{0.53}Ga_{0.47}As$ in the DESSIS device simulator. Although other materials were used, these two are common to all InP-based HBTs whose f_T and f_{MAX} exceed 400 GHz. The calibration of many of these model parameters are discussed throughout this dissertation so they are presented here without discussion. All material parameters were consolidated into a series of material specific files and stored in a central materials library to facilitate batch simulations and maintain consistency. As an additional aid, the thermal conductivity model parameters for a variety of materials are summarized in a single table.

E.1 InP Material File

```
* ISE Defaults
Epsilon
{ *  Ratio of the permittivities of material and vacuum
      epsilon     = 12.4      # [1]
}
* Data from Ioffe Site
LatticeHeatCapacity
{ * cv() = cv + cv_b * T + cv_c * T^2 + cv_d * T^3
      cv    = 1.35            # [J/(K cm^3)]
      cv_b  = 4.8100e-04      # [J/(K^2 cm^3)]
      cv_c  = 0.0000e+00      # [J/(K^3 cm^3)]
      cv_d  = 0.0000e+00      # [J/(K^4 cm^3)]
}
* Data from Ioffe Site and Quay
Kappa
{ * kappa() = kappa + kappa_b * T + kappa_c * T^2
        kappa   = 1.9470e+00    # [W/(K cm)]
        kappa_b =-5.4890e-03    # [W/(K^2 cm)]
        kappa_c = 4.2160e-06    # [W/(K^3 cm)]
}
EnergyRelaxationTime
{ *  Energy relaxation times in picoseconds
      (tau_w)_ele = 1.3751e+00      # [ps]
      (tau_w)_hol = 4.0000e-01      # [ps]
      Formula(tau_w)_ele = 2
      Numerator(0)_ele{
        A(0)  =  2.75775000e+02
        P(0)  =  0.00000000e+00
        A(1)  =  3.00198634e+05
        P(1)  =  1.00000000e+00
        A(2)  = -9.74516775e+05
        P(2)  =  2.00000000e+00
        A(3)  =  8.18315321e+05
        P(3)  =  3.00000000e+00
        A(4)  =  1.24117824e+05
        P(4)  =  4.00000000e+00
        G     =  1.00000000e+00
      }
      Denominator(0)_ele{
        A(0)  =  1.03548703e+05
        P(0)  =  0.00000000e+00
        A(1)  = -3.20739927e+05
        P(1)  =  1.00000000e+00
        A(2)  =  3.62417837e+05
        P(2)  =  2.00000000e+00
        A(3)  = -6.09432788e+05
        P(3)  =  3.00000000e+00
        A(4)  =  9.68783001e+05
        P(4)  =  4.00000000e+00
        G     =  1.00000000e+00
```

```
      }
}
EnergyFlux
{ *  Coefficient in front of the energy flux equation
      energy_flux_coef_ele    = 1.0 # [1]
      energy_flux_coef_hol    = 1.0 # [1]
}
ThermalDiffusion
{ *  Thermal diffusion factor (0 <= td <= 1)
      td_n  = 1.0000e+00      # [1]
      td_p  = 1.0000e+00      # [1]
}
HeatFlux
{ *  Heat flux factor (0 <= hf <= 1)
      hf_n  = 1   # [1]
      hf_p  = 1   # [1]
      F(0)_ele     = 1.9710e+00
      Numerator(0)_ele{
        A(0)  = -1.04354878e+03
        P(0)  =  0.00000000e+00
        A(1)  =  1.08356969e+05
        P(1)  =  1.00000000e+00
        A(2)  = -5.49633820e+05
        P(2)  =  2.00000000e+00
        A(3)  = -1.81829516e-04
        P(3)  =  3.00000000e+00
        A(4)  =  5.85851046e-03
        P(4)  =  4.00000000e+00
        G     =  1.00000000e+00
      }
      Denominator(0)_ele{
        A(0)  =  5.27404242e+03
        P(0)  =  0.00000000e+00
        A(1)  = -1.09869808e+05
        P(1)  =  1.00000000e+00
        A(2)  =  9.99999861e+05
        P(2)  =  2.00000000e+00
        A(3)  = -3.33154776e-04
        P(3)  =  3.00000000e+00
        A(4)  =  4.25422758e-03
        P(4)  =  4.00000000e+00
        G     =  1.00000000e+00
      }
}
AvalancheFactors
{ *  Coefficients for avalanche generation with hydro
      n_l_f = 1.0000e+00      # [1]
      p_l_f = 1.0000e+00      # [1]
      n_gamma     = 0.0000e+00      # [1]
      p_gamma     = 0.0000e+00      # [1]
      n_delta     = 0.0000e+00      # [1]
      p_delta     = 0.0000e+00      # [1]
}
* P,As are all shallow donor (S,Si,Sn,Ge)
```

```
* Boron = Carbon
* Sb,In = Mid Gap states for SI material
Ionization
{
      E_As_0      = 0.0057          # [eV]
      alpha_As    = 1.8416e-08      # [eV cm]
      g_As        = 2               # [1]
      Xsec_As     = 1.0000e-12      # [cm^2/sec]
      E_P_0       = 0.0057          # [eV]
      alpha_P     = 1.8416e-08      # [eV cm]
      g_P         = 2               # [1]
      Xsec_P      = 1.0000e-12      # [cm^2/sec]
      E_Sb_0      = 0.7100          # [eV]
      alpha_Sb    = 0.0000e+00      # [eV cm]
      g_Sb        = 2               # [1]
      Xsec_Sb     = 1.0000e-12      # [cm^2/sec]
      E_B_0       = 0.040           # [eV]
      alpha_B     = 2.4572e-08      # [eV cm]
      g_B         = 4               # [1]
      Xsec_B      = 1.0000e-12      # [cm^2/sec]
      E_In_0      = 0.7100          # [eV]
      alpha_In    = 0.0000e+00      # [eV cm]
      g_In        = 4               # [1]
      Xsec_In     = 1.0000e-12      # [cm^2/sec]
      E_N_0       = 0.045           # [eV]
      alpha_N     = 2.7643e-08      # [eV cm]
      g_N         = 4               # [1]
      Xsec_N      = 1.0000e-12      # [cm^2/sec]
      E_NDopant_0 = 0.0057          # [eV]
      alpha_NDopant = 1.8416e-08    # [eV cm]
      g_NDopant   = 2               # [1]
      Xsec_NDopant= 1.0000e-12      # [cm^2/sec]
      E_PDopant_0 = 0.040           # [eV]
      alpha_PDopant = 2.4572e-08    # [eV cm]
      g_PDopant   = 4               # [1]
      Xsec_PDopant= 1.0000e-12      # [cm^2/sec]
      NdCrit      = 2.9652e+16      # [cm-3]
      NaCrit      = 4.3140e+18      # [cm-3]
}
Bandgap
{ * Eg = Eg0 + alpha Tpar^2 / (beta + Tpar) - alpha T^2 / (beta + T)
      Chi0  = 4.4       # [eV]
      Eg0   = 1.4205    # [eV]
      alpha = 4.1000e-04      # [eV K^-1]
      beta  = 1.3600e+02      # [K]
      Tpar  = 0.0000e+00      # [K]
      Bgn2Chi = 0.5           # []
}
TableBGN
{
  Donor     1.0000e+14,   0.00000   # [ cm-3, eV ]
  Donor     1.0000e+15,   0.00225   # [ cm-3, eV ]
  Donor     2.0000e+15,   0.00283   # [ cm-3, eV ]
  Donor     5.0000e+15,   0.00385   # [ cm-3, eV ]
```

```
  Donor     1.0000e+16,   0.00485   # [ cm-3, eV ]
  Donor     2.0000e+16,   0.00611   # [ cm-3, eV ]
  Donor     5.0000e+16,   0.00829   # [ cm-3, eV ]
  Donor     1.0000e+17,   0.01044   # [ cm-3, eV ]
  Donor     2.0000e+17,   0.01316   # [ cm-3, eV ]
  Donor     5.0000e+17,   0.01786   # [ cm-3, eV ]
  Donor     1.0000e+18,   0.02250   # [ cm-3, eV ]
  Donor     2.0000e+18,   0.02835   # [ cm-3, eV ]
  Donor     5.0000e+18,   0.03847   # [ cm-3, eV ]
  Donor     1.0000e+19,   0.04848   # [ cm-3, eV ]
  Donor     2.0000e+19,   0.06107   # [ cm-3, eV ]
  Donor     5.0000e+19,   0.08289   # [ cm-3, eV ]
  Donor     1.0000e+20,   0.10444   # [ cm-3, eV ]
  Acceptor  1.0000e+14,   0.00000   # [ cm-3, eV ]
  Acceptor  1.0000e+15,   0.00363   # [ cm-3, eV ]
  Acceptor  2.0000e+15,   0.00441   # [ cm-3, eV ]
  Acceptor  5.0000e+15,   0.00573   # [ cm-3, eV ]
  Acceptor  1.0000e+16,   0.00699   # [ cm-3, eV ]
  Acceptor  2.0000e+16,   0.00854   # [ cm-3, eV ]
  Acceptor  5.0000e+16,   0.01118   # [ cm-3, eV ]
  Acceptor  1.0000e+17,   0.01373   # [ cm-3, eV ]
  Acceptor  2.0000e+17,   0.01690   # [ cm-3, eV ]
  Acceptor  5.0000e+17,   0.02235   # [ cm-3, eV ]
  Acceptor  1.0000e+18,   0.02769   # [ cm-3, eV ]
  Acceptor  2.0000e+18,   0.03442   # [ cm-3, eV ]
  Acceptor  5.0000e+18,   0.04612   # [ cm-3, eV ]
  Acceptor  1.0000e+19,   0.05779   # [ cm-3, eV ]
  Acceptor  2.0000e+19,   0.07270   # [ cm-3, eV ]
  Acceptor  5.0000e+19,   0.09910   # [ cm-3, eV ]
  Acceptor  1.0000e+20,   0.12591   # [ cm-3, eV ]
}
LatticeParameters
{
  X = (0,1,0)
  Y = (1,0,0)
}
* ISE Defaults (consistent with IOFFE 03/09/2006)
eDOSMass
{ * Nc(T) = Nc300 * (T/300)^3/2
      Formula     = 2   # [1]
      Nc300 = 5.6600e+17      # [cm-3]
}
* From IOFFE website (03/09/2006)
hDOSMass
{ * Nv(T) = Nv300 * (T/300)^3/2
      Formula     = 2   # [1]
      Nv300 = 1.1805e+19      # [cm-3]
}
* Dopant dependent effective mass
Poly3x_EffectiveMass
{
      emp0_e = -3.2684e+01    # []
      emp1_e = +5.5799e+00    # []
      emp2_e = -3.1698e-01    # []
```

```
      emp3_e = +6.0073e-03    # []
      emp4_e = +8.0000e-02    # []
      emp0_h = +8.6121e-01    # []
      emp1_h = +0.0000e+00    # []
      emp2_h = +0.0000e+00    # []
      emp3_h = +0.0000e+00    # []
      emp4_h = +8.6121e-01    # []
}
* Based on Ioffe site
DopingDependence:
{ * mu_dop = muminA + mudA/(1.+(N/N00)^AA)
      formula     = 2 , 2     # [1]
      Ar_mumin    = 0.0000e+00 ,    8.0521e+00  # [cm^2/Vs]
      Ar_alm      = -1.5000e+00 ,   -1.7914e+00 # [1]
      Ar_mud      = 5.1378e+03 ,    1.5425e+02  # [cm^2/Vs]
      Ar_ald      = -9.5086e-01 ,   -2.2521e+00 # [1]
      Ar_N0       = 5.1000e+17 ,    7.7700e+17  # [cm^(-3)]
      Ar_alN      = 1.6031e+00 ,    2.3200e+00  # [1]
      Ar_a        = 4.3780e-01 ,    7.9731e-01  # [1]
      Ar_ala      = -2.0000e+00 ,   0.0000e+00  # [1]
}
DopingDependence_aniso:
{
      formula     = 2 , 2     # [1]
      Ar_mumin    = 0.0000e+00 ,    8.0521e+00  # [cm^2/Vs]
      Ar_alm      = -1.5000e+00 ,   -1.7914e+00 # [1]
      Ar_mud      = 5.1378e+03 ,    1.5425e+02  # [cm^2/Vs]
      Ar_ald      = -9.5086e-01 ,   -2.2521e+00 # [1]
      Ar_N0       = 5.1000e+17 ,    7.7700e+17  # [cm^(-3)]
      Ar_alN      = 1.6031e+00 ,    2.3200e+00  # [1]
      Ar_a        = 4.3780e-01 ,    7.9731e-01  # [1]
      Ar_ala      = -2.0000e+00 ,   0.0000e+00  # [1]
}
HighFieldDependence:
{ * Transferred-Electron Effect:
      E0_TrEf           = 8.8000e+03 , 1.0000e+05     # [1]
      Ksmooth_TrEf      = 2.13 , 1              # [1]
      Vsat_Formula      = 2 , 2                 # [1]
      A_vsat      = 1.2500e+07 , 1.0000e+06     # [1]
      B_vsat      = 2.5000e+06 , 0.0000e+00     # [1]
      vsat_min    = 5.0000e+06 , 1.0000e+06     # [1]
}
HighFieldDependence_aniso:
{ * Transferred-Electron Effect:
      E0_TrEf           = 8.8000e+03 , 1.0000e+05     # [1]
      Ksmooth_TrEf      = 2.13 , 1              # [1]
      Vsat_Formula      = 2 , 2                 # [1]
      A_vsat      = 1.2500e+07 , 1.0000e+06     # [1]
      B_vsat      = 2.5000e+06 , 0.0000e+00     # [1]
      vsat_min    = 5.0000e+06 , 1.0000e+06     # [1]
}
Scharfetter * relation and trap level for SRH recombination:
{ * tau = taumin + ( taumax - taumin ) / ( 1 + ( N/Nref )^gamma)
      taumin      = 1.0000e-08 ,    3.0000e-06  # [s]
```

```
      taumax      = 1.0000e-08 ,    3.0000e-06  # [s]
      Nref        = 1.0000e+16 ,    1.0000e+16  # [cm^(-3)]
      gamma       = 1 , 1                       # [1]
      Talpha      = 0.0000e+00 ,    0.0000e+00  # [1]
      Tcoeff      = 0.0000e+00 ,    0.0000e+00  # [1]
      Etrap       = 0.0000e+00                  # [eV]
}
Auger * coefficients:
{ * R_Auger = ( C_n n + C_p p ) ( n p - ni_eff^2)
  * with C_n,p = (A + B (T/T0) + C (T/T0)^2) (1 + H exp(-{n,p}/N0))
      A     = 1.0000e-30 ,    1.0000e-30  # [cm^6/s]
      B     = 0.0000e+00 ,    0.0000e+00  # [cm^6/s]
      C     = 0.0000e+00 ,    0.0000e+00  # [cm^6/s]
      H     = 0.0000e+00 ,    0.0000e+00  # [1]
      N0    = 1.0000e+18 ,    1.0000e+18  # [cm^(-3)]
}
* Impact ionization factors from IOFFE
vanOverstraetendeMan * Impact Ionization:
{ * G_impact = alpha_n n v_drift_n  +  alpha_p p v_drift_p
      a(low)      = 7.6683e+06 ,    4.8159e+06  # [1/cm]
      a(high)     = 7.6683e+06 ,    4.8159e+06  # [1/cm]
      b(low)      = 2.9759e+06 ,    2.5111e+06  # [V/cm]
      b(high)     = 2.9759e+06 ,    2.5111e+06  # [V/cm]
      E0          = 4.0000e+05 ,    4.0000e+05  # [V/cm]
      hbarOmega   = 0.038 , 0.038               # [eV]
}
vanOverstraetendeMan_aniso * Impact Ionization:
{ * G_impact = alpha_n n v_drift_n  +  alpha_p p v_drift_p
      a(low)      = 7.6683e+06 ,    4.8159e+06  # [1/cm]
      a(high)     = 7.6683e+06 ,    4.8159e+06  # [1/cm]
      b(low)      = 2.9759e+06 ,    2.5111e+06  # [V/cm]
      b(high)     = 2.9759e+06 ,    2.5111e+06  # [V/cm]
      E0          = 4.0000e+05 ,    4.0000e+05  # [V/cm]
      hbarOmega   = 0.038 , 0.038               # [eV]
}
* Updated hole factors with mhh+mlh (02/08/2006)
* IOFFE, E.H. Li, & Madelung report lower values of mhh (03/09/2006)
BarrierTunneling
{ * Non Local Barrier Tunneling
      g     = 0.08 , 0.689    # [1]
      mt    = 0.08 , 0.689    # [1]
}
* Value taken from Ioffe site
RadiativeRecombination * coefficients:
{ * R_Radiative = C (n p - ni_eff^2)
      C     = 1.2000e-10      # [cm^3/s]
}
```

E.2 $In_{0.53}Ga_{0.47}As$ Material File

```
Epsilon
{ *  Ratio of the permittivities of material and vacuum
      Xmax(0)           = 0.0000e+00      # [1]
      epsilon(0)        = 15.10           # [1]
      Xmax(1)           = 1.0000e+00      # [1]
      epsilon(1)        = 12.90           # [1]
      B(epsilon(1))     = 6.7000e-01
      C(epsilon(1))     = 2.1005e-06
}
* GaAs and InAs values from Shur and IOFFE (12/23/2005)
LatticeHeatCapacity
{ *  lumped electron-hole-lattice heat capacity
      cv(0)       = 1.3632e+00      # [J/(K cm^3)]
      cv_b(0)     = 2.2550e-04      # [J/(K^2 cm^3)]
      cv_c(0)     = 0.0000e+00      # [J/(K^3 cm^3)]
      cv_d(0)     = 0.0000e+00      # [J/(K^4 cm^3)]
      cv(1)       = 1.7556e+00      # [J/(Kcm^3)]
      cv_b(1)     = 0.0000e+00      # [J/(K^2*cm^3)]
      cv_c(1)     = 0.0000e+00      # [J/(K^3*cm^3)]
      cv_d(1)     = 0.0000e+00      # [J/(K^4*cm^3)]
}
* New values from Liu, IOFFE, Madelung, and Quay
Kappa
{ *  Lattice thermal conductivity
      Formula = 1
      Xmax(0)     = 0.0000e+00      # [1]
      kappa(0)    = 5.8670e-01      # [W/(K cm)]
      kappa_b(0)  =-1.3140e-03      # [W/(K^2 cm)]
      kappa_c(0)  = 8.6610e-07      # [W/(K^3 cm)]
      Xmax(1)           = 0.4700e+00      # [1]
      kappa(1)          = 1.4120e-01      # [W/(K cm)]
      B(kappa(1))       = 0.0000e+00      # [W/(K cm)]
      C(kappa(1))       = 0.0000e+00      # [W/(K cm)]
      kappa_b(1)        =-4.1250e-04      # [W/(K^2 cm)]
      B(kappa_b(1))     = 0.0000e+00      # [W/(K^2 cm)]
      C(kappa_b(1))     = 0.0000e+00      # [W/(K^2 cm)]
      kappa_c(1)        = 3.6120e-07      # [W/(K^3 cm)]
      B(kappa_c(1))     = 0.0000e+00      # [W/(K^3 cm)]
      C(kappa_c(1))     = 0.0000e+00      # [W/(K^3 cm)]
      Xmax(2)           = 1.0000e+00      # [1]
      kappa(2)          = 1.1770e+00      # [W/(K cm)]
      B(kappa(2))       = 0.0000e+00      # [W/(K cm)]
      C(kappa(2))       = 0.0000e+00      # [W/(K cm)]
      kappa_b(2)        =-3.1750e-03      # [W/(K^2 cm)]
      B(kappa_b(2))     = 0.0000e+00      # [W/(K^2 cm)]
      C(kappa_b(2))     = 0.0000e+00      # [W/(K^2 cm)]
      kappa_c(2)        = 2.6250e-06      # [W/(K^3 cm)]
      B(kappa_c(2))     = 0.0000e+00      # [W/(K^3 cm)]
      C(kappa_c(2))     = 0.0000e+00      # [W/(K^3 cm)]
}
```

```
EnergyRelaxationTime
{ *  Energy relaxation times in picoseconds
      (tau_w)_ele = 9.4327e-01      # [ps]
      (tau_w)_hol = 4.0000e-01      # [ps]
      Formula(tau_w)_ele = 2
      Numerator(0)_ele{
        A(0)  =  1.66481714e+02
        P(0)  =  0.00000000e+00
        A(1)  =  2.71630770e+05
        P(1)  =  1.00000000e+00
        A(2)  = -8.34331369e+05
        P(2)  =  2.00000000e+00
        A(3)  =  3.15625484e+05
        P(3)  =  3.00000000e+00
        A(4)  =  7.09082090e+05
        P(4)  =  4.00000000e+00
        G     =  1.00000000e+00
      }
      Denominator(0)_ele{
        A(0)  =  2.51050209e+04
        P(0)  =  0.00000000e+00
        A(1)  = -1.29156848e+05
        P(1)  =  1.00000000e+00
        A(2)  =  4.28248172e+05
        P(2)  =  2.00000000e+00
        A(3)  = -9.99999866e+05
        P(3)  =  3.00000000e+00
        A(4)  =  9.73743174e+05
        P(4)  =  4.00000000e+00
        G     =  1.00000000e+00
      }
}
EnergyFlux
{ *  Coefficient in front of the energy flux equation
      energy_flux_coef_ele    = 1.0 # [1]
      energy_flux_coef_hol    = 1.0 # [1]
}
ThermalDiffusion
{ *  Thermal diffusion factor (0 <= td <= 1)
      td_n  = 1.0000e+00      # [1]
      td_p  = 1.0000e+00      # [1]
}
HeatFlux
{ *  Heat flux factor (0 <= hf <= 1)
      hf_n  = 1   # [1]
      hf_p  = 1   # [1]
      F(0)_ele     = 1.3106e+00
      Numerator(0)_ele{
        A(0)  = -1.46942036e+03
        P(0)  =  0.00000000e+00
        A(1)  =  1.09057358e+05
        P(1)  =  1.00000000e+00
        A(2)  = -7.10130509e+05
        P(2)  =  2.00000000e+00
```

```
        A(3)  = -1.81829516e-04
        P(3)  =  3.00000000e+00
        A(4)  =  5.85850793e-03
        P(4)  =  4.00000000e+00
        G     =  1.00000000e+00
      }
      Denominator(0)_ele{
        A(0)  =  6.58556530e+03
        P(0)  =  0.00000000e+00
        A(1)  = -1.29114789e+05
        P(1)  =  1.00000000e+00
        A(2)  =  9.53251350e+05
        P(2)  =  2.00000000e+00
        A(3)  = -3.33154780e-04
        P(3)  =  3.00000000e+00
        A(4)  =  4.05842567e-03
        P(4)  =  4.00000000e+00
        G     =  1.00000000e+00
      }
}
AvalancheFactors
{ *  Coefficients for avalanche generation with hydro
      n_l_f       = 1.0000e+00      # [1]
      p_l_f       = 1.0000e+00      # [1]
      n_gamma     = 0.0000e+00      # [1]
      p_gamma     = 0.0000e+00      # [1]
      n_delta     = 0.0000e+00      # [1]
      p_delta     = 0.0000e+00      # [1]
}
* Si = Phosphorus = Ndopant; Shallow Telerium = Arsenic
* Deep States = Antimony and Indium
* Carbon = Beryllium = Shallow Acceptor = Boron = Pdopant
Ionization
{
      E_As_0      = 0.030           # [eV]
      alpha_As    = 2.1453e-07      # [eV cm]
      g_As        = 2               # [1]
      Xsec_As     = 1.0000e-12      # [cm^2/sec]
      E_P_0       = 0.006           # [eV]
      alpha_P     = 4.2906e-08      # [eV cm]
      g_P         = 2               # [1]
      Xsec_P      = 1.0000e-20      # [cm^2/sec]
      E_Sb_0      = 0.350           # [eV]
      alpha_Sb    = 0.0000e+00      # [eV cm]
      g_Sb        = 2               # [1]
      Xsec_Sb     = 1.0000e-12      # [cm^2/sec]
      E_B_0       = 0.020           # [eV]
      alpha_B     = 4.7756e-08      # [eV cm]
      g_B         = 4               # [1]
      Xsec_B      = 1.0000e-12      # [cm^2/sec]
      E_In_0      = 0.350           # [eV]
      alpha_In    = 0.0000e+00      # [eV cm]
      g_In        = 4               # [1]
      Xsec_In     = 1.0000e-20      # [cm^2/sec]
```

```
      E_N_0       = 0.030           # [eV]
      alpha_N     = 7.1634e-08      # [eV cm]
      g_N         = 4               # [1]
      Xsec_N      = 1.0000e-12      # [cm^2/sec]
      E_NDopant_0 = 0.006           # [eV]
      alpha_NDopant = 4.2906e-08    # [eV cm]
      g_NDopant   = 2               # [1]
      Xsec_NDopant= 1.0000e-12      # [cm^2/sec]
      E_PDopant_0 = 0.020           # [eV]
      alpha_PDopant = 4.7756e-08    # [eV cm]
      g_PDopant   = 4               # [1]
      Xsec_PDopant= 1.0000e-12      # [cm^2/sec]
      NdCrit      = 2.7345e+15      # [cm-3]
      NaCrit      = 7.3451e+16      # [cm-3]
}
* All parameters re-extracted (see James Li's spreadsheet 12/21/2005)
Bandgap
{ * Eg = Eg0 + alpha Tpar^2 / (beta + Tpar) - alpha T^2 / (beta + T)
      Tpar              = 0.0000e+00      # [K]
      Xmax(0)           = 0.0000e+00      # [1]
      Eg0(0)            = 0.4200e+00      # [eV]
      alpha(0)          = 4.1900e-04      # [eV K^-1]
      beta(0)           = 2.7100e+02      # [K]
      Chi0(0)           = 4.9000e+00      # [eV]
      Bgn2Chi           = 0.5             # []
      Xmax(1)           = 1.0000e+00      # [1]
      Eg0(1)            = 1.5200e+00      # [eV]
      B(Eg0(1))         = 0.4750e+00      # [eV]
      C(Eg0(1))         = 0.0000e+00      # [eV]
      alpha(1)          = 5.8000e-04      # [eV K^-1]
      B(alpha(1))       = 7.1600e-06      # [eV K^-1]
      C(alpha(1))       = 0.0000e+00      # [eV K^-1]
      beta(1)           = 3.0000e+02      # [K]
      B(beta(1))        = 4.7492e-01      # [K]
      C(beta(1))        = 0.0000e+00      # [K]
      Chi0(1)           = 4.0700e+00      # [eV]
      B(Chi0(1))        =-0.47500e+00     # [eV]
      C(Chi0(1))        = 0.0000e+00      # [eV]
}
TableBGN
{
  Donor     1.0000e+13,   0.00000   # [ cm-3, eV ]
  Donor     1.0000e+14,   0.00259   # [ cm-3, eV ]
  Donor     2.0000e+14,   0.00323   # [ cm-3, eV ]
  Donor     5.0000e+14,   0.00434   # [ cm-3, eV ]
  Donor     1.0000e+15,   0.00543   # [ cm-3, eV ]
  Donor     2.0000e+15,   0.00679   # [ cm-3, eV ]
  Donor     5.0000e+15,   0.00913   # [ cm-3, eV ]
  Donor     1.0000e+16,   0.01143   # [ cm-3, eV ]
  Donor     2.0000e+16,   0.01431   # [ cm-3, eV ]
  Donor     5.0000e+16,   0.01927   # [ cm-3, eV ]
  Donor     1.0000e+17,   0.02415   # [ cm-3, eV ]
  Donor     2.0000e+17,   0.03027   # [ cm-3, eV ]
  Donor     5.0000e+17,   0.04081   # [ cm-3, eV ]
```

```
  Donor     1.0000e+18,   0.05119   # [ cm-3, eV ]
  Donor     2.0000e+18,   0.06421   # [ cm-3, eV ]
  Donor     5.0000e+18,   0.08668   # [ cm-3, eV ]
  Donor     1.0000e+19,   0.10879   # [ cm-3, eV ]
  Donor     2.0000e+19,   0.13657   # [ cm-3, eV ]
  Donor     5.0000e+19,   0.18451   # [ cm-3, eV ]
  Donor     1.0000e+20,   0.23173   # [ cm-3, eV ]
  Acceptor  1.0000e+13,   0.00000   # [ cm-3, eV ]
  Acceptor  1.0000e+14,   0.00159   # [ cm-3, eV ]
  Acceptor  2.0000e+14,   0.00193   # [ cm-3, eV ]
  Acceptor  5.0000e+14,   0.00250   # [ cm-3, eV ]
  Acceptor  1.0000e+15,   0.00304   # [ cm-3, eV ]
  Acceptor  2.0000e+15,   0.00371   # [ cm-3, eV ]
  Acceptor  5.0000e+15,   0.00483   # [ cm-3, eV ]
  Acceptor  1.0000e+16,   0.00592   # [ cm-3, eV ]
  Acceptor  2.0000e+16,   0.00726   # [ cm-3, eV ]
  Acceptor  5.0000e+16,   0.00954   # [ cm-3, eV ]
  Acceptor  1.0000e+17,   0.01177   # [ cm-3, eV ]
  Acceptor  2.0000e+17,   0.01456   # [ cm-3, eV ]
  Acceptor  5.0000e+17,   0.01938   # [ cm-3, eV ]
  Acceptor  1.0000e+18,   0.02414   # [ cm-3, eV ]
  Acceptor  2.0000e+18,   0.03018   # [ cm-3, eV ]
  Acceptor  5.0000e+18,   0.04077   # [ cm-3, eV ]
  Acceptor  1.0000e+19,   0.05144   # [ cm-3, eV ]
  Acceptor  2.0000e+19,   0.06517   # [ cm-3, eV ]
  Acceptor  5.0000e+19,   0.08972   # [ cm-3, eV ]
  Acceptor  1.0000e+20,   0.11490   # [ cm-3, eV ]
}
LatticeParameters
{
  X = (0,1,0)
  Y = (1,0,0)
}
* GaAs (x=1) parameters from Ioffe and Shur (12/21/2005)
* InAs (x=0) parameters from Ioffe and Shur (12/21/2005)
eDOSMass
{ * Nc(T) = Nc300 * (T/300)^3/2
      Formula     = 2   # [1]
      Nc300(0)    = 8.8598e+16      # [cm-3]
      Nc300(1)    = 4.0165e+17      # [cm-3]
      B(Nc300(1)) = 9.8231e+16
      C(Nc300(1)) = 0.0000e+00
}
* GaAs (x=1) parameters from Ioffe and Shur (12/21/2005)
* InAs (x=0) parameters from Ioffe and Shur (03/09/2006)
hDOSMass
{ * Nv(T) = Nv300 * (T/300)^3/2
      Formula     = 2   # [1]
      Nv300(0)    = 6.6682e+18      # [cm-3]
      Nv300(1)    = 9.8474e+18      # [cm-3]
      B(Nv300(1)) = 2.7180e+17
      C(Nv300(1)) = 0.0000e+00
}
* Dopant dependent effective mass (x=0.47 only)
```

```
Poly3x_EffectiveMass
{
      emp0_e = -4.2629e+01    # []
      emp1_e = +7.2756e+00    # []
      emp2_e = -4.1373e-01    # []
      emp3_e = +7.8474e-03    # []
      emp4_e = +4.1000e-02    # []
      emp0_h = +4.5700e-01    # []
      emp1_h = +0.0000e+00    # []
      emp2_h = +0.0000e+00    # []
      emp3_h = +0.0000e+00    # []
      emp4_h = +4.5700e-01    # []
}
* Values calibrated for In0.53Ga0.47As only
DopingDependence:
{ * mu_dop = muminA + mudA/(1.+(N/N00)^AA)
      formula     = 2 , 2     # [1]
      Ar_mumin    = 3.3505e+03 ,    2.0000e+01  # [cm^2/Vs]
      Ar_alm      =-1.5000e+00 , -1.5000e+00    # [1]
      Ar_mud      = 1.1897e+04 ,    2.0000e+02  # [cm^2/Vs]
      Ar_ald      =-1.5000e+00 , -1.5000e+00    # [1]
      Ar_N0       = 7.9461e+16 ,    3.3300e+18  # [cm^(-3)]
      Ar_alN      = 0.0000e+00 ,    0.0000e+00  # [1]
      Ar_a        = 5.5924e-01 ,    8.5000e-01  # [1]
      Ar_ala      = 0.0000e+00 ,    0.0000e+00  # [1]
}
DopingDependence_aniso:
{
      formula     = 2 , 2     # [1]
      Ar_mumin    = 3.3505e+03 ,    2.0000e+01  # [cm^2/Vs]
      Ar_alm      =-1.5000e+00 , -1.5000e+00    # [1]
      Ar_mud      = 1.1897e+04 ,    2.0000e+02  # [cm^2/Vs]
      Ar_ald      =-1.5000e+00 , -1.5000e+00    # [1]
      Ar_N0       = 7.9461e+16 ,    3.3300e+18  # [cm^(-3)]
      Ar_alN      = 0.0000e+00 ,    0.0000e+00  # [1]
      Ar_a        = 5.5924e-01 ,    8.5000e-01  # [1]
      Ar_ala      = 0.0000e+00 ,    0.0000e+00  # [1]
}
* Transferred electron values calibrated for In0.53Ga0.47As only
HighFieldDependence:
{ * Transferred-Electron Effect:
      E0_TrEf           = 3.5000e+03 ,    1.0000e+05  # [1]
      Ksmooth_TrEf      = 1.3300e+00 ,    2.0000e+01  # [1]
      Vsat_Formula      = 2 , 2     # [1]
      A_vsat            = 1.4150e+07 ,    4.8000e+06  # [1]
      B_vsat            = 1.6500e+06 ,    0.0000e+00  # [1]
      vsat_min          = 5.0000e+06 ,    4.8000e+06  # [1]
}
HighFieldDependence_aniso:
{ * Transferred-Electron Effect:
      E0_TrEf           = 3.5000e+03 ,    1.0000e+05  # [1]
      Ksmooth_TrEf      = 1.3300e+00 ,    2.0000e+01  # [1]
      Vsat_Formula      = 2 , 2     # [1]
      A_vsat            = 1.4150e+07 ,    4.8000e+06  # [1]
```

```
      B_vsat            = 1.6500e+06 ,    0.0000e+00  # [1]
      vsat_min          = 5.0000e+06 ,    4.8000e+06  # [1]
}
* Values calibrated for In0.53Ga0.47As only
Scharfetter * relation and trap level for SRH recombination:
{ * tau = taumin + ( taumax - taumin ) / ( 1 + ( N/Nref )^gamma)
      taumin      = 5.0000e-10 ,    5.0000e-10  # [s]
      taumax      = 5.0000e-07 ,    5.0000e-07  # [s]
      Nref        = 1.5000e+17 ,    5.1000e+17  # [cm^(-3)]
      gamma       = 1.6500e+00 ,    1.6000e+00  # [1]
      Talpha      = 0.0000e+00 ,    0.0000e+00  # [1]
      Tcoeff      = 0.0000e+00 ,    0.0000e+00  # [1]
      Etrap       = 0.0000e+00                  # [eV]
}
* Values calibrated to In0.53Ga0.47As only
Auger * coefficients:
{ * R_Auger = ( C_n n + C_p p ) ( n p - ni_eff^2)
      A     = 7.0000e-29 ,    7.0000e-29  # [cm^6/s]
      B     = 0.0000e+00 ,    0.0000e+00  # [cm^6/s]
      C     = 0.0000e+00 ,    0.0000e+00  # [cm^6/s]
      H     = 0.0000e+00 ,    0.0000e+00  # [1]
      N0    = 1.0000e+18 ,    1.0000e+18  # [cm^(-3)]
}
* Values calibrated to In0.53Ga0.47As only
vanOverstraetendeMan * Impact Ionization:
{ * G_impact = alpha_n n v_drift_n  +  alpha_p p v_drift_p
      a(low)      = 3.3183e+05 ,    6.3937e+05  # [1/cm]
      a(high)     = 3.3183e+05 ,    6.3937e+05  # [1/cm]
      b(low)      = 1.2083e+06 ,    1.5403e+06  # [V/cm]
      b(high)     = 1.2083e+06 ,    1.5403e+06  # [V/cm]
      E0          = 4.0000e+05 ,    4.0000e+05  # [V/cm]
      hbarOmega   = 0.0340e+00 ,    0.0340e+00  # [eV]
}
vanOverstraetendeMan_aniso * Impact Ionization:
{ * G_impact = alpha_n n v_drift_n  +  alpha_p p v_drift_p
      a(low)      = 3.3183e+05 ,    6.3937e+05  # [1/cm]
      a(high)     = 3.3183e+05 ,    6.3937e+05  # [1/cm]
      b(low)      = 1.2083e+06 ,    1.5403e+06  # [V/cm]
      b(high)     = 1.2083e+06 ,    1.5403e+06  # [V/cm]
      E0          = 4.0000e+05 ,    4.0000e+05  # [V/cm]
      hbarOmega   = 0.0340e+00 ,    0.0340e+00  # [eV]
}
* Values taken from Ioffe and Shur (12/21/2005)
* Updated mhh+mlh, In0.53Ga0.47As mhh=0.457,mlh=0.05232 (02/08/2006)
BarrierTunneling
{ * Non Local Barrier Tunneling
      g     = 0.041 , 0.509   # [1]
      mt    = 0.041 , 0.509   # [1]
}
* Value taken from Ioffe site
RadiativeRecombination * coefficients:
{ * R_Radiative = C (n p - ni_eff^2)
      C     = 0.9600e-10      # [cm^3/s]
}
```

E.3 Thermal Conductivities

The DESSIS thermal conductivity model uses a second-order polynomial to represent the temperature dependence,

$$\mathrm{K} = \mathrm{K}\_a + \mathrm{K}\_b \cdot T + \mathrm{K}\_c \cdot T^2 \tag{E-1}$$

where the parameters *K_a*, *K_b*, *K_c* are specificied by the user, and *T* is the lattice temperature in Kelvin. The following table summarizes the parameters used in the thermal simulations presented in Chapters 3 and 4.

Table E-1: Summary of the thermal conductivity model parameters used in the thermal simulations presented Chapters 3 and 4.

Material	*K_a*	*K_b*	*K_c*
InP	1.9470e+00	-5.4890e-03	4.2160e-06
$In_{1-x}Ga_xAs$ (x = 0.00)	5.8670e-01	-1.3140e-03	8.6610e-07
$In_{1-x}Ga_xAs$ (x = 0.47)	1.4120e-01	-4.1250e-04	3.6120e-07
$In_{1-x}Ga_xAs$ (x = 1.00)	1.1770e+01	-3.1750e-03	2.6250e-06
Gold	3.1000e+00	0.0000e+00	0.0000e+00
BCB	1.0000e-03	0.0000e+00	0.0000e+00